ATMIRE

Title	Data-driven study of mineral mapping for geothermal exploration, A
Item Type	Text
Authors	Yu, Yu-Ting
Publisher	Colorado School of Mines. Arthur Lakes Library
Rights	Copyright of the original work is retained by the author.
Download date	2026-11-28 04:41:53
Link to Item	https://hdl.handle.net/11124/181197

A DATA-DRIVEN STUDY OF MINERAL MAPPING FOR GEOTHERMAL EXPLORATION

by

Yu-Ting Yu

© Copyright by Yu-Ting Yu, 2025

All Rights Reserved

A thesis submitted to the Faculty and the Board of Trustees of the Colorado School of Mines in partial fulfillment of the requirements for the degree of Doctor of Philosophy (Earth Resources Development Engineering).

Golden, Colorado

Date _____

Signed: _____

Yu-Ting Yu

Signed: _____

Dr. H. Sebnem Duzgun
Thesis Advisor

Golden, Colorado

Date _____

Signed: _____

Bill Zisch
Department Head
Department of Mining Engineering

ABSTRACT

Geothermal energy has emerged to play a pivotal role in the green energy transition. It is considered a critical renewable energy source due to its reliability as a baseload energy source. Geothermal exploration and development are challenging due to geological complexities. Mineral mapping is a powerful tool that supports geological surveys. However, making unbiased decisions during mapping procedures and efficiently interpreting mineral maps can be challenging. A data-driven study was introduced to evaluate mineral mapping approaches and explore the relations between mapped indicator minerals and other geothermal exploration parameters, including faults and land surface temperatures (LST). The study established a local Coso Spectral Library based on the sample of the Coso geothermal field in the USA. The library offers spectra for mapping tasks and provides ground truth information for accuracy assessment for mineral maps.

To identify the influence of mapping methods in mineral mapping, mineral maps were evaluated based on varied implementations of mapping algorithms, fusion combinations, and splice correction. The result identified that different mapping algorithms offered different mapping accuracies. Additionally, the fusion of mineral maps and splice correction increases mapping accuracy.

The study further assesses the influence of spectra sources on mineral maps, including spectral variabilities and spectral libraries. The result identified that spectral variability could significantly impact the accuracy of specific mapping algorithms. The local spectra library also proved to offer mineral maps with higher accuracy levels.

With the refined mineral mapping strategy based on the study of Coso, the coverage of study areas was expanded to Brady geothermal fields and Desert Peak geothermal fields to discover relations between the maps of indicator minerals, faults, and LSTs. The study integrated non-spatial and spatial techniques to explore significant relations between the selected geothermal exploration parameters. The results have discovered that different indicator minerals present varied tendencies toward faults and elevated LST. The finding elucidates the ability of data analysis to identify subtle patterns for geological interpretation and geothermal exploration.

TABLE OF CONTENTS

ABSTRACT iii
TABLE OF CONTENTS iv
LIST OF FIGURES vii
LIST OF TABLES ix
LIST OF ABBREVIATIONS x
ACKNOWLEDGMENTS xi
CHAPTER 1 INTRODUCTION 1
1.1 The Research Goal 5
1.2 The Research Objectives, Questions, and Hypotheses 6
1.3 The Original Contribution of the Dissertation 8
1.4 Organization of the Dissertation 8
CHAPTER 2 METHODOLOGY 9
2.1 Satellite Data Processing and Mineral Mapping 11
2.2 Accuracy Assessment and Refining Mapping Strategy 14
CHAPTER 3 STUDY AREAS 16
3.1 Coso Geothermal Field 16
3.2 Brady Geothermal Field and Desert Peak Geothermal Field 18
CHAPTER 4 ESTABLISHMENT OF THE COSO SPECTRAL LIBRARY 21
4.1 Implementation for Establishing Spectral Library 21
4.1.1 Sample Collection and Field Survey 22
4.1.2 Laboratory Measurements 23
4.1.3 Spectral Data Processing 26
4.1.4 Establishment of Spectral Library 28
4.2 The Coso Spectral Library and Geodatabase 29
CHAPTER 5 STAGE I: STUDY OF MAPPING METHODS IN MINERAL MAPPING 32
5.1 Implementation of the Analysis 32
5.2 Results and Discussion 36
5.2.1 Mapping With Various Mapping Algorithms 36
5.2.2 Mapping With Various Fusion Combinations 39

5.2.3 Mapping With Various Employments of Splice Correction 41
CHAPTER 6 STAGE II: STUDY OF SPECTRA SOURCE IN MINERAL MAPPING 42
6.1 Implementation of the Analysis 42
6.2 Results and Discussion 46
6.2.1 Mapping With Different Spectral Variabilities 46
6.2.2 Mapping With Different Spectral Libraries 55
6.3 CGF Mineral Maps Based on the Refined Mineral Mapping Strategy 60
CHAPTER 7 STAGE III: DATA-DRIVEN STUDY OF EXPLORATION PARAMETERS 61
7.1 Implementation of the Analysis 61
7.1.1 Data Collection and Preparation 61
7.1.2 Data Analysis 67
7.2 Results of the Data Analysis 70
7.2.1 Non-Spatial Analysis 70
7.2.2 Spatial Analysis 77
7.3 Discussion of the Data-Driven Analysis 83
CHAPTER 8 OVERALL CONCLUSIONS AND RECOMMENDATIONS FOR FUTURE WORKS 85
8.1 Objective One: Evaluate the influence of mapping methods 85
8.2 Objective Two: Evaluate the influence of spectra sources 86
8.3 Objective Three: Explore the relations between the SGP 87
8.4 Recommendations for Future Work 88
REFERENCES 89
APPENDIX A PHOTOS OF THE COSO SAMPLES 102
APPENDIX B MINERALOGICAL ASSESSMENT OF COSO SAMPLES 125
APPENDIX C HISTOGRAMS AND CDF OF RELATIONS BETWEEN SGP 129
APPENDIX D SUPPLEMENTARY DATA OF LINEAR REGRESSIONS BETWEEN SGP 133
APPENDIX E PERMISSION 134
APPENDIX F ARTICLE ON MINERAL MAPPING WITH VARIOUS METHODOLOGIES 135
F.1 Abstract 135
APPENDIX G ARTICLE OF MINERAL MAPPING WITH SPECTRAL VARIABILITY (UNPUBLISHED) 136
G.1 Abstract 136
G.2 Introduction 136
G.3 Study Materials 138

G.4 Methodology 144
G.5 Result and Discussion 147
G.6 Conclusion 158

APPENDIX H ARTICLE OF DATA-DRIVEN STUDY ON SGP (UNPUBLISHED) 160

H.1 Abstract 160
H.2 Introduction 160
H.3 The Study Areas 162
H.4 Methodology 165
H.5 Results 171
H.6 Discussion 181
H.7 Conclusion 183

LIST OF FIGURES

Figure 2.1 The overall research framework. 9
Figure 2.2 The framework of mineral mapping and accuracy assessment. 10
Figure 2.3 The detailed framework of mineral mapping. 11
Figure 2.4 The detailed framework of accuracy assessment. 14
Figure 3.1 Map of the Coso Geothermal Field. 17
Figure 3.2 Map of the Brady and Desert Peak Geothermal Field. 19
Figure 4.1 Framework for establishing the Coso Spectral Library and geodatabase. 21
Figure 4.2 Sample and spectra collection at the CGF. 22
Figure 4.3 Location of samples selected for automated mineralogy analysis. 24
Figure 4.4 Structure of the proposed geodatabase 28
Figure 4.5. The sample distribution of collected MOI spectra. 31
Figure 5.1. The selected CGF spectra of MOI for the mineral mapping study. 35
Figure 5.2 MOI spectra of the USGS Spectral Library and the Coso Spectral Library. 35
Figure 5.3 The mineral density maps by the selected CGF spectra. Each column is one type of MOI, and each row is one mapping algorithm. 37
Figure 5.4 ROC curves of the five MOI with different mapping algorithms. 38
Figure 5.5 ROC curves of the five MOI with various fusion combinations. 40
Figure 6.1 The alunite and kaolinite spectra of the Coso Spectral Library. 43
Figure 6.2 The alunite and kaolinite spectra of the USGS Spectral Library. 44
Figure 6.3 The resampled alunite spectra in ASTER bands. 44
Figure 6.4 The resampled kaolinite spectra in ASTER bands. 45
Figure 6.5 The alunite mineral density maps. Each raw is one spectrum from the Coso Spectral Library and the USGS spectral library. Each column refers to one mapping algorithm. 47
Figure 6.6 The kaolinite mineral density maps. Each raw is one spectrum from the Coso Spectral Library and the USGS spectral library. Each column refers to one mapping algorithm. 48
Figure 6.7 The ROC curves and AUC values from accuracy assessments of alunite mappings. 49
Figure 6.8 The ROC curves and AUC values from accuracy assessments of kaolinite mappings. 50
Figure 6.9 Comparison of alunite maps based on a control group of Coso-034 54
Figure 6.10 Comparison of kaolinite maps based on a control group of Coso-032 55
Figure 6.11 Density maps of mineral mapping by CGF and USGS spectra. 56
Figure 6.12 ROC curves of mineral maps by CGF spectra (blue) and USGS spectra (red). 57

Figure 6.13 Comparison of mineral maps using CGF spectra and USGS spectra in opal mapping through the SAM algorithm. 59

Figure 7.1 Workflow of indicator mineral map data preparation. Two datasets, in bold, were prepared based on indicator mineral maps: Two-Class Mineral Maps and Mineral Density Maps. 62

Figure 7.2 Illustration of indicator mineral map datasets. 63

Figure 7.3 Workflow of fault map data preparation. Three datasets, in bold, were prepared based on faults: Fault Traces (bottom left), Fault Distance Maps, and Fault Density Maps. 64

Figure 7.4 Illustration of fault map datasets. 64

Figure 7.5 Workflow of LST data preparation. Two datasets, in bold, were prepared based on LSTs: Multiclass Temperature Maps (right) and Two-class Temperature Maps (bottom-right). 65

Figure 7.6 Illustration of LST datasets. 66

Figure 7.7 Histograms (gray boxes) and CDF plots (red lines) of the patterns between Two-Class Mineral Maps and Fault Distance Maps at CGF. Multiple MOI show distributions closer to faults than the locations without MOI (bottom-right), with CDF plots shifting closer to the top-right corners. The patterns between MOI are also different. 71

Figure 7.8 Histograms (gray boxes) and CDF plots (red lines) of the patterns between Two-Class Temperature Maps and Fault Distance Maps at each study area. High temperatures (top) of CGF (left) and BGF (middle) show distributions closer to faults than DPGF (right). 72

Figure 7.9 Histograms (gray boxes) and CDF plots (red lines) of the patterns between Two-Class Mineral Maps and Multiclass Temperature Maps at CGF. Alunite and kaolinite are closer to higher temperatures, while chalcedony and opal are closer to lower temperatures. 72

Figure 7.10 The multiple comparisons of ANOVA. The plots show the mean estimates (circles) and 95% confidence intervals (bars) for each group of SGP. Red symbols highlight groups with Significant Differences from the control group (blue). Gray symbols indicate groups with Insignificant Differences where confidence intervals overlap with the control group. 75

Figure 7.11 Colocation maps of faults and neighboring indicator minerals at CGF. 78

Figure 7.12 Colocation of faults and neighboring indicator minerals at BGF. 79

Figure 7.13 Colocation of faults and neighboring indicator minerals at DPGF. 79

Figure 7.14 Colocation maps of faults and neighboring high temperatures. 80

Figure 7.15 Colocation of high temperatures and neighboring indicator minerals at CGF. 81

Figure 7.16 Colocation of high temperatures and neighboring indicator minerals at BGF. 82

Figure 7.17 Colocation of high temperatures and neighboring indicator minerals at DPGF. 82

LIST OF TABLES

Table 1-1 Research objectives, questions, and hypotheses. 8

Table 2-1 A typical example of a True/False confusion matrix. 15

Table 3-1 Geothermal features of the CGF, BGF, and DPGF. 20

Table 4-1 The ranking of SAM results by THOR Material Identification in ENVI software. 27

Table 4-2 A summary of the SEM-based automated mineralogy. 30

Table 4-3 The Coso samples with identified spectra of the MOI. 31

Table 5-1 Correlation matrix for alunite spectra. 33

Table 5-2 Correlation matrix for chalcedony spectra. 33

Table 5-3 Correlation matrix for epidote spectra. 34

Table 5-4 Correlation matrix for hematite spectra. 34

Table 5-5 Correlation matrix of kaolinite spectra. 34

Table 5-6 Correlation matrix for opal spectra. 34

Table 5-7 The AUC levels of mineral maps of the CGF by different mapping algorithms. 37

Table 5-8 The studies comparing algorithm performance. 38

Table 5-9 The AUC levels of mineral maps of various fusion combinations. 39

Table 5-10 Comparison of the AUC levels of mineral maps based on the CGF spectra with the different applications of splice correction. 41

Table 6-1 Alunite spectra by ASD FieldSpec in the USGS Spectral Library 43

Table 6-2 Kaolinite spectra by ASD FieldSpec in the USGS Spectral Library 43

Table 6-3 The AUC values and associated averages and ranges by spectrum. 51

Table 6-4 The statistics of AUC by each mapping algorithm. 52

Table 6-5 Summary of AUC values of mineral maps by CGF spectra and USGS spectra. 58

Table 6-6 Comparison of AUC values of mineral maps by CGF spectra and USGS spectra with the three-percent threshold. 58

Table 7-1 Adopted data analysis methods and corresponding input datasets. 69

Table 7-2 The K-S test result. The null hypothesis was rejected in most cases, showing that the distributions of datasets are primarily different. 73

Table 7-3 Regression parameters for Fault Density Maps against Mineral Density Maps 76

Table 7-4 Regression parameters for Multiclass Temperature Maps against Fault Density and Mineral Density Maps 77

Table 7-5 Relations between SGP from non-spatial analyses. 83

LIST OF ABBREVIATIONS

Remote Sensing…….……	RS
Geographic Information System……	GIS
Mineral of Interest…….……	MOI
Selected Geothermal Parameters……..……	SGP
Coso Geothermal Field…….....…	CGF
Brady Geothermal Field……...…	BGF
Desert Peak Geothermal Field……..……	DPGF
United States Geological Survey……..…	USGS
Advanced Spaceborne Thermal Emission and Reflection Radiometer……....…	ASTER
Visible and Near-Infrared…….……	VNIR
Short-Wave Infrared…….……	SWIR
Environment for Visualizing Images (software)……..…	ENVI
Adaptive Coherence Estimator……...…..	ACE
Constrained Energy Minimization……	CEM
Matched Filtering……..…	MF
Mixture Tuned Matched Filtering……..…	MTMF
Spectral Angle Mapper……..……	SAM
Receiver Operating Characteristic……..…	ROC
Area Under the Curve……	AUC
Minimum Noise Fraction……...…	MNF
Fully Constrained Linear Spectral Unmixing……	FCLSU
Land Surface Temperature……..…	LST

ACKNOWLEDGMENTS

I am deeply grateful to my advisor, Dr. H. Sebnem Duzgun, for her tremendous support and guidance throughout this research. I also extend my sincere appreciation to my committee members, Dr. Thomas Monecke, Dr. Zhaoshan Chang, and Dr. Wendy Zhou, for their valuable feedback. In particular, I thank Dr. Monecke for illustrating hydrothermal mineralogy, Dr. Chang for his insights into hyperspectral analysis, and Dr. Zhou for her guidance in GIS data analysis.

I am thankful for the generous support from the Navy Geothermal Program Office and Coso Operating Company, especially Dr. Andrew Sabin, Kelly Blake, Jade Zimmerman, Christopher Ellis, and Cliff Buck. This research was funded by the U.S. Department of Energy (Grant No. DE-EE0008760). I also appreciate the resources provided by the Colorado School of Mines, including access to laboratory facilities and the High-Performance Computing Center.

I sincerely appreciate the contributions of my research collaborators, Dr. Ebubekir Demir, Dr. Mahmut Cavur, Dr. Jaime Moraga, and Erika Erika, particularly in mineral mapping and accuracy assessment. I also thank Kemalcan Aydogdu for his assistance in fieldwork.

I extend my gratitude to Dr. Katharina Pfaff, Filip Kasprowicz, and Kelsey Livingston from Mineral and Materials Characterization at the Colorado School of Mines for their assistance with laboratory measurements. Special thanks to Mary Doherty for a wonderful experience working together as a TA and to MURF student Charlie Marrs for his contributions. I am also grateful to David Hatchell for his expertise with ASD FieldSpec. Additionally, I appreciate Dr. David Hsu and Dr. Oliver Chang for their insights into data analysis and remote sensing.

Finally, I am deeply grateful to my family and friends for their unwavering support and encouragement. My love and appreciation also go to my homeland, which has shaped my identity and fueled my passion for science and exploration.

CHAPTER 1 INTRODUCTION

Geothermal energy can provide a sustainable baseload energy supply and enhance regional energy independence (Troccoli, 2009). However, geothermal exploration requires lengthy and costly geological surveys to understand resource potential, including fluid pathways, fluid characteristics, and temperature ranges (Gehringer & Loksha, 2012; Harvey et al., 2014; Moeck, 2014). Geological uncertainties introduce complexities to any exploration program, thereby increasing the risks and costs in geothermal systems' early exploration and development (Cole et al., 2016; Wall et al., 2017; Witter et al., 2019).

Geothermal systems are found in multiple geological settings, including both magmatic and amagmatic settings (Jolie et al., 2021; Sigurdsson et al., 2015). Geothermal field exploration in all systems typically includes geologic mapping, geochemical and geophysical studies, and drilling with logging (Ármannsson & Fridriksson, 2009; Boden, 2016; D'amore & Panichi, 1985; Domra Kana et al., 2015; Gasperikova & Cumming, 2020; Harvey et al., 2014; Minissale, 2018; Ochieng, 2014; Rodriguez-Gomez et al., 2021; Stober & Bucher, 2021; van der Meer, Hecker, et al., 2014; Witter et al., 2019; Wright et al., 1985). Mapping has various objectives, including determining the structural setting of a prospective area and identifying any surficial features associated with active or paleo-hydrothermal systems like fumaroles, hot springs, and hydrothermal alteration assemblages (Boden, 2016; Harvey et al., 2014). Assessing the distribution of geothermal features across multiple fields provides insights into the overall setting of a potential geothermal system, aiding in identifying critical indicators and efficiently targeting geothermal resources.

Aiming to reduce geological uncertainties and enhance efficiency in geothermal exploration, this dissertation presented a data-driven analysis to address multiple objectives of utilizing remote sensing (RS) methods in geothermal resource exploration. The subsequent sections encapsulate the challenges linked to RS-based mineral mapping in geothermal exploration, the methodologies employed in mineral mapping via RS, the spectra sources utilized in mineral mapping, and the interrelations among geothermal exploration parameters, including mineral maps, which are meticulously examined and enhanced throughout this dissertation.

RS-based Mineral Mapping for Geothermal Exploration

Investigating the distribution of hydrothermal alteration minerals holds the potential to unravel the conditions of geothermal fields (Savitri et al., 2021). Geological surveys benefit from RS, which utilizes spectral signatures for mineral mapping to detect alteration zones associated with current and ancient geothermal systems (C. Bishop et al., 2018; Kratt et al., 2010; Rodriguez-Gomez et al., 2021; Savitri et al., 2021; Simpson & Rae, 2018). Mineral mapping has been widely applied by using RS images from

different platforms, such as ASTER (Advanced Spaceborne Thermal Emission and Reflection Radiometer) (Calvin et al., 2015; van der Meer, Hecker, et al., 2014), Landsat 8 (Nait Amara et al., 2019; Salamba et al., 2019), or WorldView-3 (Kruse & Perry, 2013; Mars, 2018). These studies demonstrate the powerful ability and potential of mineral mapping in geothermal exploration, as large areas can be quickly prioritized for more detailed field analyses based on interpretations of these RS data. However, there is a lack of statistical support behind the decision-making in mineral mapping strategy, such as the application of mapping methods and the selection of spectra sources.

Mapping Methods in Mineral Mapping Using RS

Multiple mapping algorithms have been developed to interpret spectral signals from images. The commercial software ENVI has eight algorithms for its Target Detection Wizard toolset (Wolfe & Black, 2018), including Adaptive Coherence Estimator (ACE), Constrained Energy Minimization (CEM), Matched Filtering (MF), Mixture-Tuned Matched Filtering (MTMF), Orthogonal Subspace Projection (OSP), Spectral Angle Mapper (SAM), Target-Constrained Interference-Minimized Filter (TCIMF), and Mixture-Tuned Target-Constrained Interference-Minimized Filter (MTTCIMF). However, studies commonly focus on limited algorithms such as SAM (Abubakar et al., 2018; Park & Choi, 2021), MF (Kratt et al., 2006; Molan et al., 2014), or MTMF (Abubakar et al., 2019; Calvin et al., 2015). Despite some researchers having demonstrated interest in ranking the performance of different mapping algorithms, none of those studies have been exclusively dedicated to mineral mapping (Jin et al., 2009; Marwaha et al., 2015; Shang et al., 2020; Jawak et al., 2022a, 2022b).

Some researchers performed fusions of mineral maps due to the potential value of integrating outputs of various mapping algorithms (Erika, 2022; Moraga & Duzgun, 2022). The studies fused multiple mineral maps to collectively consider all the mapped areas from various mapping algorithms. However, these studies with mineral map fusions did not further assess if the accuracies of the fused mineral maps were actually higher than those offered by individual mapping algorithms. The studies also did not evaluate the mapping accuracies from various combinations of selected algorithms to fused (hereafter referred to as fusion combination).

In addition, spectral studies often employ splice corrections to address discontinuities or steps that arise when merging data from different sensors within a spectrometer (Gaigalas et al., 2009). This process improves the quality of spectra by adjusting spectral data to smooth out those signal gaps. Although splice correction is commonly used in spectral studies, its impact on the accuracy of mineral mapping remains unclear, particularly when comparing the results from splice-corrected and uncorrected spectra.

Spectra Sources in Mineral Mapping

Spectral libraries offer valuable references to hyperspectral signals used in mineral mapping. The most widely recognized spectral libraries for Earth's materials, like rocks and minerals, include the USGS (United States Geological Survey) Spectral Library Version 7 (Kokaly et al., 2017), the Terrestrial Tephra Spectral Library (USGS; Leight et al., 2022), NASA ASTER Spectral Library (Baldridge et al., 2009), and the National Mineral Reference Collection Digital Spectral Library (Percival et al., 2018). The USGS Spectral Library has been widely utilized in mineral mapping studies (Abubakar et al., 2018; Amer et al., 2016; Calvin et al., 2015; Mars, 2018; Sun et al., 2017; van der Meer, van der Werff, et al., 2014).

Geologically, it is common for the spectra and physical properties of a mineral type to vary across locations. Impurities or trace elements may lead to diverse physical properties of a mineral type, consequently leading to varied spectral signals (Fan et al., 2012). Therefore, mineral mapping applications using spectra from different origins may yield different results. Particularly, the USGS Spectral Library Version 7 often has multiple spectral datasets for a single type of mineral (Kokaly et al., 2017). Mineral spectra of the USGS Spectral Library are not always the same spectrum from totally pure species. The library also includes several mineral spectra that contain minor impurities. Such as the alunite spectrum of sample RES-9 contains quartz and trace amounts of kaolinite plus rutile; the epidote spectrum of sample GDS26 contains a significant amount of quartz and a minor addition of other minerals; and the kaolinite spectrum of sample CM9 contains a small amount of quartz (Kokaly et al., 2017). Despite the spectral variability in spectral libraries, studies usually apply a single spectral variety selected or averaged from the spectral library for their mineral mappings (Abubakar et al., 2018; Amer et al., 2016; Calvin et al., 2015; Kratt et al., 2006; Mars, 2018; Moraga, 2022; Sun et al., 2017). The impact of using varied spectral signals on mineral mappings remains uncertain, and the significance of this variation requires further investigation.

It is also unclear how spectral variability will influence mineral maps in different spectral target detection algorithms. In a published case (Abubakar et al., 2018), three mineral spectra chosen from the USGS Spectral Library were utilized, though the selection reason was not discussed. They employed the SAM algorithm for spectral target detection but did not explore other spectra variability and mapping algorithms. They also did not statistically evaluate their map`s accuracy using ground truth data. There is a dearth of supporting information that can justify the choice of spectral variability for various target detection algorithms in mineral mapping.

On the other hand, there are also mineral mapping studies utilizing local spectral libraries established from locally collected spectra (Bedini, 2011; Calvin et al., 2015; Flores et al., 2021; Reath & Ramsey, 2013; Rodriguez-Gomez et al., 2021). Spectra to be included in local spectral libraries can be collected from local samples (Calvin et al., 2015; Flores et al., 2021; Mars, 2018; Reath & Ramsey, 2013;

Rodriguez-Gomez et al., 2021; Soydan et al., 2021; M. Wang et al., 2021). Previous studies that developed local spectral libraries for mineral mapping with supporting mineralogical assignments such as X-ray diffraction (XRD)(Flores et al., 2021; Reath & Ramsey, 2013; Soydan et al., 2021), X-ray fluorescence (XRF)(Flores et al., 2021), scanning electron microscopy (SEM) -based energy-dispersive X-ray spectroscopy (SEM-EDS; Reath & Ramsey, 2013; Rodriguez-Gomez et al., 2021), or inductively coupled plasma mass spectrometry (ICP-MS) (Rodriguez-Gomez et al., 2021; Soydan et al., 2021).

The above-mentioned studies using either local spectral libraries or the USGS Spectral Library did not include a thorough comparison of the mineral maps from different sources of spectra. Since different geological settings offer various impurities to the same mineral, a local spectral library and the USGS Spectral library may offer different mineral mapping results regarding their state of composition. Although it is important to select a spectral library in spectral RS studies properly, a statistical comparison of mineral mapping results between a local spectral library and the USGS spectral library has yet to be carried out.

Accuracy assessment of mineral mapping offers a method to properly evaluate mineral mapping derived from different approaches. It compares mapping results with ground-truth information, which statistically evaluates the accuracy of maps and eventually identifies better mineral mapping approaches. Since it is not feasible to interpret ground-truthing points of geology and mineralogy solely based on RS images, many studies could not include sufficient accuracy assessments based on ground-truth information, as they did not incorporate field studies (Bedini, 2011; Calvin et al., 2015; Hirai & Tonooka, 2019; Moraga, 2022; Reath & Ramsey, 2013; Roy et al., 2020; Sun et al., 2017). Although some studies performed field surveys to evaluate their mineral maps, they did not cover a statistical accuracy assessment for their vast research areas (Abdelkareem et al., 2018; Abubakar et al., 2019; Ramazani et al., 2022).

Relations Between Geothermal Exploration Parameters

Mapping the types and distribution of indicator minerals is valuable in geothermal exploration (Browne, 1978; Savitri et al., 2021; Villeneuve et al., 2019). Various alteration minerals may reflect regional temperatures (Browne, 1978; Henley & Ellis, 1983; Reyes, 1990), pH levels (Reyes, 1990), permeability (Lagat, 2009; Reyes, 1990), and the paleo-fluid chemistries (Reyes, 1990; Vidal et al., 2018). In addition to the mapping of indicator minerals, faults, and land surface temperatures (LST) are also important parameters in geothermal exploration.

Faults serve as conduits for hydrothermal fluids in geothermal systems (Curewitz & Karson, 1997; Lemgruber-Traby et al., 2023; McNamara et al., 2019; Siler, 2023; Trainor-Guitton et al., 2023). Exploration efforts can be more effectively directed by identifying the structural setting of a prospective

area and distinguishing between active and inactive faults. There is also a close relation between fault systems and mineral alteration in many geothermal systems (Liotta et al., 2020, 2021; Micklethwaite et al., 2010; Taussi et al., 2023). Geothermal exploration can be refined when fault maps are integrated with mineral alteration maps (Carranza et al., 2008; Jolie et al., 2015; Mahzari et al., 2021). Fault mapping traditionally relies on ground-based geologic mapping, but recently, emerging RS techniques, including LiDAR, have improved the efficiency of fault mapping (Ahmadi & Pekkan, 2021; Bemis et al., 2014; Cawood et al., 2017).

Land Surface Temperature (LST) is directly linked to geothermal gradients. A region with higher LST generally suggests a potential for a geothermal system, as it may be a proxy for deeper, elevated temperatures (Boden, 2016; Domra Kana et al., 2015; Harvey et al., 2014; Sekioka & Yuhara, 1974; van der Meer, Hecker, et al., 2014). LST can be acquired through ground-based surveys employing temperature probes (Blake et al., 2020; Coolbaugh, Sladek, et al., 2007; Zehner et al., 2012; Zimmerman et al., 2023). Using satellite images like ASTER or Landsat 8 with RS analyses is another way to acquire LST. (Coolbaugh, Kratt, et al., 2007; Gemitzi et al., 2021; Silvestri et al., 2020), which can be used alone or integrated with ground-based temperature mapping.

Several geothermal studies incorporate maps of (1) indicator minerals and faults (Achieng et al., 2017; Vaughan et al., 2005), (2) faults and LST (Chan et al., 2018; Gemitzi et al., 2021), (3) indicator minerals and LST (Reath & Ramsey, 2013; Rodriguez-Gomez et al., 2021), but the studies mainly focused on visual comparisons between the distribution of limited attributes. While some researchers have explored all three parameters of indicator minerals, faults, and LSTs in geothermal research (Abubakar et al., 2019; Calvin et al., 2015), an in-depth, data-driven analysis of their relations is lacking, especially regarding how these connections apply across geothermal fields in different geological settings. There is still much to discover about the relations between mineral maps, fault maps, and LSTs. Furthermore, there is a shortage of data-driven research supporting these relations in geothermal exploration, as well as the applicability of these relations across different geothermal systems. With the growing application of machine learning (ML) and artificial intelligence (AI) in geothermal exploration (Muther et al., 2022; Okoroafor et al., 2022), some studies have included the three parameters above (Assouline et al., 2019; Moraga et al., 2022; Mudunuru et al., 2022). However, to fully leverage AI and ML performance, systematic data-driven research is needed to assess relations between parameters for modeling.

1.1 The Research Goal

The overall research goal is to evaluate various mineral mapping approaches and explore relations between indicator mineral maps and other geothermal exploration parameters based on rigorous data-driven studies. Thereby increasing the efficiency of geothermal exploration. In mineral mapping, under-

prediction could miss valuable targets, while over-prediction can lead to wasted time and budget on unrelated sites. Therefore, there is a critical need for a mineral mapping study with accuracy assessments that can compare mineral maps from various mapping approaches. Eventually, it improves the quality of the study of mineral maps and other geothermal exploration parameters.

For this purpose, field and laboratory investigations at the Coso geothermal field (CGF), USA, were conducted to develop a local spectral library and ground-truth dataset focused on indicator minerals of interest (hereafter referred to as MOI). The Coso Spectral Library provides local spectra for mineral mapping purposes. The geodatabase provides ground-truth datasets that facilitate accuracy assessments for comparing mapping accuracies. MOI were mapped following multiple approaches, and accuracy assessments were conducted to evaluate the differences. The dissertation aims to resolve the influence of mapping methods in mineral mapping, including the implementation of mapping algorithms, fusion combinations, and splice correction. This part of the study provides guidelines for mineral mapping in geothermal exploration.

In addition to the influence of mapping methods, this dissertation assesses the influence of various spectra sources, including spectral variabilities and spectral libraries. This study examines whether labor-intensive local spectral libraries enhance mineral mapping accuracy compared to the publicly available USGS Spectral Library.

With the refined mineral mapping strategy, this study extended to discover relations between the maps of indicator minerals, faults, and LSTs. This part of the study extends from CGF and covers Brady geothermal fields (BGF) and Desert Peak geothermal fields (DPGF), USA, aiming for a more comprehensive assessment of the relations between the maps of three exploration parameters (hereafter referred to as SGP, Selected Geothermal Parameters) in various geothermal fields. The proposed data-driven approach integrates non-spatial and spatial analysis to elucidate significant relations among the SGP statistically.

1.2 The Research Objectives, Questions, and Hypotheses

The major research questions, associated research hypotheses, and objectives are:

Question one (Q1): How do mapping methods influence mineral mapping?

Q1.1: Which mapping algorithms provide more accurate mineral maps?

Q1.2: Which fusion combination provides more accurate mineral maps?

Q1.3: How does splice correction impact the accuracy of mineral maps?

Question two (Q2): How do spectra sources influence mineral mapping?

Q2.1: How does mineral spectral variability impact mapping accuracy?

Q2.2: How do varied spectral libraries impact mapping accuracy?

Question three (Q3): What are the relations between the maps of SGP?

The corresponding research hypotheses of this research question are:

Hypothesis one (H1): Different mapping methods can influence mineral mapping accuracy.

H.1.1: Different mapping algorithms lead to varied accuracy levels.

H1.2: Fusion mineral maps could offer higher mapping accuracy.

H1.3: Splice correction of spectra could increase mapping accuracy.

Hypothesis two (H2): Different spectra sources can influence mineral mapping accuracy.

H2.1: Varied spectral details lead to varied levels of mapping accuracy.

H2.2: A local spectral library could provide higher accuracy than the USGS Spectral Library in mineral mapping.

Hypothesis three (H3): The distribution of indicator minerals corresponds to the distribution of faults or LSTs.

To address the research questions and hypotheses, this study established a local mineral spectral library and geodatabase that supports further mineral mappings and accuracy assessments in this study. The spectral library facilitates the research on the impact of spectra sources in mineral mapping (Q2). The ground truth information in the geodatabase facilitates the accuracy assessment to examine the impact of mapping methods and spectra sources (Q1 and Q2). The research objectives of this dissertation include the following:

Objective one (O1): To evaluate the influence of mapping methods in mineral mapping.

Based on assessing mineral maps from different mapping methods, this objective aims to evaluate the impact of mapping methods in mineral mapping (Q1 and H1), including the choice of the mapping algorithm, fusion combinations, and splice correction.

Objective two (O2): To evaluate the influence of spectra sources in mineral mapping.

Based on assessing mineral maps from various spectra sources, this objective aims to evaluate the impact of spectra sources in mineral mapping (Q2 and H2), including the mappings based on varied spectra and different spectral libraries.

Objective three (O3): To explore the relations between mineral maps and other geothermal exploration parameters.

This study investigates the distribution relations between the maps of SGP (indicator minerals, faults, and LSTs). The data-driven learning approach includes both non-spatial and spatial analytical methods. This part aims to reveal how closely the indicator minerals are linked to faults and LSTs in the study areas. Hence, it supports interpretation and judgment for future geothermal exploration (Q6).

Table 1-1 summarizes the relation between the objectives (O), questions (Q), and hypotheses (H).

Table 1-1 Research objectives, questions, and hypotheses.

Objective	Question	Hypothesis
O1	Q1	H1
O2	Q2	H2
O3	Q3	H3

1.3 The Original Contribution of the Dissertation

This dissertation covered the study that utilizes data-driven approaches that quantify the differences among the research objectives, thereby improving the procedures of mineral mapping and supporting geothermal exploration. To the author's knowledge, the dissertation has several points of innovative contributions.

This study represents the first statistical investigation into the effects of various mapping algorithms on mineral mapping within a geothermal field. It is the very first literature that quantifies the performance of different fusion combinations in mineral mapping. This study also includes a first examination of the effects of mis-performing splice correction in mineral mapping. The study also comprises a novel statistical investigation into the impact of mapping with diverse spectra or spectral libraries on the accuracy of mineral maps.

Last but not least, this study represents a pioneer study employing both non-spatial and spatial analytical techniques to statistically investigate the relations among the SGP map (indicator minerals, faults, and LSTs) across multiple geothermal fields.

1.4 Organization of the Dissertation

This dissertation has eight chapters. Following the introduction in chapter one, the dissertation was organized with a second chapter about the methodology that explains the research frameworks in detail; A third chapter about the selection of research sites; A fourth chapter about the establishment of the Coso Spectral Library; A fifth chapter examining the impact of mapping methods in mineral mapping; A sixth chapter examining the impact of spectra source in mineral mapping; A seventh chapter about the data-driven study of geothermal exploration parameters; and a final chapter that summarizes the overall conclusions and the recommendations for future studies, followed by appendix and reference.

CHAPTER 2 METHODOLOGY

Figure 2.1 presents the overall research framework of the study. The flowchart illustrated the research stages and the associated research objectives, questions, and hypotheses.

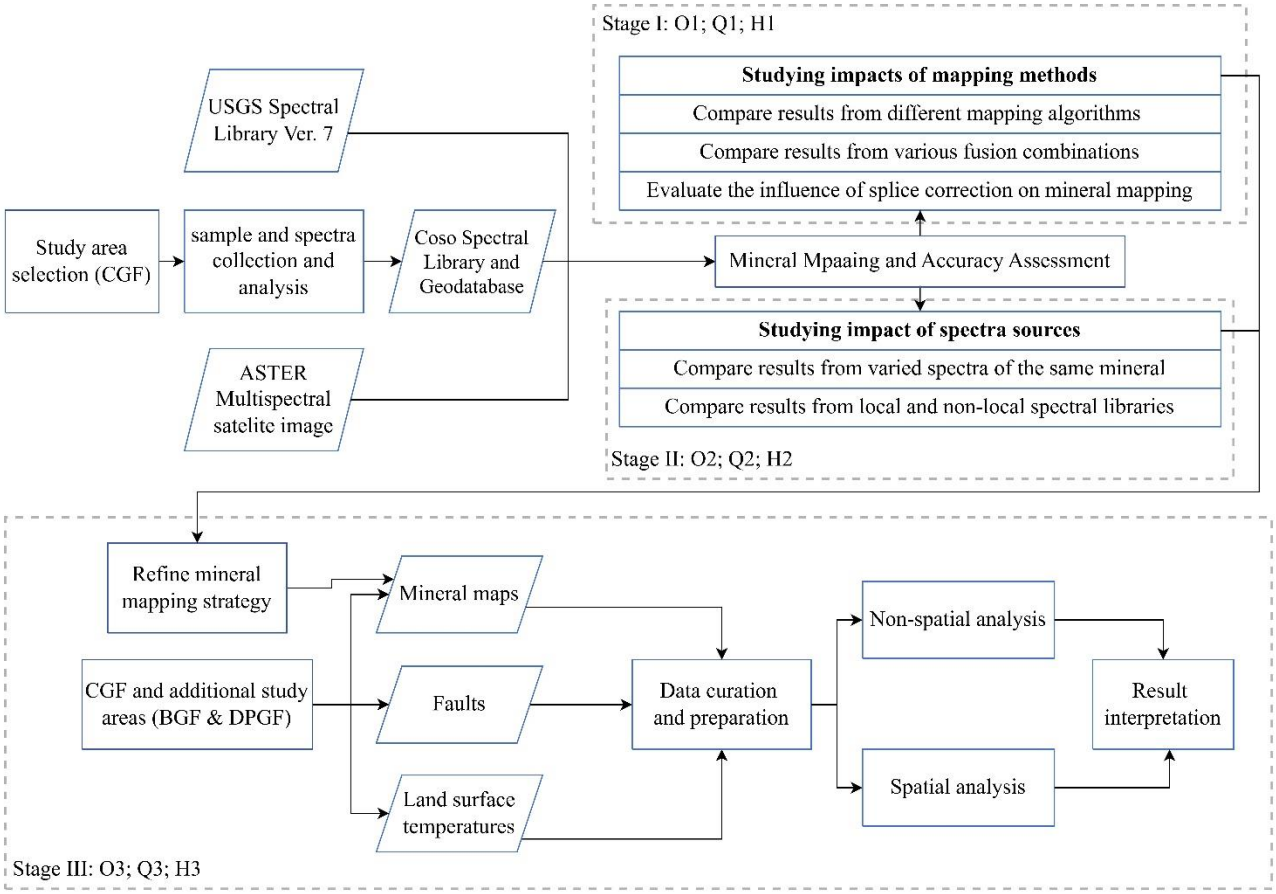

Figure 2.1 The overall research framework.

The study starts with data preparation and the establishment of a local spectra library (Chapter Four), as given in Figure 2.1. Based on the selected study area of CGF, the field samples were collected and analyzed to establish a local spectral library. The CGF samples went through spectra collection and mineralogical assessment. The resultant Coso Spectral Library includes spectra for mineral mapping and a geodatabase to facilitate ground-truthing for accuracy assessment of mineral maps. Simultaneously, reference spectra of indicator minerals were compiled from the USGS Spectral Library (Figure 2.1). The spectra from the USGS Spectral Library were selected, following the same instrument used to collect spectra for the Coso Spectral Library. Both the CGF and USGS spectra were utilized in mineral mapping based on the ASTER multispectral satellite image for the study (Figure 2.1).

Multiple mineral mapping tasks were performed following the research questions to be resolved. Stage I (Chapter Five) of the study focused on studying the impact of mapping methods (Q1). Stage II (Chapter Six) of the study focused on studying the impact of spectra sources (Q2). Through the evaluation of different mapping approaches, the study integrates the findings and refines the mineral mapping strategy. In Stage III (Chapter Seven), the mineral maps based on the refined mapping strategy were combined with the fault and LST data of each study area for data analysis. The data-driven study facilitates non-spatial analysis and spatial analysis to explore the relations between the SGP(Q3). Further details about the implications and results are presented in subsequent chapters.

The workflow of mineral mapping and accuracy assessment is shown in Figure 2.2.

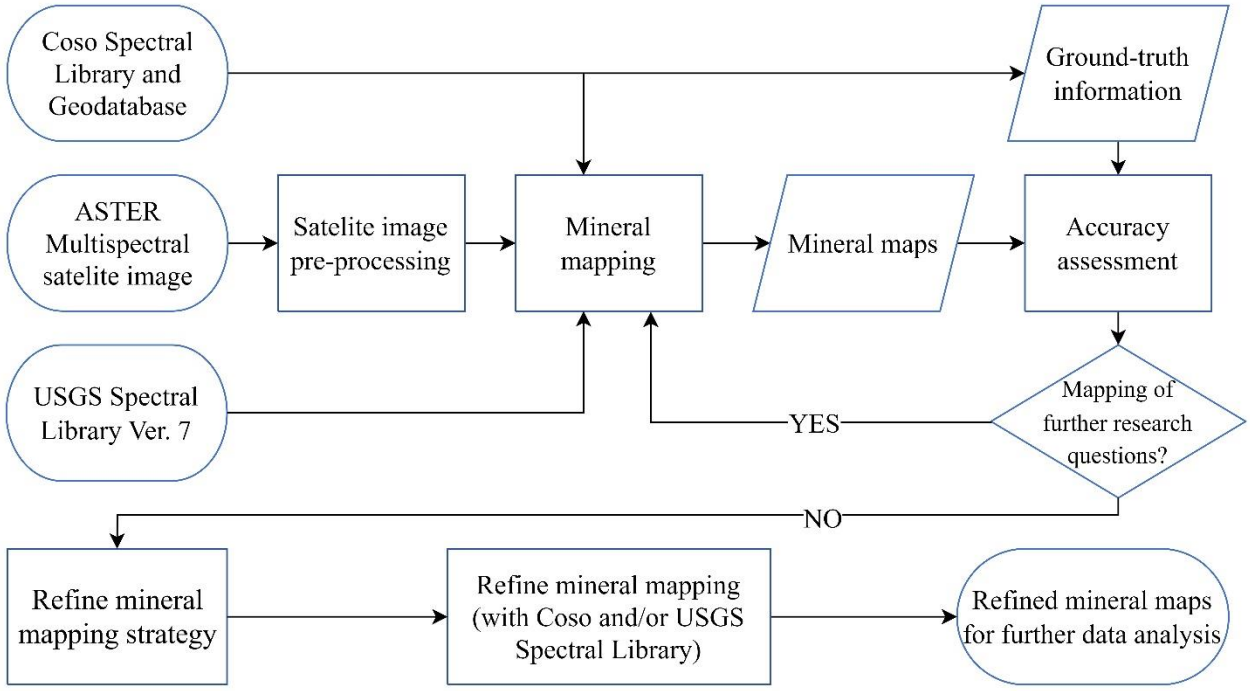

Figure 2.2 The framework of mineral mapping and accuracy assessment.

Initially, the ASTER image underwent pre-processing to facilitate subsequent mineral mapping. Spectra from the Coso Spectral Library or the USGS Spectral Library were applied to mineral mapping. The details of mineral mapping are explained in section 2.1. The mineral maps were obtained through various approaches that aim to evaluate the hypotheses of the first two objectives of this study (section 1.2). The mineral maps went through accuracy assessments that utilized the ground-truth information from the geodatabase of the Coso Spectral Library to evaluate the mapping accuracies. During the process of mineral mapping and accuracy assessment, preliminary results lead to the modification of mapping strategies. Therefore, multiple iterations of mineral mapping tasks were performed in this study to fully address the research questions and to refine the mineral mapping strategy. The details of the accuracy

assessments were illustrated in section 2.2. Lastly, the refined mapping strategy facilitated the indicator mineral maps that were applied to further data analysis with the other SGP.

2.1 Satellite Data Processing and Mineral Mapping

Figure 2.3 illustrates the framework of mineral mapping based on ASTER multispectral images and spectral libraries. Utilizing target mineral spectra and satellite images, dominant RS spectral signals were matched with target spectra to identify the potential areas where different target minerals occur.

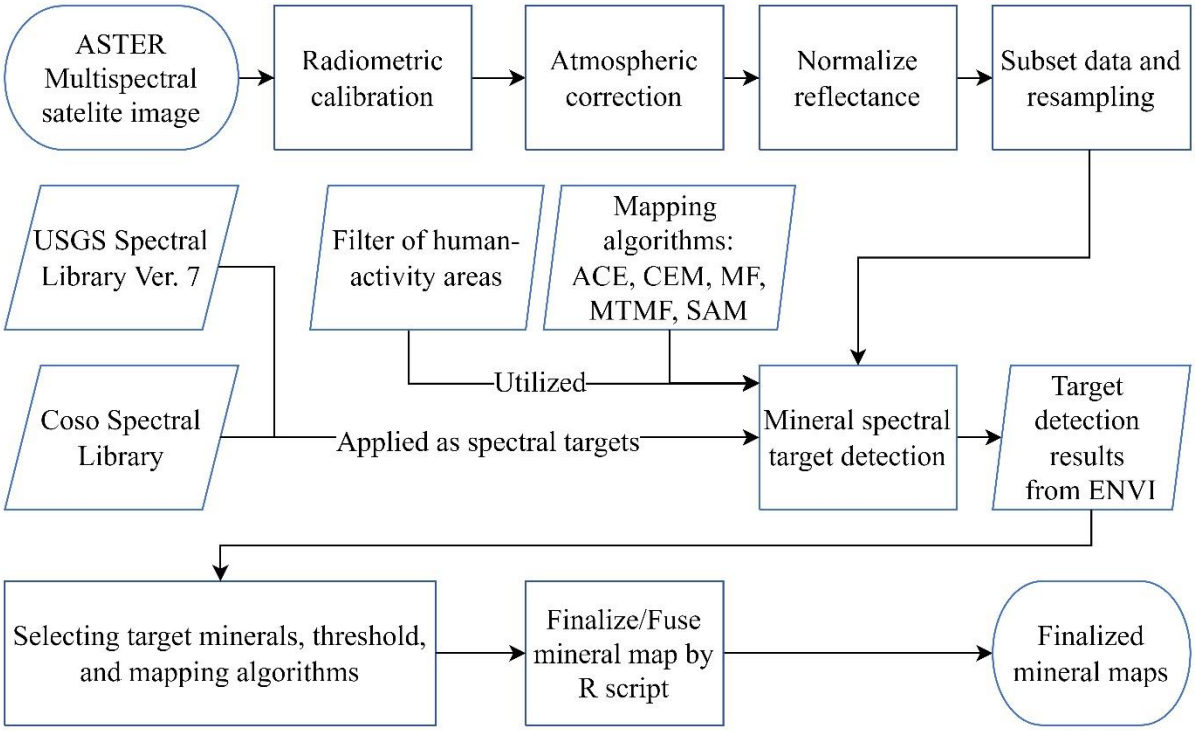

Figure 2.3 The detailed framework of mineral mapping.

The mineral mapping was based on VNIR (visible and near-infrared) and SWIR (short-wavelength infrared) datasets of the ASTER multispectral satellite image. The utilized ASTER product was AST_L1T (Level 1 Precision Terrain Corrected Registered At-Sensor Radiance), which was generated from a single resampling of the corresponding ASTER L1A (AST_L1A) product. The AST_L1T dataset provides calibrated at-sensor radiance. It has been geometrically corrected and reoriented to a north-up UTM projection (NASA LP DAAC, 2015).

The software ENVI was utilized to pre-process the ASTER dataset. The image was processed through radiometric calibration, followed by atmospheric correction using the QUAC algorithm (QUick Atmospheric Correction) (Bernstein, Adler-Golden, Sundberg, Levine, Perkins, & Berk, 2005; Bernstein, Adler-Golden, Sundberg, Levine, Perkins, Berk, et al., 2005; Bernstein et al., 2012). The reflectance

values of the processed image were normalized to a range between 0 and 1 to compare with spectra from the USGS Spectral Library and the established Coso Spectral Library. Subsets of the study areas were extracted from the processed image, and the resolution was resampled to 3 meters by 3 meters. The resampling uniformed the various resolutions offered by different ASTER sensors. During the mineral mapping process, areas of human activity were masked, excluding potential interference from non-natural disturbance during the mineral mapping. The Target Detection Wizard toolset in ENVI and an R-based mapping script (Moraga et al., 2022; Moraga & Duzgun, 2022) were utilized for mineral mapping. Raw target detection datasets were first carried out by ENVI, which comprised the spectral matching value of each target spectrum by each applied mapping algorithm at each pixel of the satellite image. With the raw datasets from ENVI target detection, the R-based mapping script further finalizes or fuses the mineral maps as raster data. In the R script, it was possible to select specific target minerals, mapping algorithms, and mapping thresholds to create mineral maps that match the needs. A mapping threshold of 99 percentile was applied in this study, which means that the best 1% target detection results were present on mineral maps. The finalized mineral maps offer the inputs for the accuracy assessment or further analyses.

Among the eight target detection algorithms in ENVI (Wolfe & Black, 2018), some algorithms require the assignment of non-target spectra from background conditions. Particularly, the algorithms of OSP, TCIMF, and MTTCIMF (Jin et al., 2009), they require further site-specific studies to identify the non-target end-member spectra. Therefore, this study considers algorithms that do not require the assignment of non-target spectra. The applied target detection algorithms were Adaptive Coherence Estimator (ACE), Constrained Energy Minimization (CEM), Matched Filtering (MF), Mixture Tuned Matched Filtering (MTMF), and Spectral Angle Mapper (SAM). The following are the concepts of the five applied mapping algorithms.

Adaptive Coherence Estimator (ACE)

The ACE algorithm calculates the ratio between the pixel and target spectra and determines if both spectra are consistent. Since the ACE algorithm does not require understanding all the end-members in research areas, it is suitable when the background conditions are unclear or variable (Manolakis et al., 2003; Kraut et al., 2005). In addition, the ACE's result does not vary due to the change in the relative scope of the input spectra dataset. The calculation of the ACE value is:

$$T_{ACE}(x) = \frac{(d^T \Sigma^{-1} x)^2}{(d^T \Sigma^{-1} d)(x^T \Sigma^{-1} x)} \tag{2.1}$$

Where d is the target spectrum, x is the pixel spectrum, and Σ is the background covariance matrix (Jin et al., 2009).

Constrained Energy Minimization (CEM)

The CEM algorithm also calculates consistency based on the target spectrum, pixel spectrum, and background correlation/covariance matrix (Chang et al., 2000; Harsanyi & Chang, 1993). The CEM algorithm also does not require an understanding of all the end-members in research areas. One challenge of the CEM algorithm is the generalization in application due to its sensitivity to the knowledge of the target signals (Du et al., 2003). The calculation of the CEM value is:

$$T_{CEM}(x) = \frac{d^T \Sigma^{-1} x}{d^T \Sigma^{-1} d} \tag{2.2}$$

Where d is the target spectrum, x is the pixel spectrum, and Σ is the background correlation or covariance matrix (Jin et al., 2009).

Matched Filtering (MF)

The MF algorithm has a concept similar to that of the CEM algorithm. The MF algorithm provides a matching level by calculation based on the target spectrum, the pixel spectrum, the background mean vector, and the background covariance matrix. The MF algorithm does not require an understanding of all the end-members in the region of interest. The shortcoming of the MF algorithm was the handling of spectral unmixing. Furthermore, the MF algorithm was not ideal for discriminating the targets with similar spectral patterns (Boardman & Kruse, 2011). The calculation of MF value is:

$$T_{MF}(x) = \frac{(d-\mu)^T \Sigma^{-1} (x-\mu)}{(d-\mu)^T \Sigma^{-1} (d-\mu)'} \tag{2.3}$$

Where d is the target spectrum, x is the pixel spectrum, μ is the background mean vector, and Σ is the background covariance matrix (Jin et al., 2009).

Mixture Tuned Matched Filtering (MTMF)

The MTMF algorithm was developed based on the MF algorithm. The difference was that the MTMF algorithm adopts the Minimum Noise Fraction (MNF) transformed image as input (Boardman, 1998). The MNF transformation calculates a score that describes the possibility of each pixel being a mixture of the known target and other background materials. With the better ability to identify and reject false positives, the MTMF algorithm was helpful in the detection and discrimination of minor target materials that present similar spectra to background materials (Boardman & Kruse, 2011).

Spectral Angle Mapper (SAM)

The SAM algorithm calculates the similarity between a target spectrum and a reference spectrum (Kruse et al., 1993). Both spectra are considered as vectors in an n-dimensional space, where n is the number of bands. If the angle between two vectors is 0, it means that the two vectors are the same vector. Therefore, the smaller SAM value means that the two spectra are similar. The SAM algorithm does not require understanding end-members in the research area. The calculation of the SAM value is:

$$T_{SAM}(x) = \frac{d^T x}{(d^T d)^{1/2}(x^T x)^{1/2}} \tag{2.4}$$

Where d is the reference spectrum, and x is the pixel spectrum (Jin et al., 2009).

2.2 Accuracy Assessment and Refining Mapping Strategy

Figure 2.4 illustrates the research framework of the accuracy assessment that helps refine the decision-making of the mapping strategy in this study.

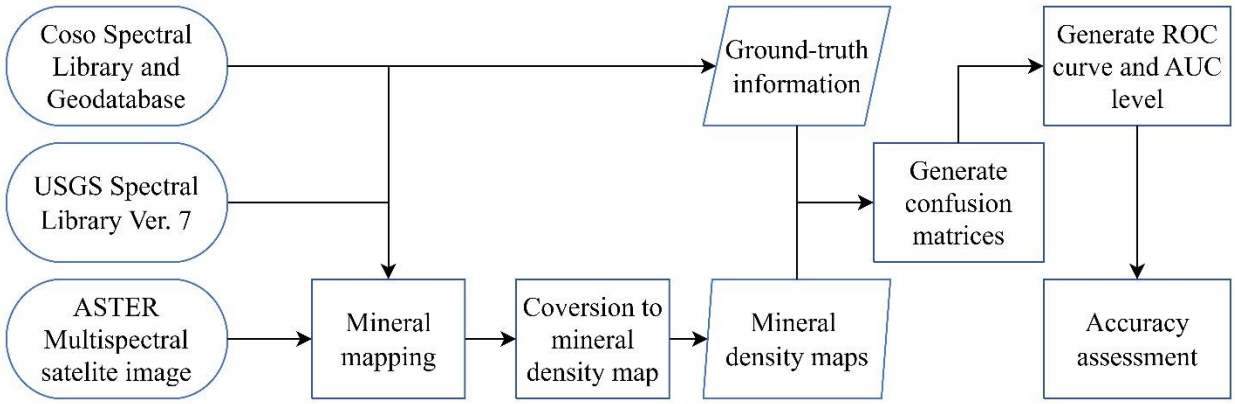

Figure 2.4 The detailed framework of accuracy assessment.

Mineral maps underwent accuracy assessments to validate their functionality for predicting mineral distribution. The assessment utilized published Python-based modules (Cavur et al., 2024). The accuracy assessment was achieved by comparing the mineral occurrence at sampling locations and the mineral maps. The modules convert mineral maps to point density maps and compare them with ground-truthing points to create confusion matrices. Confusion matrix compiles the comparing results between actual and prediction values, as shown in the example in Table 2-1. By generating confusion matrices according to the gradually changing thresholds of density maps, the modules produced Receiver Operating Characteristic (ROC) curves by plotting the false positive rates and true positive rates (Hanley & McNeil, 1982). The module then calculates the corresponding area under the ROC curve (AUC) for further evaluation. AUC values range from 0 to 1, where 1 represents the most effective prediction model and 0

indicates the least. An AUC of 0.5 refers to a scenario of random prediction. Therefore, higher AUC values reflect more accurate mineral maps. This procedure allows us to evaluate the accuracy of mineral maps generated by different mapping approaches and gradually refine our mineral mapping strategy. Thereby, the refined indicator mineral maps with improved accuracy could be applied in further data analysis with other SGP. The methodology of mineral mapping and accuracy assessment was published in the journal Remote Sensing (Cavur et al., 2024), attached in APPENDIX F . The detailed implementations and results of mineral mapping and accuracy assessment are presented in Chapters Five and Six.

Table 2-1 A typical example of a True/False confusion matrix.

Confusion Matrix		**Actual value**	
		Positive	**Negative**
Prediction value	**Positive**	True Positive	False Positive
	Negative	False Negative	True Negative

CHAPTER 3 STUDY AREAS

The Coso geothermal field (CGF) was selected as the primary study area due to its extensive history and great energy capacity. The study first focused on CGF to examine the accuracy of mineral maps. The study extends the study areas to the Brady geothermal field (BGF) and the Desert Peak geothermal field (DPGF) to understand the relations between SGP in various geothermal fields.

3.1 Coso Geothermal Field

The Coso geothermal field (CGF, Figure 3.1) is approximately 260 km northeast of Los Angeles and about 50 km northwest of Ridgecrest in southeastern California, USA. It is situated at the Coso Range of the Mojave Desert east of the Sierra Nevada. It has a rich history of geothermal exploration and exploitation, evolving from a sacred site for Native American Indigenous communities to a modern tourist destination and ultimately transitioning into a significant power generation facility (Monastero, 2002). Austin and Pringle initially suggested the prospect of harnessing geothermal energy for electricity production in the region in 1970 (Hulen, 1978). Following several years of thorough exploration and development, power generation activities commenced at the CGF during the 1980s, providing a substantial energy contribution to the local area for over three decades (Monastero, 2002). The CGF is home to one of the largest geothermal fields in the U.S., with a capacity of 270 MWe (Monastero, 2002) derived from four power blocks (Navy I, Navy II, BLM East, and BLM West, see Figure 3.1).

The CGF is spatially and temporally associated with the Coso Volcanic Field (CVF), with the CGF located at the center of the CVF. The CVF is a Pleistocene-Holocene age volcanic field comprised mostly of rhyolite domes and flows, pyroclastic successions, and minor amounts of basalt flows and cinder cones (Duffield & Bacon, 1981; Whitmarsh, 1998). Figure 3.1 shows the select landmarks from the CGF, including hydrothermal alteration (Devil's Kitchen, Coso Hot Springs, Nicol Pad, and Wheeler Pad), rhyolite domes (e.g., Sugarloaf Mountain and Cactus Peak), and geothermal landscapes (fumarole and Travertine). CGF is a volcanic geothermal field in an extensional tectonic setting (Jolie et al., 2021; Monastero et al., 2005; Sigurdsson et al., 2015). The resource is hosted by altered Jurassic and Cretaceous granitic and metamorphic rocks. The surface volcanic features and the heat flow are the product of the shallow rhyolite magma chamber under the CVF (Duffield & Bacon, 1981; Manley & Bacon, 2000; Whitmarsh, 1998).

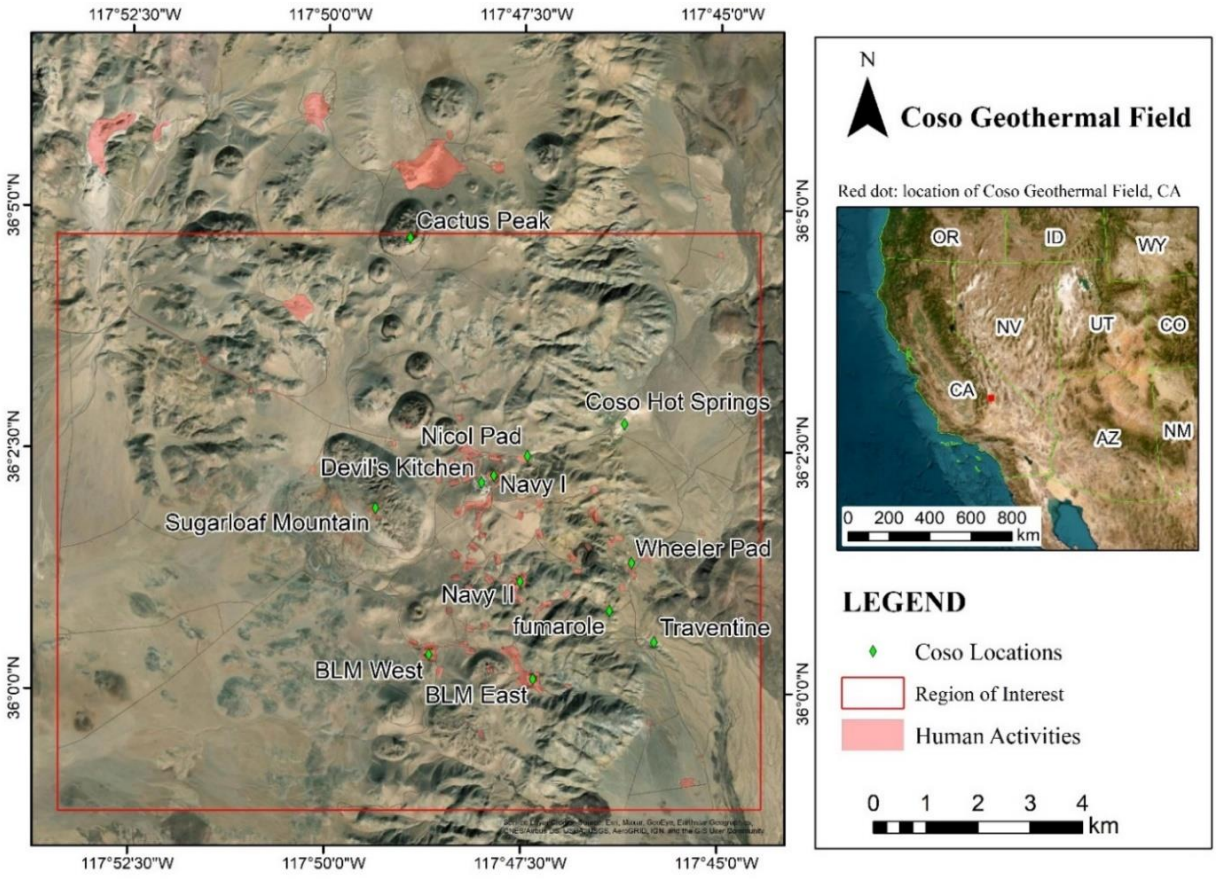

Figure 3.1 Map of the Coso Geothermal Field.

Since the commencement of the geothermal development at CGF, geological mapping has been carried out to understand the regional geology. In 1976, Duffield and Bacon carried out a preliminary map of the Coso rhyolite dome and the adjacent area with a mapping scale of 1:50,000 and introduced one of the earliest geological frameworks of the region (Duffield & Bacon, 1976); In 1978, Hulen proposed a local geologic map of CGF with several conceptual cross sections with a mapping scale of 1:24,000, based on Duffield and Bacon's earlier work (Hulen, 1978); In 1980, Duffield proposed a generalized update about the regional geology on a smaller scale than their earlier work (Duffield et al., 1980); In 1981, Duffield and Bacon organized their earlier works and created a detailed geologic map of the Coso volcanic field and the adjacent area on a mapping scale of 1:50,000, the map also presented multiple cross-sections for the concept of the geological framework (Duffield & Bacon, 1981); In 1987, Bishop and Bird focused on the Coso Hot Spring area and presented a simplified geologic map and cross-section (B. P. Bishop & Bird, 1987), but the mapping scale was not specified; In 1998, Whitmarsh summarized earlier research and proposed the latest detailed geologic map for the Coso area in a mapping scale of

1:24,000, the map was presented in a way with 12 quadrangles (Whitmarsh, 1998). The Cactus Peak Quadrangle of Whitmarsh's map covered the primary area of geothermal developments at CGF.

Since fault systems are a major parameter in geological studies and geothermal exploration, multiple fault mappings of the CGF have been proposed over time. In 1976, Duffield and Bacon mapped a fault system with their geological map (Duffield & Bacon, 1976); In 1978, Hulen also mapped a fault system with the proposed geological map (Hulen, 1978); In 1981, Duffield and Bacon refined their earlier work and updated the fault system with their newer geological map (Duffield & Bacon, 1981); In 1998, Whitmarsh proposed a detailed fault system along with the geological mapping (Whitmarsh, 1998); In 2010, the California Geological Survey organized the Fault Activity Map of California (Jennings & Bryant, 2010) that replaced the earlier version that finished in 1994 (Jennings & Saucedo, 1994). The fault activity map included two datasets for both the Quaternary and Pre-Quaternary faults in California, which include multiple fault traces around the CGF; In 2016, the FORGE project created a fault system for its region of interest in the west Flank of the CGF (Blankenship, 2016); In 2020, USGS updated its U.S. Quaternary Fault and Fold Database, which included several Quaternary faults near the CGF (Schmitt & Gold, 2020), the USGS dataset matched with the Quaternary part of the earlier Fault Activity Map by the California Geological Survey.

Numerous studies have focused on investigating the alteration types and mineralogy of the CGF since its discovery of geothermal resources in the 1970s (Adams et al., 2000; B. P. Bishop & Bird, 1987; Davatzes & Hickman, 2006; Echols et al., 1986; Galbraith, 1978; Hulen, 1978; Hwang et al., 2014; Kovac et al., 2005; Lutz et al., 1996; Mclin et al., 2006). These studies provide valuable insights about the alteration and mineral assemblages at the CGF. However, these mineralogical studies did not extend to spectral collection and analysis. Based on the aforementioned mineralogical studies, Erika (Erika, 2022) compiled a mineral list summarizing the common rock-forming and hydrothermal alteration minerals of the CGF. Five alteration minerals – chalcedony, epidote, hematite, kaolinite, and opal were selected for mineral mapping by Erika (2022). Erika's (2022) findings provide a reference for selecting major indicator minerals of interest in this dissertation. In addition, alunite is also included in the minerals of interest based on its potential indication for steam-heated surface alteration (Hulen, 1978; Thompson et al., 1999). Thereby, the initial indicator minerals of interest in this dissertation focused on alunite, chalcedony, epidote, hematite, kaolinite, and opal (hereafter referred to as MOI, Mineral of Interest).

3.2 Brady Geothermal Field and Desert Peak Geothermal Field

The Brady geothermal field (BGF) and the Desert Peak geothermal field (DPGF) are approximately 70 km northeast of Reno within the Great Basin in western central Nevada (Figure 3.2). The power generation capacities are 26.1 MWe at BGF and 32.5 MWe at DPGF (Faulds et al., 2006). Figure 3.2

presents the map of BGF and DPGF with the locations of the geothermal power plants and the area's major landmarks (Brady Hot Springs and Desert Peak).

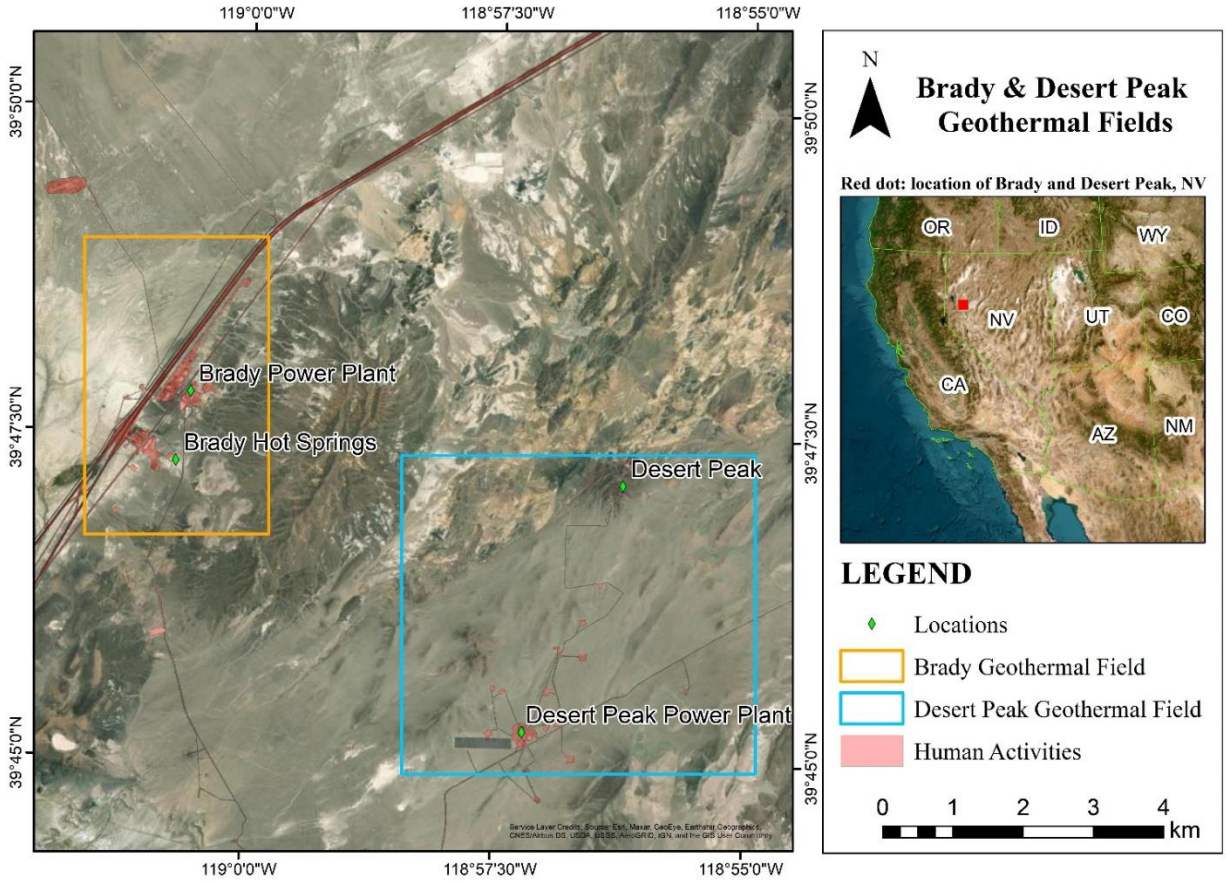

Figure 3.2 Map of the Brady and Desert Peak Geothermal Field.

Detailed geological maps of the BGF and DPGF were carried out in the 2010s (Faulds et al., 2012, 2017). The CGF, BGF, and DPGF are all within the Basin and Range physiographic province. Unlike the CGF, however, no active volcanism is associated with the BGF or the DPGF (Jolie et al., 2021; Kratt et al., 2006; Sigurdsson et al., 2015). The BGF and DPGF are primarily comprised of Tertiary volcanic and sedimentary rocks that overlie Mesozoic age metamorphic and plutonic basement rocks (Benoit et al., 1982; Faulds et al., 2003). They are within a northeast-trending zone locally referred to as the Humboldt structural zone (Faulds et al., 2003; Rowan & Wetlaufer, 1981). Both geothermal fields are characterized by the Humboldt structural zone's northeast-striking, normal, and left-lateral faults and localized high-heat flows. These faults serve as the main conduits for the upflow of geothermal fluids (Faulds et al., 2012, 2017; Kratt et al., 2006). Although BGF and DPGF are in similar geological settings, their surface features differ. Brady contains geothermal manifestations, including fumaroles and silica sinter (Faulds et

al., 2012, 2017). By contrast, Desert Peak is a blind geothermal system with no apparent geothermal feature on the surface (Benoit et al., 1982; Calvin et al., 2015; Craig et al., 2021).

Table 3-1 lists selected features from the three study areas from the aforementioned works of literature and the Open Energy Information (Brodt-Giles, 2014), including the geologic features in the three areas, including the types of geological settings, reservoir conditions, and surficial geothermal manifestations. The variabilities across the study areas facilitate this study in assessing the transferability of relations between SGPs.

Table 3-1 Geothermal features of the CGF, BGF, and DPGF.

	CGF	**BGF**	**DPGF**
Geological settings	magmatic	amagmatic	amagmatic
Geothermal surface manifestations	present	present	absent
Average temperature of geofluid*	275°C	187 °C	213 °C
Depth to reservoir top*	500 m	300 m	762 m
Depth to reservoir bottom*	3500 m	1676 m	1280 m
Average depth to the reservoir.*	2000 m	988 m	1021 m
Study area dimensions	148 km^2	11 km^2	23 km^2

*: data from the Open Energy Information (Brodt-Giles, 2014).

CHAPTER 4 ESTABLISHMENT OF THE COSO SPECTRAL LIBRARY

In this study, a local spectral library and geodatabase were established based on the samples from CGF. The spectral library includes the spectra of alunite, chalcedony, epidote, hematite, kaolinite, and opal, which facilitate mineral mapping. In addition, the geodatabase provides ground-truthing information to evaluate the accuracy of mineral maps. To present the research with the best visualization, the following abbreviations of minerals were used for the selected tables and figures in subsequent sections: alu. (alunite), cdy. (chalcedony), epd. (epidote), hem. (hematite), kln. (kaolinite), and opl. (opal)

4.1 Implementation for Establishing Spectral Library

This study follows a workflow to develop a local spectral library and geodatabase for mineral mapping and accuracy assessments, as present in Figure 4.1.

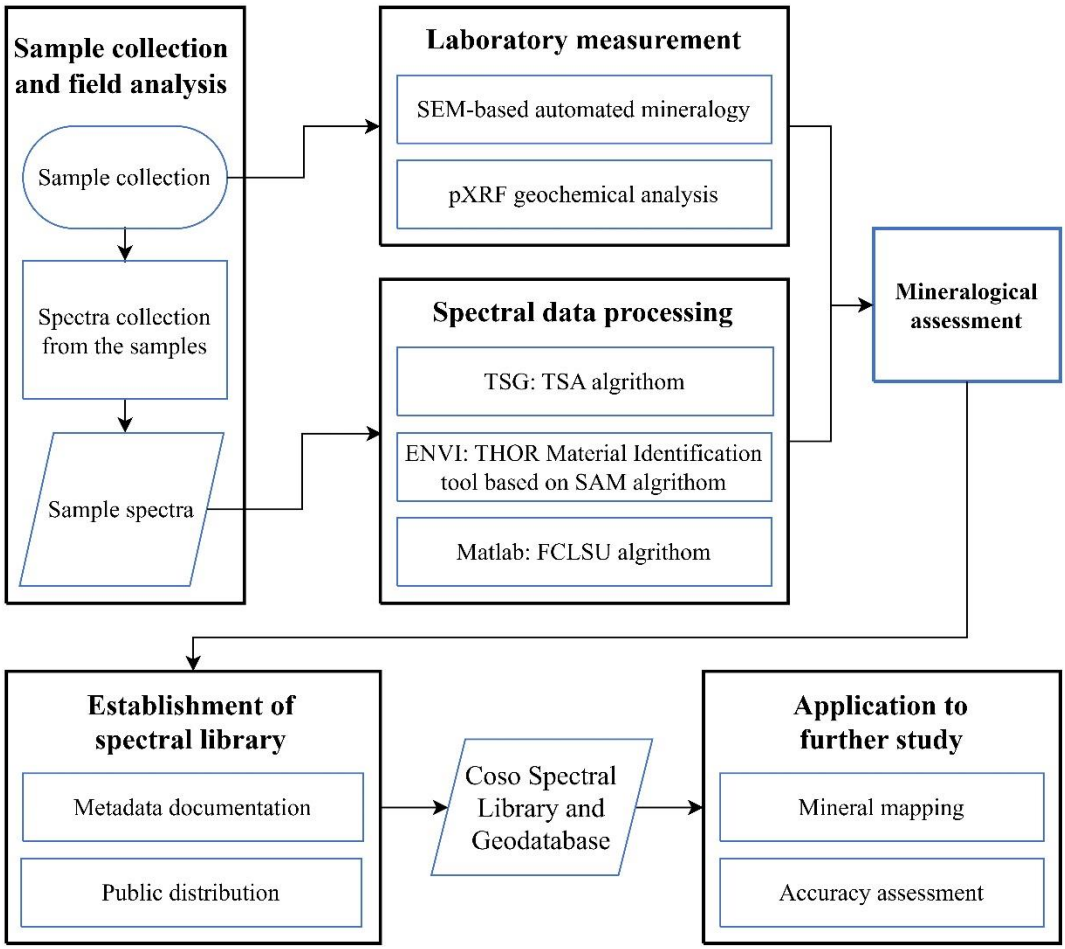

Figure 4.1 Framework for establishing the Coso Spectral Library and geodatabase.

The workflow starts from sample collection and field analysis (4.1.1), laboratory measurement (4.1.2), and spectral data processing (4.1.3). Based on the mineralogical assessment, the local spectral library and geodatabase of CGF were established (4.1.4). The Coso Spectral Library and Geodatabase were further applied in mineral mapping and accuracy assessment to address the research questions of the study.

4.1.1 Sample Collection and Field Survey

The research team conducted two field surveys of the CGF in 2022. A total of 89 samples were collected systematically from the CGF, as presented in Figure 4.2. The photos of the samples are organized in APPENDIX A . Concurrent with sample collection, spectral data were acquired using the ASD FieldSpec 4 Hi-RES N.G. portable spectroradiometer during the field survey of October 2022. The instrument captures the VNIR (350 to 1000 nm) and SWIR (1000 to 2500nm) reflectance spectra with 2151 channels. Spectral datasets were obtained from 64 locations across the CGF utilizing the pistol grip of the ASD FieldSpec (Figure 4.2). However, the spectra collected in the field showed substantial noise due to the vapor released from the geothermal field. Therefore, laboratory-collected spectra were used for further analysis.

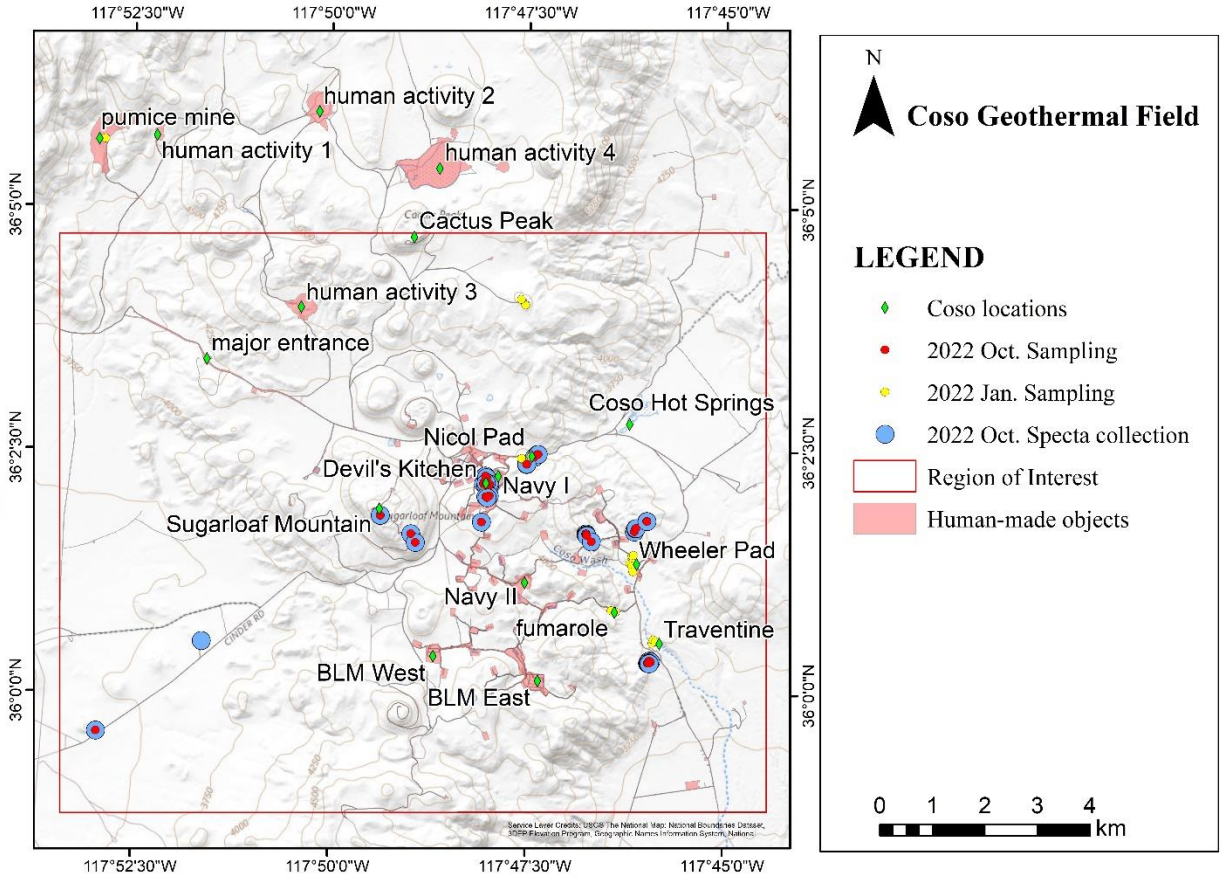

Figure 4.2 Sample and spectra collection at the CGF.

A total of 536 spectral datasets were obtained from the CGF samples in a laboratory using the ASD FieldSpec with contact probe equipment. Employing the ASD FieldSpec contact probe offers a controlled environment that effectively reduces variations during spectra collection. The equipment ensures a more standardized and consistent spectral data acquisition procedure. White reference spectra were collected before the measurements of each sample. The integration time was set on auto-integration. The collected spectra underwent splice correction using the ViewSpec Pro software to correct the signal discontinuities between sensors (Gaigalas et al., 2009) before being applied to further analyses and mineral mappings.

4.1.2 Laboratory Measurements

The mineralogical identification of the collected samples is not feasible to rely solely on the physical properties of the samples due to the prevalence of fine-grained alteration minerals. Hence, further analyses are necessary to provide supporting information for mineralogy. To enhance efficiency and minimize damage to the samples, this study utilizes SEM-based automated mineralogy on selected samples to elucidate the general alteration mineralogy and mineral modal abundance. Along with automated mineralogy, portable XRF (pXRF) spectrometry was employed to infer the samples' geochemistry. With the laboratory measurements that support hyperspectral analysis, this study identified the spectra associated with the MOI of the CGF and developed the local spectral library.

Scanning Electron Microscopy (SEM) -based Automated Mineralogy

Automated mineralogy is a powerful technique that provides quantitative mineralogical and textural data based on automated point counting. The quantitative mineralogical and textural data can support hyperspectral analysis (Rotem et al., 2023) and provide the foundation for more detailed analysis. In this study, 12 of the 89 samples from the CGF were analyzed in the Mineral and Materials Characterization (MMC) facility in the Department of Geology and Geological Engineering at the Colorado School of Mines to determine their mineralogy. The first batch of the six samples was from Devil's Kitchen, the most intense site of geothermal alteration and the center of local geothermal development (Coso-026, Coso-027, Coso-029, Coso-031, Coso-032, Coso-034). A subsequent sample batch was collected from Devil's Kitchen (Coso-028), Wheeler Pad (Coso-012), Nicol Pad (Coso-018 and Coso-023), a piece of diorite with epidote veins (Coso-039), and a pumice mine (Coso-042). The sample selection aimed to identify the general alteration mineralogy of the CGF (Figure 4.3). Due to instrument availability, six samples were analyzed using the TESCAN Integrated Mineral Analyzer (TIMA), whereas six subsequent samples were analyzed using AMICS (Advanced Mineral Identification and Classification) from Bruker.

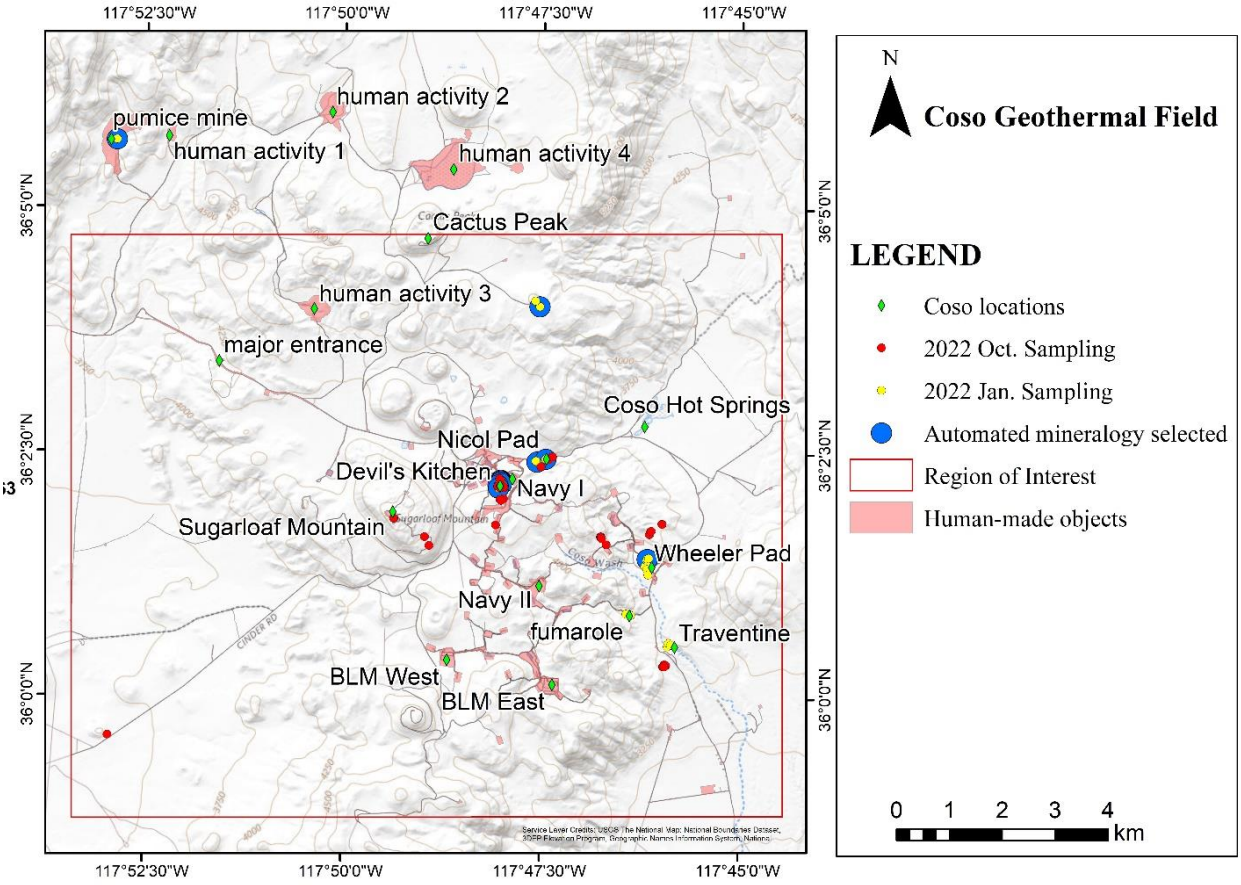

Figure 4.3 Location of samples selected for automated mineralogy analysis.

Both systems are based on an electron-beam platform with dispersive X-ray spectrometers (EDS) for mineral and phase identification. Samples were loaded into the TESCAN-VEGA-3 Model LMU VP-SEM platform, and analysis was initiated using the control program TIMA-X, or into the Hitachi field-emission SEM SU5000 platform, and analysis was initiated using the control program AMICS, respectively. In either case, energy dispersive X-ray (EDS; EDAX or Bruker, respectively) spectrometers acquired spectra from each point with a user-defined resolution. For TIMA, the resolution of the beam-stepping interval was 7 microns for backscattered electrons (BSE) and 21 microns for EDS analysis. For ACIMS, the resolution was 1.6 microns at 100x magnification and a minimum segment size of 20 microns. An acceleration voltage of 25 keV, and beam intensity of 14 (TIMA) or a specimen current of 65 nA (AMICS), respectively, was used during analysis. The Monte Carlo simulation modeled interactions between the beam and the sample. The EDS spectra were compared with spectra held in a look-up table, allowing a mineral or phase assignment to be made at each acquisition point. The assignment makes no distinction between mineral species and amorphous grains of similar composition. Such as between quartz, chalcedony, and opal; illite and muscovite; or calcite and aragonite. Results were output by the

TIMA or AMICS software as a spreadsheet, giving the area percentage of each composition in the look-up table. This procedure allows a compositional map to be generated. Composition assignments were grouped appropriately. Automated mineralogy analysis requires destructive sample preparation, entails higher costs, and involves longer data-collection times than hyperspectral analysis and portable X-ray fluorescence (pXRF) analysis.

Portable X-ray Fluorescence (pXRF)

Portable X-ray fluorescence (pXRF) spectrometers can provide approximate information regarding the geochemistry at the measured points. One advantage of pXRF is that it enables non-destructive data acquisition, where samples remain intact throughout the measurement process. Furthermore, pXRF analysis is faster and has a lower cost than automated mineralogy analysis. However, pXRF is not suitable for detecting certain elements' signals, and the error range can be considerable. Geochemical data acquired using pXRF can provide information that can be used as a proxy for mineralogical reference.

This study used pXRF analysis to measure the chemical abundance in 73 out of the 89 samples collected from the CGF. The remaining samples were either loose, angular, or duplicate-material samples. Utilizing a pXRF analyzer, the chemical compositions were obtained non-destructively and directly from the samples' surface in their natural state. The pXRF measurements were taken in the MMC facility in the Department of Geology and Geological Engineering at the Colorado School of Mines using a Bruker Tracer 5g handheld XRF spectrometer. Depending on the sample condition and size, various measurements were taken on each sample. Measurements were collected using Bruker's matrix-matched GeoExploration factory calibration, operated in oxide mode, and run as three-phase measurements, with spectra collected using three consecutive primary beam conditions that enable optimal excitation of elements across the energy spectrum being targeted:

1) 30 keV, 40 μA, 25 μm Ti + 300 μm Al primary beam filter, 30 seconds
2) 50 keV, 35 μA, 100 μm Cu, 25 μm Ti + 300 μm Al primary beam filter, 30 seconds
3) 15 keV, 38 μA, no primary beam filter, 30 seconds.

Although transmission of the low-energy X-rays that correspond to light elements ($Z \leq Al$) is relatively weak due to attenuation in the air path, geochemical trends can still be observed. To ensure data quality throughout the measurement process, a calibration sample was measured approximately every ten to fifteen measurements, depending on the number of points collected on each sample. This approach provided continuous monitoring and further assessment of the data quality at varying stages of the measurements.

Since pXRF analysis can only provide partial geochemical information, resulting in limited mineralogical information, the mineralogical judgment in this study did not primarily rely on pXRF

results. Instead, the pXRF data served as a piece of final supporting information, particularly in cases with an exceptional enrichment of specific elements relevant to the mineral of interest. The study employed an approach that considered multiple techniques and datasets to arrive at a robust mineralogical conclusion.

4.1.3 Spectral Data Processing

Spectral analysis offers a non-destructive method that is generally faster and more cost-effective than destructive analyses. Since different mineral groups usually exhibit distinctive spectral characteristics in various wavelength ranges, spectral analysis featuring varied wavelength ranges would be suitable for detecting minerals that present diagnostic spectral features in different wavelength ranges. The VNIR to SWIR range used in this study is applicable for identifying the hydroxide-bearing and oxide mineralogy (Thomas & Walter, 2002), which commonly occur in geothermal alteration environments.

This study employed three different spectral analysis methods. Each method utilizes a technique with unique capabilities for identifying mineral spectra. If the collected spectra were strongly associated with a single MOI, they were named and discussed following the corresponding MOI. It is the naming logic applied by the USGS Spectral Library (Kokaly et al., 2017) and multiple spectral studies (Calvin et al., 2015; Flores et al., 2021; Kruse, 2012; Mars, 2018), regarding the minor impurity in mineral samples. Particularly, in the USGS Spectral Library, multiple spectra were named after a single mineral after considering the minority of other mineral content (see Chapter One). Therefore, this study adopts the same naming logic to create a scenario comparable to that of the USGS Spectral Library.

Fully Constrained Linear Spectral Unmixing (FCLSU)

The exploration of spectral data started with spectral unmixing, following general applications in spectral RS. Spectral unmixing explores the composition of unidentified mixtures by deconvoluting them into end-members. The FCLSU is a spectral unmixing algorithm that analyzes the ratios of different end-members among a mixture, based on the spectra of the mixture and potential end-members (Heinz & Chang, 2001). The algorithm assumes that an unknown spectrum represents a linear combination of spectra of constituent end-members, weighted by their respective percentages. This study implemented the FCLSU algorithm within the MATLAB environment according to a GitHub module (Borsoi et al., 2021). Since it is not feasible to include all mineral varieties for unmixing, the FCLSU analysis was based on the alteration minerals listed in the earlier CGF study (Erika, 2022). The reference spectra from the USGS Spectral Library were accordingly organized by averaging the spectra of the corresponding mineral and instrument.

Subsequently, the CGF spectra (VNIR to SWIR) went through the FCLSU algorithm using the reference USGS spectra. However, there are two major challenges in performing unmixing. First, knowing all the exact end-member minerals is not practicable. Second, mineral spectra of the same

mineral from different geological settings are not always identical. Therefore, FCLSU has its restrictions on suggesting mineralogy based on limited known end-members. Due to the restriction, it is improper to backtrace pure mineral spectra using FCLSU, but it can indicate potential dominant mineralogy for further study. This study considered the FCLSU results that showed single minerals with percentages higher than 90% as a significant indication of mineralogy.

THOR Material Identification Tool in ENVI

ENVI Geospatial Software, renowned for its application in RS, includes the THOR (Tactical Hyperspectral Operations Resource) package with the Material Identification tool. This tool utilizes the SAM (Spectral Angle Mapper) algorithm to compare a sample spectrum with spectral libraries. The algorithm assesses the similarity between the two spectra by calculating their spectral angle (Kruse et al., 1993). A smaller spectral angle indicates a better match between the two spectra. THOR Material Identification provides rankings of good, fair, poor, or very poor spectra matchings based on spectral angles, as presented in Table 4-1.

Table 4-1 The ranking of SAM results by THOR Material Identification in ENVI software.

Spectral Angle	Less than 0.08	0.081 to 0.14	0.141 to 0.25	Greater than 0.251
Quality	Good	Fair	Poor	Very Poor

The collected CGF spectra were compared with the mineral spectra from the USGS Spectra Library Version 7, which was compiled in ENVI. This comparison utilized the spectral range from VNIR to SWIR (350 to 2500 nm), indicating the minerals that best matched the CGF spectra. By focusing on the good or fair matchings, the analysis narrows the scope of potential mineralogy to identify the MOI spectra.

The Spectral Geologist (TGS)

The Spectral Geologist (TSG) software, developed by CSIRO (Commonwealth Scientific and Industrial Research Organisation) of Australia, is a specialized software for geological spectral analysis (Berman et al., 1999, 2011; Herrmann et al., 2001). The TSG software employs an unmixing algorithm named The Spectral Assistant (TSA), which analyzes VNIR and SWIR bands separately. TSA analyzes the spectral patterns of VNIR and SWIR bands to indicate the potential mineralogy within the spectra based on its built-in spectral library. TSA of TSG was applied to the collected CGF spectra to determine the probable mineralogy of the CGF samples.

4.1.4 Establishment of Spectral Library

The laboratory measurements and spectral data processing offer valuable information that aids in the mineralogical identification of the CGF samples. The distinct physical properties of different minerals also provide clues for identification. Each analytical approach has distinct advantages and limitations. Therefore, this study synthesizes the mineralogical indications from each of the applied analyses to establish the spectral library. The mineralogical assessment identifies the spectra dominated by MOI spectra that could be utilized in mineral mapping. Furthermore, the occurrence of MOI in each sample was also logged to facilitate ground-truth information. The documentation of mineral occurrence with coordinates plays a critical role as ground-truth information for the accuracy assessment of mineral maps.

The establishment of the database integrates spectra with their corresponding metadata, figures, and information. In this study, Microsoft Excel was utilized to create tables that facilitated hyperlinks to the folders of CGF spectra, spectral plots, and sample photos. With appropriate metadata documentation, the Coso Spectral Library was designed for public distribution to support future studies and applications.

The metadata documentation preserves the details, including sample ID, field spectrum ID, sampling site, coordinates, collection date, field geological description, applied analytical methods, and potential mineral occurrence. Metadata documentation also connects the corresponding sample photos, spectra files, and spectra plots. The metadata allows for the proper organization of the spectral library and supports further study. Furthermore, a geospatial database of the CGF spectra was constructed to facilitate GIS applications. Figure 4.4 illustrates the simplified structure of the geodatabase. The database includes point shapefiles of alteration minerals with hyperlinks to access the spectral files and spectra plots. Additional tables also organize the spectral files of different formats. Lastly, the polygon shapefiles indicate the Region of Interest (ROI). The geodatabase also documents the occurrences of MOI at each sampling location, which could be applied for accuracy assessments.

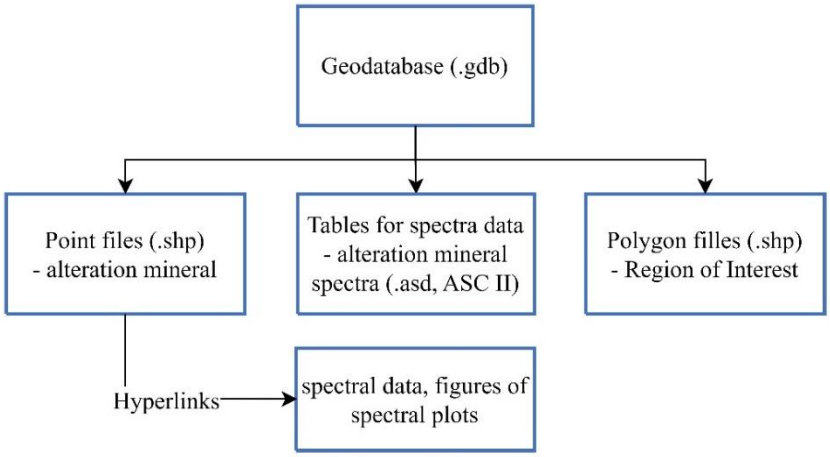

Figure 4.4 Structure of the proposed geodatabase

Making the Coso Spectral Library available supports future studies and applications. To enhance accessibility, the dataset has been made readily available on the Geothermal Data Repository (GDR) (https://gdr.openei.org/home), a website supported by the U.S. Department of Energy that provides open access to data for future geothermal research.

The proposed spectral library and geodatabase were further applied in mineral mapping and accuracy assessment to address the research questions in this study. The Coso Spectral Library facilitated the research on the impact of spectra sources in mineral mapping. Meanwhile, the geodatabase facilitates accuracy assessments that evaluate the mapping accuracies achieved by various mapping approaches.

4.2 The Coso Spectral Library and Geodatabase

According to the analyses from multiple approaches, mineralogy was identified from the samples and spectra. SEM-based automated mineralogy identified the alteration of alunite and kaolinite at the CGF; Epidote was identified from veinlets of rocks; Silicon dioxide was assigned as quartz. However, the quartz assignment was due to the instrument's limit. The identified silicon dioxide could refer to chalcedony or opal components. The result of automated mineralogy is presented in Table 4-2. The geochemical information by pXRF also provides clues for mineralogy. The higher percentage of silicon dioxide suggests that the samples may contain quartz, chalcedony, or opal. In addition, the higher iron content suggests that the samples may contain hematite or rich iron-bearing minerals.

Due to complex mineralogy, it was not always possible to unmix sample spectra into individual spectra of end-member minerals during the FCLSU processing. However, multiple unmixing results suggest that several minerals contribute more than 90% of particular spectrum signals. Identified MOI spectra include alunite, chalcedony, hematite, kaolinite, and opal. The THOR Material Identification successfully identifies multiple spectra that present a good match with the MOI. The TSG software also identifies multiple spectra that match alunite, epidote, hematite, kaolinite, and opal. The limitation of TSA is that the TSG database did not include chalcedony for reference.

Based on the samples' physical properties, laboratory measurements, and spectral data processing, the study obtained the spectra of the six MOI from CGF: alunite, chalcedony, epidote, hematite, kaolinite, and opal.

Table 4-3 organizes a list of samples that present the MOI spectra. The mineralogical assessment details are logged and available in APPENDIX B . A map of the sampling locations that provide the MOI spectra in Table 4-3 is presented in Figure 4.5. The established Coso Spectral Library is the first hyperspectral study and database of the CGF. The approach minimized the amount of destructive mineralogical analysis, which is enlightening to increase the efficiency of spectral library development.

It is important to acknowledge that while the analytical methods applied in this study are effective, they have some limitations in fully distinguishing certain minerals with similar spectral patterns and chemical compositions. For example, differentiating between hematite, goethite, and jarosite, kaolinite and halloysite, or chalcedony, opal, and smectite may be less precise. Incorporating additional mineralogical techniques, such as XRD (X-ray diffraction), could offer more detailed insights and is recommended for future studies to further refine mineral identification.

Table 4-2 A summary of the SEM-based automated mineralogy.

1st Batch	Coso026	Coso027	Coso029	Coso031	Coso032	Coso034
Quartz	83.35%	86.27%	99.75%	98.88%	73.84%	17.90%
Kaolinite	0.03%	2.93%	0.02%	0.01%	11.01%	0.03%
Alunite	12.35%	5.50%	0.07%	0.01%	6.43%	79.35%
Muscovite	1.43%	1.80%	0.02%	0.00%	0.92%	1.92%
Illite	1.60%	0.57%	0.04%	0.01%	0.59%	0.42%
Al-Si-Ti-(K) sulfate	0.25%	0.63%	0.01%	0.00%	4.13%	0.06%
Rutile	0.24%	0.42%	0.02%	0.56%	1.42%	0.02%
Fe-oxides/-hydroxides	0.11%	0.64%	0.00%	0.00%	0.05%	0.00%
Others	0.13%	1.10%	0.04%	0.34%	0.74%	0.00%
[Unclassified]	0.50%	0.14%	0.03%	0.20%	0.88%	0.30%
2nd Batch	**Coso012**	**Coso018**	**Coso023**	**Coso028**	**Coso039**	**Coso042**
Quartz	98.82%	88.92%	33.65%	59.53%	0.24%	52.89%
Alunite	0.00%	4.19%	47.08%	33.02%	0.00%	0.00%
Kaolinite	0.04%	4.50%	6.93%	0.00%	0.01%	0.01%
Illite	0.28%	1.49%	8.91%	5.30%	29.37%	3.26%
Epidote	0.00%	0.00%	0.00%	0.00%	16.40%	0.07%
Albite	0.00%	0.17%	0.04%	0.00%	24.54%	8.21%
K-Feldspar	0.00%	0.00%	0.00%	0.00%	0.58%	33.69%
Hornblende	0.00%	0.00%	0.00%	0.00%	23.52%	1.81%
Others	0.38%	0.36%	1.59%	0.50%	2.12%	0.05%
[Unclassified]	0.49%	0.37%	1.79%	1.65%	3.22%	0.00%

Table 4-3 The Coso samples with identified spectra of the MOI.

Mineral	Spectra collected from the samples of
Alunite	Coso-019, Coso-033, Coso-034
Chalcedony	Coso-015, Coso-042, Coso054, Coso-059, Coso-060, Coso-091, Coso-096
Epidote	Coso-037, Coso-039
Hematite	Coso-087
Kaolinite	Coso-032
Opal	Coso-012, Coso-015, Coso-029, Coso-059, Coso-063

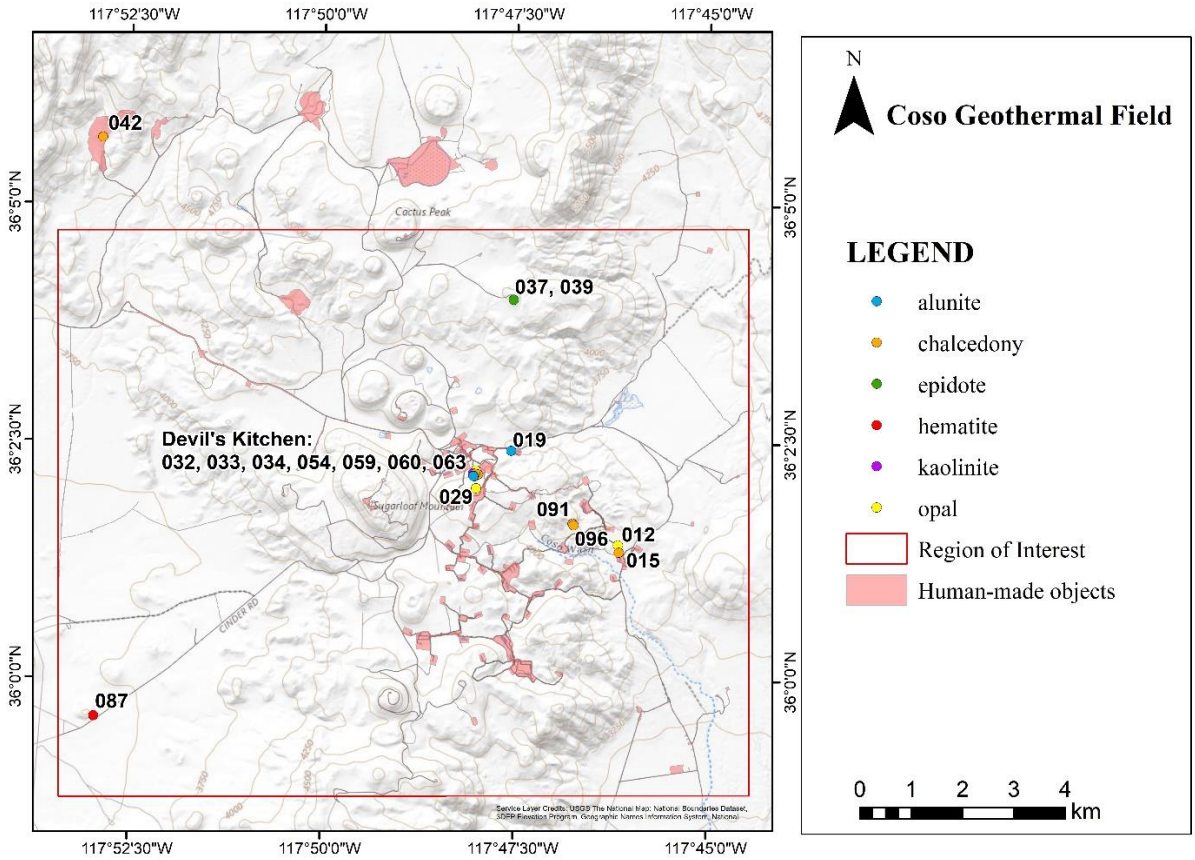

Figure 4.5. The sample distribution of collected MOI spectra.

Following the procedure mentioned in Section 4.1.4, the metadata of the collected samples and spectra were documented in the Coso Spectral Library. The database with corresponding ASD spectral files, ASC II spectral files, spectra plots, and sample photos is available on the GDR website for public availability (https://gdr.openei.org/submissions/1528).

CHAPTER 5 STAGE I: STUDY OF MAPPING METHODS IN MINERAL MAPPING

The study in this chapter seeks to answer research question one (Q1): “How do mapping methods influence mineral mapping?” This question corresponds to research hypothesis H1 and research objective O1. The accuracy of mineral mapping may be affected by the varied application of mapping methods, as discussed in the introduction. Consequently, this part of the study evaluates the influences of implementing mapping algorithms, fusion combinations, and splice correction. An article about mineral mapping, “Mapping Geothermal Indicator Minerals Using Fusion of Target Detection Algorithm”, which covers the study of different mapping algorithms and fusion combinations, has been published in the journal of Remote Sensing (APPENDIX F). The following sections provide a detailed account of the implementations and results of the study.

5.1 Implementation of the Analysis

The study starts by evaluating the mapping accuracies offered by different mapping algorithms. Based on ranking the performances of the mapping algorithms, various fusion combinations were proposed to examine their mapping accuracies further. Additionally, the study compared the mapping accuracies offered by both splice-corrected and non-splice-corrected spectra.

In this part, the study evaluates the mapping accuracy of the algorithms ACE, CEM, MF, MTMF, and SAM, as previously listed in section 2.1. Target spectra have to be defined before proceeding to mineral mapping. Therefore, the CGF spectra that presented the strongest overall fitting with the reference USGS spectra were selected based on correlation coefficients. The reference USGS spectra were prepared by averaging the MOI spectra that were also collected by ASD FieldSpec. Correlation matrices were prepared based on the correlation coefficients between the CGF and USGS spectra (VNIR to SWIR). The matrices help to identify the CGF spectra that present the highest similarities with the USGS spectra. The correlation matrices are organized in Table 5-3 to Table 5-6. It was observed that most CGF spectra presented high correlations with the USGS spectra at correlation levels of more than 90 percent. The representative CGF spectra with the highest correlations to the USGS spectra of alunite at 0.976 (Coso-034), chalcedony at 0.977 (Coso-060), epidote at 0.985 (Coso-039), hematite at 0.875 (Coso-087), kaolinite at 0.948 (Coso-032), and opal at 0.997 (Coso-059). These CGF spectra are presented in Figure 5.1, and Figure 5.2 shows the CGF spectra in comparison with the USGS spectra. The selected CGF spectra were further applied to mineral mapping to evaluate the performance of mapping algorithms.

From this point, epidote was removed from the list of MOI for further mineral mapping and assessment. Epidote typically forms in environments with temperatures higher than 200 degrees Celsius (Henley & Ellis, 1983; Reyes, 1990). Therefore, it is not suitable to include epidote as a target mineral in

mineral mapping for geothermal energy, as active surface alteration at temperatures above 200 degrees is not practical in the study areas.

The selected CGF spectra (Figure 5.1, except epidote) were further applied in mineral mapping with the algorithms ACE, CEM, MF, MTMF, and SAM. Then, the performance of the mapping algorithms was compared and ranked based on the result of the accuracy assessment.

Table 5-1 Correlation matrix for alunite spectra.

Alunite	**Coso019**	**Coso033**	**Coso034**	**CGF avg.***	**USGS alu.**
Coso-019	1				
Coso-033	0.931	1			
Coso-034	0.930	0.968	1		
CGF avg. *	0.966	0.985	0.990	1	
USGS alu.	0.957	0.945	0.976	0.980	1
***CGF avg.: Average Coso alunite**					

Table 5-2 Correlation matrix for chalcedony spectra.

Chalcedony	**Coso 015**	**Coso 042**	**Coso 054**	**Coso 059**	**Coso 060**	**Coso 091**	**Coso 096**	**CGF avg.***	**USGS cdy.**
Coso-015	1								
Coso-042	0.937	1							
Coso-054	0.970	0.905	1						
Coso-059	0.925	0.958	0.954	1					
Coso-060	0.948	0.962	0.966	0.992	1				
Coso-091	0.915	0.871	0.920	0.902	0.910	1			
Coso-096	0.943	0.891	0.961	0.924	0.943	0.955	1		
CGF avg.*	0.979	0.960	0.984	0.978	0.988	0.944	0.970	1	
USGS cdy.	0.974	0.939	0.976	0.965	0.977	0.894	0.944	0.984	1
***CGF avg.: Average CGF chalcedony**									

Table 5-3 Correlation matrix for epidote spectra.

Epidote	Coso037	Coso039	CGF avg.*	USGS epd.
Coso-037	1			
Coso-039	0.998	1		
CGF avg. *	0.999	0.999	1	
USGS epd.	0.979	0.985	0.982	1
***CGF avg.: Average CGF epidote**				

Table 5-4 Correlation matrix for hematite spectra.

Hematite	Coso087	USGS hem.
Coso-087	1	
USGS hem.	0.875	1

Table 5-5 Correlation matrix of kaolinite spectra.

Kaolinite	Coso032	USGS kln.
Coso-032	1	
USGS kln.	0.948	1

Table 5-6 Correlation matrix for opal spectra.

Opal	Coso012	Coso015	Coso029	Coso059	Coso063	CGF avg.*	USGS opl.
Coso-012	1						
Coso-015	0.901	1					
Coso-029	0.926	0.978	1				
Coso-059	0.887	0.960	0.982	1			
Coso-063	0.958	0.935	0.977	0.972	1		
CGF avg.*	0.964	0.984	0.981	0.954	0.968	1	
USGS opl.	0.877	0.964	0.977	0.997	0.961	0.952	1
***CGF: avg.: Average Coso opal**							

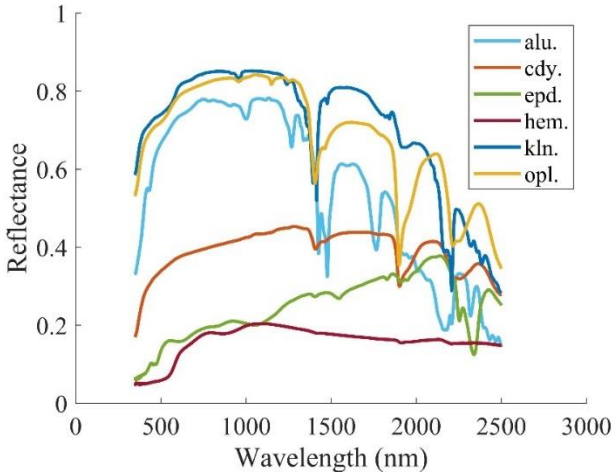

Figure 5.1. The selected CGF spectra of MOI for the mineral mapping study.

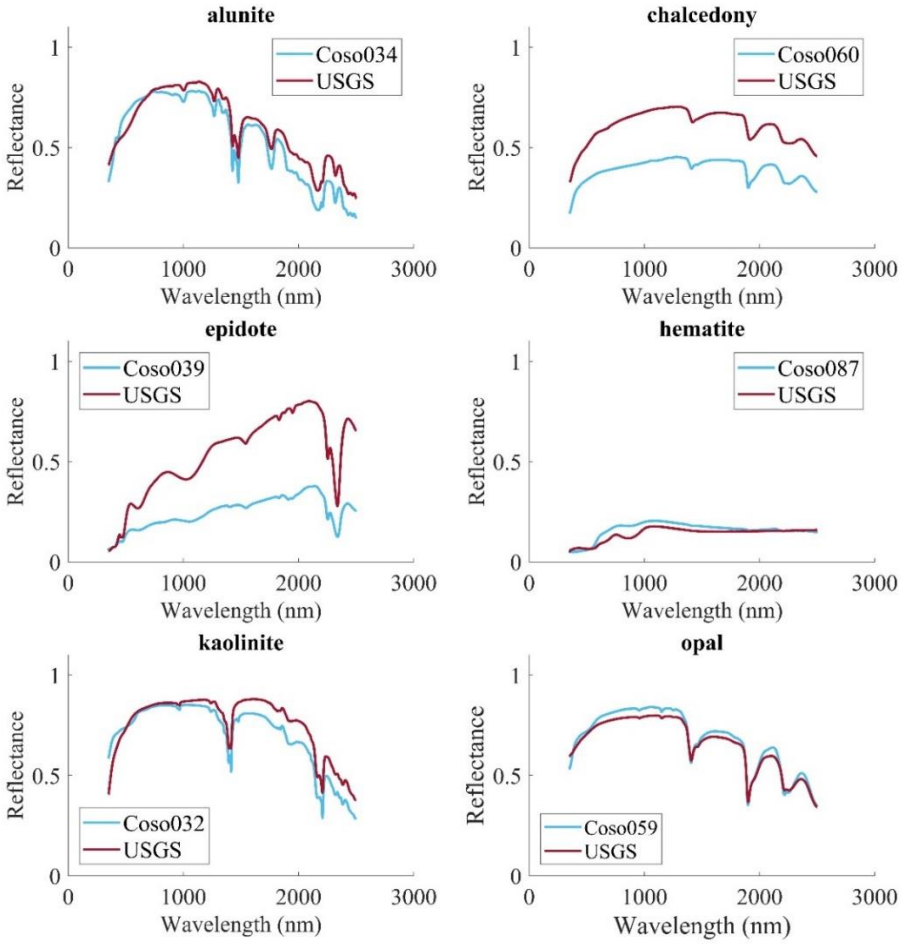

Figure 5.2 MOI spectra of the USGS Spectral Library and the Coso Spectral Library.

Based on the evaluation of mapping algorithms in generating accurate mineral maps (5.2.1), the study ranks the mapping algorithms and proposes multiple fusion combinations. Each fusion combination compiles the mapping results from selected mapping algorithms based on the R-based module mentioned in section 2.1. The mineral maps by the CGF spectra were further fused according to the fusion combinations. The fused mineral maps underwent accuracy assessments to examine whether the fusion of mineral maps increases mapping accuracy.

The mineral maps based on the selected CGF spectra were further compared with the earlier mappings that used CGF spectra that did not go through splice correction. The mappings have the same procedure except for the only difference in the input spectra. The comparison was not based on fusion mineral maps to assess the impact of splice correction on the mapping result of individual algorithms.

5.2 Results and Discussion

Based on the assessment of mineral maps, this part of the study discovered several key findings, including: (1) The performance of mapping algorithms is not the same. CEM, MF, and MTMF offer the highest accuracies, while ACE was the lowest. SAM was in between. (2) The fusion of mineral maps increases the accuracy of mineral maps. Particularly, the fusion combination of all five studied mapping algorithms offered more accurate maps. (3) Splice correction has been shown to enhance mapping accuracies in the cases studied, going beyond a necessary procedure in spectral data processing. The following sections illustrate the detailed results.

5.2.1 Mapping With Various Mapping Algorithms

The mapping result is presented in Figure 14 after being converted to mineral density maps for best visualization. The maps showed that varied mapping algorithms offered different patterns on maps. It was observed that CEM, MF, and MTMF offered similar mapping results. After overlapping the results of the three algorithms and subtracting their prediction levels, it was found that the mapping results of the three algorithms were the same. The close results of CEM, MF, and MTMF reflect that they were based on a similar logic of calculation (Boardman & Kruse, 2011; Chang et al., 2000).

The AUC levels of mineral maps are summarized in Table 5-7. The corresponding ROC curves are presented in Figure 5.4. Although all algorithms provided high accuracies for the alunite mapping, it was observed that the AUC levels were different among the algorithms. In this part of the study, CEM, MF, and MTMF offered the highest accuracies, followed by SAM, and ACE provided the lowest accuracies. The findings align with earlier studies (Jawak et al., 2022b; Shang et al., 2020), which are compiled in Table 5-8. Earlier studies also found that CEM, MF, and MF have close performance that is better than SAM. The performance of the ACE algorithm in other previous studies was varied, but it was also

identified to be the worst in one study. The potential reason for the varied performance of ACE will be covered in the later part of this dissertation in the section about the impacts of spectral variability in mineral mapping (6.2.1).

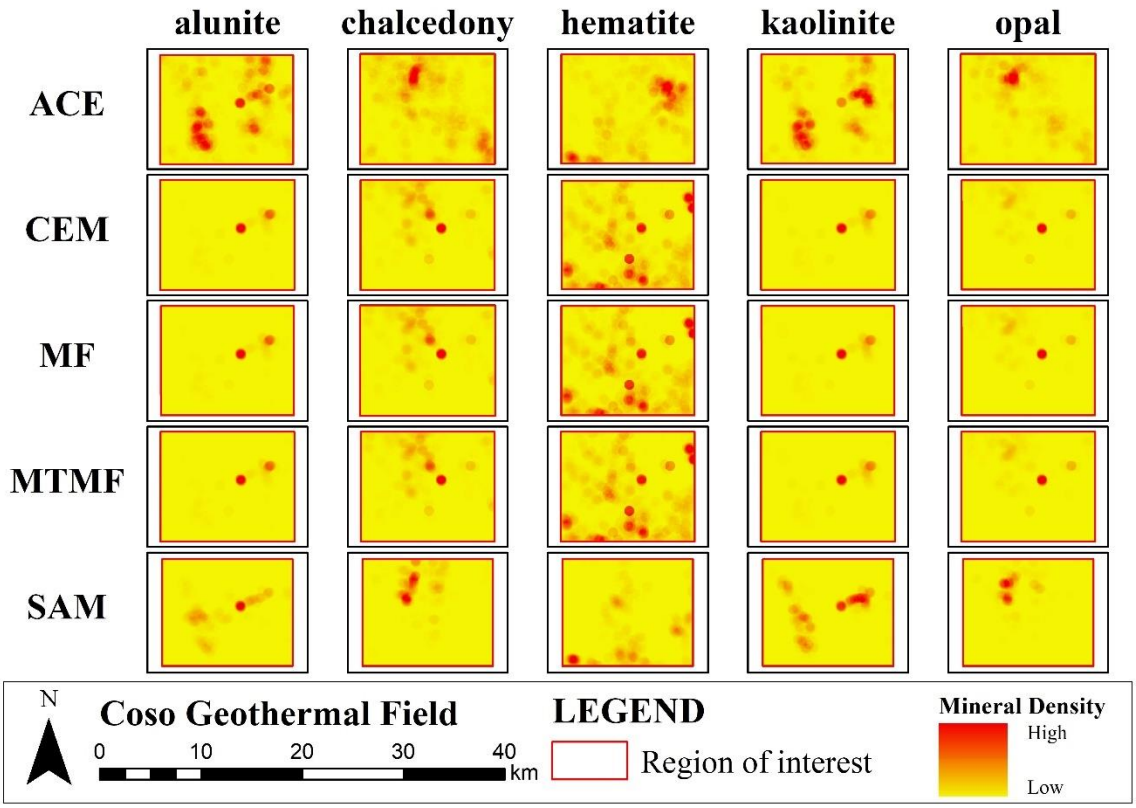

Figure 5.3 The mineral density maps by the selected CGF spectra. Each column is one type of MOI, and each row is one mapping algorithm.

Table 5-7 The AUC levels of mineral maps of the CGF by different mapping algorithms.

Algorithm	Alunite	Chalcedony	Hematite	Kaolinite	Opal	Average
ACE	1.000	0.233	0.582	0.954	0.164	0.587
CEM	1.000	0.867	0.702	0.975	0.955	0.900
MF	1.000	0.867	0.702	0.975	0.955	0.900
MTMF	1.000	0.867	0.702	0.975	0.955	0.900
SAM	1.000	0.727	0.741	0.953	0.818	0.848

Table 5-8 The studies comparing algorithm performance.

The studies	Comparison of performance
This study	CEM = MF = MTMF > SAM > ACE
Jawak et al., 2022	ACE > MF > CEM > MTMF > SAM
Shang et al., 2020	CEM = MF > MTMF > SAM > ACE

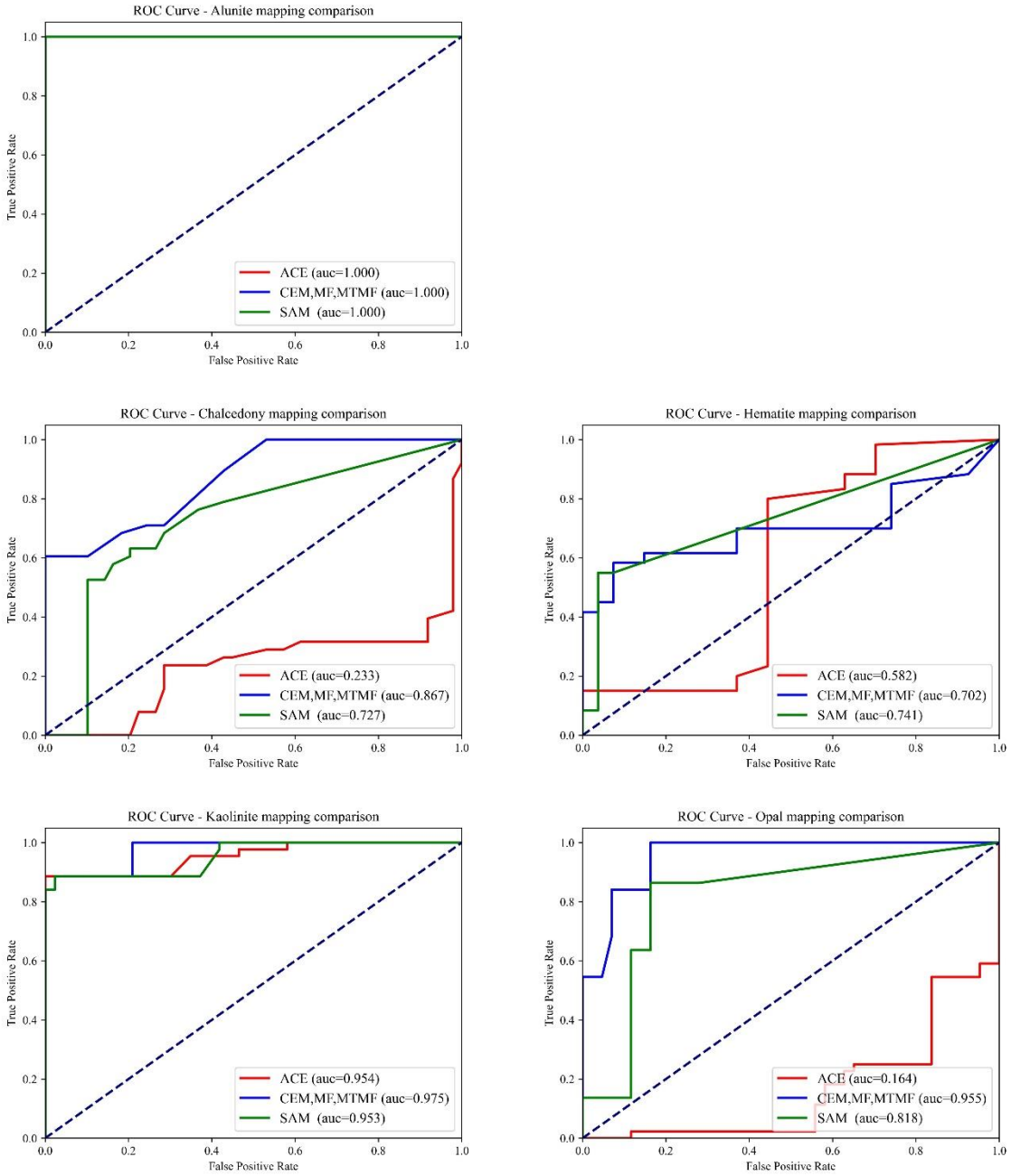

Figure 5.4 ROC curves of the five MOI with different mapping algorithms.

5.2.2 Mapping With Various Fusion Combinations

Based on the findings from the evaluation of mapping algorithms, three fusion combinations were proposed, following the performance of the mapping algorithms from the best to the worst.

1) Fusion of three algorithms (3A): CEM, MF, and MTMF

2) Fusion of four algorithms (4A): CEM, MF, MTMF, and SAM

3) Fusion of five algorithms (5A): ACE, CEM, MF, MTMF, and SAM

The fused mineral maps went through accuracy assessments. The AUC levels of the fused mineral maps are summarized in Table 5-9 with the AUC levels offered by individual mapping algorithms. The corresponding ROC curves are presented in Figure 5.5. The comparison showed that the fusion mineral maps offered higher average AUC levels than those by individual mapping algorithms. Particularly, the fusion combination of five algorithms has the highest average AUC. It was proved that the fusion of mineral maps could improve overall mapping accuracies and that the fusion combination of ACE, CEM, MF, MTMF, and SAM was the best.

Table 5-9 The AUC levels of mineral maps of various fusion combinations.

Accuracy	Alunite	Chalcedony	Hematite	Kaolinite	Opal	Average
ACE	1.000	0.233	0.582	0.954	0.164	0.587
CEM	1.000	0.867	0.702	0.975	0.955	0.900
MF	1.000	0.867	0.702	0.975	0.955	0.900
MTMF	1.000	0.867	0.702	0.975	0.955	0.900
SAM	1.000	0.727	0.741	0.953	0.818	0.848
Fusion 3A	1.000	0.847	0.725	0.976	0.978	0.905
Fusion 4A	1.000	0.832	0.751	0.970	0.964	0.903
Fusion 5A	1.000	0.806	0.909	0.977	0.977	0.934

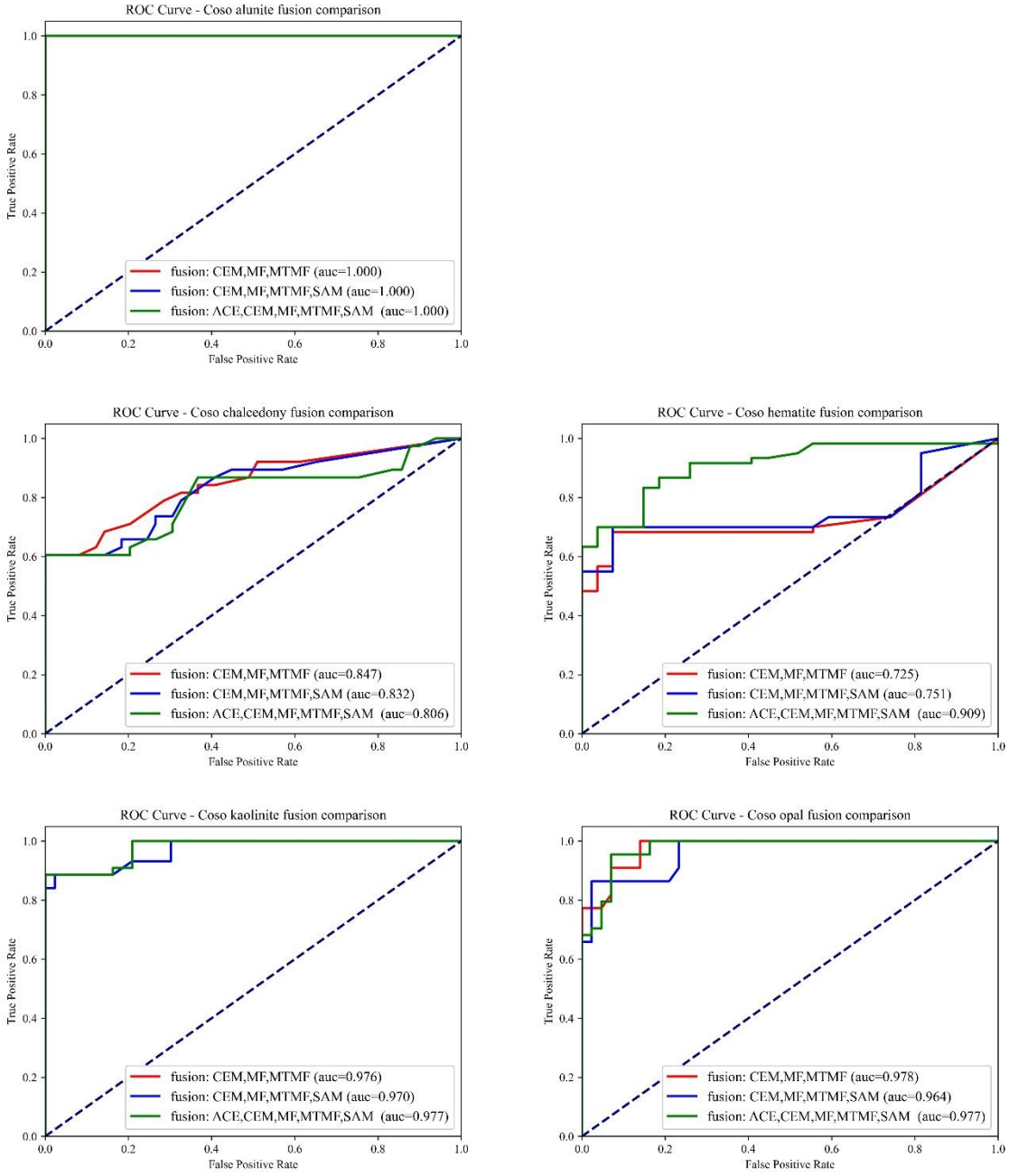

Figure 5.5 ROC curves of the five MOI with various fusion combinations.

5.2.3 Mapping With Various Employments of Splice Correction

Moving forward, the study compares the results from the previous section (5.2.1) with earlier mineral maps by the same spectra without splice correction (Cavur et al., 2024). Table 5-10 summarizes the AUC levels of mineral maps. It was found that splice-corrected spectra provided more mineral maps with higher accuracies than non-splice-corrected spectra, especially in the cases of CEM, MF, MTMF, and SAM. The average AUC levels increased by around five percent (SAM) and ten percent (CEM/MF/MTMF). The non-splice-corrected spectra provided the higher average AUC level in the case of ACE (around ten percent higher), but ACE was identified to offer lower accuracies in mineral mapping. Therefore, the splice correction of target spectra is still critical in mineral mapping.

Table 5-10 Comparison of the AUC levels of mineral maps based on the CGF spectra with the different applications of splice correction.

Algorithms	Splice correction	Alunite	Chalcedony	Hematite	Kaolinite	Opal	Average
ACE	**applied**	1.000*	0.233	0.582	0.954	0.164	0.587
	not applied	0.87	0.56*	0.71*	0.91*	0.42*	0.694*
CEM, MF, MTMF	**applied**	1.000*	0.867*	0.702*	0.975*	0.955*	0.900*
	not applied	0.88	0.8	0.68	0.88	0.76	0.800
SAM	**applied**	1.000*	0.727	0.741*	0.953*	0.818*	0.848*
	not applied	0.87	0.85*	0.59	0.88	0.79	0.796
The AUCs with a star (*): the higher AUC.							

CHAPTER 6 STAGE II: STUDY OF SPECTRA SOURCE IN MINERAL MAPPING

The study in this chapter seeks to answer research question two (Q2): "How do spectra sources influence mineral mapping?" This question corresponds to research hypothesis H2 and research objective O2. The accuracy of mineral mapping may be affected by the variation of spectral details, as discussed in the introduction. Consequently, this part of the study evaluates the influences of selecting spectral variabilities and spectral libraries. An article that covers the study that evaluates mineral maps with varied spectra from various spectral libraries is under review by the Journal of Applied Remote Sensing (APPENDIX G). The following sections provide a detailed account of the implementations and results of the study.

6.1 Implementation of the Analysis

The study focused on evaluating alunite and kaolinite maps to explore the impact of spectral variability in mineral mapping. The study also compared the accuracies of mineral maps offered by both the Coso Spectral Library and the USGS Spectral Library to understand the difference between using a local spectral library and a universal open-access spectral library.

For the evaluation of spectral variability, the study focused on alunite and kaolinite mappings with various mapping algorithms (ACE, CCEM, MF, MTMF, and SAM). Alunite and kaolinite are documented alteration minerals at CGF (Davatzes & Hickman, 2010; Hulen, 1978), the proposed Coso Spectral Library, and the USGS Spectral Library version 7. The selection of alunite and kaolinite was based on their common occurrence in multiple geothermal systems (Savitri et al., 2021) and hydrothermal mineral deposits (Hedenquist & Arribas, 2022), presenting as the indicator minerals of steam-heated alteration (Thompson et al., 1999).

As presented in section 4.2, the Coso Spectral Library includes mineral spectra of alunite (Coso-019, Coso-033, and Coso-034) and kaolinite (Coso-032). Figure 6.1 presents the CGF spectra of alunite and kaolinite, including the average alunite spectra (Coso-AVG). The USGS Spectral Library collected spectra from four spectrometers that cover different wavelength ranges (Kokaly et al., 2017). This study utilized alunite and kaolinite spectra from the USGS Spectral Library that were also collected by the ASD FieldSpec for a comparable scenario to the Coso Spectral Library. The alunite and kaolinite spectra in the USGS Spectral Library were obtained from various locations in the USA. Table 6-1 and Table 6-2 list the selected spectra and their title, record numbers, and collection locality. None of the samples came from CGF. Figure 6.2 presents the selected spectra from the USGS Spectral Library, including the average spectra of the alunite and kaolinite (USGS-AVG). Figure 6.1 and Figure 6.2 illustrate significant variations in the spectral signatures of the selected minerals from the Coso and USGS spectral libraries.

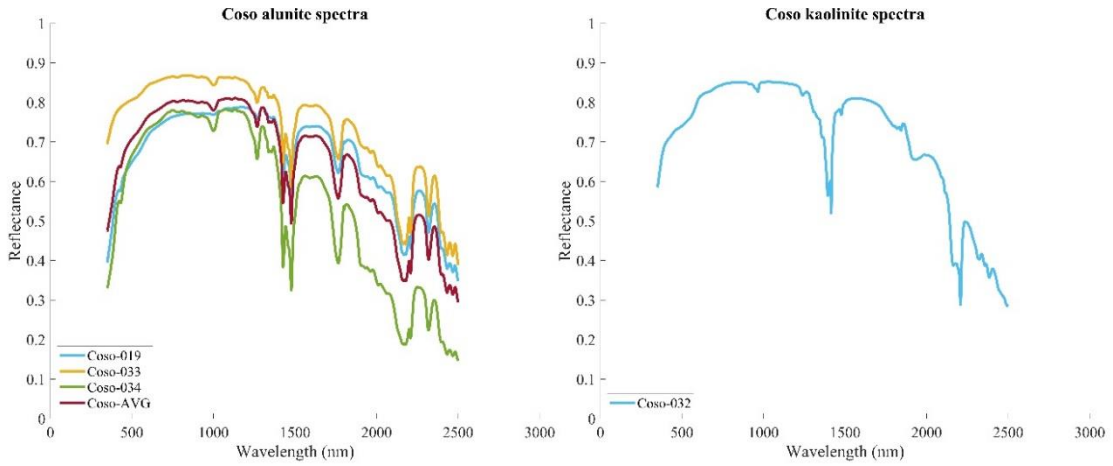

Figure 6.1 The alunite and kaolinite spectra of the Coso Spectral Library.

Table 6-1 Alunite spectra by ASD FieldSpec in the USGS Spectral Library

Spectrum title	Record number	Collection locality (USA)
Alunite_HS295.1B_ASDFRa_AREF	s07_ASD 765	Utah
Alunite_HS295_ASDFRa_AREF	s07_ASD 771	Utah
Alunite_HS295.3B_ASDFRa_AREF	s07_ASD 789	Utah
Alunite_HS295.3B_ASDNGa_AREF	s07_ASD 795	Utah
Alunite_HS295.4B_ASDFRa_AREF	s07_ASD 813	Utah
Alunite_HS295.6_ASDFRb_AREF	s07_ASD 819	Utah
Alunite_RES-9_Summitv_(400C)_ASDNGb_AREF	s07_ASD 856	Summitville, Colorado

Table 6-2 Kaolinite spectra by ASD FieldSpec in the USGS Spectral Library

Spectrum title	Record number	Collection locality (USA)
Kaolinite_CM9_ASDNGb_AREF	s07_ASD 6274	Mesa Alta, New Mexico
Kaolinite_KGa-1_(wxl)_ASDNGb_AREF	s07_ASD 6336	Washington County, Georgia
Kaolinite_KGa-2_(pxl)_ASDNGb_AREF	s07_ASD 6371	Warren County, Georgia

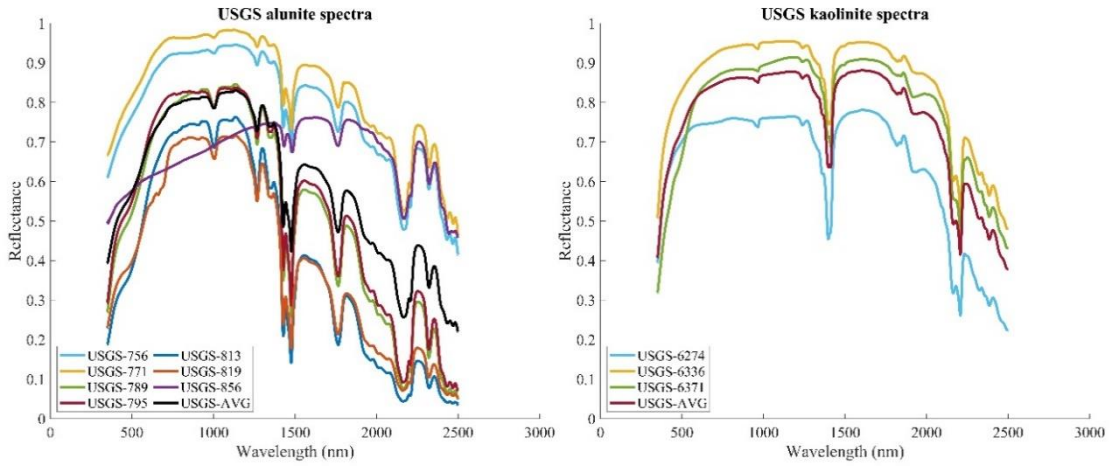

Figure 6.2 The alunite and kaolinite spectra of the USGS Spectral Library.

Based on the Target Detection Wizard of ENVI, the toolset resamples the target spectra regarding the spectral bands of the studied image. Figure 6.3 and Figure 6.4 illustrate that the target alunite and kaolinite spectra (Figure 6.1 and Figure 6.2) are not identical after being resampled according to the bands of the ASTER dataset. All the alunite and kaolinite spectra from the Coso and USGS spectral libraries were applied to mineral mapping with the selected five mapping algorithms to evaluate the impact of spectral variability in mineral mapping.

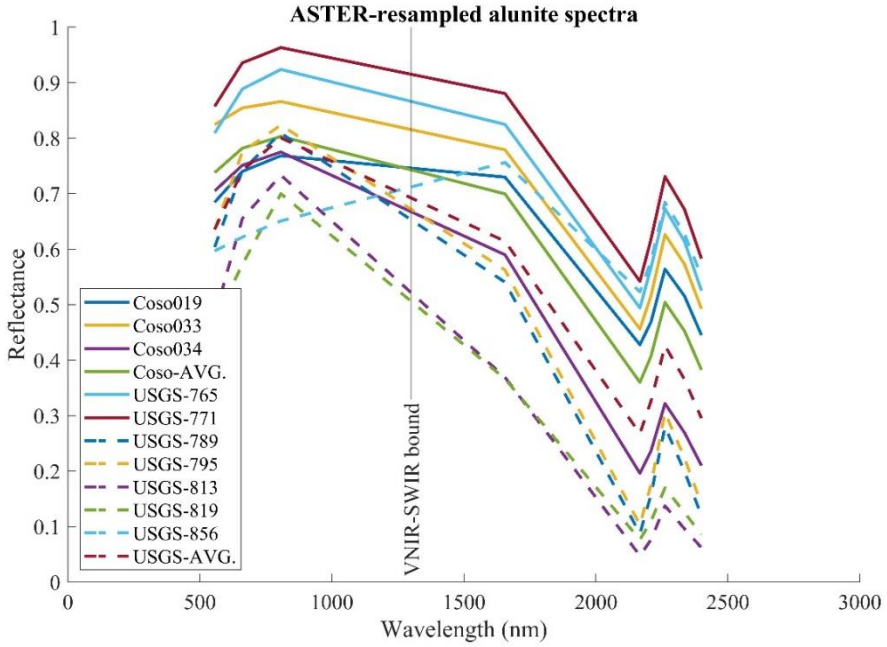

Figure 6.3 The resampled alunite spectra in ASTER bands.

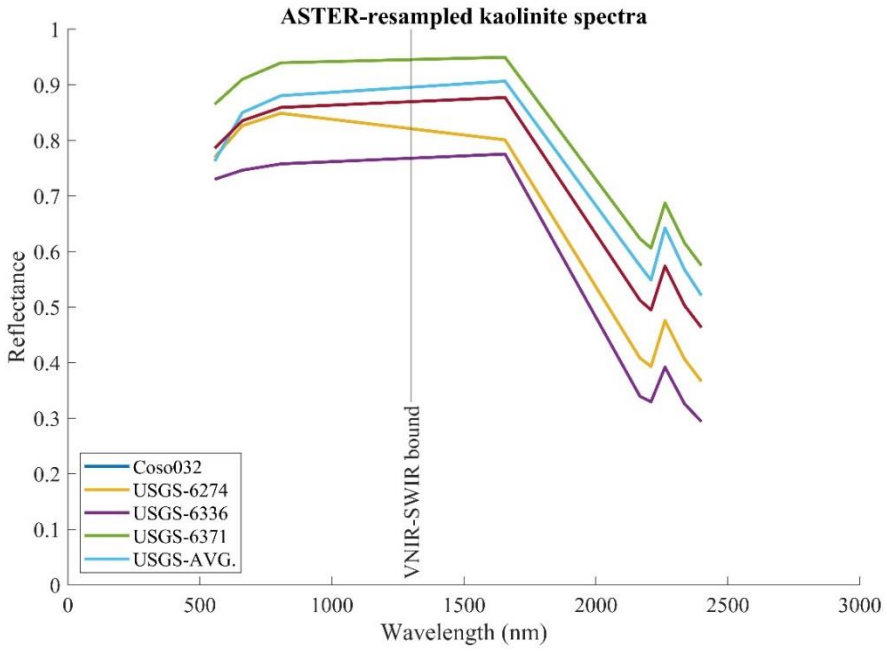

Figure 6.4 The resampled kaolinite spectra in ASTER bands.

Evaluating the influence of spectral variability on mineral mapping accuracies (6.2.1) revealed that using the USGS spectra could generally improve the accuracy of mineral mapping. Therefore, in the study comparing the mapping results of various spectral libraries, the average USGS spectra and the CGF spectra that presented the highest correlation coefficients with the average USGS spectra were applied. Those are the same spectra previously organized in section 5.1 and presented in Figure 5.2. The maps of alunite, chalcedony, hematite, kaolinite, and opal were generated with the five mapping algorithms (ACE, CEM, MF, MTMF, and SAM). The results of the AUC level were compared pairwise between the USGS spectra and the CGF spectra to identify the library that offers the higher mapping accuracies.

6.2 Results and Discussion

Several findings were discovered based on assessing mineral maps by various spectra, including: (1) Spectral variability affects mapping accuracy depending on mapping algorithms. CEM, MF, and MTMF are less sensitive to spectral variability while providing higher accuracy. ACE was more sensitive to spectral variability. Additionally, using the average spectra of the USGS Spectral Library could increase overall accuracy. (2) Mineral maps by the local Coso Spectral Library have higher accuracies, but USGS spectra are not significantly worse. The following sections illustrate the detailed results.

6.2.1 Mapping With Different Spectral Variabilities

The selected CGF and USGS spectra (Figure 6.3 and Figure 6.4) were applied to create alunite and kaolinite mineral maps. The generated mineral maps are organized in Figure 6.5 and Figure 6.6 as density maps for the best visualization. Alunite and kaolinite generally have similar mapped patterns with clusters northeast and west of CGF. However, the detailed patterns on maps varied between spectra. For example, the alunite maps using the spectra USGS-819, USGS-856, and USGS-AVG based on the SAM algorithm are visually different (lower-right of Figure 6.5). In addition, different mapping algorithms could yield different results.

The CEM, MF, and MTMF algorithms presented similar mapping results with few areas of high mineral density northeast of CGF (Coso Hot Springs and Devil's Kitchen). The mineral maps of these three algorithms also showed slight variations due to varied spectra. In contrast, the ACE and SAM algorithms produced mineral maps with more high-mineral-density areas. The mapped patterns of these two algorithms showed distinct variations due to the application of various spectra. The mapping results suggest that algorithms ACE and SAM are more sensitive to spectral variability.

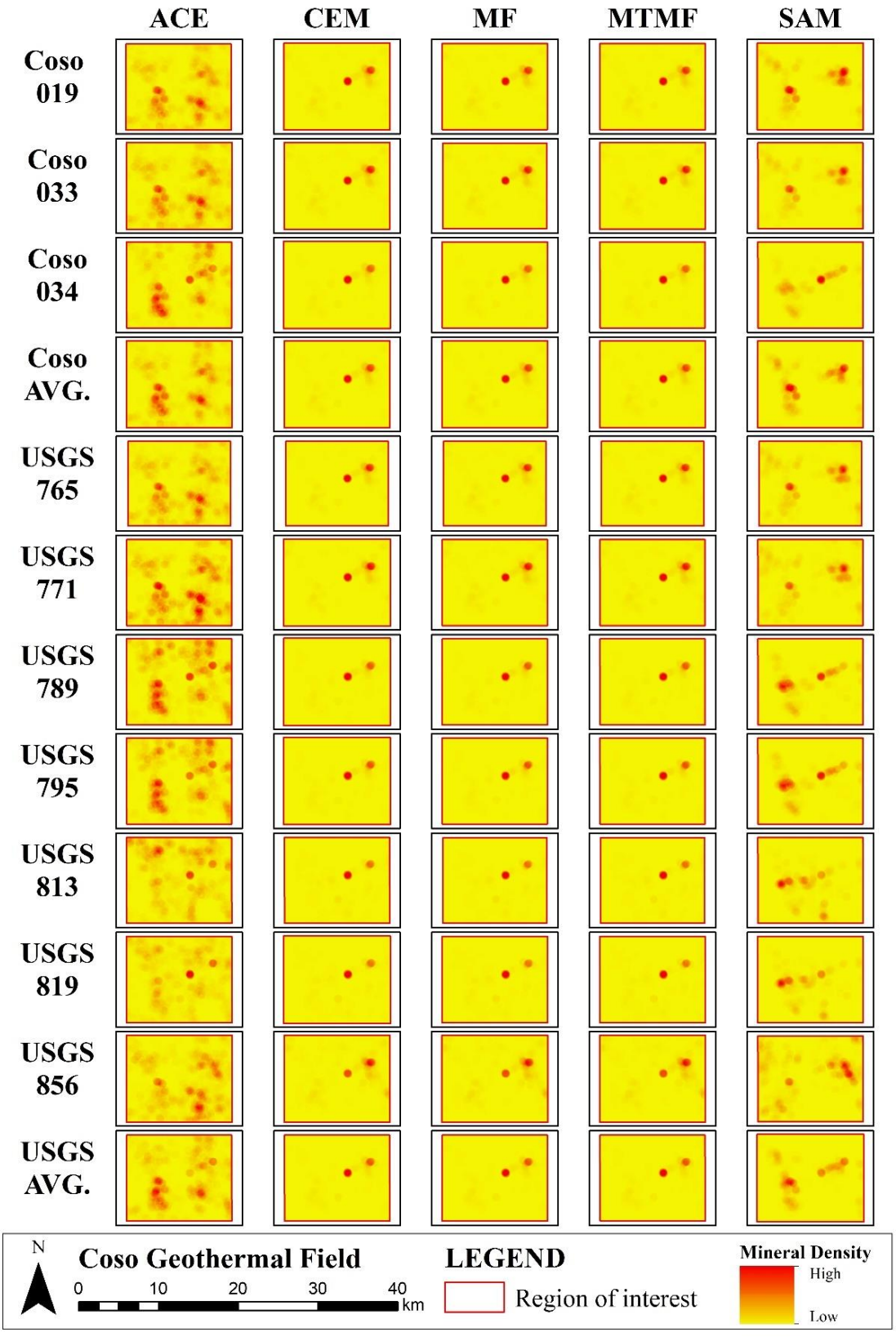

Figure 6.5 The alunite mineral density maps. Each raw is one spectrum from the Coso Spectral Library and the USGS spectral library. Each column refers to one mapping algorithm.

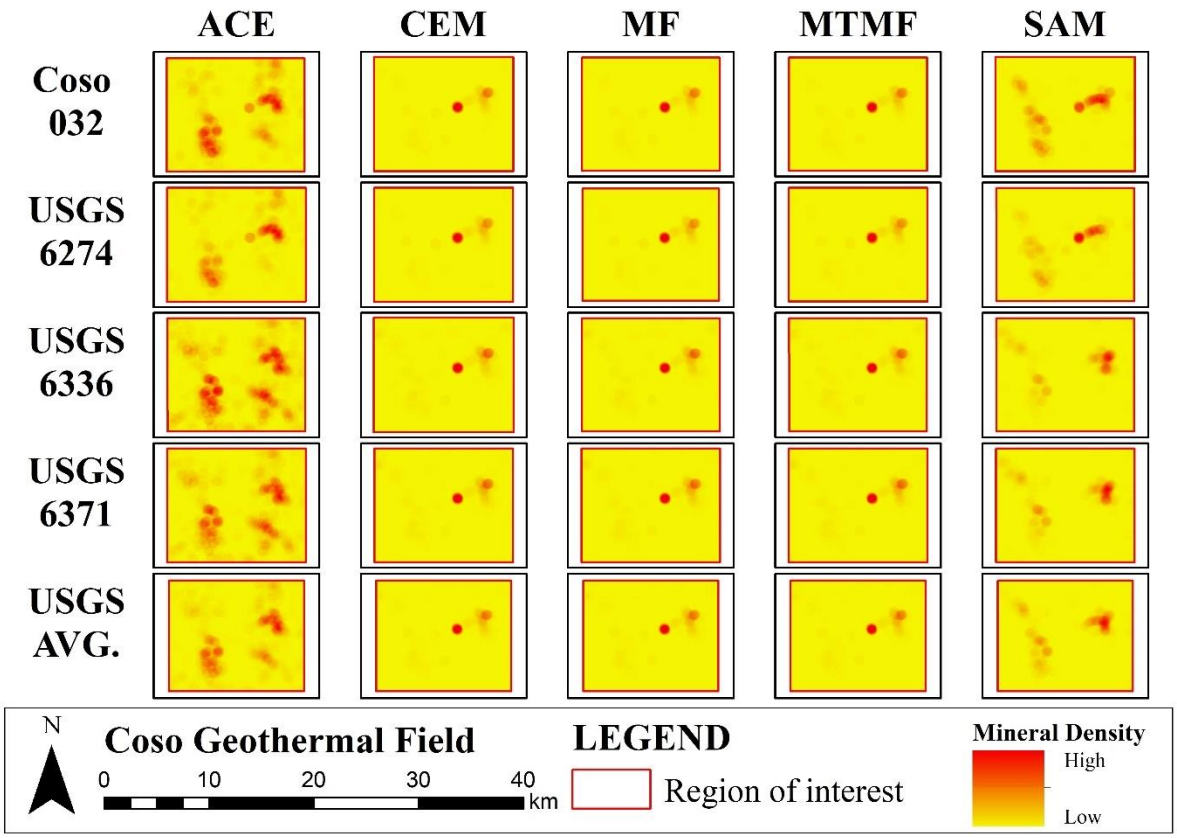

Figure 6.6 The kaolinite mineral density maps. Each raw is one spectrum from the Coso Spectral Library and the USGS spectral library. Each column refers to one mapping algorithm.

The ROC curves of varied alunite and kaolinite spectra for each mapping algorithm are organized in Figure 6.7 and Figure 6.8. The ROC curves of ACE and SAM presented a higher level of variations than CEM, MF, and MTMF. The corresponding AUC values and associated statistics by each spectrum are summarized in Table 6-3. Table 6-4 summarizes the statistics of AUC by each mapping algorithm.

According to Table 6-3, the alunite maps showed that multiple spectra, Coso-034, USGS-789, USGS-795, and USGS-AVG, have the highest accuracy. The performance has an average AUC of up to 1 and an AUC range low to 0. The lowest average AUC was 0.827 by USGS-856. For the kaolinite maps, the spectrum Coso-032 yielded the most accurate map. The average AUC was 0.966, and the AUC range was 0.022. The USGS-AVG and USGS-6274 also provided accurate mineral maps with average AUCs higher than 0.93 and AUC ranges lower than 0.17. The lowest average AUC was 0.851 by USGS-6336.

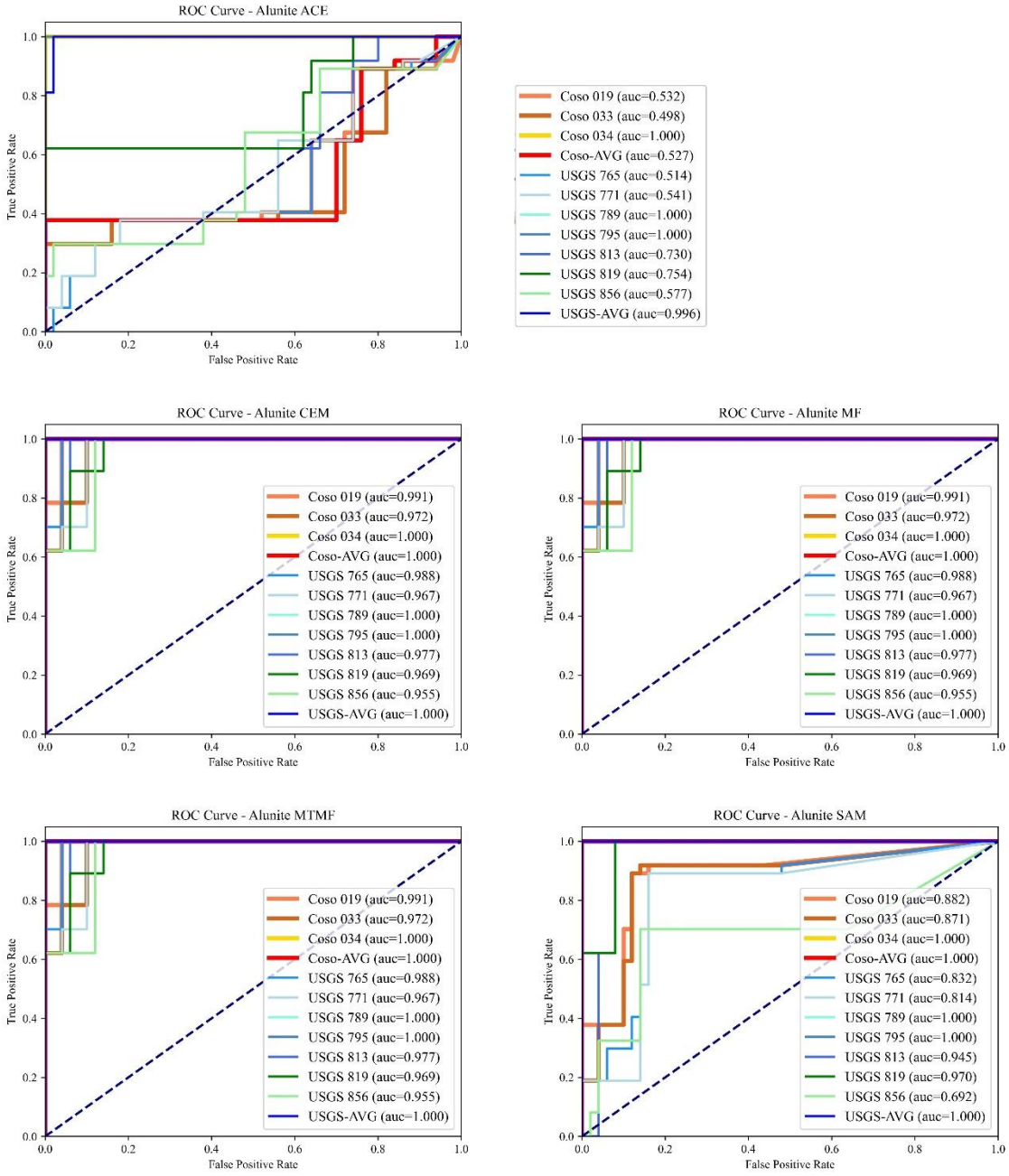

Figure 6.7 The ROC curves and AUC values from accuracy assessments of alunite mappings.

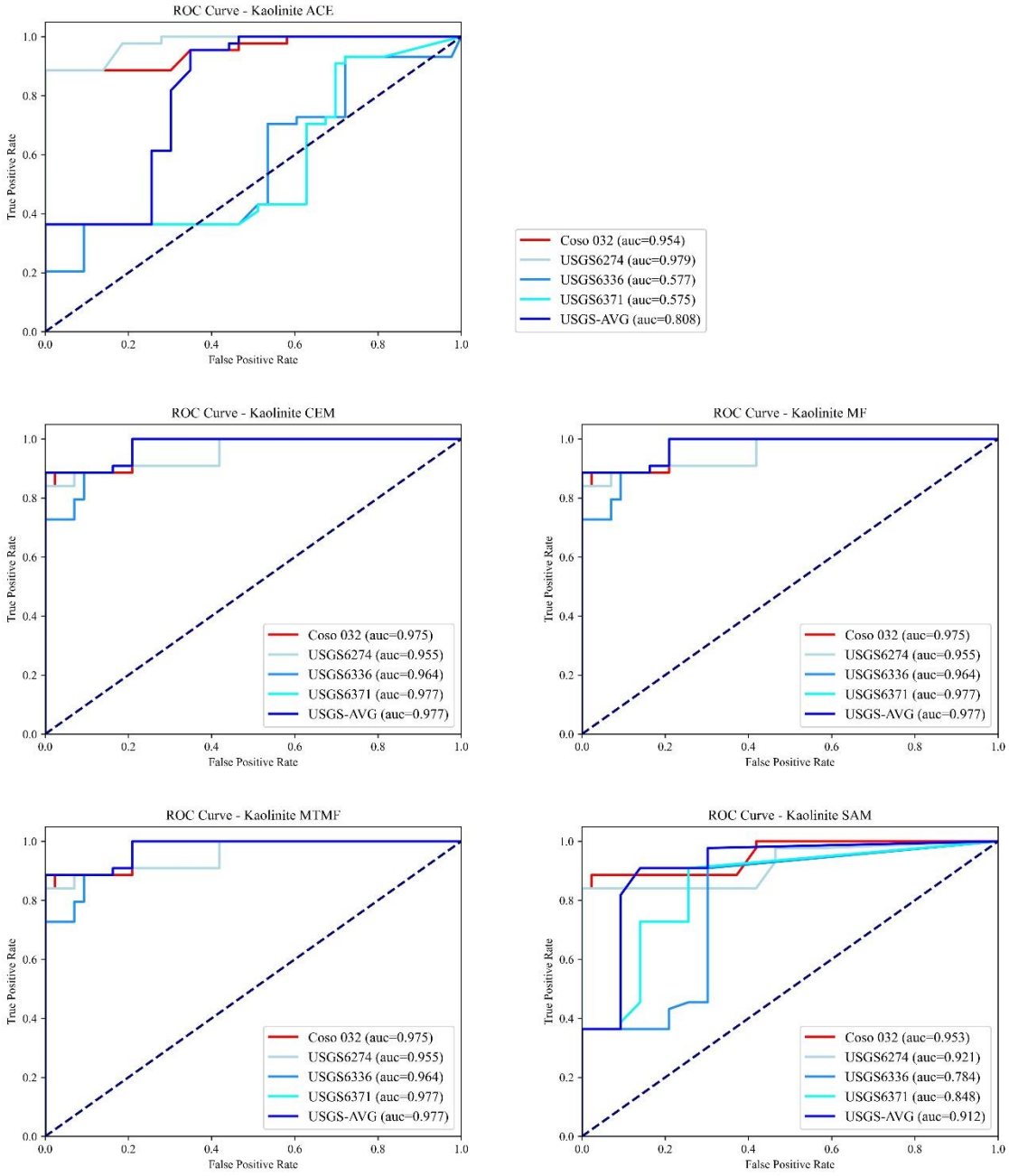

Figure 6.8 The ROC curves and AUC values from accuracy assessments of kaolinite mappings.

In general, the local spectra provided higher accuracy for mineral maps. Notably, the Coso-034 of alunite and Coso-32 of kaolinite used for the mineral maps bring about the highest average AUCs and the lowest AUC ranges, indicating a better map quality. Although the local alunite spectra Coso-019 and Coso-033 yielded lower average AUCs than Coso-034, Coso-034 went through more detailed analyses than Coso-019 and Coso-033 during the establishment of the Coso Spectral Library, suggesting that the mineralogy of Coso-034 was more detailed identified.

Table 6-3 The AUC values and associated averages and ranges by spectrum.

Mineral	Spectra	ACE	CEM	MF	MTMF	SAM	Average AUC	AUC Range
alunite	**Coso-019**	0.532	0.991	0.991	0.991	0.882	0.877	0.459
	Coso-033	0.498	0.972	0.972	0.972	0.871	0.857	0.474
	Coso-034	1.0	1.0	1.0	1.0	1.0	1.0*	0.0*
	Coso-AVG	0.527	1.0	1.0	1.0	1.0	0.905	0.473
	USGS-765	0.514	0.988	0.988	0.988	0.832	0.862	0.474
	USGS-771	0.541	0.967	0.967	0.967	0.814	0.851	0.426
	USGS-789	1.0	1.0	1.0	1.0	1.0	1.0*	0.0*
	USGS-795	1.0	1.0	1.0	1.0	1.0	1.0*	0.0*
	USGS-813	0.730	0.977	0.977	0.977	0.945	0.921	0.247
	USGS-819	0.754	0.969	0.969	0.969	0.970	0.926	0.216
	USGS-856	0.577	0.955	0.955	0.955	0.692	0.827	0.378
	USGS-AVG	0.996	1.0	1.0	1.0	1.0	0.999*	0.004
kaolinite	**Coso 032**	0.954	0.975	0.975	0.975	0.953	0.966*	0.022*
	USGS-6274	0.979	0.955	0.955	0.955	0.921	0.953	0.058
	USGS-6336	0.577	0.964	0.964	0.964	0.784	0.851	0.387
	USGS-6371	0.575	0.977	0.977	0.977	0.848	0.871	0.402
	USGS-AVG	0.808	0.977	0.977	0.977	0.912	0.930	0.169

The highest average AUCs and the lowest AUC ranges were denoted with a star (*).

The results also show that multiple USGS spectra contribute to the maps with average AUC levels higher than 0.9, but some USGS spectra result in the lowest average AUCs. Using the average spectra from the USGS library yields relatively higher accuracies. Both USGS-AVG spectra offered the second-highest average AUC and the second-lowest AUC range among the USGS spectra. By randomly selecting

a USGS spectrum for mineral mapping, the average AUC of the alunite map could change from 0.827 (USGS-856) to 1.0 (USGS-789, USGS-795), and the average AUC of the kaolinite map could change from 0.851 (USGS-6336) to 0.953 (USGS-6274). Using USGS average spectra for mineral mapping can avoid inaccurate mineral maps based on a randomly chosen spectrum from the USGS Spectral Library.

Based on Table 6-3, it was further observed that the AUC levels varied following the mapping algorithms. The AUCs of CEM, MF, and MTMF are generally the highest, whereas those of ACE and SAM remain lower in comparison. One exception occurs in the case of USGS-819 and USGS-6274, where ACE and SAM were slightly higher by 0.024 and 0.001. The other exception occurs in the case of Coso-034, Coso-AVG(alunite), USGS-789, USGS-795, and USGS-AVG (alunite), where ACE and/or SAM reached the same AUC of CEM, MF, and MTMF at 1. Other than the aforementioned two exceptions, the AUCs of ACE and SAM are notably lower. The difference between the AUC values of CEM/MF/MTMF and ACE results in 14 AUC ranges out of 17 studied cases of spectra, indicating the best and the worst-performing algorithms.

Table 6-4 The statistics of AUC by each mapping algorithm.

Mineral	AUC statistics	ACE	CEM	MF	MTMF	SAM
alunite	**Average AUC**	0.722	0.985	0.985	0.985	0.917
	AUC Range	0.502	0.045	0.045	0.045	0.308
kaolinite	**Average AUC**	0.779	0.970	0.970	0.970	0.884
	AUC Range	0.404	0.022	0.022	0.022	0.169

The average AUC and AUC range by each mapping algorithm are summarized in Table 6-4. CEM, MF, and MTMF provided the highest average AUCs and the lowest AUC ranges for alunite and kaolinite, suggesting that they are the most accurate and precise algorithms. ACE has the lowest average AUC and the highest AUC range for both alunite and kaolinite. The average AUC and the AUC range of SAM were between CEM/MF/MTMF and ACE for the studied cases. In this study, varied spectra significantly impact ACE by influencing the AUC level from more than 40 percent (kaolinite) to 50 percent (alunite). Varied spectra also impact SAM by changing the AUC level from around 17 percent (kaolinite) to 31 percent (alunite). Meanwhile, the impact of varied spectra on CEM, MF, and MTMF remains less than 5 percent. It was found that varied input spectra greatly change the AUC level of ACE and SAM, whereas CEM, MF, and MTMF present better consistency. The finding suggests that CEM, MF, and MTMF are less sensitive to spectral variability while providing accurate and precise mineral maps. On the other hand, ACE and SAM are more sensitive to spectral variability.

The best-performing mapping algorithms that offered the highest average AUC and lowest AUC range were CEM, MF, and MTMF, followed by SAM. ACE yielded the lowest average AUC and the highest AUC range. The results align with earlier findings in section 5.2.1 and the earlier studies compiled in Table 5-8. These studies also found that CEM, MF, and MF have close performance that is better than SAM, while ACE provided varied performances in providing accurate mapping. As previously discussed in section 5.2.1, CEM, MF, and MTMF have close results because their logic of calculation was similar (Boardman & Kruse, 2011; Chang et al., 2000). The ranked performance of ACE and SAM potentially reflects the characteristics of the algorithms: ACE enhances the contrast between spectral signals to increase target identification from the background (Jin et al., 2009), potentially introducing more mapping variations due to spectral variability. Previous studies indicate that SAM struggles when target spectra are unevenly distributed and exhibit high dispersions among the analyzed pixels. (Manolakis & Shaw, 2002). Therefore, the nature of mineral spectral variability and irregular distribution may be the reason for lowering SAM accuracy.

Based on the accuracy assessment, it was identified that local spectra Coso-034 and Coso-032 resulted in the mineral maps with the highest AUC of alunite and kaolinite, respectively. Therefore, Coso-034 and Coso-032 were selected as the control groups to further explore the difference between the mineral maps with varied spectra. By subtracting the normalized mineral density map, it is possible to inspect the regions where each spectrum presented higher and lower estimations than the control group. The comparison maps are shown in Figure 6.9 and Figure 6.10. The difference between each mapping algorithm also supports the findings from the AUC values. The algorithms ACE and SAM have more areas of variation on maps, showing that these algorithms have lower precision on mapping results regarding spectral variability.

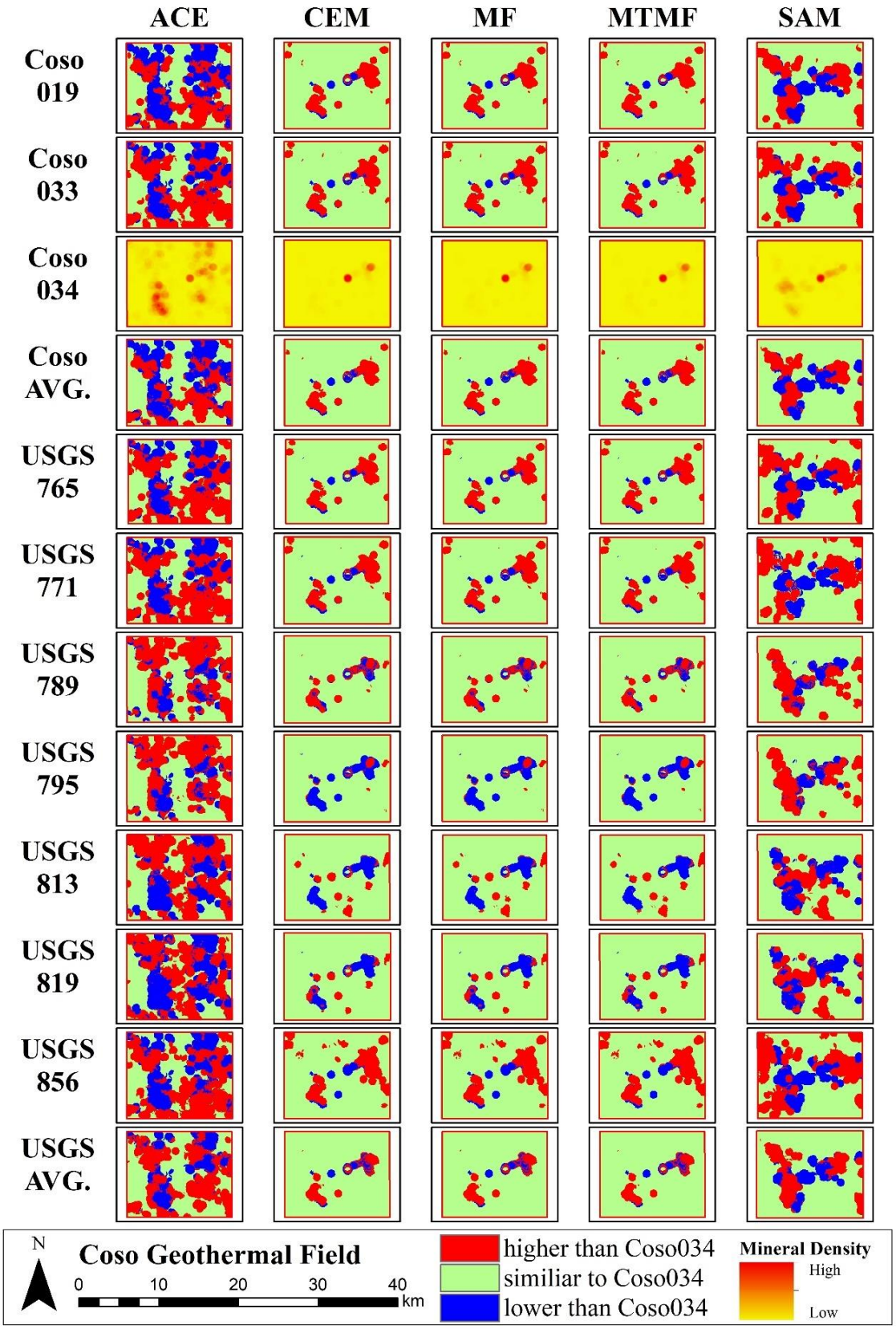

Figure 6.9 Comparison of alunite maps based on a control group of Coso-034.

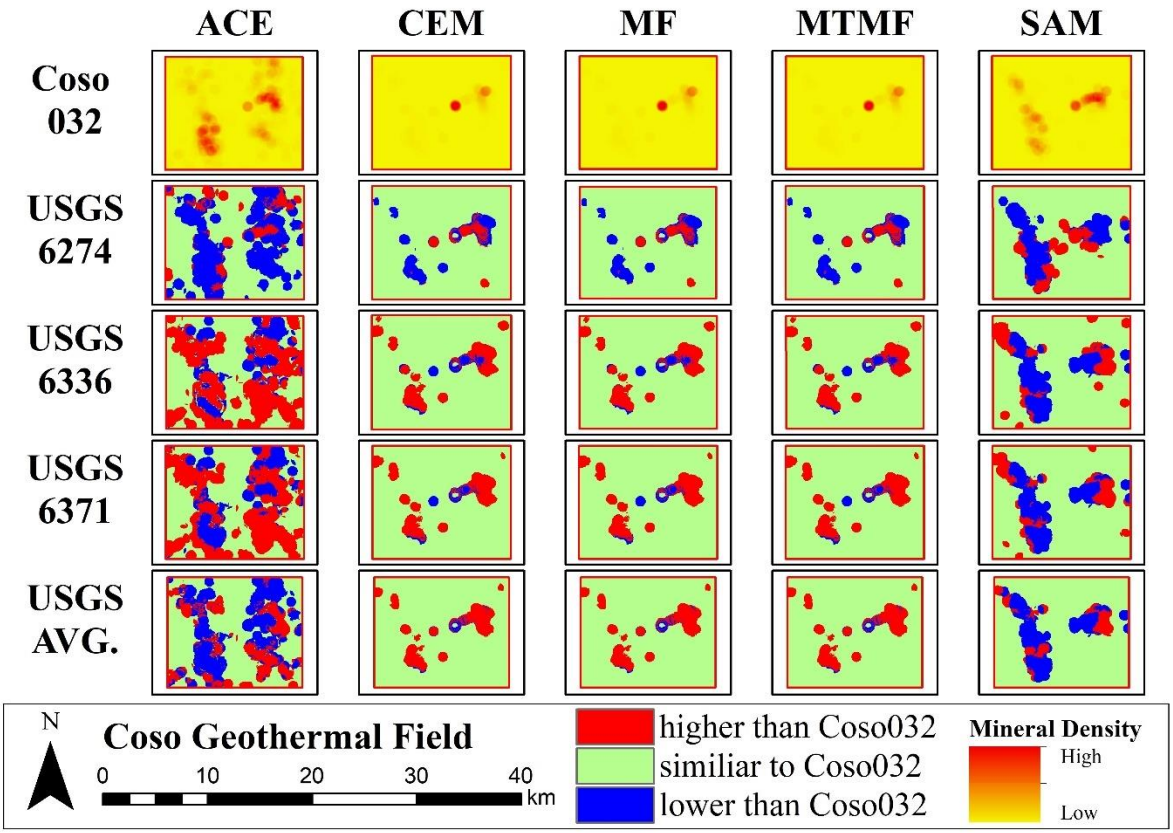

Figure 6.10 Comparison of kaolinite maps based on a control group of Coso-032.

6.2.2 Mapping With Different Spectral Libraries

Based on the findings from the previous section, it was revealed that using the USGS spectra could generally improve the accuracy of mineral mapping. Therefore, the average USGS spectra and the CGF spectra that exhibit strong correlations with the referenced average USGS spectra are applied to compare the mapping results of the two spectral libraries. Those are the same spectra previously organized in section 5.1 and presented in Figure 5.2 (except epidote). The mineral mapping of the five MOI was based on the five mapping algorithms. The mineral maps were converted to mineral density maps and presented in Figure 6.11. As in all the cases in previous sections, CEM, MF, and MTMF provide the same predictions in this part of the study.

With the accuracy assessment, the resulting ROC curves are presented in Figure 6-12, and the corresponding AUC values are summarized in Table 6-5. The outcomes of algorithms CEM, MF, and MTMF were illustrated together based on their similarity.

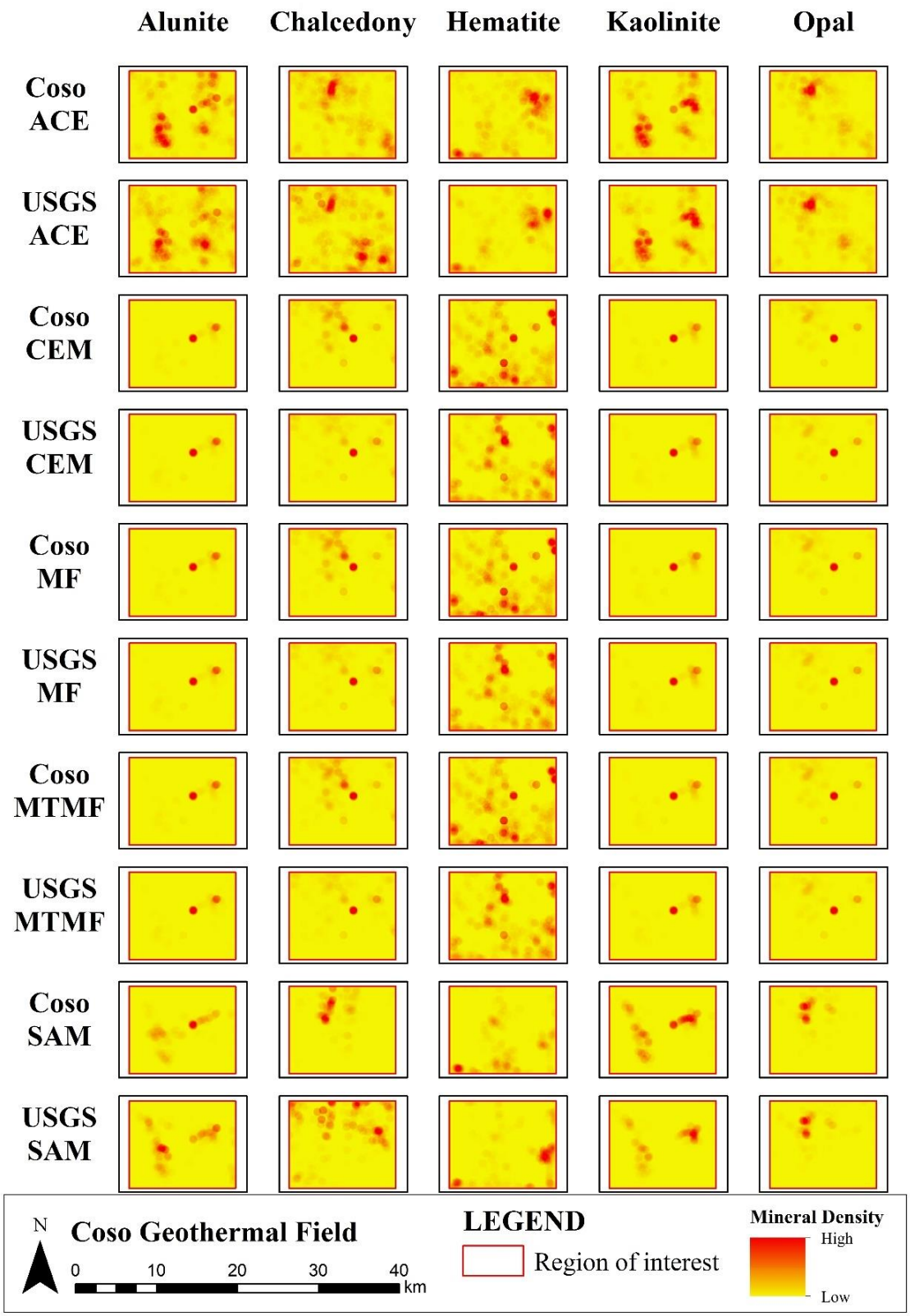

Figure 6.11 Density maps of mineral mapping by CGF and USGS spectra.

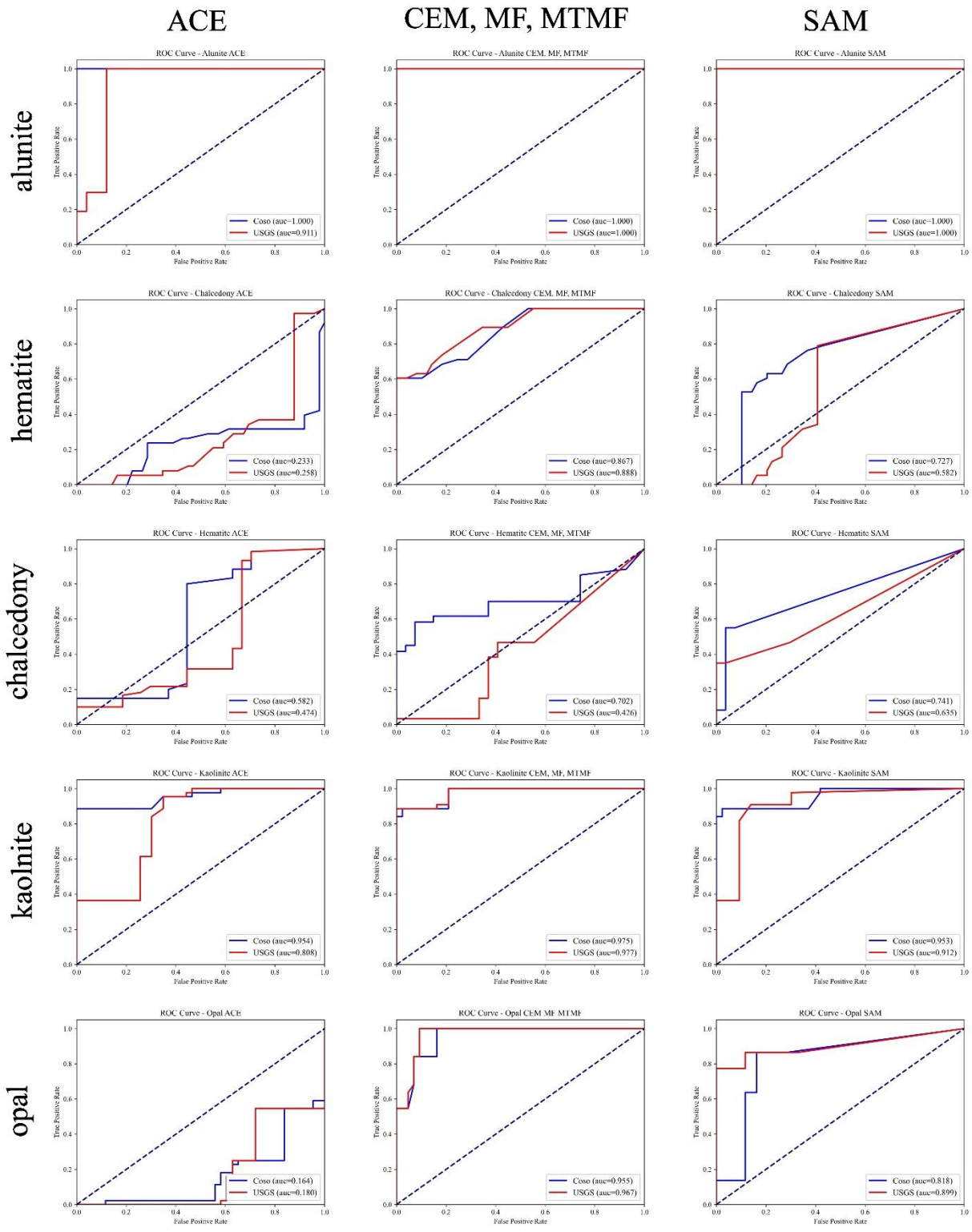

Figure 6.12 ROC curves of mineral maps by CGF spectra (blue) and USGS spectra (red).

Table 6-5 Summary of AUC values of mineral maps by CGF spectra and USGS spectra.

Algorithms	library	Alunite	Chalcedony	Hematite	Kaolinite	Opal	Average
ACE	**Coso**	1.000	0.233	0.582	0.954	0.164	0.587
	USGS	0.911	0.258	0.474	0.808	0.180	0.526
CEM, MF, MTMF	**Coso**	1.000	0.867	0.702	0.975	0.955	0.900
	USGS	1.000	0.888	0.426	0.977	0.967	0.852
SAM	**Coso**	1.000	0.727	0.741	0.953	0.818	0.848
	USGS	1.000	0.582	0.635	0.912	0.899	0.806

Among the maps by the CGF spectra, most of the AUC values are higher than 0.5 (Table 6-5), which refers to a better model than a random prediction. By algorithm, CEM, MF, MTMF, and SAM delivered results with average AUCs higher than 0.8. On the other hand, the average AUCs of ACE were significantly lower at around 0.5 to 0.6 (Table 6-5). The results correspond with the findings in the previous sections 5.2.1 and 6.2.1. CEM, MF, and MTMF offered the highest accuracies, followed by SAM, and ACE provided the lowest accuracies.

It was identified that the average AUCs by the mapping of CGF spectra were always higher than those of USGS spectra. To further evaluate the differences, the AUC values of Table 6-5 were compared and summarized in Table 6-6. Table 6-6 presents the comparison results with a threshold of 3% AUC difference, which indicates close performances. Overall, the ratio between Coso-higher: close-performance: USGS-higher was 9:15:1. Even by considering CEM, MF, and MTMF as one single output, the ratio was 7:7:1. This study suggests that using locally collected spectra improves mineral mapping accuracy in detailed prediction.

Table 6-6 Comparison of AUC values of mineral maps by CGF spectra and USGS spectra with the three-percent threshold.

Algorithms	Alunite	Chalcedony	Hematite	Kaolinite	Opal
ACE	Coso	close	Coso	Coso	close
CEM	close	close	Coso	close	close
MF	close	close	Coso	close	close
MTMF	close	close	Coso	close	close
SAM	close	Coso	Coso	Coso	USGS

Coso: Higher AUC by CGF spectra; USGS: Higher AUC by USGS spectra;
close: The AUC difference is less than 3%.

For alunite, chalcedony, hematite, and kaolinite, utilizing the CGF spectra consistently provides more accurate or comparable maps than those generated through the USGS spectra. The USGS spectra only perform higher accuracy on opal mapping with the SAM algorithm.

Opal maps using SAM are the only case in which the USGS spectra provided a higher AUC value than the CGF spectra (AUC difference of 0.081). The mappings, however, are visually similar (Figure 6.11). The two normalized density maps were overlapped and compared. The resulting map in Figure 6.13 identifies where one map presents different predictions from the other. The green zones indicate areas where the CGF spectrum provides higher predictions, while the red zones indicate areas where the USGS spectrum provides higher predictions. The USGS spectra performed better around the Nicol Pad, Sugarloaf Mountain, and a northern sampling site. However, the CGF spectra performed better around Devil's Kitchen, one of the largest geothermal landscapes surrounded by major developments. Although the AUC value is higher by the USGS spectra for opal-SAM mapping, using the CGF spectra still provides reliable mapping that identifies geothermal landscapes with an AUC level of 0.818.

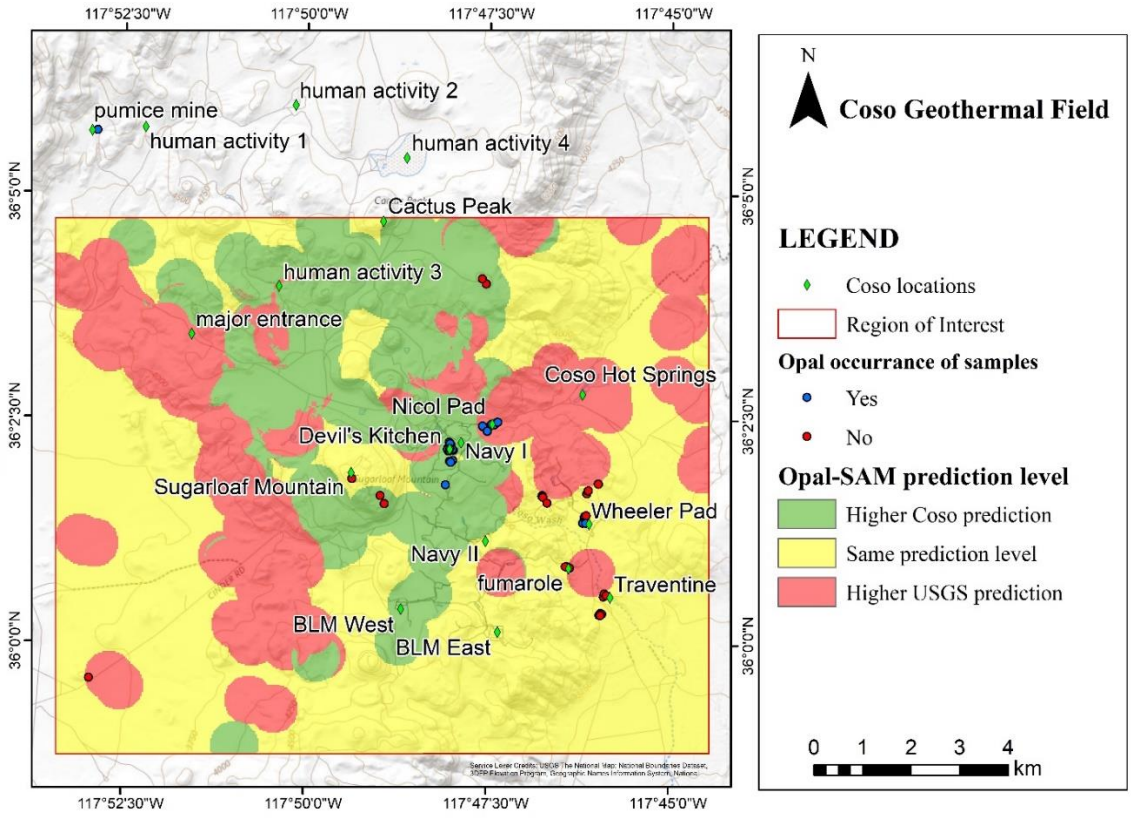

Figure 6.13 Comparison of mineral maps using CGF spectra and USGS spectra in opal mapping through the SAM algorithm.

6.3 CGF Mineral Maps Based on the Refined Mineral Mapping Strategy

Based on the findings of Chapters Five and Six, a refined mineral mapping strategy was proposed to generate mineral maps for further applications. The mapping strategy includes: (1) Apply splice correction to the target spectra. (2) Fuse mapping results of algorithms ACE, CEM, MF, MTMF, and SAM. (3) Use local spectra that are close to average USGS spectra or use USGS average spectra if local spectra are not available. With the refined mineral mapping strategy, mineral maps with higher accuracy help improve the efficiency of geothermal exploration. The refined mineral mapping strategy was applied to map the MOI of CGF, BGF, and DPGF for further study to discover potential relations between the SGP (Chapter Seven).

CHAPTER 7 STAGE III: DATA-DRIVEN STUDY OF EXPLORATION PARAMETERS

The study in this chapter seeks to answer research question three (Q3): "What are the relations between the maps of SGP (indicator minerals, faults, and LSTs)?" This question corresponds to research hypothesis H3 and research objective O3. This part of the study integrates spatial and non-spatial techniques to explore the connections between the SGP. An article that covers the study that is dedicated to data analysis for the relation between the map of indicator minerals, faults, and LSTs is under review by the journal of Geoenergy (APPENDIX H). The following sections provide a detailed account of the implementations and results of the study.

7.1 Implementation of the Analysis

The study followed a two-stage methodology. The first stage is data collection and preparation of the SGP. The second is non-spatial and spatial analyses to explore the relation between the SGP.

7.1.1 Data Collection and Preparation

SGP datasets of the CGF, BGF, and DPGF are acquired and pre-processed according to the needs of statistical analysis. All the raster datasets were organized with 30-meter by 30-meter pixel resolution, using the resolution of the mineral maps, and then transformed into points for statistical analyses. A total of seven datasets were derived from the SGP: Two-Class Mineral Maps, Mineral Density Maps, Fault Trace, Fault Distance Maps, Fault Density Maps, Multiclass Temperature Maps, and Two-class Temperature Maps. The following sections provide the details of the data collection and preparation.

Indicator Mineral Map

The workflow of indicator mineral map data preparation is presented in Figure 7.1. The mineral maps for data analysis between the SGP were prepared based on mineral spectra from the Coso Spectral Library for the CGF and from the USGS Spectral Library (Kokaly et al., 2017) for the BGF and DPGF. The MOI—alunite, chalcedony, hematite, kaolinite, and opal—were further applied because they occur across all three study areas (Erika, 2022). The mineral maps were initially generated by algorithms of ACE, CEM, MF, MTMF, and SAM, then fused into a single map according to the findings from the mapping strategy (Chapters Five and Six).

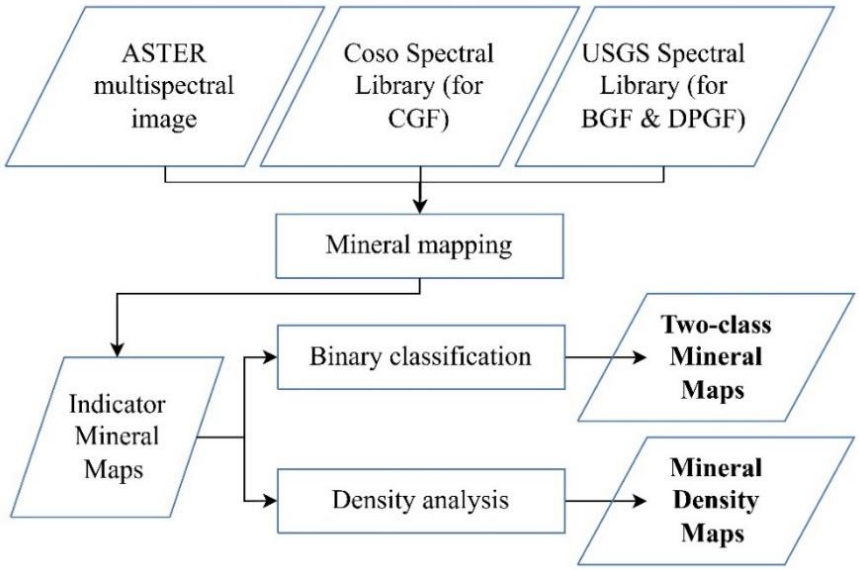

Figure 7.1 Workflow of indicator mineral map data preparation. Two datasets, in bold, were prepared based on indicator mineral maps: Two-Class Mineral Maps and Mineral Density Maps.

Two datasets based on the indicator mineral maps were prepared for data analysis. The first dataset is the Two-Class Mineral Maps. The pixels where indicator minerals were mapped were converted to point datasets in GIS. In addition, the study summarized pixels lacking indicator minerals and created point datasets to represent background conditions where no indicator mineral was present. Second, the mineral maps were converted to Mineral Density Maps through the Kernel Density tool in ArcGIS. After conducting a series of tests on various distance bands, a 1000-meter distance band was optimal. This distance band effectively preserves most details in the mineral densities for each study area. Mineral Density Maps were normalized by rescaling to a range of 0 to 1. Figure 7.2 presents an example (alunite) of the indicator mineral maps, the converted Two-Class Mineral Map, and the Mineral Density Maps.

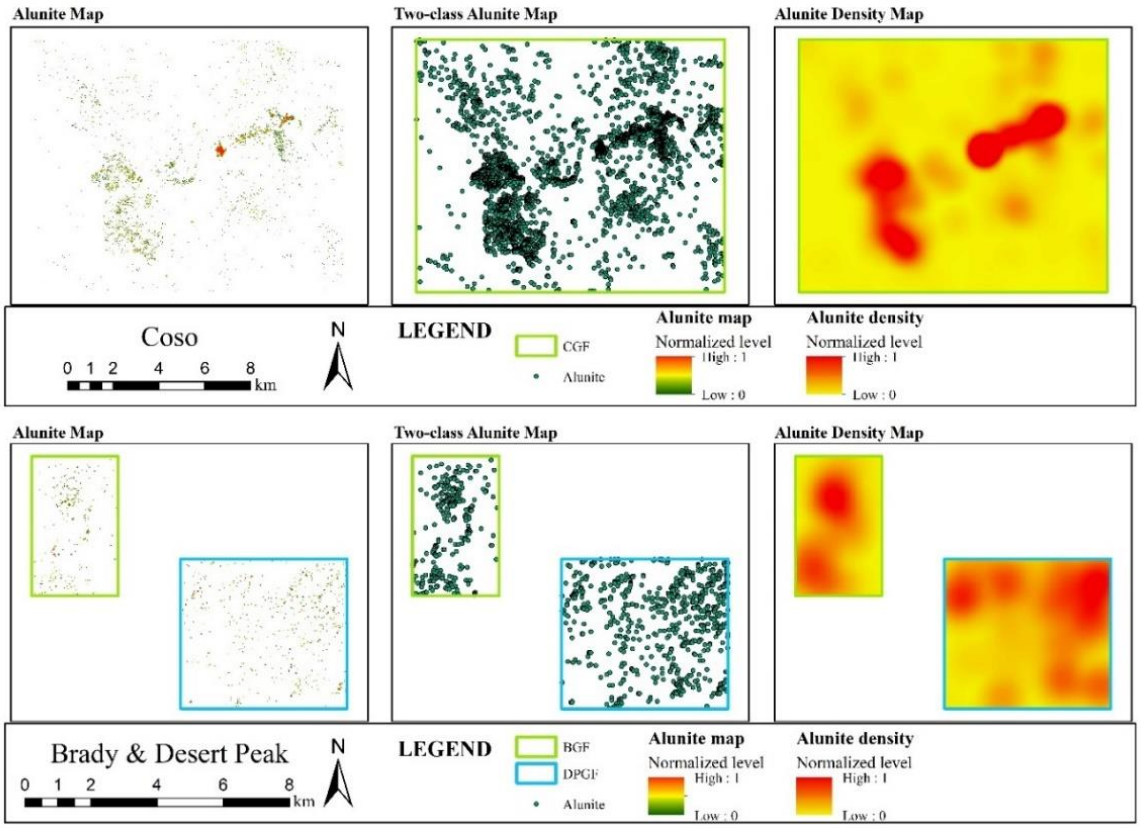

Figure 7.2 Illustration of indicator mineral map datasets.

Fault Map

The Fault maps of GIS polylines were compiled from previous literature for the CGF (Blankenship, 2016; Duffield & Bacon, 1981; Hulen, 1978; Jennings & Bryant, 2010; Whitmarsh, 1998) and BGF-DPGF (Faulds et al., 2012, 2017). The workflow of fault map data preparation is presented in Figure 7.3. Three datasets were derived from the fault traces. First, the polylines of fault were converted to Fault Trace with an interval of 30 meters due to the set resolution. Second, Fault Distance Maps are raster data that indicate the distance to the closest fault from each pixel. Third, Fault Density Maps were generated using the Kernel Density tool in ArcGIS, with a 1000-meter distance band applied to ensure detailed representation across all study areas. The Fault Density Maps were normalized by rescaling to a range of 0 to 1. Figure 7.4 illustrates the fault map datasets, including the Fault Traces, the Fault Distance Maps, and the Fault Density Maps.

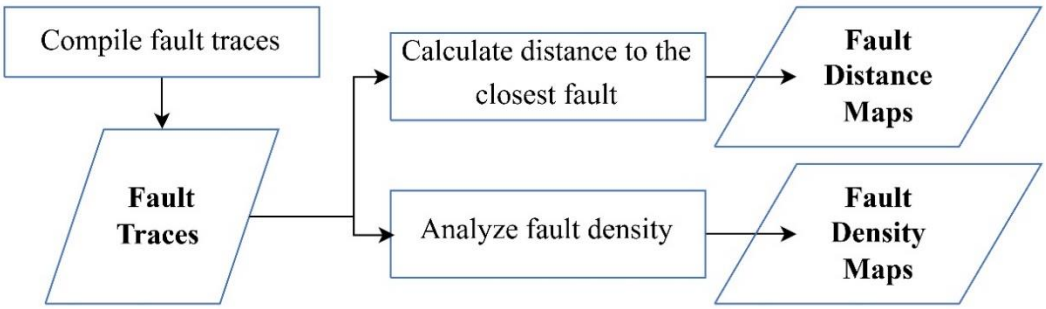

Figure 7.3 Workflow of fault map data preparation. Three datasets, in bold, were prepared based on faults: Fault Traces (bottom left), Fault Distance Maps, and Fault Density Maps.

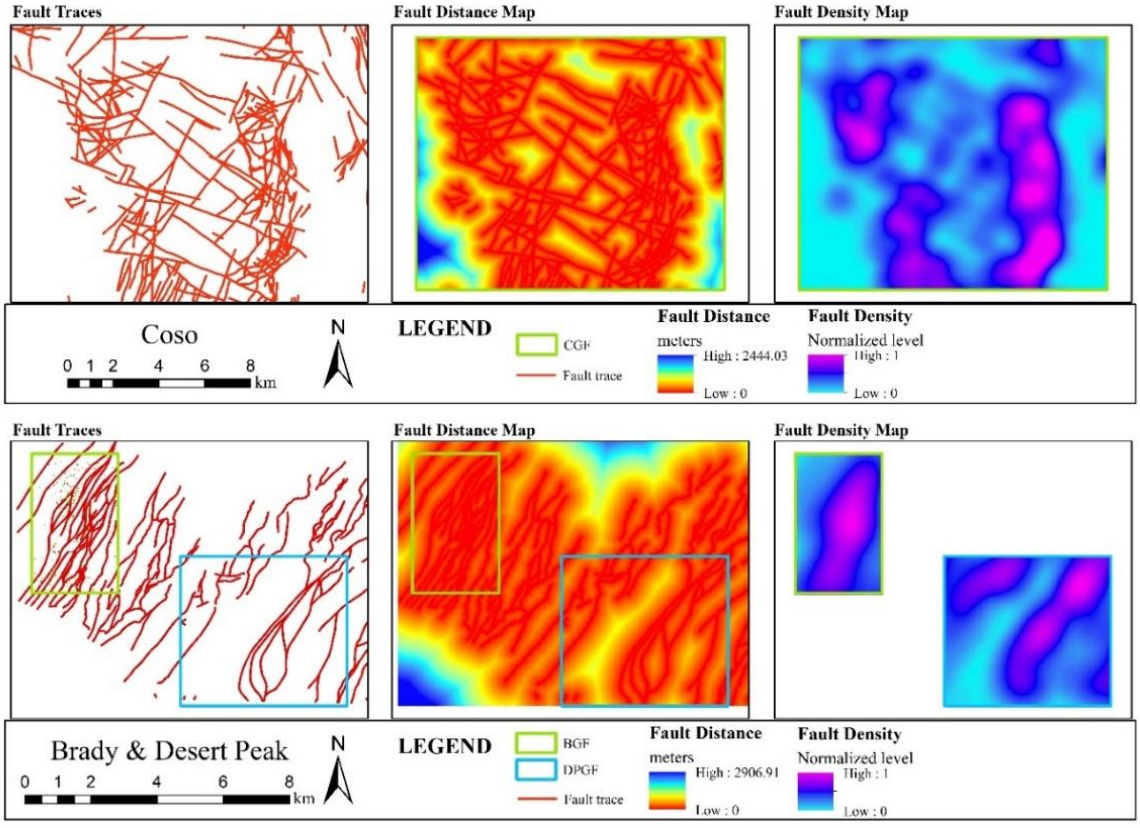

Figure 7.4 Illustration of fault map datasets.

Land Surface Temperature (LST)

Figure 7.5 presents the workflow for preparing LST data. The LST used for the CGF was based on a 2-meter temperature probe survey (Blake et al., 2020; Zimmerman et al., 2023). Measured and corrected temperatures were interpolated to obtain raster data using the Kriging tool in ArcGIS. LST datasets for the BGF and DPGF were obtained from Landsat 8 data from the Geothermal Data Repository (GDR,

https://gdr.openei.org/submissions/1305). The LST raster data of Landsat 8 was pre-processed to study the BGF and the DPGF (Moraga, 2022; Moraga et al., 2021b, 2021a). Two datasets were prepared using the LSTs. First, Multiclass Temperature Maps were normalized by rescaling LST from 0 to 1. Second, Two-class Temperature Maps were generated in need of categorized data in the analysis. Multiclass Temperature Maps were reclassified into high and low temperatures using Jenks Natural Break optimization in ArcGIS, which minimizes differences within each class while maximizing differences between each class. Figure 7.6 illustrates the preparation of the LST datasets, including the raw data, Multiclass Temperature Maps, and the Two-class Temperature Maps.

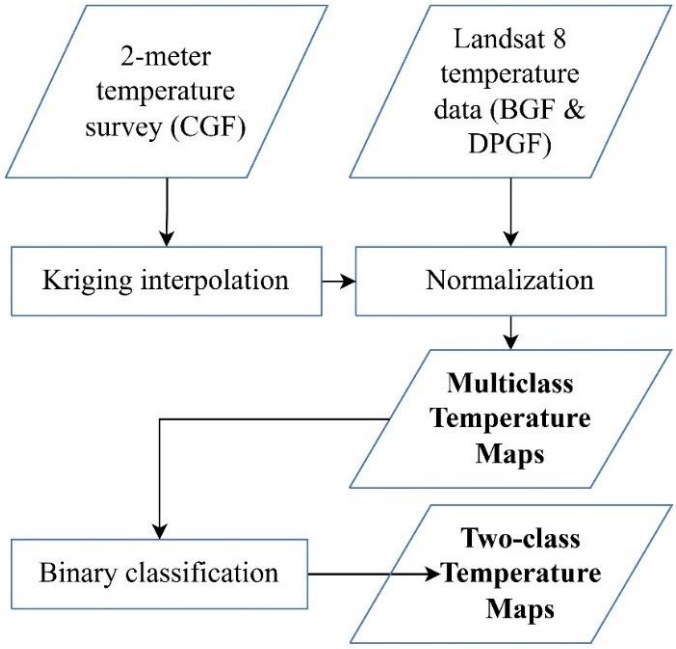

Figure 7.5 Workflow of LST data preparation. Two datasets, in bold, were prepared based on LSTs: Multiclass Temperature Maps (right) and Two-class Temperature Maps (bottom-right).

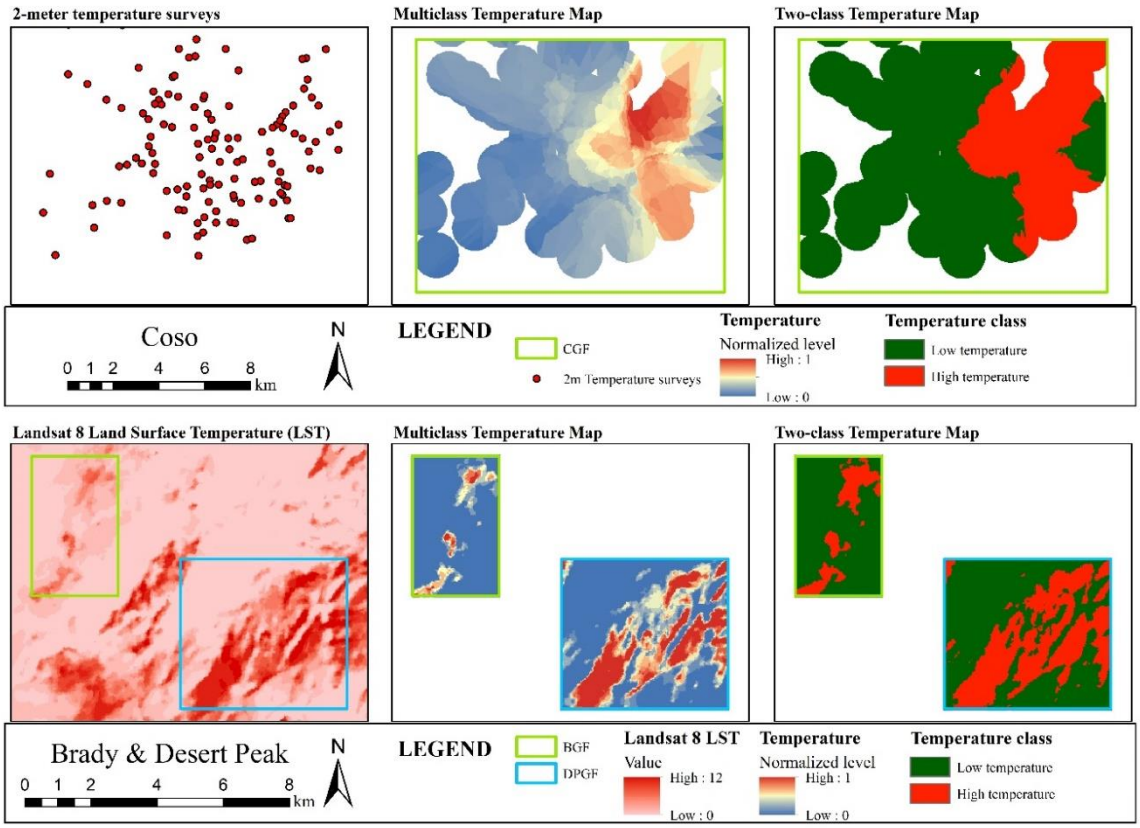

Figure 7.6 Illustration of LST datasets.

7.1.2 Data Analysis

The data analyses explore possible relations between SGP. Table 7-1 illustrates adopted data analysis methods and corresponding input datasets. The hypothesis test of the relations between SGP was based on non-spatial and spatial analyses. The non-spatial analyses include histograms with CDF (cumulative distribution function) plots, two-sample Kolmogorov-Smirnov test (K-S test), one-way analysis of variance (ANOVA), and linear regression. The spatial analysis includes colocation analysis. The input datasets are varied for each analytical method and hypothesis, as listed in the table. The application of various approaches concurrently assesses the patterns identified in each technique. The non-spatial analyses provided inference on possible connections between the SGP, while the spatial analysis explored the spatial relations of the SGP.

Non-spatial analysis

The selected input datasets listed in Table 7-1 were joined in GIS. Histograms with CDF plots are constructed to explore potential patterns between the SGP. The histograms with CDF plots help compare each MOI's data distribution against faults and LSTs. They also help compare the distribution of high and low temperature data against faults. The K-S test, ANOVA, and linear regression were used to make inferences from histograms with CDF plots. The evaluation was conducted using Matlab functions of kstest2, anova1, and fitlm.

K-S test is a nonparametric test that compares two datasets by analyzing the maximum absolute difference between their CDFs and judges whether they have comparable distributions. (Marsaglia et al., 2003; Massey Jr, 1951; Miller, 1956). The study examined whether each MOI presented distinct distributions relative to faults and LSTs, compared to the background condition where no indicator minerals were mapped. Additionally, the study examined whether high and low temperatures present distinct distributions relative to faults.

ANOVA indicates whether various datasets have a common mean or distribution (Dunn & Clark, 1986; Wackerly et al., 2008). While the K-S test identifies differences in distributions, ANOVA complements this by providing a quantitative framework to evaluate variations between datasets. Following the K-S test, the study compares the distributions of each MOI regarding their relations to faults and LSTs. The distributions of high and low temperatures regarding their relations to faults were also compared.

Linear regression could provide models that indicate the relation between a dependent variable and one or more independent variables (Dumouchel & O'Brien, 1989; Holland & Welsch, 1977; Street et al., 1988). The study used simple linear regression, $y=a+bx$, where a is the intercept and b is the slope, indicating the degree of correlation between y (dependent variable) and x (independent variable). Correlation (b) is the key parameter to interpret the relation between indicators. The regression models

explore the positive or negative correlation between the SGP. The regression was applied by setting the Fault Density Maps and Multiclass Temperature Maps as the dependent variables while setting the other datasets as independent variables (Table 7-1).

Spatial Analysis

It evaluates the spatial relations of SGP using colocation analysis (Leslie & Kronenfeld, 2011; F. Wang et al., 2017), which examines two groups of SGP points to determine if one group colocates with the other neighboring group. Since colocation analysis requires an assigned distance band, multiple distance bands were tested and reviewed based on the plots of the LCLQ (local colocation quotient) and p-value to decide the best distance band. The selected distance band of 750 meters minimized the p-values on plots' tails (maximums & minimums) while optimizing the LCLQ level. The analysis outputs provide four LCLQ types between the SGP: Significant Isolated, Not Significant Isolated, Significant Colocated, Not Significant Colocated, and Undefined. The distribution of LCLQ types helps identify where the SGP are colocated or isolated. In addition, the colocation patterns were compared with the known reservoir extension (Demir et al., 2024) to explore the connections between SGP colocations and their proximity to reservoirs. The colocation analysis was applied to compare (1) fault traces and neighboring MOI, (2) fault traces and neighboring high temperatures, and (3) the high temperatures and neighboring MOI.

Table 7-1 Adopted data analysis methods and corresponding input datasets.

Relation between:	**Hypothesis**	**Analyses used for hypothesis testing**			
		Non-spatial analysis		**Spatial analysis**	
		Method	**Input data**	**Method**	**Input data**
Indicator mineral & fault	**H0:** Patterns of indicator minerals are not related to faults **H1:** Patterns of indicator minerals are related to faults		• Two-class Mineral Maps † • Mineral Density Maps‡ • Fault Distance Maps† • Fault Density Maps†‡		• Two-class Mineral Maps • Fault Traces
Indicator mineral & LST	**H0:** Patterns of indicator minerals are not related to LST **H1:** Patterns of indicator minerals are related to LST	• Histograms & CDF plots • K-S test • ANOVA • Linear regression	• Two-class Mineral Maps† • Mineral Density Maps‡ • Multiclass Temperature Maps†‡	Colocation analysis	• Two-class Mineral Maps • Two-class Temperature Maps
Fault & LST	**H0:** Patterns of fault are not related to LST **H1:** Patterns of faults are related to LST		• Multiclass Temperature Maps‡ • Two-class Temperature Maps† • Fault Distance Maps† • Fault Density Maps†‡		• Two-class Temperature Maps • Fault Traces

H0:null hypothesis; **H1:** alternative hypothesis;

†: used in histograms, CDF plots, K-S tests, and ANOVA; ‡: used in linear regressions.

7.2 Results of the Data Analysis

With both non-spatial and spatial analysis. The results reveal several key findings, including: (1) different MOI present varied distributions against faults and LST. (2) High and low temperatures also present different distributions against faults. (3) The behaviors of SGP are different at CGF and BGF from DPGF. To improve the visualization, the abbreviations listed below will be used for tables and figures in the following sections: N.M. (no MOI), H.T. (high-temperature zones), and L.T. (low-temperature zones). The following sections present the detailed results.

7.2.1 Non-Spatial Analysis

In the non-spatial analysis, the histograms with CDF plots reveal multiple potential trends where each MOI and LST levels exhibit distinct patterns regarding fault proximity. The K-S test, ANOVA, and linear regression prove that each MOI has different tendencies toward faults and LSTs. High-temperature areas also present different fault tendencies on fault proximity than low temperatures. The analyses also identified that LST at DPGF displays weaker connections with both MOI and faults than the other study areas. The following sections summarize the key findings from the non-spatial analyses.

Histograms with CDF plot

Histograms with CDF plots show the distribution of datasets. Due to the large number of datasets, this section presents a few examples to support discussions. Complete histograms and CDF plots are organized in APPENDIX C . The following paragraphs summarize the potential patterns between the SGP revealed by histograms and CDF plots.

Figure 7.7 presents an example of histograms and CDF plots that show the patterns between Two-Class Mineral Maps and Fault Distance Maps at CGF. The CDF plots shift toward the top-left corner for distributions closer to faults, whereas they move away from the top-left corner for distributions further from faults. In the case of CGF, alunite, chalcedony, kaolinite, and opal are closer to faults than the background (N.M.) level. Alunite and kaolinite show stronger tendencies toward faults. Overall, for all study areas, the MOI were observed to be closer to faults than the background levels in each study area (APPENDIX C , Figure C.1). Comparable patterns were also discovered between Two-Class Mineral Maps and Fault Density Maps (APPENDIX C , Figure C.2), where MOI tend to occur at higher fault densities than the background levels. The relations between MOI and faults varied noticeably by minerals.

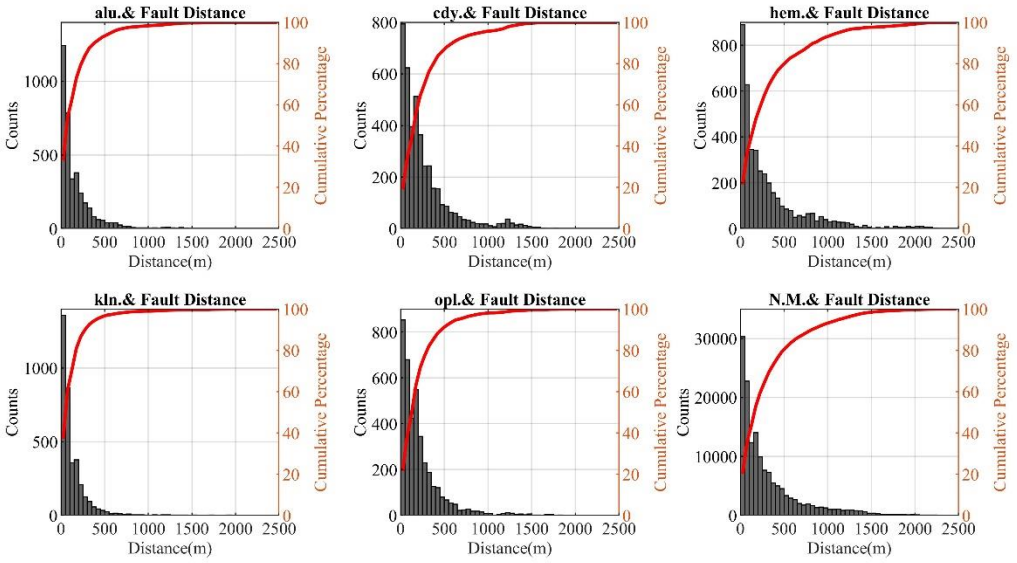

Figure 7.7 Histograms (gray boxes) and CDF plots (red lines) of the patterns between Two-Class Mineral Maps and Fault Distance Maps at CGF. Multiple MOI show distributions closer to faults than the locations without MOI (bottom-right), with CDF plots shifting closer to the top-right corners. The patterns between MOI are also different.

Figure 7.8 presents an example of histograms and CDF plots that show the patterns between Two-class Temperature Maps and Fault Distance Maps in each study area. Similar to Figure 7.7, the CDF plots shift toward the top-left corner for distributions closer to faults. High and low temperatures have different patterns against faults in each study area. In geothermal systems with surface manifestations (CGF and BGF), high temperatures are closer to faults. In the blind system (DPGF), the opposite pattern is observed. Similarly, high temperatures correspond to areas of higher fault density in CGF and BGF but occur in lower fault-density regions in DPGF (APPENDIX C , Figure C.3).

Figure 7.9 presents an example of histograms and CDF plots that show the patterns between Two-Class Mineral Maps and Multiclass Temperature Maps at CGF. The CDF plots shift further from the top-left corner if distributions are close to higher temperatures. In the case of CGF, alunite and kaolinite occur at higher temperature areas, while chalcedony and opal are associated with lower temperature areas compared to the background (N.M.) level. Overall, for all study areas, the patterns between Two-Class Mineral Maps and Multiclass Temperature Maps are inconsistent from histograms and CDF plots (APPENDIX C , Figure C.3 and Figure C.4). Still, it was observed that tendencies varied between MOI.

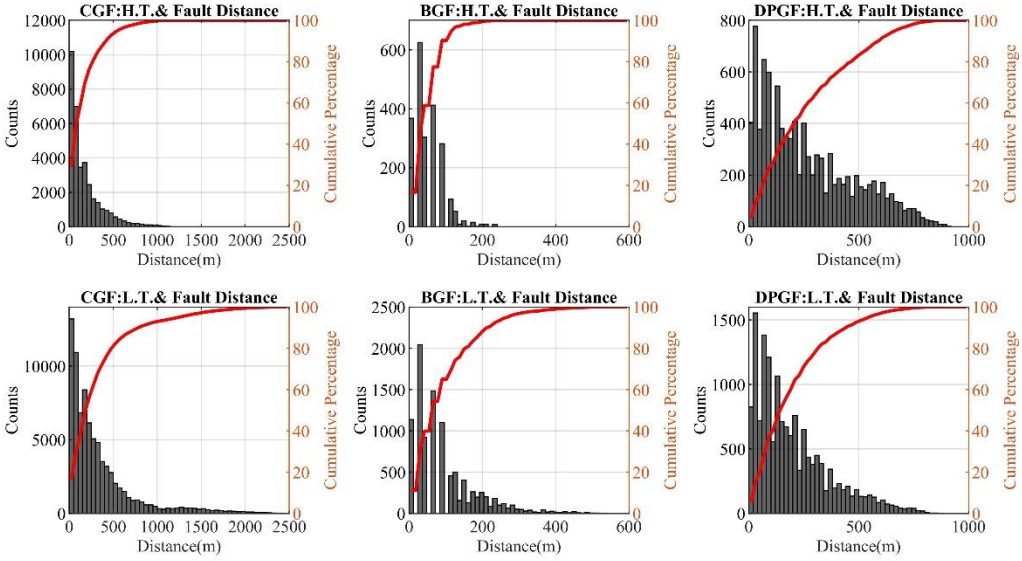

Figure 7.8 Histograms (gray boxes) and CDF plots (red lines) of the patterns between Two-Class Temperature Maps and Fault Distance Maps at each study area. High temperatures (top) of CGF (left) and BGF (middle) show distributions closer to faults than DPGF (right).

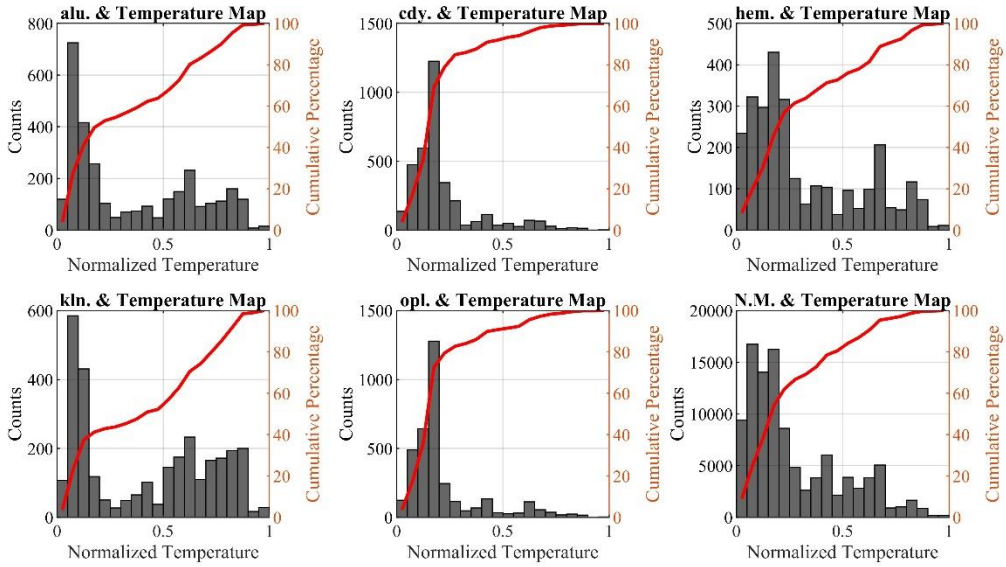

Figure 7.9 Histograms (gray boxes) and CDF plots (red lines) of the patterns between Two-Class Mineral Maps and Multiclass Temperature Maps at CGF. Alunite and kaolinite are closer to higher temperatures, while chalcedony and opal are closer to lower temperatures.

K-S test

The K-S test evaluates whether two datasets originate from the same distribution, with a null hypothesis that the datasets originate from the same distribution. Table 7-2 summarizes the results of the K-S test, indicating whether the null hypothesis was rejected or not in each test.

The results show that the null hypothesis of the K-S test was predominantly rejected, which means that the datasets exhibit distinct distributions. The distribution of MOI differed from the background level (N.M.) regarding the Fault Distance Map, Fault Density Map, and Multiclass Temperature Map. Simultaneously, high and low temperatures exhibited distinct distributions against the faults.

Since the K-S test cannot identify the intensity of difference between datasets, further ANOVA and linear regression were applied to explore the relations and indicate the differences in distribution between the SGP.

Table 7-2 The K-S test result. The null hypothesis was rejected in most cases, showing that the distributions of datasets are primarily different.

SGP	Fault Distance Map			Fault Density Map			Multiclass Temperature Map		
	CGF	BGF	DPGF	CGF	BGF	DPGF	CGF	BGF	DPGF
alu. vs. N.M.	1	0	1	1	1	1	1	1	0
cdy. vs. N.M.	1	1	1	1	1	1	1	1	1
hem. vs. N.M.	1	0	1	0	1	1	1	1	1
kln. vs. N.M.	1	0	1	1	1	1	1	1	1
opl. vs. N.M.	1	1	1	1	1	1	1	1	1
H.T. vs. L.T.	1	1	1	1	1	1	NA		

0: failed to reject the null hypothesis, and 1: reject the null hypothesis

ANOVA

ANOVA compares the data distribution and discovers the level of difference. The Two-Class Mineral Map and Temperature Map datasets were studied with the control groups (blue in Figure 7.10) of N.M. (no MOI) and H.T. (high-temperature). The ANOVA results are given in Figure 7.10, indicating the Significant (red) and Insignificant (gray) Differences from the control group.

All Significant Differences identified by ANOVA corresponded to rejections in the K-S test, highlighting a strong agreement between the two methods. While the K-S test detected some additional differences that ANOVA did not, all failed rejections in the K-S test (no difference in data distribution) were consistently classified as insignificant by ANOVA.

In the analyses for MOI and faults, each MOI's tendencies varied. Compared with the background level (N.M.) at each study area, alunite, kaolinite, and opal presented tendencies toward smaller fault distances and higher fault density, or at least close to the background. In contrast, chalcedony and hematite have similar background patterns or lower fault proximity. No apparent patterns between the indicator mineral maps and fault maps were observed in ANOVA to differentiate the study areas.

In the analyses for LST and faults, the outcome reflects the characteristics of the blind geothermal field at DPGF. The high temperatures at CGF and BGF presented tendencies toward smaller fault distances and higher fault density. In contrast, the high temperatures at DPGF were further from faults, and the tendency with fault density was not as evident as in CGF and BGF. The finding indicates that the behavior between faults and LST differed in a blind geothermal system like DPGF.

In the analyses for indicator minerals and LSTs, the MOI did not present evident and consistent patterns across all study areas. At CGF and BGF, alunite, hematite, and kaolinite tend to be at higher temperatures, while chalcedony and opal tend to be at lower temperatures or close to the background. In contrast, the case of DPGF showed that hematite, kaolinite, and opal tend to be at lower temperatures. This difference between CGF, BGF, and DPGF indicates that the behavior between MOI and LSTs also differed in a blind geothermal system.

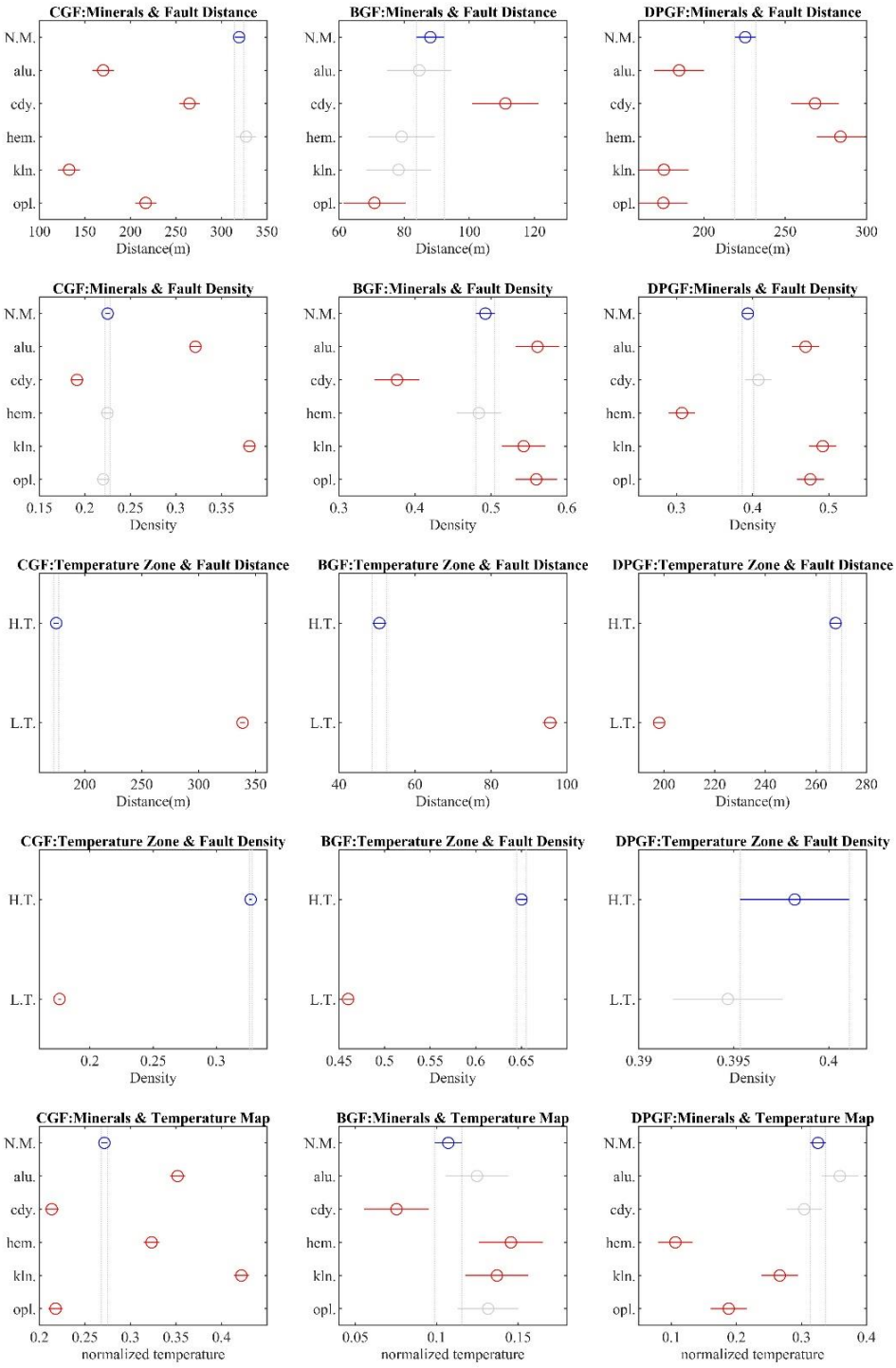

Figure 7.10 The multiple comparisons of ANOVA. The plots show the mean estimates (circles) and 95% confidence intervals (bars) for each group of SGP. Red symbols highlight groups with Significant Differences from the control group (blue). Gray symbols indicate groups with Insignificant Differences where confidence intervals overlap with the control group.

Linear regression

The linear regression cross-evaluates the ANOVA results from a different approach. The regression provides correlation coefficients that indicate whether the SGP is positively or negatively correlated in each study area.

Table 7-3 presents the intercepts and coefficients for Fault Density Maps as the dependent variable (y) and Mineral Density Maps as the independent variable (x). Table 7-4 shows the results for Multiclass Temperature Maps as the dependent variable (y), with Fault Density Maps and Mineral Density Maps as the independent variable (x). Further statistical details are provided in APPENDIX D , including the p-values of intercepts and coefficients and the AIC values (Akaike Information Criterion). The p-values of the intercepts and coefficients are mostly 0, except for a few non-zero cases with a maximum p-value of 0.016. The p-values denote the significance of the regression models.

The correlation coefficients from the regression models were compared with the ANOVA outcomes. None of the coefficients conflict with the tendencies of Significant Differences in ANOVA (Figure 7.10, Table 7-3 and Table 7-4). The regression models consolidate these substantial differences and offer additional insights into the insignificant outcomes in ANOVA, eventually enhancing overall analysis.

Table 7-3 Regression parameters for Fault Density Maps against Mineral Density Maps

SGP (x)	**Fault Density (y)**					
	CGF		**BGF**		**DPGF**	
	intercept	**coefficient**	**intercept**	**coefficient**	**intercept**	**coefficient**
alu.	0.206	0.415†	0.397	0.318†	0.190	0.590†
cdy.	0.236	-0.130†	0.609	-0.497†	0.412	-0.107 ‡
hem.	0.229	-0.010 ‡	0.456	0.142‡	0.462	-0.561 †
kln.	0.200	0.474†	0.422	0.277†	0.262	0.504 †
opl.	0.227	0.014 ‡	0.263	0.582†	0.339	0.362†

†: Significant Differences in ANOVA; ‡: Insignificant Differences in ANOVA.

Table 7-4 Regression parameters for Multiclass Temperature Maps against Fault Density and Mineral Density Maps

SGP (x)	Multiclass Temperature (y)					
	CGF		BGF		DPGF	
	intercept	coefficient	intercept	coefficient	intercept	coefficient
fault	0.144	0.584†	-0.016	0.253 †	0.346	-0.073‡
alu.	0.240	0.548†	0.071	0.124‡	0.340	-0.065‡
cdy.	0.291	-0.221†	0.129	-0.087 †	0.345	-0.181‡
hem.	0.213	0.666†	0.049	0.226 †	0.345	-0.235 †
kln.	0.232	0.573†	0.084	0.094 †	0.406	-0.331†
opl.	0.284	-0.185†	0.028	0.203‡	0.406	-0.561†

†: Significant Differences in ANOVA; ‡: Insignificant Differences in ANOVA.

It was found in each study area that alunite, kaolinite, and opal positively correlate with Fault Density Maps, while chalcedony and hematite show lower or negative correlations (Table 7-3). The patterns against Multiclass Temperature Maps varied according to the study area. At CGF and BGF, alunite, hematite, and kaolinite show positive correlations with Multiclass Temperature Maps. Whereas all indicator minerals at DPGF negatively correlate with Multiclass Temperature Maps (Table 7-4). Fault Density Maps and Multiclass Temperature Maps correlate positively at CGF and BGF but negatively at DPGF, following ANOVA results between Two-class Temperature Maps and Fault Density Maps. The linear regression further indicates that the behavior between SGP at DPGF differed, with elevated LST weakly correlated with the map of MOI and faults.

7.2.2 Spatial Analysis

The colocation analysis examines the distributions of colocated SGP and helps reveal their relations against reservoirs. The results corroborated the non-spatial analysis, showing that mineral maps of different indicator minerals exhibit diverse tendencies against faults or LSTs. Some indicator minerals exhibit comparable distributions in similar regions. The following sections illustrate the findings from the spatial analysis.

Faults and indicator minerals

The colocation maps between faults and MOI of CGF, BGF, and DPGF are respectively present from Figure 7.11 to Figure 7.13. At CGF (Figure 7.11), alunite and kaolinite show similar colocations in two major clusters, with the eastern one within the reservoir. Chalcedony and opal have similar colocations in the north. Hematite has colocations surrounding the reservoir, but some hematite in the southwest was not

colocated with faults. Chalcedony, hematite, and opal are generally colocated with faults on the reservoir's edge.

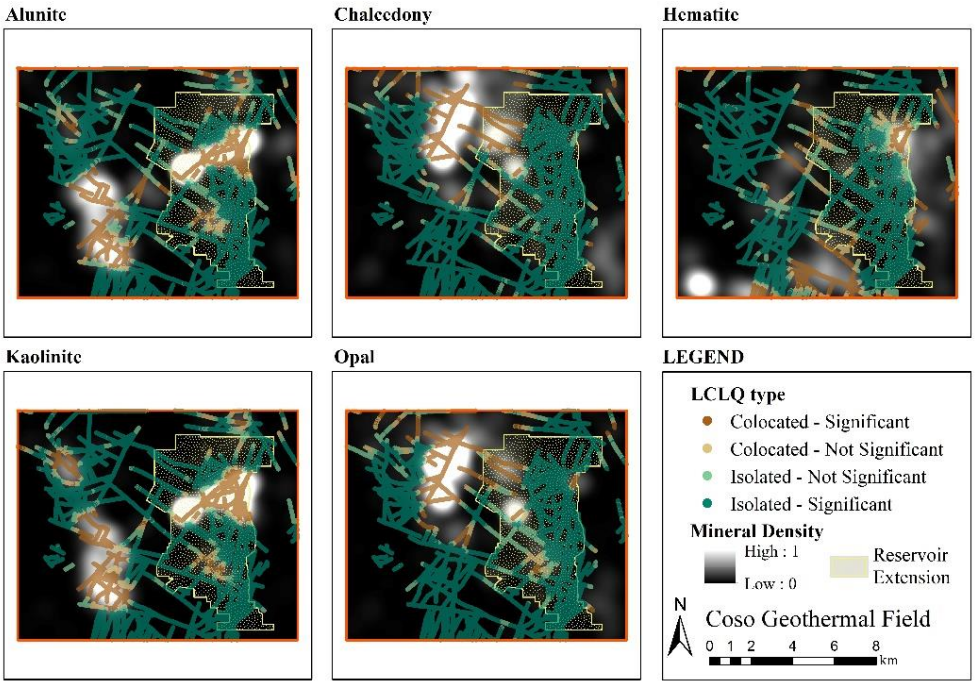

Figure 7.11 Colocation maps of faults and neighboring indicator minerals at CGF.

At BGF (Figure 7.12), alunite, kaolinite, and opal present similar colocation patterns within the reservoir's western part. Chalcedony has limited colocations within the known reservoir. Hematite has colocations at the northern and eastern edges of the reservoir. At DPGF (Figure 7.13), alunite and kaolinite have similar patterns with major colocations northeast of the reservoir. Chalcedony, hematite, and opal present distinctive patterns that generally fall outside the reservoir. Chalcedony and hematite also exist further from faults.

Alunite and kaolinite consistently exhibit similar colocations across all study areas, whereas opal demonstrates variable patterns, aligning with chalcedony, alunite, or kaolinite, depending on the site. Hematite shows distinct patterns compared to other indicator minerals in each study area. Notably, alunite and kaolinite are the most prevalent indicator minerals that colocate with faults within reservoirs. Opal also colocates with faults in the reservoir of CGF and BGF but not in the DPGF. Chalcedony and hematite have the lowest levels of fault colocation, typically found at the peripheries of the reservoirs. In DPGF, only a few instances of mapped chalcedony, hematite, and opal are colocated with faults within the reservoir.

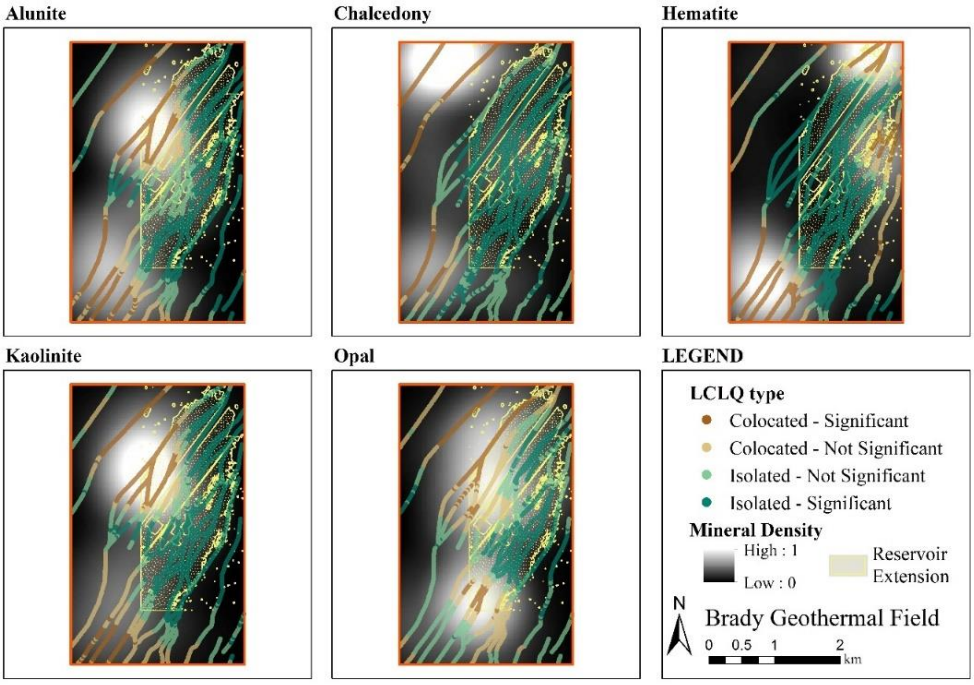

Figure 7.12 Colocation of faults and neighboring indicator minerals at BGF.

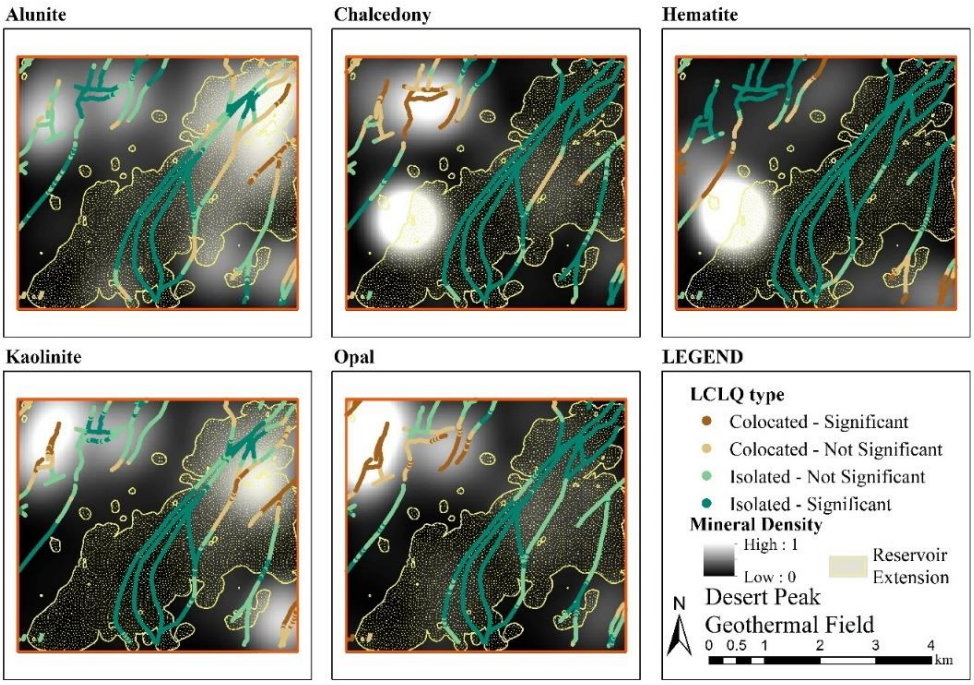

Figure 7.13 Colocation of faults and neighboring indicator minerals at DPGF.

Faults and LSTs.

The colocation maps between faults and LSTs of CGF, BGF, and DPGF are present in Figure 7.14. Faults present strong colocations with high temperatures around the reservoir of CGF. At BGF, faults colocate with high temperatures in the northeast and southwest of the study area. The northern clusters fall within the known reservoir. Some faults are colocated with high temperatures at DPGF, but those faults follow the thin regions of lower temperatures, suggesting weaker connections between the fault and LST at DPGF.

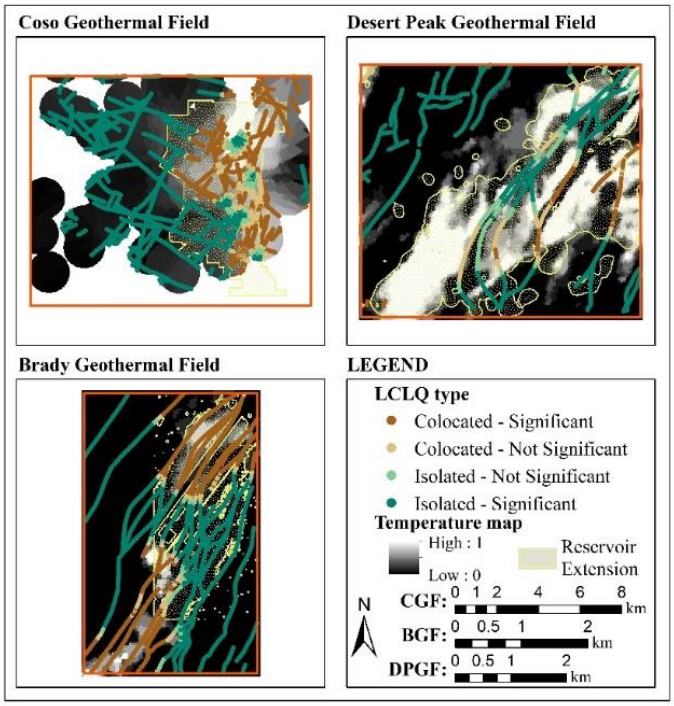

Figure 7.14 Colocation maps of faults and neighboring high temperatures.

LSTs and indicator minerals

The colocation maps between LSTs and MOI of CGF, BGF, and DPGF are respectively present from Figure 7.15 to Figure 7.17. At CGF, alunite and kaolinite have similar colocations with significant clusters in the reservoir. Chalcedony, hematite, and opal have fewer colocations within the reservoir and mainly occur on the reservoir's edge. At BGF, alunite, kaolinite, and opal have similar colocations with significant clusters in the reservoir. Chalcedony has limited observed colocations in the reservoir. Hematite has colocations mainly on the edge of the known reservoir. At DPGF, alunite and kaolinite have similar patterns with major colocations northeast of the reservoir. Chalcedony and hematite have major colocations that fall on the western edge of the reservoir, in an area without faults. Opal has limited observed colocations in the reservoir.

Based on the colocation between high temperatures and indicator minerals, it was found again that alunite and kaolinite have similar patterns, while chalcedony, hematite, and opal did not consistently follow other indicator minerals. Furthermore, alunite and kaolinite are the most common indicator minerals colocating with high temperatures within reservoirs. In contrast, chalcedony and hematite have lower levels of colocations within the reservoirs and are often located at the edge of the reservoirs. Although chalcedony and hematite have major colocations at the western edge of the DPGF reservoir, that is also a region without faults. Opal colocation patterns vary across reservoirs. At CGF, it follows chalcedony distribution but shows more colocations within the reservoir. At BGF, opal colocates with alunite and kaolinite, extending south beyond the reservoir boundary. In contrast, at DPGF, opal has limited colocations within the reservoir area.

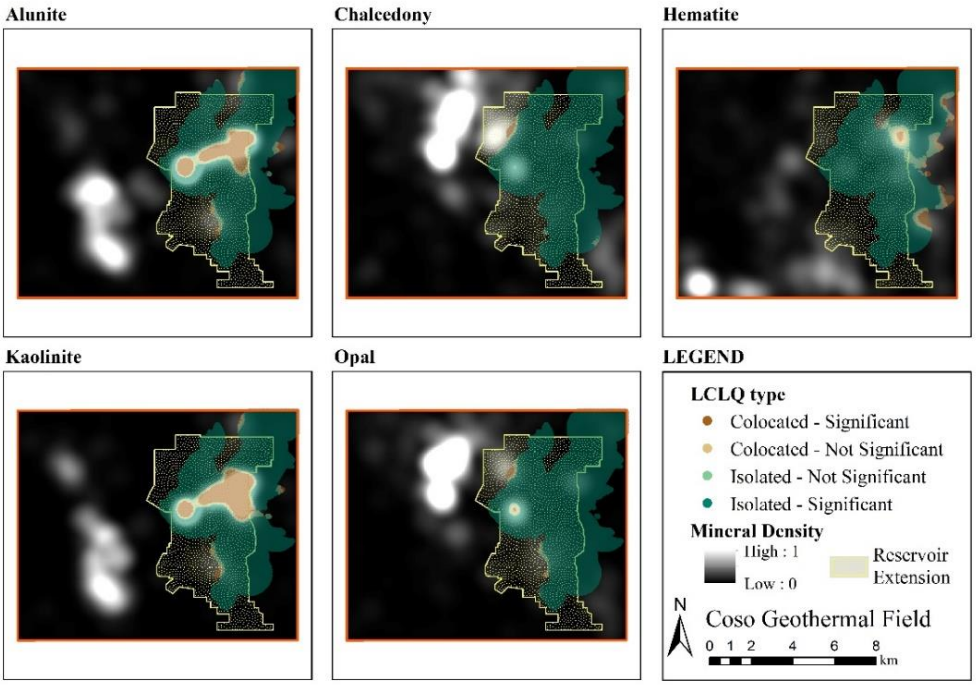

Figure 7.15 Colocation of high temperatures and neighboring indicator minerals at CGF.

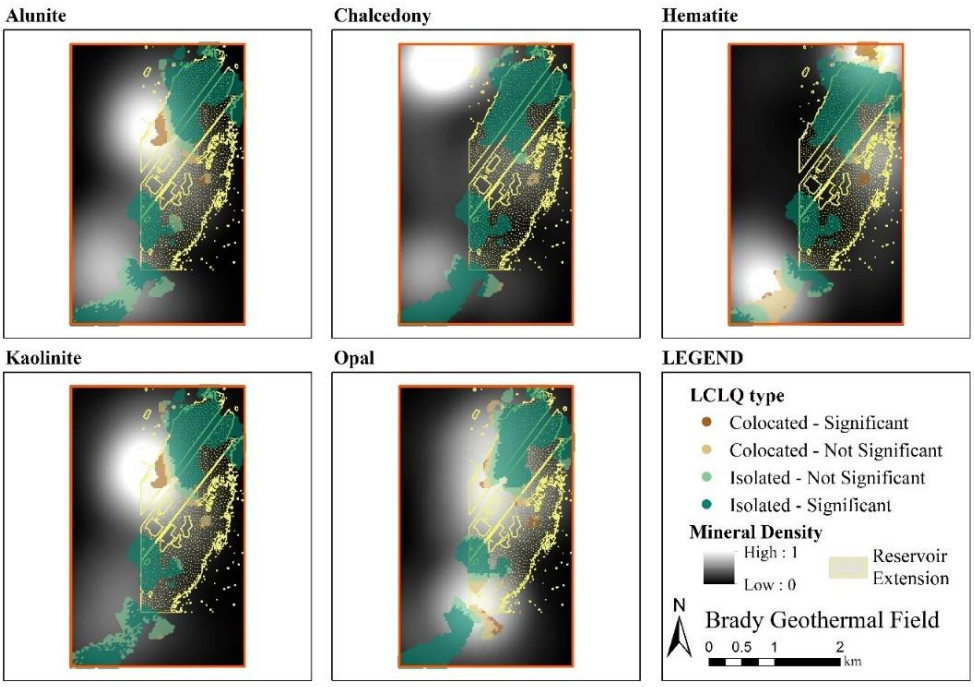

Figure 7.16 Colocation of high temperatures and neighboring indicator minerals at BGF.

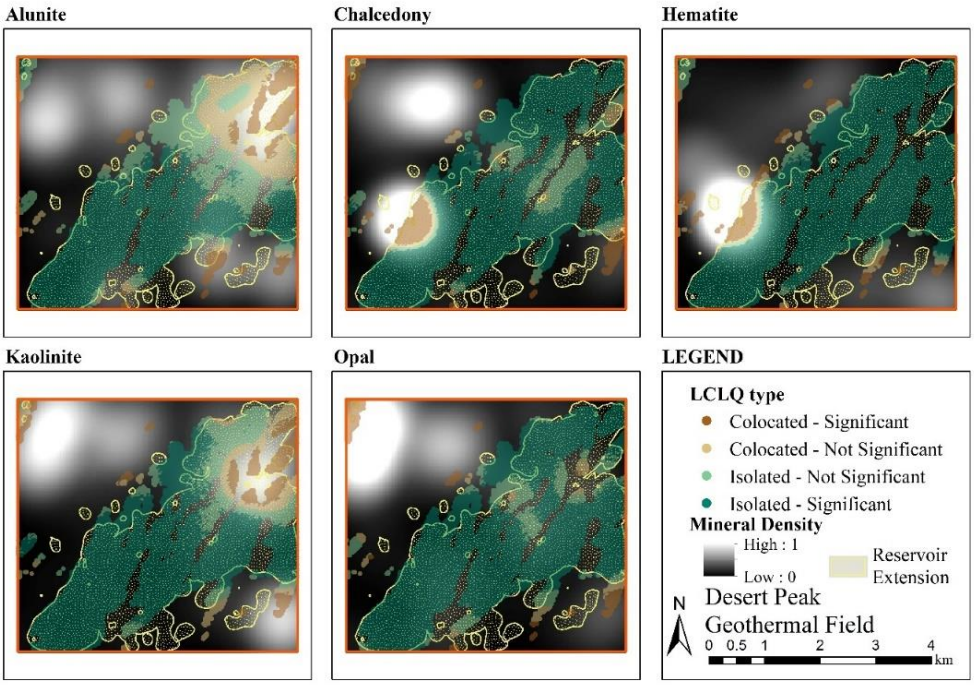

Figure 7.17 Colocation of high temperatures and neighboring indicator minerals at DPGF.

7.3 Discussion of the Data-Driven Analysis

The patterns of MOI from the non-spatial analyses are summarized in Table 7-5. Patterns of MOI against the Fault Distance Map were based on ANOVA. At the same time, those against the Fault Density Map and Multiclass Temperature Map were determined using linear regressions and ANOVA. MOI were categorized into two groups based on their relation with faults: Alunite, kaolinite, and opal showed positive associations, while chalcedony and hematite showed negative associations. The connections between MOI and LST reveal the differences between the study areas. The study found that alunite, hematite, and kaolinite are positively related to elevated LSTs at CGF and BGF. However, these minerals are negatively associated with elevated LSTs at DPGF. In addition, chalcedony and opal have weaker relations to elevated LSTs at CGF and BGF. Overall, the correlation tendencies of MOI with faults and LSTs varied by mineral. However, in the blind geothermal system, MOI were not associated with elevated LSTs. Additionally, non-spatial analyses revealed a strong association between faults and elevated LSTs at CGF and BGF, whereas DPGF exhibits an opposite relation.

Table 7-5 Relations between SGP from non-spatial analyses.

Sites	SGP	alu.	cdy.	hem.	kln.	opl.
CGF	Fault Distance Map	+	+	**x**	+	+
	Fault Density Map	+	-	-	+	+
	Multiclass Temperature Map	+	-	+	+	-
BGF	Fault Distance Map	**x**	-	**x**	**x**	+
	Fault Density Map	+	-	+	+	+
	Multiclass Temperature Map	+	-	+	+	+
DPGF	Fault Distance Map	+	-	-	+	+
	Fault Density Map	+	-	-	+	+
	Multiclass Temperature Map	-	-	-	-	-

+: positively related; -: negatively related; x: limited discovered-pattern

The spatial analyses of colocation further support the idea that MOI exhibit various behaviors regarding faults and LSTs. Alunite and kaolinite consistently display similar spatial patterns, colocating with faults and high temperatures within reservoirs, while chalcedony and hematite show fewer colocations and mostly near reservoir edges. Opal's distribution varies by study area, showing moderate to high colocation with faults and high temperatures at CGF and BGF but not at DPGF. In addition, the colocations between faults and high temperatures also suggest a weaker connection between faults and LSTs in blind geothermal fields such as DPGF.

In summary, the study discovered multiple patterns on each MOI: Alunite and kaolinite were strongly associated with faults across all study areas and positively correlated with elevated LSTs at CGF and BGF. Chalcedony showed limited associations with both faults and elevated LSTs. Hematite displayed weak associations with faults but positive correlations with elevated LSTs at CGF and BGF. Opal was associated with faults, but its correlation with elevated LSTs was weaker than alunite and kaolinite.

Alunite and kaolinite mineralization have long been recognized as part of the alteration assemblage in hydrothermal systems, typically forming when hydrogen sulfide (H_2S) from magmatic sources reacts with oxygen to produce sulfuric acid, which subsequently alters the surrounding rocks (Arribas Jr, 1995; Sillitoe, 1993; White & Hedenquist, 1995). In active geothermal systems, this can be manifest as steam-heated, hydrothermally altered ground (advanced argillic alteration), which generally utilizes faults as major channels to rise (Hedenquist & Arribas, 2022; Jolie et al., 2021). This study demonstrates a strong association of alunite and kaolinite with fault systems and LSTs at CGF and BGF, driven by the rapid ascent of hydrothermal fluids along high-angle faults in the sites (Faulds et al., 2017; Monastero et al., 2005; Siler et al., 2021; Whitmarsh, 1998).

Opal in geothermal fields is often associated with silica sinters formed by the discharging of alkali-chloride near-neutral hot water (Hedenquist & Arribas, 2022; Jolie et al., 2021; Rodgers et al., 2004). The discharge of fluids is strongly influenced by groundwater levels and geology, leading to surface manifestations with footprints that vary from significant halos of advanced argillic alteration. The alteration model is supported by the strong connection between opal and fault maps and the relatively weaker connection between opal and LSTs. This also explains why opal sometimes follows alunite and kaolinite at the alteration halo but sometimes on the edges of geothermal reservoirs. The chalcedony and hematite in this study showed limited links with faults, suggesting that the genesis of these minerals on the surface may not be associated with fluid supplies from faults. Instead, other parameters, such as weathering or rock-forming, may contribute more to these mineral occurrences on surfaces.

The SGP tendencies at DPGF differed from those of CGF and BGF. All indicator minerals exhibited negative correlations with LST at DPGF. Additionally, faults at DPGF were negatively associated with elevated LSTs, contrasting the positive relations observed at CGF and BGF. These findings highlight the significance of ground-based temperature surveys in blind geothermal systems, where LST anomalies are not linked to faults or indicator minerals.

CHAPTER 8 OVERALL CONCLUSIONS AND RECOMMENDATIONS FOR FUTURE WORKS

Addressing geological uncertainties is a critical step to unleash the potential of geothermal energy. This study applied data-driven approaches to support decision-making and interpretations of mineral mapping in geothermal exploration. The Coso Spectral Library was established to offer spectra data for mineral mapping and ground-truth information for accuracy assessment. The study evaluates various mineral mapping approaches at CGF. With the mineral maps based on a refined mineral mapping strategy, the study explores the relations between indicator mineral maps and other SGP at CGF, BGF, and DPGF. Following the research questions, the study results support the correctness of the proposed research hypotheses (1.2). The following section summarizes the conclusions of each research objective.

8.1 Objective One: Evaluate the influence of mapping methods

This part of the study examines research hypothesis one (H1): "Different mapping methods can influence mineral mapping accuracy." Using various mapping methods, the study utilized the spectra of MOI from the Coso Spectral Library for mineral mapping at CGF.

The study examines the performance of five mapping algorithms by mapping five MOI. Among the five selected mapping algorithms, it was discovered that CEM, MF, and MTMF provided the highest accuracy at an average AUC of 0.900. The three algorithms offered similar outcomes since they were based on similar calculation concepts. Following CEM/MF/MTMF, SAM offered the second-highest average AUC level at 0.848. The algorithm that offered the lowest average AUC level was ACE at 0.587. The finding aligns with other earlier remote sensing studies of non-geological targets, suggesting that CEM/MF/MTMF have similar performance that is better than SAM. The performance of ACE was varied compared to earlier studies. ACE offers varied accuracy compared to other algorithms because it is more sensitive to spectral variability, which was identified in stage two of the study (6.2.1).

Based on the findings from the examination of different mapping algorithms, this study proposed multiple fusion combinations based on the ranking of the algorithms' performance. The fusion combinations are 3A (CEM, MF, and MTMF), 4A (CEM, MF, MTMF, and SAM), and 5A (ACE, CEM, MF, MTMF, and SAM). By assessing the accuracy of the fusion maps, it was discovered that the average AUC level of 3A (0.905) and 4A (0.903) only slightly increases the average AUC of the mineral maps compared to the best-performed individual algorithms, CEM, MF, and MTMF (0.900). Still, the fusion map of five algorithms increases the average AUC level (0.934) by around 3% compared to CEM/MF/MTMF, suggesting that fusing mineral maps generally improves mapping accuracy.

The study further compares the accuracy of mineral maps with earlier maps that are based on the identical CGF spectra without splice corrections. It was discovered that the average AUCs of CEM, MF, MTMF, and SAM were increased after splice correction was applied to the target spectra. Although the

average ACU was not increased for the case of ACE, ACE was identified as an algorithm that offers lower mapping accuracy. The results showed that splice correction is not only a necessary step in spectra processing but also increases mapping accuracy.

In brief summary, the significant discoveries are as follows: (1) CEM, MF, and MTMF are the algorithms that offer higher accuracy in mineral mapping. (2) The fusion of mineral maps increases mapping accuracy. (3) Splice correction is necessary to increase mapping accuracy.

8.2 Objective Two: Evaluate the influence of spectra sources

This part of the study examines research hypothesis two (H2): "Different spectra sources can influence mineral mapping accuracy." Using various spectra sources, the study utilized the algorithms ACE, CEM, MF, MTMF, and SAM for mineral mapping at CGF.

The study assesses the mapping outcomes of various alunite and kaolinite spectra from the Coso Spectral Library and the USGS Spectral Library. The accuracy assessment reveals that spectral variability can significantly influence mapping accuracy when different mapping algorithms are applied. It was observed that local CGF spectra offered the highest AUCs for the alunite map (Coso-034) and kaolinite map (Coso-032). The local spectra proved their ability to create accurate mineral maps. Using the USGS spectra sometimes offers AUCs as high as 1.0. However, the USGS spectra sometimes resulted in some of the lowest average AUCs in this study. The study further identified that using the average USGS spectra yields higher average AUCs and the lowest AUC range among the studied USGS spectra. Therefore, for cases without local spectra, the finding suggests using the average spectrum from the USGS Spectral Library instead of a randomly selected one to improve mineral mapping accuracy.

It was observed that different mapping algorithms offer varied levels of average AUC and AUC range in this study. With the different spectra used in mapping, the mineral maps by ACE provided the lowest average AUC and the highest AUC range. On the other hand, CEM, MF, and MTMF offered the highest average AUC and the lowest AUC ranges. These algorithms are less sensitive to spectral variability while providing accurate mineral maps. SAM offered mineral maps with performance between ACE and CEM/MF/MTMF.

For ACE, varied alunite spectra impact mineral mapping by dropping the AUC from 1.0 to 0.5. Varied kaolinite spectra also impact the ACE mapping by dropping the AUC from 0.98 to 0.58. It shows that a random selection of target spectrum in mapping with ACE produces AUC ranges of more than 50 percent for alunite maps and more than 40 percent for kaolinite. In contrast, CEM, MF, and MTMF not only provided accurate mineral maps but also kept the AUC ranges within five percent despite the spectral variability. The result corresponds with the earlier findings that CEM, MF, and MTMF are better mapping algorithms than ACE. Therefore, this study suggests that utilizing the CEM, MF, and MTMF can minimize the impact of spectral variability and improve the accuracy of mineral maps.

The other key contribution in this part of the study is the comparative analysis between the Coso Spectral Library and the USGS Spectral Library for mineral mapping. It was observed that the average AUC level increased by around five percent by using local CGF spectra. Even by comparing the results of individual cases, the CGF spectra provided more mineral maps that have higher accuracy than the USGS spectra. The evidence suggests that using local spectra could improve the quality of mineral mapping. The result from this part also corresponds with the earlier findings that CEM, MF, and MTMF are offering higher mapping accuracies, followed by SAM, and ACE offers the lowest accuracies.

In brief summary, the significant discoveries are as follows: (1) Using the average spectrum from the USGS Spectral Library can improve mineral mapping accuracy. (2) CEM, MF, and MTMF can minimize the impact of spectral variability while improving the accuracy of mineral maps. (3) Using a local spectral library can increase mapping accuracy.

8.3 Objective Three: Explore the relations between the SGP

This part of the study examines research hypothesis three (H3): "The distribution of indicator minerals corresponds to the distribution of faults or LSTs." The study investigated the relations between the map of SGP (indicator minerals, faults, and LSTs) from three geothermal fields (CGF, BGF, and DPGF) using a novel data-driven approach.

This study result demonstrates that mapping alunite, kaolinite, or opal through spectral RS can support targeting fault zones in geothermal fields. The result also highlights the importance of LST surveys in exploring blind geothermal areas.

Multiple identified relations between the SGP would advance data collection and analysis efforts for geothermal exploration. At CGF and BGF, alunite and kaolinite are correlated with faults and elevated LSTs. This indicates that these minerals serve as reliable indicators of active hydrothermal systems in which faults function as pathways for ascending hydrothermal fluids. The presence of alunite and kaolinite is linked to steam-heated argillic alteration, and their spatial distribution may indicate the location of reservoirs like CGF and BGF. Opal is positively correlated with faults but is negatively correlated with elevated LSTs. The formation of opal is associated with silica sinter from discharged near-neutral hot waters, accounting for its variable association with LSTs. Chalcedony and hematite show relatively limited or no significant associations with faults and elevated LSTs, suggesting their formation may be influenced more by surface or near-surface processes rather than deep hydrothermal fluid.

Unlike CGF and BGF, all MOI at DPGF exhibit negative correlations with elevated LST. This indicates that the LST anomalies at DPGF are inconsistent with the occurrence of MOI. The faults at DPGF exhibit a negative correlation with elevated LSTs. The findings contrast with the positive correlations observed at CGF and BGF, suggesting that the behaviors between SGP may fundamentally

differ in blind geothermal fields like DPGF. However, the examination still provides insights into the SGP distribution in blind geothermal sites.

8.4 Recommendations for Future Work

The findings of this study underscore the effectiveness of using data-driven approaches in decision-making and interpretation for geological studies. With the aid of data analysis, statistical evaluation efficiently decreases bias in judgments.

The study also highlights that mineral mapping is a powerful tool in geothermal exploration. For future mineral mapping studies, the study recommends the following:

(1) Apply splice correction to the target spectra.

(2) Fuse mineral maps from various mapping algorithms to consider their outcomes simultaneously.

(3) Use local spectra that are close to the average USGS spectra, or use the USGS average spectra if local spectra are not available.

(4) Utilize the algorithms CEM, MF, or MTMF for better mapping accuracy if focusing on individual mapping algorithms.

In addition to the spectra identified in the Coso Spectral Library, further analysis of the CGF samples, including the employment of techniques such as XRD, could help resolve additional mineralogical details. This would contribute to expanding the current spectral database and support future academic research and industrial applications.

For the potential future research, it is suggested that studies could extend to the following topics:

(1) Include more mineral varieties to understand their distribution behavior in geothermal fields.

(2) Consider more spectral RS images to evaluate the performance of different instruments.

(3) Apply different weights to different mapping algorithms in the study of fusion combination.

(4) Combine the study area of BGF and DPGF and evaluate how the observations change.

(5) Separate different fault systems in tectonic settings and assess if each fault system presents different connections with indicator minerals and LSTs.

(6) Extend the study to underground drilling datasets to explore further the connections between indicator minerals, faults, and LSTs.

REFERENCES

Abdelkareem, M., Kamal El-Din, G. M., & Osman, I. (2018). An integrated approach for mapping mineral resources in the Eastern Desert of Egypt. *International Journal of Applied Earth Observation and Geoinformation*, *73*, 682–696. https://doi.org/10.1016/j.jag.2018.07.005

Abubakar, A. J., Hashim, M., & Pour, A. B. (2018). Using ASTER Satellite Data for Mapping Hydrothermal Alteration as a Tool in Geothermal Exploration with GPS Field Validation. *Advanced Science Letters*, *24*(6), 4489–4495. https://doi.org/10.1166/asl.2018.11632

Abubakar, A. J., Hashim, M., & Pour, A. B. (2019). Remote sensing satellite imagery for prospecting geothermal systems in an aseismic geologic setting: Yankari Park, Nigeria. *International Journal of Applied Earth Observation and Geoinformation*, *80*, 157–172. https://doi.org/10.1016/j.jag.2019.04.005

Achieng, J., Mutua, J., Mibei, G., Olaka, L., & Waswa, A. K. (2017). Mapping of Hydrothermal Minerals Related to Geothermal Activities Using Remote Sensing and GIS: Case Study of Paka Volcano in Kenyan Rift Valley. *International Journal of Geosciences*, *08*(05), 711–725. https://doi.org/10.4236/ijg.2017.85039

Adams, M. C., Moore, J. N., Bjornstad, S., & Norman, D. I. (2000). Geologic history of the Coso geothermal system. *World Geothermal Congress*. https://www.geothermal-energy.org/pdf/IGAstandard/WGC/2000/R0105.PDF

Adiri, Z., Lhissou, R., El Harti, A., Jellouli, A., & Chakouri, M. (2020). Recent advances in the use of public domain satellite imagery for mineral exploration: A review of Landsat-8 and Sentinel-2 applications. In *Ore Geology Reviews* (Vol. 117). Elsevier B.V. https://doi.org/10.1016/j.oregeorev.2020.103332

Ahmadi, H., & Pekkan, E. (2021). Fault-based geological lineaments extraction using remote sensing and GIS—a review. *Geosciences (Switzerland)*, *11*(5). https://doi.org/10.3390/geosciences11050183

Amer, R., El Mezayen, A., & Hasanein, M. (2016). ASTER spectral analysis for alteration minerals associated with gold mineralization. *Ore Geology Reviews*, *75*, 239–251. https://doi.org/10.1016/j.oregeorev.2015.12.008

Ármannsson, H., & Fridriksson, T. (2009). *Application of geochemical methods in geothermal exploration*. https://www.researchgate.net/publication/228706025

Arribas Jr, A. (1995). Characteristics of high-sulfidation epithermal deposits, and their relation to magmatic fluid. *Mineralogical Association of Canada Short Course*, *23*, 419–454.

Assouline, D., Mohajeri, N., Gudmundsson, A., & Scartezzini, J. L. (2019). A machine learning approach for mapping the very shallow theoretical geothermal potential. *Geothermal Energy*, *7*(1). https://doi.org/10.1186/s40517-019-0135-6

Baldridge, A. M., Hook, S. J., Grove, C. I., & Rivera, G. (2009). The ASTER spectral library version 2.0. *Remote Sensing of Environment*, *113*(4), 711–715. https://doi.org/10.1016/j.rse.2008.11.007

Bedini, E. (2011). Mineral mapping in the Kap Simpson complex, central East Greenland, using HyMap and ASTER remote sensing data. *Advances in Space Research*, *47*(1), 60–73. https://doi.org/10.1016/j.asr.2010.08.021

Bemis, S. P., Micklethwaite, S., Turner, D., James, M. R., Akciz, S., Thiele, S. T., & Bangash, H. A. (2014). Ground-based and UAV-Based photogrammetry: A multi-scale, high-resolution mapping

tool for structural geology and paleoseismology. *Journal of Structural Geology*, *69*(PA), 163–178. https://doi.org/10.1016/j.jsg.2014.10.007

Benoit, W. R., Hiner, J. E., & Forest, R. T. (1982). *Discovery and geology of the Desert Peak geothermal field: A case history*. University of Nevada.

Berman, M., Bischof, L., & Huntington, J. (1999). Algorithms and Software for the Automated Identification of Minerals Using Field Spectra or Hyperspectral Imagery. *13th International Conference on Applied Geologic Remote Sensing*, 222–232. https://www.researchgate.net/publication/284479221

Berman, M., Bischof, L., Lagerstrom, R., Guo, Y., Huntington, J., & Mason, P. (2011). *An Unmixing Algorithm Based on a Large Library of Shortwave Infrared Spectra*.

Bernstein, L. S., Adler-Golden, S. M., Sundberg, R. L., Levine, R. Y., Perkins, T. C., & Berk, A. (2005). *A New Method for Atmospheric Correction and Aerosol Optical Property Retrieval for VIS-SWIR Multi-and Hyperspectral Imaging Sensors: QUAC (QUick Atmospheric Correction)*. https://apps.dtic.mil/sti/citations/ADA452963

Bernstein, L. S., Adler-Golden, S. M., Sundberg, R. L., Levine, R. Y., Perkins, T. C., Berk, A., Ratkowski, A. J., Felde, G., & Hoke, M. L. (2005). Validation of the QUick atmospheric correction (QUAC) algorithm for VNIR-SWIR multi- and hyperspectral imagery. *Algorithms and Technologies for Multispectral, Hyperspectral, and Ultraspectral Imagery XI*, *5806*, 668. https://doi.org/10.1117/12.603359

Bernstein, L. S., Jin, X., Gregor, B., & Adler-Golden, S. M. (2012). Quick atmospheric correction code: algorithm description and recent upgrades. *Optical Engineering*, *51*(11), 111719. https://doi.org/10.1117/1.oe.51.11.111719

Bishop, B. P., & Bird, D. K. (1987). Variation in sericite compositions from fracture zones within the Coso Hot Springs geothermal system. *Geochimica et Cosmochimica Acta*, *51*(5), 1245–1256. https://doi.org/10.1016/0016-7037(87)90216-X

Bishop, C., Rivard, B., de Souza Filho, C., & van der Meer, F. (2018). Geological remote sensing. *International Journal of Applied Earth Observation and Geoinformation*, *64*, 267–274. https://doi.org/10.1016/j.jag.2017.08.005

Blake, K., Sabin, A., Eneva, M., Nale, S., Lazaro, M., Tiedeman, A., Meade, D., & Huang, W.-C. (2020). Updated Shallow Temperature Survey and Resource Evolution for the Coso Geothermal Field. *World Geothermal Congress*.

Blankenship, D. (2016). *West Flank Coso FORGE: ArcGIS Data for Geologic Model*. USDOE Geothermal Data Repository (United States); Sandia National …. https://doi.org/10.15121/1287562

Boardman, J. W. (1998). Leveraging the high dimensionality of AVIRIS data for improved sub-pixel target unmixing and rejection of false positives: mixture tuned matched filtering. *Summaries of the Seventh JPL Airborne Geoscience Workshop, JPL Publication, 1998*, *97*(1), 55–56.

Boardman, J. W., & Kruse, F. A. (2011). Analysis of imaging spectrometer data using N -dimensional geometry and a mixture-tuned matched filtering approach. *IEEE Transactions on Geoscience and Remote Sensing*, *49*(11 PART 1), 4138–4152. https://doi.org/10.1109/TGRS.2011.2161585

Boden, D. R. (2016). *Geologic fundamentals of geothermal energy*. CRC Press.

Borsoi, R. A., Imbiriba, T., Bermudez, J. C. M., Richard, C., Chanussot, J., Drumetz, L., Tourneret, J. Y., Zare, A., & Jutten, C. (2021). Spectral Variability in Hyperspectral Data Unmixing: A

comprehensive review. In *IEEE Geoscience and Remote Sensing Magazine* (Vol. 9, Issue 4, pp. 223–270). Institute of Electrical and Electronics Engineers Inc. https://doi.org/10.1109/MGRS.2021.3071158

Brodt-Giles, D. (EERE), O. of E. E. & R. Energy. (2014, November). *Open Energy Information (OpenEI.org)*. https://data.openei.org/submissions/389

Browne, P. R. L. (1978). Hydrothermal alteration in active geothermal fields. *Annual Review of Earth and Planetary Sciences*, *6*(1), 229–248.

Calvin, W. M., Littlefield, E. F., & Kratt, C. (2015). Remote sensing of geothermal-related minerals for resource exploration in Nevada. *Geothermics*, *53*, 517–526. https://doi.org/10.1016/j.geothermics.2014.09.002

Calvin, W. M., & Pace, E. L. (2016). Mapping alteration in geothermal drill core using a field portable spectroradiometer. *Geothermics*, *61*, 12–23. https://doi.org/10.1016/j.geothermics.2016.01.005

Carranza, E. J. M., Wibowo, H., Barritt, S. D., & Sumintadireja, P. (2008). Spatial data analysis and integration for regional-scale geothermal potential mapping, West Java, Indonesia. *Geothermics*, *37*(3), 267–299. https://doi.org/10.1016/j.geothermics.2008.03.003

Cavur, M., Yu, Y. T., Demir, E., & Duzgun, S. (2024). Mapping Geothermal Indicator Minerals Using Fusion of Target Detection Algorithms. *Remote Sensing*, *16*(7). https://doi.org/10.3390/rs16071223

Cavur, M., Yu, Y.-T., Demir, E., Duzgun, H. S., Pfaff, K., Sabin, A. E., & Buck, C. (2023). *Coso Geothermal Spectral Library for Rock and Minerals*. USDOE Geothermal Data Repository (United States); Mining Engineering …. https://doi.org/10.15121/1999403

Cawood, A. J., Bond, C. E., Howell, J. A., Butler, R. W. H., & Totake, Y. (2017). LiDAR, UAV or compass-clinometer? Accuracy, coverage and the effects on structural models. *Journal of Structural Geology*, *98*, 67–82. https://doi.org/10.1016/j.jsg.2017.04.004

Chan, H. P., Chang, C. P., & Dao, P. D. (2018). Geothermal Anomaly Mapping Using Landsat ETM+ Data in Ilan Plain, Northeastern Taiwan. *Pure and Applied Geophysics*, *175*(1), 303–323. https://doi.org/10.1007/s00024-017-1690-z

Chang, C.-I., Liu, J.-M., Chieu, B.-C., Ren, H., Wang, C.-M., Lo, C.-S., Chung, P.-C., Yang, C.-W., & Ma, D.-J. (2000). Generalized constrained energy minimization approach to subpixel target detection for multispectral imagery. *Optical Engineering*, *39*(5), 1275. https://doi.org/10.1117/1.602486

Cole, W., Mai, T., Logan, J., Steinberg, D., Mccall, J., Richards, J., Sigrin, B., & Porro, G. (2016). *2016 Standard Scenarios Report: A U.S. Electricity Sector Outlook*. www.nrel.gov/publications.

Coolbaugh, M. F., Kratt, C., Fallacaro, A., Calvin, W. M., & Taranik, J. V. (2007). Detection of geothermal anomalies using Advanced Spaceborne Thermal Emission and Reflection Radiometer (ASTER) thermal infrared images at Bradys Hot Springs, Nevada, USA. *Remote Sensing of Environment*, *106*(3), 350–359. https://doi.org/10.1016/j.rse.2006.09.001

Coolbaugh, M. F., Sladek, C., Faulds, J. E., Zehner, R. E., & Oppliger, G. L. (2007). Use of rapid temperature measurements at a 2-meter depth to augment deeper temperature gradient drilling. *Proceedings, Thirty-Second Workshop on Geothermal Reservoir Engineering, Stanford University*, *8*.

Craig, J. W., Faulds, J. E., Hinz, N. H., Earney, T. E., Schermerhorn, W. D., Siler, D. L., Glen, J. M., Peacock, J., Coolbaugh, M. F., & Deoreo, S. B. (2021). Discovery and analysis of a blind

geothermal system in Southeastern Gabbs Valley, Western Nevada, USA. *Geothermics*, *97*. https://doi.org/10.1016/j.geothermics.2021.102177

Curewitz, D., & Karson, J. A. (1997). Structural settings of hydrothermal outflow: Fracture permeability maintained by fault propagation and interaction. *Journal of Volcanology and Geothermal Research*, *79*(3–4), 149–168. https://doi.org/10.1016/S0377-0273(97)00027-9

D'amore, F., & Panichi, C. (1985). Geochemistry in geothermal exploration. *International Journal of Energy Research*, *9*(3), 277–298. https://doi.org/10.1002/er.4440090307

Davatzes, N. C., & Hickman, S. (2006). Stress and faulting in the Coso Geothermal Field: Update and recent results from the East Flank and Coso Wash. *31st Workshop on Geothermal Reservoir Engineering*, 13–19.

Davatzes, N. C., & Hickman, S. H. (2010). The Feedback Between Stress, Faulting, and Fluid Flow: Lessons from the Coso Geothermal Field, CA, USA. In *Proceedings World Geothermal Congress*.

Demir, E., Cavur, M., Yu, Y. T., & Duzgun, H. S. (2024). An Evaluation of AI Models' Performance for Three Geothermal Sites. *Energies* , *17*(13). https://doi.org/10.3390/en17133255

Domra Kana, J., Djongyang, N., Danwe Raïdandi, Njandjock Nouck, P., & Abdouramani Dadjé. (2015). A review of geophysical methods for geothermal exploration. *Renewable and Sustainable Energy Reviews*, *44*, 87–95. https://doi.org/10.1016/j.rser.2014.12.026

Du, Q., Ren, H., & Chang, C. I. (2003). A comparative study for orthogonal subspace projection and constrained energy minimization. *IEEE Transactions on Geoscience and Remote Sensing*, *41*(6 PART II), 1525–1529. https://doi.org/10.1109/TGRS.2003.813704

Duffield, W. A., & Bacon, C. R. (1976). *Preliminary geologic map of the Coso rhyolite domes and adjacent areas, Inyo County, California*. https://doi.org/https://doi.org/10.3133/ofr76238

Duffield, W. A., & Bacon, C. R. (1981). *Geologic map of the Coso volcanic field and adjacent areas, Inyo County, California*. https://doi.org/https://doi.org/10.3133/i1200

Duffield, W. A., Bacon, C. R., & Dalrymple, G. B. (1980). Later Cenozoic volcanism, geochronology, and structure of the Coso Range, Inyo County, California. *Journal of Geophysical Research*, *85*(B5), 2381–2404. https://doi.org/10.1029/JB085iB05p02381

Dumouchel, W., & O'Brien, F. (1989). Integrating a robust option into a multiple regression computing environment. *Computer Science and Statistics: Proceedings of the 21st Symposium on the Interface*, 297–302.

Dunn, O. J., & Clark, V. A. (1986). *Applied statistics: analysis of variance and regression*. John Wiley & Sons, Inc.

Echols, T. J., Hulen, J. B., Moore, J. N., & Crane, G. K. (1986). Surficial alteration and spring deposits of the Wheeler mercury prospect, with initial results from Wheeler Corehole 64-16, Coso geothermal area, California. *GRC Transactions*, *10*.

Erika. (2022). *Indicator mineral mapping for geothermal sites using multi/hyperspectral imagery* [Master's thesis, Colorado School of Mines]. https://repository.mines.edu/handle/11124/15389

Fan, C., Wu, J., Xie, H., & Birnbaum, S. (2012). Analysis of United States Geological Survey spectral library of silicate minerals: implication for remote sensing applications. *Journal of Applied Remote Sensing*, *6*(1), 063514. https://doi.org/10.1117/1.JRS.6.063514

Faulds, J. E., Coolbaugh, M. F., Vice, G. S., & Edwards, M. L. (2006). Characterizing structural controls of geothermal fields in the northwestern Great Basin: A progress report. *Geothermal Resources Council Transactions*, *30*, 69–76.

Faulds, J. E., Garside, L. J., & Oppliger, G. L. (2003). Structural analysis of the Desert Peak-Brady geothermal field, Northwestern Nevada: implications for understanding linkages between northeast-trending structures and geothermal reservoirs in the Humboldt structural zone. *Transactions-Geothermal Resources Council*, 859–864.

Faulds, J. E., Ramelli, A. R., Coolbaugh, M. F., Hinz, N. H., Garside, L. J., & Queen, J. H. (2017). Preliminary geologic map of the Bradys geothermal area, Churchill County, Nevada. In *Nevada Bureau of Mines and Geology, Open-File Report*. https://pubs.nbmg.unr.edu/Prel-geol-Bradys-geothermal-p/of2017-04.htm

Faulds, J. E., Ramelli, A. R., Garside, L. J., Coolbaugh, M. F., & Green, H. L. (2012). *Preliminary Geologic Map of the Desert Peak Quadrangle, Churchill County, Nevada*. Nevada Bureau of Mines and Geology. https://pubs.nbmg.unr.edu/Geol-Desert-Peak-quad-p/of2012-05.htm

Flores, H., Lorenz, S., Jackisch, R., Tusa, L., Cecilia Contreras, I., Zimmermann, R., & Gloaguen, R. (2021). UAS-based hyperspectral environmental monitoring of acid mine drainage affected waters. *Minerals*, *11*(2), 1–25. https://doi.org/10.3390/min11020182

Gaigalas, A. K., Wang, L., He, H.-J., & DeRose, P. (2009). Procedures for Wavelength Calibration and Spectral Response Correction of CCD Array Spectrometers. *Journal of Research of the National Institute of Standards and Technology*, *114*(4), 215. https://doi.org/10.6028/jres.114.015

Galbraith, R. M. (1978). *Geological and geophysical analysis of Coso Geothermal Exploration Hole No. 1 (CGEH-1), Coso Hot Springs KGRA, California*.

Gasperikova, E., & Cumming, W. (2020). How geophysics can help the geothermal industry. *SEG Technical Program Expanded Abstracts*, *2020-October*, 3379–3383. https://doi.org/10.1190/segam2020-3425875.1

Gehringer, M., & Loksha, V. (2012). *Geothermal Handbook: Planning and Financing Power Generation*. https://www.esmap.org/node/2001

Gemitzi, A., Dalampakis, P., & Falalakis, G. (2021). Detecting geothermal anomalies using Landsat 8 thermal infrared remotely sensed data. *International Journal of Applied Earth Observation and Geoinformation*, *96*. https://doi.org/10.1016/j.jag.2020.102283

Hanley, J. A., & McNeil, B. J. (1982). The meaning and use of the area under a receiver operating characteristic (ROC) curve. *Radiology*, *143*(1), 29–36. https://doi.org/10.1148/radiology.143.1.7063747

Harsanyi, J. C., & Chang, C.-I. (1993). *Detection and classification of subpixel spectral signatures in hyperspectral image sequences*. https://www.proquest.com/docview/304082316?pq-origsite=gscholar&fromopenview=true

Harvey, C., Beardsmore, G., Moeck, I., Ruter, H., & Bauer, S. (2014). *Best practices guide for geothermal exploration*. https://documents.worldbank.org/en/publication/documents-reports/documentdetail/190071480069890732/best-practices-guide-for-geothermal-exploration

Hedenquist, J. W., & Arribas, A. (2022). Exploration Implications of Multiple Formation Environments of Advanced Argillic Minerals. *Economic Geology*, *117*(3), 609–643. https://doi.org/10.5382/econgeo.4880

Heinz, D. C., & Chang, C. I. (2001). Fully constrained least squares linear spectral mixture analysis method for material quantification in hyperspectral imagery. *IEEE Transactions on Geoscience and Remote Sensing*, *39*(3), 529–545. https://doi.org/10.1109/36.911111

Henley, R. W., & Ellis, A. J. (1983). Geothermal systems ancient and modern: a geochemical review. *Earth-Science Reviews*, *19*(1), 1–50. https://doi.org/10.1016/0012-8252(83)90075-2

Herrmann, W., Blake, M., Doyle, M., Huston, D., Kamprad, J., Merry, N., & Pontual, S. (2001). Short Wavelength Infrared (SWIR) Spectral Analysis of Hydrothermal Alteration Zones Associated with Base Metal Sulfide Deposits at Rosebery and Western Tharsis, Tasmania, and Highway-Reward, Queensland. *Economic Geology*, *96*(5), 939–955. https://doi.org/10.2113/gsecongeo.96.5.939

Hirai, A., & Tonooka, H. (2019). Mineral discrimination by combination of multispectral image and surrounding hyperspectral image. *Journal of Applied Remote Sensing*, *13*(02), 1. https://doi.org/10.1117/1.jrs.13.024517

Holland, P. W., & Welsch, R. E. (1977). Robust regression using iteratively reweighted least-squares. *Communications in Statistics-Theory and Methods*, *6*(9), 813–827.

Hulen, J. B. (1978). *Geology and alteration of the Coso geothermal area, Inyo County, California*. https://www.osti.gov/biblio/6279619

Hwang, B., Cole, D., & Michael Barton Ann Cook, A. (2014). *Water-Rock Interaction in the Coso Geothermal System* [Master's thesis, Ohio State University]. http://rave.ohiolink.edu/etdc/view?acc_num=osu1417724456

Jawak, S. D., Wankhede, S. F., Luis, A. J., & Balakrishna, K. (2022a). Impact of Image-Processing Routines on Mapping Glacier Surface Facies from Svalbard and the Himalayas Using Pixel-Based Methods. *Remote Sensing*, *14*(6). https://doi.org/10.3390/rs14061414

Jawak, S. D., Wankhede, S. F., Luis, A. J., & Balakrishna, K. (2022b). Multispectral Characteristics of Glacier Surface Facies (Chandra-Bhaga Basin, Himalaya, and Ny-Ålesund, Svalbard) through Investigations of Pixel and Object-Based Mapping Using Variable Processing Routines. *Remote Sensing*, *14*(24). https://doi.org/10.3390/rs14246311

Jennings, C. W., & Bryant, W. A. (2010). Fault activity map of California. *California Geological Survey Geologic Data Map*, *6*. https://www.conservation.ca.gov/cgs/publications/fam

Jennings, C. W., & Saucedo, G. J. (1994). *Fault activity map of California and adjacent areas with locations and ages of recent volcanic eruptions*. Department of Conservation, Division of Mines and Geology.

Jin, X., Paswaters, S., & Cline, H. (2009). A comparative study of target detection algorithms for hyperspectral imagery. *Algorithms and Technologies for Multispectral, Hyperspectral, and Ultraspectral Imagery XV*, *7334*, 73341W. https://doi.org/10.1117/12.818790

Jolie, E., Moeck, I., & Faulds, J. E. (2015). Quantitative structural-geological exploration of fault-controlled geothermal systems-A case study from the Basin-and-Range Province, Nevada (USA). *Geothermics*, *54*, 54–67. https://doi.org/10.1016/j.geothermics.2014.10.003

Jolie, E., Scott, S., Faulds, J., Chambefort, I., Axelsson, G., Gutiérrez-Negrín, L. C., Regenspurg, S., Ziegler, M., Ayling, B., Richter, A., & Zemedkun, M. T. (2021). Geological controls on geothermal resources for power generation. *Nature Reviews Earth & Environment*, *2*(5), 324–339. https://doi.org/10.1038/s43017-021-00154-y

Jones, K. L., Schulenburg, N. W., & Wright, C. (2010). Hyperspectral remote sensing techniques for locating geothermal areas. In G. C. Gilbreath & C. T. Hawley (Eds.), *Active and Passive Signatures* (Vol. 7687, p. 76870J). SPIE. https://doi.org/10.1117/12.855444

Kokaly, R. F., Clark, R. N., Swayze, G. A., Livo, K. E., Hoefen, T. M., Pearson, N. C., Wise, R. A., Benzel, W. M., Lowers, H. A., Driscoll, R. L., & Klein, A. J. (2017). *USGS Spectral Library Version 7*. https://doi.org/https://doi.org/10.3133/ds1035

Kovac, K. M., Moore, J. N., & Lutz, S. J. (2005). Geologic framework of the East Flank, Coso geothermal field: Implications for EGS Development. *30th Workshop on Geothermal Reservoir Engineering*.

Kratt, C., Calvin, W., & Coolbaugh, M. (2006). Geothermal exploration with Hymap hyperspectral data at Brady-Desert Peak, Nevada. *Remote Sensing of Environment*, *104*(3), 313–324. https://doi.org/10.1016/j.rse.2006.05.005

Kratt, C., Calvin, W. M., & Coolbaugh, M. F. (2010). Mineral mapping in the Pyramid Lake basin: Hydrothermal alteration, chemical precipitates and geothermal energy potential. *Remote Sensing of Environment*, *114*(10), 2297–2304. https://doi.org/10.1016/j.rse.2010.05.006

Kraut, S., Scharf, L. L., & Butler, R. W. (2005). The adaptive coherence estimator: A uniformly most-powerful-invariant adaptive detection statistic. *IEEE Transactions on Signal Processing*, *53*(2 I), 427–438. https://doi.org/10.1109/TSP.2004.840823

Kruse, F. A. (2012). Mapping surface mineralogy using imaging spectrometry. *Geomorphology*, *137*(1), 41–56. https://doi.org/10.1016/j.geomorph.2010.09.032

Kruse, F. A., Lefkoff, A. B., Boardman, J. W., Heidebrecht, K. B., Shapiro, A. T., Barloon, P. J., & Goetz, A. F. H. (1993). The spectral image processing system (SIPS)—interactive visualization and analysis of imaging spectrometer data. *Remote Sensing of Environment*, *44*(2–3), 145–163. https://doi.org/10.1016/0034-4257(93)90013-N

Kruse, F. A., & Perry, S. L. (2013). Mineral mapping using simulated worldview-3 short-wave-infrared imagery. *Remote Sensing*, *5*(6), 2688–2703. https://doi.org/10.3390/rs5062688

Lagat, J. (2009). Hydrothermal alteration mineralogy in geothermal fields with case examples from Olkaria domes geothermal field, Kenya. *Dipresentasikan Dalam Short Course IV on Exploration for Geothermal Resources*.

Leight, C. J., Mccanta, M. C., Glotch, T. D., Thomson, B. J., Ye, C., & Darby Dyar, M. (2022). *Characterization of tephra deposits using VNIR and MIR spectroscopy: A comprehensive terrestrial tephra spectral library*. https://doi.org/10.5066/P9O54M4Q

Lemgruber-Traby, A., Bossennec, C., Béthune, G., Souque, C., Divies, R., van der Vaart, J., Bär, K., & Sass, I. (2023). Basin-scale 3D modelling of the northern Upper Rhine Graben: insights into basement fault-related geothermal flow pathways. *Geoenergy*, *1*(1). https://doi.org/10.1144/geoenergy2023-002

Leslie, T. F., & Kronenfeld, B. J. (2011). The Colocation Quotient: A New Measure of Spatial Association Between Categorical Subsets of Points. *Geographical Analysis*, *43*(3), 306–326.

Liotta, D., Brogi, A., Ruggieri, G., Rimondi, V., Zucchi, M., Helgadóttir, H. M., Montegrossi, G., & Friðleifsson, G. Ó. (2020). Fracture analysis, hydrothermal mineralization and fluid pathways in the Neogene Geitafell central volcano: insights for the Krafla active geothermal system, Iceland. *Journal of Volcanology and Geothermal Research*, *391*. https://doi.org/10.1016/j.jvolgeores.2018.11.023

Liotta, D., Brogi, A., Ruggieri, G., & Zucchi, M. (2021). Fossil vs. active geothermal systems: A field and laboratory method to disclose the relationships between geothermal fluid flow and geological structures at depth. *Energies*, *14*(4). https://doi.org/10.3390/en14040933

Lutz, S. J., Moore, J. N., & Copp, J. F. (1996). Integrated mineralogical and fluid inclusion study of the Coso geothermal systems, California (No. SGP-TR-151-27). *21st Workshop on Geothermal Reservoir Engineering*.

Mahzari, P., Stanton-Yonge, A., Sanchez-Roa, C., Saldi, G., Mitchell, T., Oelkers, E. H., Hjorleifsdottir, V., Snaebjornsdottir, S. O., Ratouis, T., Striolo, A., & Jones, A. P. (2021). Characterizing fluid flow paths in the Hellisheidi geothermal field using detailed fault mapping and stress-dependent permeability. *Geothermics*, *94*. https://doi.org/10.1016/j.geothermics.2021.102127

Manley, C. R., & Bacon, C. R. (2000). Rhyolite Thermobarometry and the Shallowing of the Magma Reservoir, Coso Volcanic Field, California. *Journal of Petrology*, *41*(1), 149–174. https://doi.org/10.1093/petrology/41.1.149

Manolakis, D., Marden, D., & Shaw, G. A. (2003). Hyperspectral Image Processing for Automatic Target Detection Applications. *Lincoln Laboratory Journal*, *14*(1).

Manolakis, D., & Shaw, G. (2002). Detection algorithms for hyperspectral imaging applications. *IEEE Signal Processing Magazine*, *19*(1), 29–43. https://doi.org/10.1109/79.974724

Mars, J. C. (2018). Mineral and lithologic mapping capability of worldview 3 data at Mountain Pass, California, using true- and false-color composite images, band ratios, and logical operator algorithms. *Economic Geology*, *113*(7), 1587–1601. https://doi.org/10.5382/econgeo.2018.4604

Marsaglia, G., Tsang, W. W., & Wang, J. (2003). Evaluating Kolmogorov's distribution. *Journal of Statistical Software*, *8*, 1–4.

Marwaha, R., Kumar, A., & Kumar, A. S. (2015). Object-oriented and pixel-based classification approach for land cover using airborne long-wave infrared hyperspectral data. *Journal of Applied Remote Sensing*, *9*(1), 095040. https://doi.org/10.1117/1.JRS.9.095040

Massey Jr, F. J. (1951). The Kolmogorov-Smirnov test for goodness of fit. *Journal of the American Statistical Association*, *46*(253), 68–78.

Mclin, K. S., Kovac, K. M., Moore, J. N., Adams, M. C., & Xu, T. (2006). Modeling the geochemical effects of injection at Coso geothermal field, CA; Comparison with field observations. *31st Workshop on Geothermal Reservoir Engineering*.

McNamara, D. D., Milicich, S. D., Massiot, C., Villamor, P., McLean, K., Sépulveda, F., & Ries, W. F. (2019). Tectonic Controls on Taupo Volcanic Zone Geothermal Expression: Insights From Te Mihi, Wairakei Geothermal Field. *Tectonics*, *38*(8), 3011–3033. https://doi.org/10.1029/2018TC005296

Micklethwaite, S., Sheldon, H. A., & Baker, T. (2010). Active fault and shear processes and their implications for mineral deposit formation and discovery. *Journal of Structural Geology*, *32*(2), 151–165. https://doi.org/10.1016/j.jsg.2009.10.009

Miller, L. H. (1956). Table of percentage points of Kolmogorov statistics. *Journal of the American Statistical Association*, *51*(273), 111–121.

Minissale, A. A. (2018). A simple geochemical prospecting method for geothermal resources in flat areas. In *Geothermics* (Vol. 72, pp. 258–267). Elsevier Ltd. https://doi.org/10.1016/j.geothermics.2017.12.001

Moeck, I. S. (2014). Catalog of geothermal play types based on geologic controls. *Renewable and Sustainable Energy Reviews*, *37*, 867–882. https://doi.org/10.1016/j.rser.2014.05.032

Molan, Y. E., Refahi, D., & Tarashti, A. H. (2014). Mineral mapping in the Maherabad area, eastern Iran, using the hyMap remote sensing data. *International Journal of Applied Earth Observation and Geoinformation*, *27*(PARTB), 117–127. https://doi.org/10.1016/j.jag.2013.09.014

Monastero, F. C. (2002). Geothermal Development An Overview of Industry-Military Cooperation in the Development of Power Operations at the Coso Geothermal Field in Southern California. *GRC Bulletin*, 188–195.

Monastero, F. C., Katzenstein, A. M., Miller, J. S., Unruh, J. R., Adams, M. C., & Richards-Dinger, K. (2005). The Coso geothermal field: A nascent metamorphic core complex. *Bulletin of the Geological Society of America*, *117*(11–12), 1534–1553. https://doi.org/10.1130/B25600.1

Moraga, J. (2022). *Geothermal AI: An Artificial Intelligence for Early Stage Geothermal Exploration*. Colorado School of Mines.

Moraga, J., Cavur, M., Duzgun, H. S., Soydan, H., & Jin, G. (2021a). *Brady Geodatabase for Geothermal Exploration Artificial Intelligence*. USDOE Geothermal Data Repository (United States); Colorado School of Mines …. https://doi.org/10.15121/1797281

Moraga, J., Cavur, M., Duzgun, H. S., Soydan, H., & Jin, G. (2021b). *Desert Peak Geodatabase for Geothermal Exploration Artificial Intelligence*. https://doi.org/10.15121/1797282

Moraga, J., & Duzgun, H. S. (2022). JigsawHSI: a network for Hyperspectral Image classification. *ArXiv:2206.02327*. http://arxiv.org/abs/2206.02327

Moraga, J., Duzgun, H. S., Cavur, M., & Soydan, H. (2022). The Geothermal Artificial Intelligence for Geothermal Exploration. *Renewable Energy*, *192*, 134–149. https://doi.org/10.1016/j.renene.2022.04.113

Mudunuru, M. K., Vesselinov, V. V., & Ahmmed, B. (2022). GeoThermalCloud: Machine Learning for Geothermal Resource Exploration. *Journal of Machine Learning for Modeling and Computing*, *3*(4), 57–72. https://doi.org/10.1615/JMachLearnModelComput.2022046445

Muther, T., Syed, F. I., Lancaster, A. T., Salsabila, F. D., Dahaghi, A. K., & Negahban, S. (2022). Geothermal 4.0: AI-enabled geothermal reservoir development- current status, potentials, limitations, and ways forward. *Geothermics*, *100*. https://doi.org/10.1016/j.geothermics.2022.102348

Nait Amara, B., Aissa, D. E., Maouche, S., Braham, M., Machane, D., & Guessoum, N. (2019). Hydrothermal alteration mapping and structural features in the Guelma basin (Northeastern Algeria): contribution of Landsat-8 data. *Arabian Journal of Geosciences*, *12*(3). https://doi.org/10.1007/s12517-019-4224-4

NASA LP DAAC. (2015). *ASTER Level 1 Precision Terrain Corrected Registered At-Sensor Radiance V003 [Data set]*. NASA EOSDIS Land Processes DAAC. https://doi.org/10.5067/ASTER/AST_L1T.003

Ochieng, L. (2014). *Overview of geothermal surface exploration Methods*. https://orkustofnun.is/gogn/unu-gtp-sc/UNU-GTP-SC-23-0101.pdf

Okoroafor, E. R., Smith, C. M., Ochie, K. I., Nwosu, C. J., Gudmundsdottir, H., & (Jabs) Aljubran, M. (2022). Machine learning in subsurface geothermal energy: Two decades in review. *Geothermics*, *102*. https://doi.org/10.1016/j.geothermics.2022.102401

Park, H., & Choi, J. (2021). Mineral Detection Using Sharpened VNIR and SWIR Bands of Worldview-3 Satellite Imagery. *Sustainability (Switzerland)*, *13*(10). https://doi.org/10.3390/su13105518

Percival, J. B., Bosman, S. A., Potter, E. G., Peter, J. M., Laudadio, A. B., Abraham, A. C., Shiley, D. A., & Sherry, C. (2018). Customized spectral libraries for effective mineral exploration: Mining national mineral collections. *Clays and Clay Minerals*, *66*(3), 297–314. https://doi.org/10.1346/CCMN.2018.064103

Peyghambari, S., & Zhang, Y. (2021). Hyperspectral remote sensing in lithological mapping, mineral exploration, and environmental geology: an updated review. *Journal of Applied Remote Sensing*, *15*(03). https://doi.org/10.1117/1.jrs.15.031501

Ramazani, M., Safari, H. O., & Shamanian, G. H. (2022). Integration of ASTER-based remote sensing with petrographic studies, XRD analysis, and field surveying as a multidisciplinary approach for prospecting Cu mineralization in the Taft-Dehshir region, Iran. *Journal of Applied Remote Sensing*, *16*(01). https://doi.org/10.1117/1.JRS.16.014508

Reath, K. A., & Ramsey, M. S. (2013). Exploration of geothermal systems using hyperspectral thermal infrared remote sensing. *Journal of Volcanology and Geothermal Research*, *265*, 27–38. https://doi.org/10.1016/j.jvolgeores.2013.08.007

Reyes, A. G. (1990). Petrology of Philippine geothermal systems and the application of alteration mineralogy to their assessment. *Journal of Volcanology and Geothermal Research*, *43*(1–4), 279–309. https://doi.org/10.1016/0377-0273(90)90057-M

Rodgers, K. A., Browne, P. R. L., Buddle, T. F., Cook, K. L., Greatrex, R. A., Hampton, W. A., Herdianita, N. R., Holland, G. R., Lynne, B. Y., Martin, R., Newton, Z., Pastars, D., Sannazarro, K. L., & Teece, C. I. A. (2004). Silica phases in sinters and residues from geothermal fields of New Zealand. *Earth-Science Reviews*, *66*(1–2), 1–61. https://doi.org/10.1016/j.earscirev.2003.10.001

Rodriguez-Gomez, C., Kereszturi, G., Reeves, R., Rae, A., Pullanagari, R., Jeyakumar, P., & Procter, J. (2021). Lithological mapping of Waiotapu Geothermal Field (New Zealand) using hyperspectral and thermal remote sensing and ground exploration techniques. *Geothermics*, *96*. https://doi.org/10.1016/j.geothermics.2021.102195

Rotem, A., Vidal, A., Pfaff, K., Tenorio, L., Chung, M., Tharalson, E., & Monecke, T. (2023). Interpretation of Hyperspectral Shortwave Infrared Core Scanning Data Using SEM-Based Automated Mineralogy: A Machine Learning Approach. *Geosciences*, *13*(7), 192. https://doi.org/10.3390/geosciences13070192

Rowan, L. C., & Wetlaufer, P. H. (1981). Relation between regional lineament systems and structural zones in Nevada. *AAPG Bulletin*, *65*(8), 1414–1432.

Roy, S., Bhattacharya, S., & Omkar, S. N. (2020). Alternating direction method-based endmember extraction for a distributed fraction cover mapping of mineralogy at Jahazpur, India. *Journal of Applied Remote Sensing*, *14*(04). https://doi.org/10.1117/1.jrs.14.044510

Salamba, K. E., Hawu Hede, A. N., & Nur Heriawan, M. (2019). Identification of alteration zones using a Landsat 8 image of densely vegetated areas of the Wayang Windu Geothermal field, West Java, Indonesia. *IOP Conference Series: Earth and Environmental Science*, *254*(1). https://doi.org/10.1088/1755-1315/254/1/012004

Savitri, K. P., Hecker, C., van der Meer, F. D., & Sidik, R. P. (2021). VNIR-SWIR infrared (imaging) spectroscopy for geothermal exploration: Current status and future directions. *Geothermics*, *96*, 102178. https://doi.org/10.1016/j.geothermics.2021.102178

Schmitt, R., & Gold, R. D. (2020). Quaternary Fault and Fold Database of the United States. *US Geological Survey Data Release*. https://www.usgs.gov/programs/earthquake-hazards/faults

Sekioka, M., & Yuhara, K. (1974). Heat flux estimation in geothermal areas based on the heat balance of the ground surface. *Journal of Geophysical Research*, *79*(14), 2053–2058. https://doi.org/10.1029/jb079i014p02053

Shang, K., Xiao, C., & Liang, S. (2020). Comparison of bare soil extraction methods in black soil zone for AHSI/GF-5 remote sensing data. *MIPPR 2019: Remote Sensing Image Processing, Geographic Information Systems, and Other Applications*, 142. https://doi.org/10.1117/12.2539360

Shirmard, H., Farahbakhsh, E., Müller, R. D., & Chandra, R. (2022). A review of machine learning in processing remote sensing data for mineral exploration. In *Remote Sensing of Environment* (Vol. 268). Elsevier Inc. https://doi.org/10.1016/j.rse.2021.112750

Sigurdsson, H., Houghton, B., McNutt, S., Rymer, H., & Stix, J. (2015). *The encyclopedia of volcanoes*. Elsevier.

Siler, D. L. (2023). Structural discontinuities and their control on hydrothermal systems in the Great Basin, USA. *Geoenergy*, *1*(1). https://doi.org/10.1144/geoenergy2023-009

Siler, D. L., Faulds, J. E., Hinz, N. H., & Queen, J. H. (2021). *Three-Dimensional Geologic Map of the Brady Geothermal Area, Nevada*. https://doi.org/https://doi.org/10.3133/sim3469

Sillitoe, R. H. (1993). Epithermal Models: Genetic Types, Geometric Controls and Shallow Features. In Mineral Deposit Modeling. *Geological Association of Canada, Special Paper*, *40*, 403–417.

Silvestri, M., Romaniello, V., Hook, S., Musacchio, M., Teggi, S., & Buongiorno, M. F. (2020). First comparisons of surface temperature estimations between ECOSTRESS, ASTER and Landsat 8 over Italian volcanic and geothermal areas. *Remote Sensing*, *12*(1). https://doi.org/10.3390/RS12010184

Simpson, M. P., & Rae, A. J. (2018). Short-wave infrared (SWIR) reflectance spectrometric characterisation of clays from geothermal systems of the Taupō Volcanic Zone, New Zealand. *Geothermics*, *73*, 74–90. https://doi.org/10.1016/j.geothermics.2018.01.006

Soydan, H., Koz, A., & Düzgün, H. Ş. (2021). Secondary Iron Mineral Detection via Hyperspectral Unmixing Analysis with Sentinel-2 Imagery. *International Journal of Applied Earth Observation and Geoinformation*, *101*. https://doi.org/10.1016/j.jag.2021.102343

Stober, I., & Bucher, K. (2021). *Geothermal Energy*. Springer International Publishing. https://doi.org/10.1007/978-3-030-71685-1

Street, J. O., Carroll, R. J., & Ruppert, D. (1988). A note on computing robust regression estimates via iteratively reweighted least squares. *The American Statistician*, *42*(2), 152–154.

Sun, Y., Tian, S., & Di, B. (2017). Extracting mineral alteration information using WorldView-3 data. *Geoscience Frontiers*, *8*(5), 1051–1062. https://doi.org/10.1016/j.gsf.2016.10.008

Taussi, M., Nisi, B., Brogi, A., Liotta, D., Zucchi, M., Venturi, S., Cabassi, J., Boschi, G., Ciliberti, M., & Vaselli, O. (2023). Deep Regional Fluid Pathways in an Extensional Setting: The Role of Transfer Zones in the Hot and Cold Degassing Areas of the Larderello Geothermal System (Northern

Apennines, Italy). *Geochemistry, Geophysics, Geosystems*, *24*(6). https://doi.org/10.1029/2022GC010838

Thomas, M., & Walter, M. R. (2002). Application of Hyperspectral Infrared Analysis of Hydrothermal Alteration on Earth and Mars. *Astrobiology*, *2*(3), 335–351. https://doi.org/10.1089/153110702762027916

Thompson, A. J. B., Hauff, P. L., & Robitaille, A. J. (1999). Alteration Mapping in Exploration: Application of Short-Wave Infrared (SWIR) Spectroscopy. *SEG Discovery*, *39*, 1–27. https://doi.org/10.5382/SEGnews.1999-39.fea

Trainor-Guitton, W., Siler, D., & Ayling, B. (2023). Temperature uncertainty modelling with proxy structural data as geostatistical constraints for well siting: an example applied to Granite Springs Valley, NV, USA. *Geoenergy*, *1*(1). https://doi.org/10.1144/geoenergy2023-010

Troccoli, A. (2009). *Management of weather and climate risk in the energy industry*. Springer.

van der Meer, F., Hecker, C., van Ruitenbeek, F., van der Werff, H., de Wijkerslooth, C., & Wechsler, C. (2014). Geologic remote sensing for geothermal exploration: A review. *International Journal of Applied Earth Observation and Geoinformation*, *33*(1), 255–269. https://doi.org/10.1016/j.jag.2014.05.007

van der Meer, F., van der Werff, H. M. A., & van Ruitenbeek, F. J. A. (2014). Potential of ESA's Sentinel-2 for geological applications. *Remote Sensing of Environment*, *148*, 124–133. https://doi.org/10.1016/j.rse.2014.03.022

Vaughan, R. G., Hook, S. J., Calvin, W. M., & Taranik, J. V. (2005). Surface mineral mapping at Steamboat Springs, Nevada, USA, with multi-wavelength thermal infrared images. *Remote Sensing of Environment*, *99*(1–2), 140–158. https://doi.org/10.1016/j.rse.2005.04.030

Vidal, J., Patrier, P., Genter, A., Beaufort, D., Dezayes, C., Glaas, C., Lerouge, C., & Sanjuan, B. (2018). Clay minerals related to the circulation of geothermal fluids in boreholes at Rittershoffen (Alsace, France). *Journal of Volcanology and Geothermal Research*, *349*, 192–204. https://doi.org/10.1016/j.jvolgeores.2017.10.019

Villeneuve, M., Kennedy, B., Gravley, D., Mordensky, S., Heap, M. J., Siratovich, P., Wyering, L., & Cant, J. (2019). Characteristics of altered volcanic rocks in geothermal reservoirs. *ISRM Congress*, ISRM-14CONGRESS.

Wackerly, D. D., Mendenhall, W., & Scheaffer, R. L. (2008). *Mathematical statistics with applications* (Vol. 7). Thomson Brooks/Cole Belmont, CA.

Wall, A. M., Dobson, P. F., & Thomas, H. (2017). Geothermal Costs of Capital: Relating Market Valuation to Project Risk and Technology. *GRC Transactions*, *41*.

Wang, F., Hu, Y., Wang, S., & Li, X. (2017). Local indicator of colocation quotient with a statistical significance test: examining spatial association of crime and facilities. *The Professional Geographer*, *69*(1), 22–31.

Wang, M., Huang, Z., Zhang, X., Zhang, Y., & Chen, M. (2021). Altered mineral mapping based on ground-airborne hyperspectral data and wavelet spectral angle mapper tri-training model: Case studies from Dehua-Youxi-Yongtai Ore District, Central Fujian, China. *International Journal of Applied Earth Observation and Geoinformation*, *102*. https://doi.org/10.1016/j.jag.2021.102409

White, N. C., & Hedenquist, J. W. (1995). Epithermal Gold Deposits: STYLES, CHARACTERISTICS AND EXPLORATION. *SEG Discovery*, *23*, 1–13. https://doi.org/10.5382/SEGnews.1995-23.fea

Whitmarsh, R. (1998). *Geologic Map of the Coso Range*. https://doi.org/10.1130/1998-whitmarsh-coso

Witter, J. B., Trainor-Guitton, W. J., & Siler, D. L. (2019). Uncertainty and risk evaluation during the exploration stage of geothermal development: A review. *Geothermics*, *78*, 233–242. https://doi.org/10.1016/j.geothermics.2018.12.011

Wolfe, J. D., & Black, S. R. (2018). *Hyperspectral Analytics in ENVI*.

Wright, P. M., Ward, S. H., Ross, H. P., & West, R. C. (1985). State-of-the-art geophysical exploration for geothermal resources. *Geophysics*, *50*(12), 2666–2699. https://doi.org/10.1190/1.1441889

Zehner, R. E., Tullar, K. N., & Rutledge, E. (2012). Effectiveness of 2-meter and geoprobe shallow temperature surveys in early stage geothermal exploration. *Geothermal Resources Council Transactions*, *36*, 835–841.

Zimmerman, J., Blake, K., Nale, S., Sabin, A., & Huang, W.-C. (2023). Evaluation of 2-Meter Temperature Surveys from the Coso Geothermal Field, CA. *GRC Transactions*, *47*.

APPENDIX A PHOTOS OF THE COSO SAMPLES

The following table organizes the photos of the samples collected from CGF.

Table A-1 Photos of the Coso samples.

Sample ID	Photos	
Coso-001		
Coso-002		
Coso-003		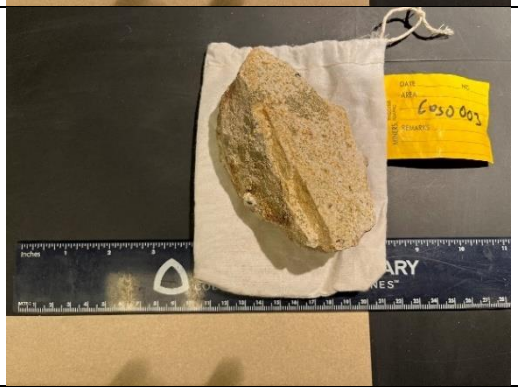

Sample ID	Photos
Coso-004	 
Coso-005	 
Coso-006	 
Coso-007	 

Sample ID	Photos	
Coso-008		
Coso-009		
Coso-010	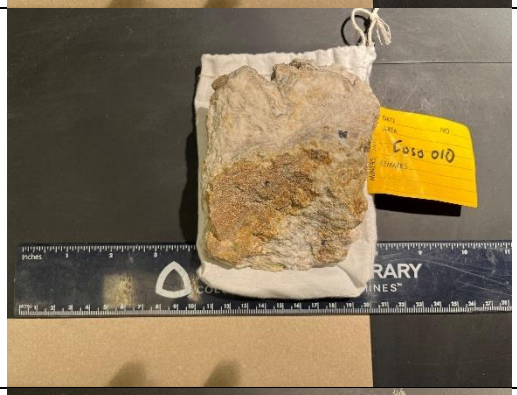	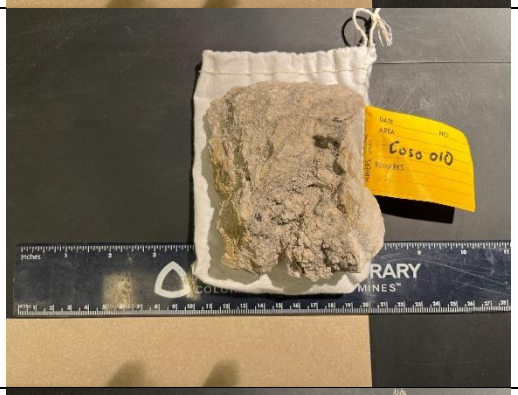
Coso-011		

Sample ID	Photos
Coso-012	 
Coso-013	 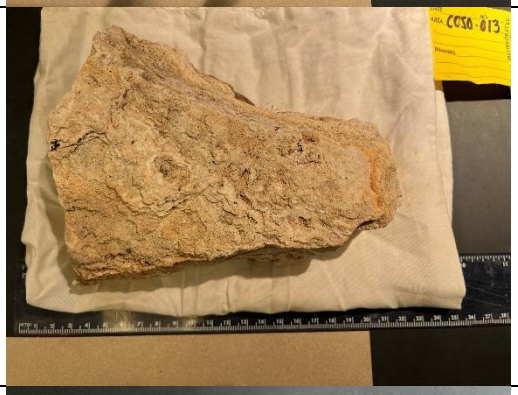
Coso-014	 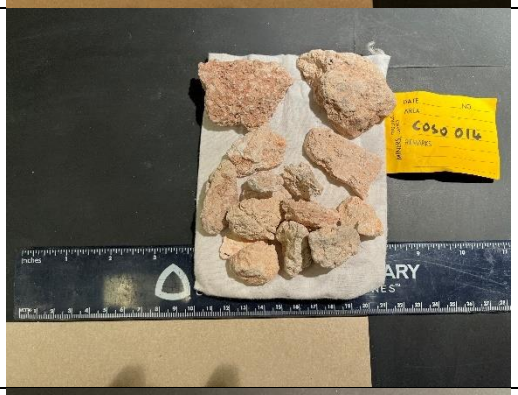
Coso-015	 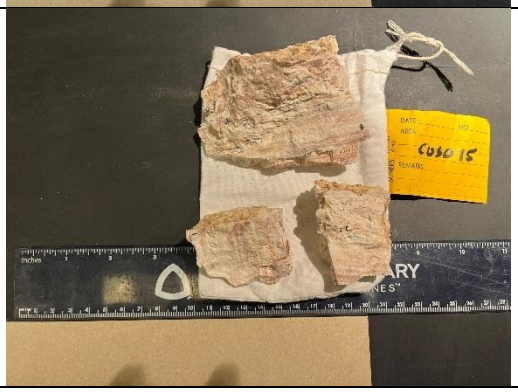

Sample ID	Photos
Coso-018	 
Coso-019	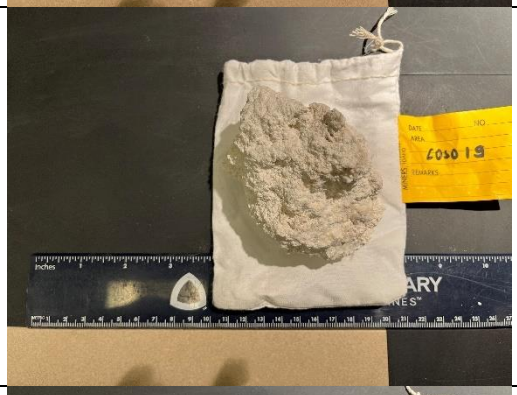 
Coso-020	 
Coso-021	 

Sample ID	Photos	
Coso-022	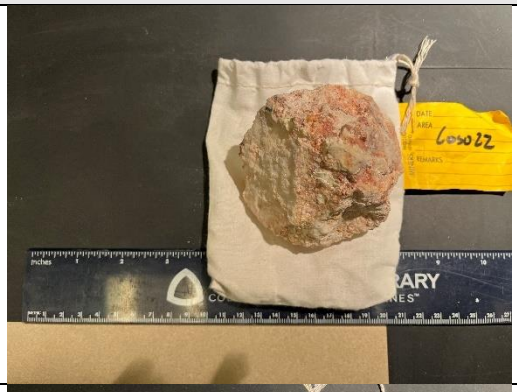	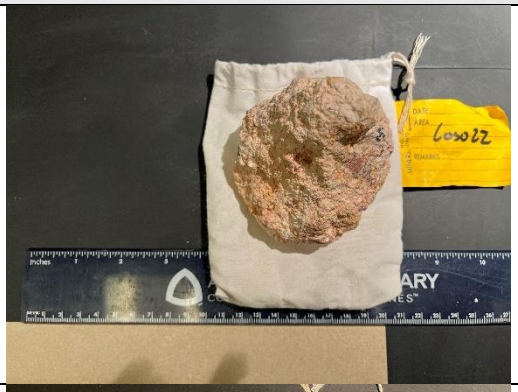
Coso-023		
Coso-024		
Coso-026	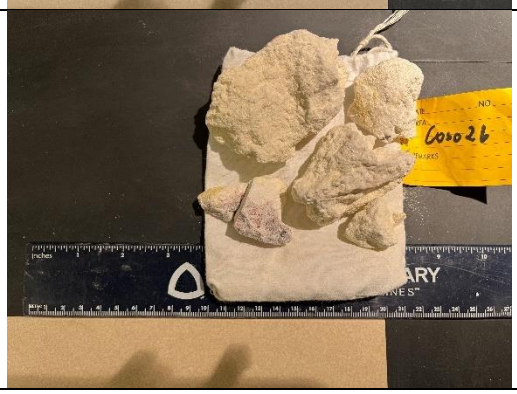	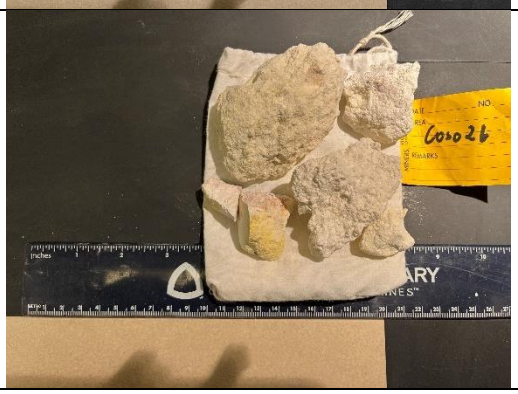

Sample ID	Photos	
Coso-027		
Coso-028		
Coso-029		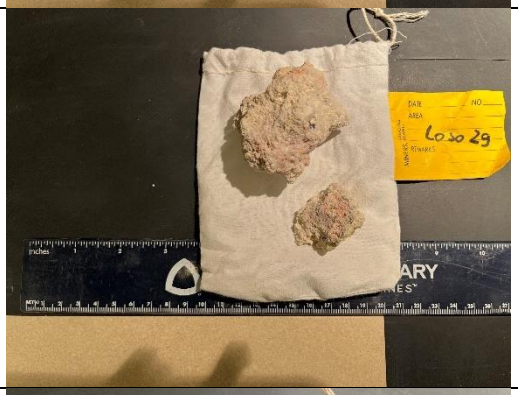
Coso-030		

Sample ID	Photos	
Coso-031		
Coso-032	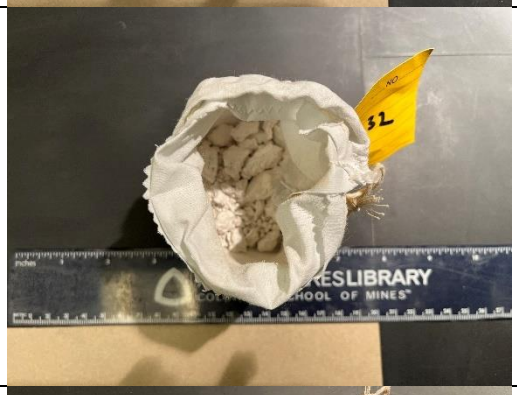	
Coso-033		
Coso-034	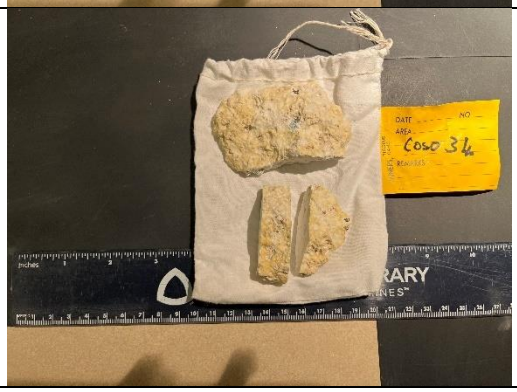	

Sample ID	Photos	
Coso-035	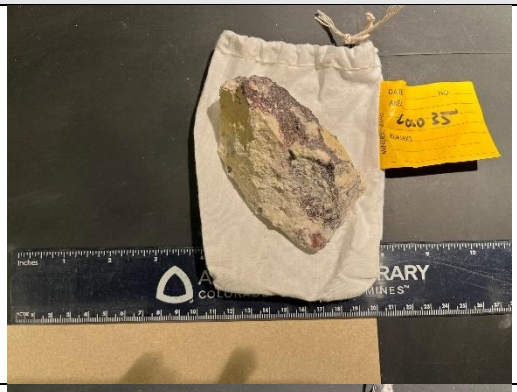	
Coso-036		
Coso-037		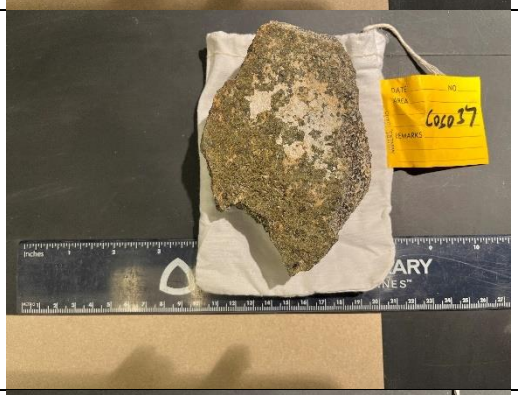
Coso-038		

Sample ID	Photos	
Coso-039		
Coso-040	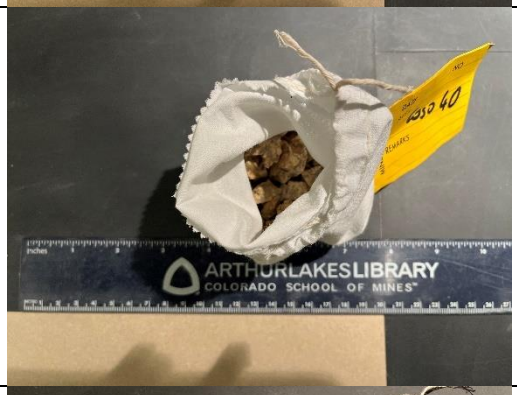	
Coso-041		
Coso-042		

Sample ID	Photos
Coso-051	 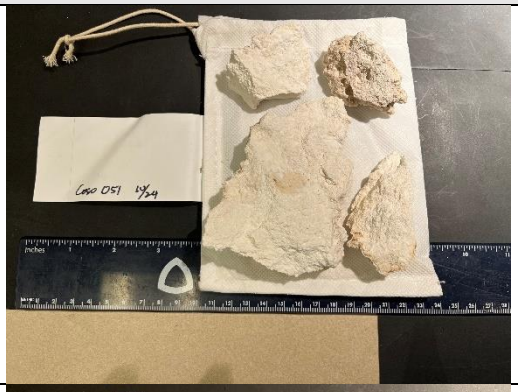
Coso-052	 
Coso-053	 
Coso-054	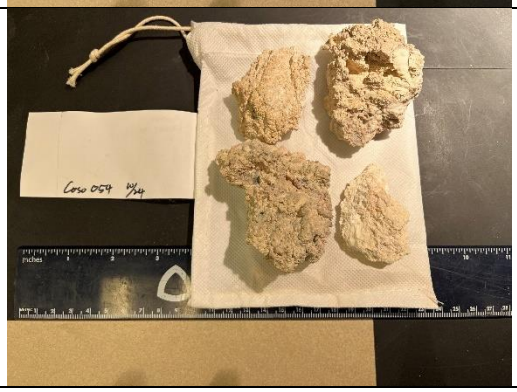 

Sample ID	Photos
Coso-055	 
Coso-056	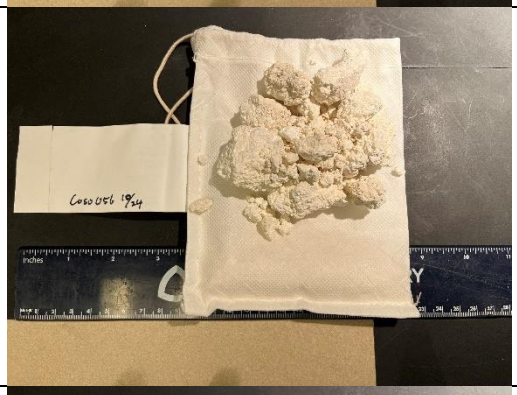 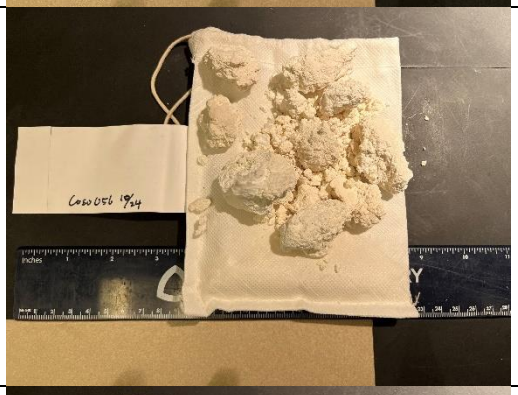
Coso-057	 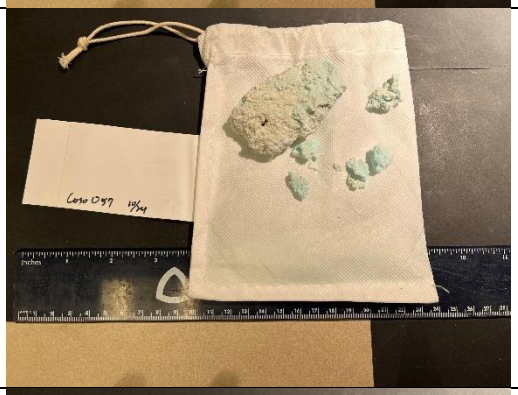
Coso-058	 

Sample ID	Photos
Coso-059	 
Coso-060	 
Coso-061	 
Coso-062	 

Sample ID	Photos
Coso-063	 
Coso-064	 
Coso-065	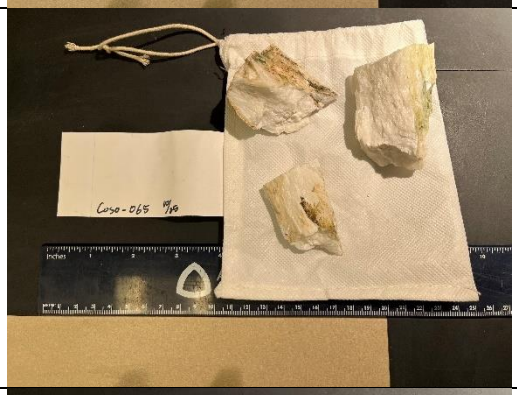 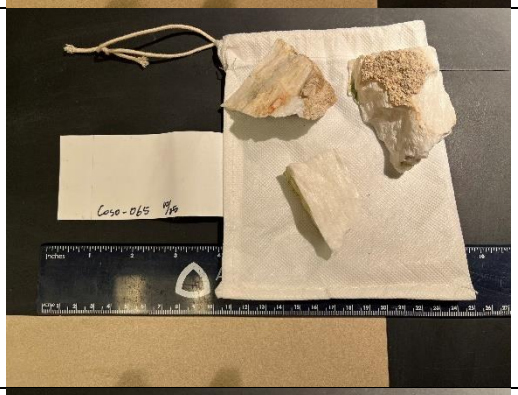
Coso-066	 

Sample ID	Photos	
Coso-067	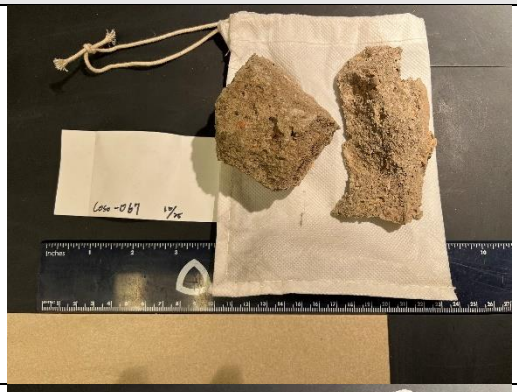	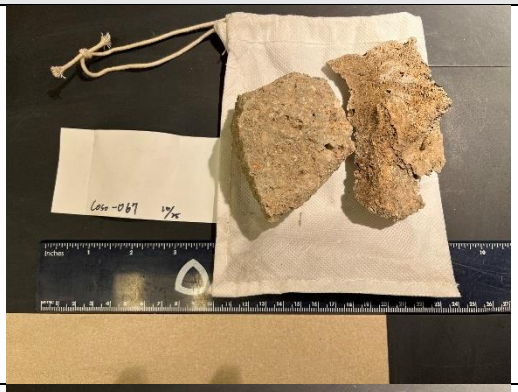
Coso-068		
Coso-069	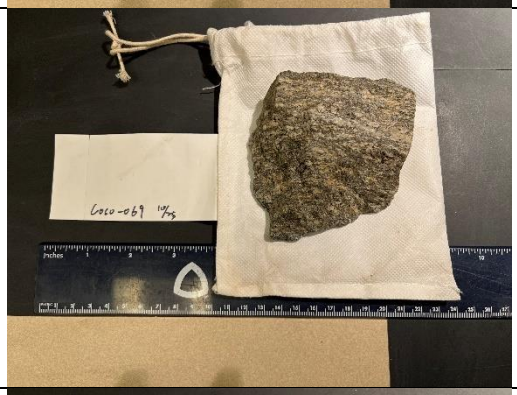	
Coso-070		

Sample ID	Photos
Coso-071	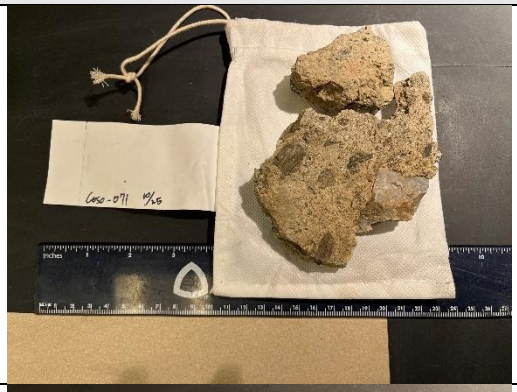 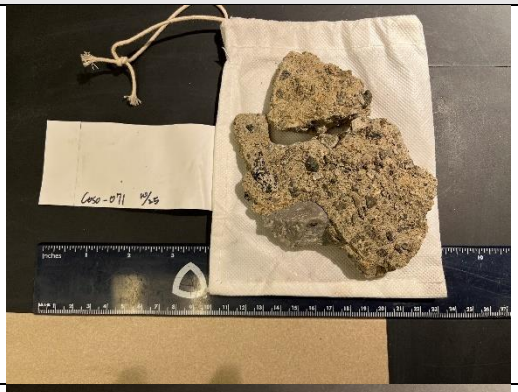
Coso-072	 
Coso-075	 
Coso-076	 

Sample ID	Photos	
Coso-077	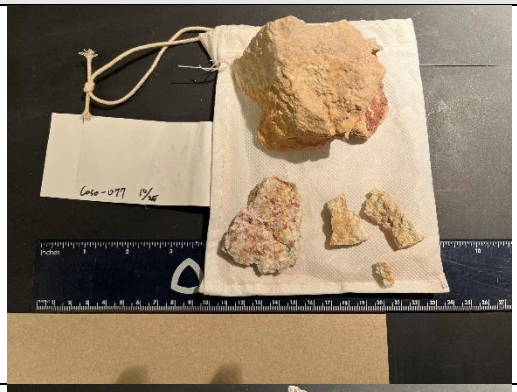	
Coso-078		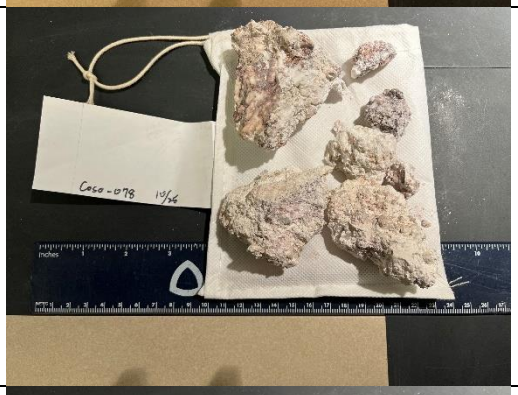
Coso-079		
Coso-080	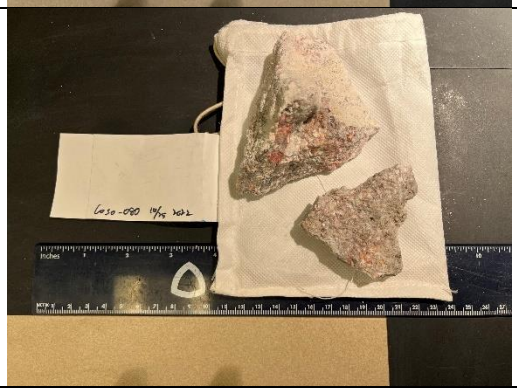	

Sample ID	Photos
Coso-081	 
Coso-087	 
Coso-088	 
Coso-089	 

Sample ID	Photos
Coso-090	 
Coso-091	 
Coso-092	 
Coso-093	 

Sample ID	Photos	
Coso-094		
Coso-095		
Coso-096		
Coso-097		

Sample ID	Photos
Coso-098	 
Coso-099	 
Coso-100	 
Coso-101	 

Sample ID	Photos
Coso-102	 
Coso-103	 
Coso-104	 
Coso-105	 

Sample ID	Photos
Coso-106	 
Coso-107	 

APPENDIX B MINERALOGICAL ASSESSMENT OF COSO SAMPLES

The table denotes the techniques being applied and considered in the mineralogical assessment to identify the spectra of MOI. The mineralogy in the table illustrates the identified MOI and the MOI spectra.

Table B-1 Mineralogical assessment of Coso samples.

ID	Description	Longitude	Latitude	P.P.†	A.M.†	pXRF	H.S.†	Mineralogy‡
Coso001	alteration coverage	117° 46' 23.548" W	36° 0' 51.822" N	O		O	O	
Coso002	alteration coverage	117° 46' 23.440" W	36° 0' 51.786" N	O		O	O	opl.
Coso003	in-situ rock/outcrop	117° 46' 23.152" W	36° 0' 51.678" N	O		O	O	cdy., hem., kln.
Coso004	in-situ rock/outcrop	117° 46' 21.784" W	36° 0' 51.102" N	O		O	O	kln., opl.
Coso005	in-situ rock/outcrop	117° 46' 25.276" W	36° 0' 51.966" N	O			O	
Coso006	travertine /sinter	117° 45' 53.884" W	36° 0' 32.058" N	O		O	O	
Coso007	travertine /sinter	117° 45' 53.056" W	36° 0' 34.038" N	O		O	O	
Coso008	travertine /sinter	117° 45' 51.436" W	36° 0' 32.922" N	O		O	O	hem.
Coso009	travertine /sinter	117° 46' 11.308" W	36° 1' 21.018" N	O		O	O	hem., kln.
Coso010	travertine /sinter	117° 46' 10.012" W	36° 1' 24.906" N	O		O	O	
Coso011	travertine /sinter	117° 46' 10.012" W	36° 1' 24.906" N	O		O	O	
Coso012	travertine /sinter	117° 46' 9.508" W	36° 1' 25.698" N	O	O	O	O	cdy., hem., kln., **opl.**
Coso013	travertine /sinter	117° 46' 9.508" W	36° 1' 25.698" N	O		O	O	cdy., kln., opl.
Coso014	travertine /sinter	117° 46' 8.536" W	36° 1' 26.130" N	O		O	O	hem., kln.
Coso015	travertine /sinter	117° 46' 8.788" W	36° 1' 21.090" N	O		O	O	**cdy.**, hem., kln., **opl.**
Coso018	in-situ rock/outcrop	117° 47' 33.460" W	36° 2' 24.918" N	O	O	O	O	alu., kln., opl.
Coso019	alteration coverage	117° 47' 33.280" W	36° 2' 24.882" N	O		O	O	**alu.**, opl.
Coso020	obsidian	117° 47' 34.216" W	36° 2' 25.170" N	O			O	kln.
Coso021	alteration coverage	117° 47' 34.288" W	36° 2' 25.422" N	O		O	O	cdy., kln.
Coso022	alteration coverage	117° 47' 26.944" W	36° 2' 26.754" N	O		O	O	kln.
Coso023	alteration coverage	117° 47' 26.944" W	36° 2' 26.754" N	O	O		O	alu., kln., opl.
Coso024	alteration coverage	117° 47' 26.944" W	36° 2' 26.754" N	O		O	O	cdy., opl.
Coso026	alteration coverage	117° 48' 0.712" W	36° 2' 13.614" N	O	O	O	O	alu., kln., opl.

ID	Description	Longitude	Latitude	P.P.†	A.M.†	pXRF	H.S.†	Mineralogy‡
Coso027	alteration coverage	117° 48' 0.496" W	36° 2' 13.182" N	O	O	O	O	alu., cdy., hem., kln.
Coso028	in-situ rock/outcrop	117° 48' 0.280" W	36° 2' 12.642" N	O	O	O	O	alu., opl.
Coso029	alteration coverage	117° 48' 0.640" W	36° 2' 12.462" N	O	O	O	O	alu., kln., **opl.**
Coso030	alteration coverage	117° 48' 0.280" W	36° 2' 11.490" N	O			O	alu., cdy., hem., kln.
Coso031	alteration coverage	117° 48' 0.280" W	36° 2' 11.490" N	O	O	O	O	alu., cdy., kln., opl.
Coso032	alteration coverage	117° 48' 2.800" W	36° 2' 10.518" N	O	O	O	O	alu., **kln.**
Coso033	alteration coverage	117° 48' 2.476" W	36° 2' 9.042" N	O		O	O	**alu.**, opl.
Coso034	alteration coverage	117° 48' 2.368" W	36° 2' 8.790" N	O	O	O	O	**alu.**, kln., opl.
Coso035	in-situ rock/outcrop	117° 48' 2.260" W	36° 2' 8.574" N	O		O	O	alu., cdy., kln., opl.
Coso036	in-situ rock/outcrop	117° 47' 32.164" W	36° 4' 0.318" N	O			O	
Coso037	in-situ rock/outcrop	117° 47' 32.164" W	36° 4' 0.318" N	O			O	**epd.**
Coso038	in-situ rock/outcrop	117° 47' 32.164" W	36° 4' 0.318" N	O			O	epd.
Coso039	in-situ rock/outcrop	117° 47' 32.164" W	36° 4' 0.318" N	O	O	O	O	**epd.**, kln.
Coso040	in-situ rock/outcrop	117° 47' 35.476" W	36° 4' 3.666" N	O		O	O	kln.
Coso041	alteration coverage	117° 52' 53.032" W	36° 5' 41.298" N	O		O	O	cdy., opl.
Coso042	alteration coverage	117° 52' 53.032" W	36° 5' 41.298" N	O	O		O	**cdy**., kln., opl.
Coso051	alteration coverage	117° 48' 2.801" W	36° 2' 10.223" N	O		O	O	alu., cdy., kln., opl.
Coso052	alteration coverage	117° 48' 3.053" W	36° 2' 9.755" N	O		O	O	hem., kln.
Coso053	alteration coverage	117° 48' 1.343" W	36° 2' 8.707" N	O		O	O	alu., cdy., hem.
Coso054	alteration coverage	117° 48' 1.357" W	36° 2' 8.675" N	O		O	O	alu., **cdy.**, hem., kln., opl.
Coso055	alteration coverage	117° 48' 1.699" W	36° 2' 14.568" N	O		O	O	alu., cdy., hem.
Coso056	alteration coverage	117° 48' 0.781" W	36° 2' 13.524" N	O		O	O	alu., kln., opl.
Coso057	alteration coverage	117° 47' 58.200" W	36° 2' 8.999" N	O		O	O	
Coso058	alteration coverage	117° 47' 58.369" W	36° 2' 9.024" N	O		O	O	alu., cdy., opl.
Coso059	alteration coverage	117° 47' 58.956" W	36° 2' 9.823" N	O		O	O	alu., **cdy., opl.**
Coso060	alteration coverage	117° 48' 1.019" W	36° 2' 10.230" N	O		O	O	**cdy.**
Coso061	alteration coverage	117° 47' 58.758" W	36° 2' 2.339" N	O		O	O	alu., hem., kln.
Coso062	alteration coverage	117° 48' 1.217" W	36° 2' 1.777" N	O		O	O	alu., cdy., hem., kln.

ID	Description	Longitude	Latitude	P.P.†	A.M.†	pXRF	H.S.†	Mineralogy‡
Coso063	alteration coverage	117° 48' 0.378" W	36° 2' 1.079" N	O		O	O	alu., hem., kln., **opl.**
Coso064	in-situ rock/outcrop	117° 48' 4.543" W	36° 1' 46.038" N	O			O	hem.
Coso065	travertine /sinter	117° 45' 56.221" W	36° 0' 20.970" N	O		O	O	hem., opl.
Coso066	travertine /sinter	117° 45' 56.113" W	36° 0' 21.053" N	O		O	O	hem., opl.
Coso067	in-situ rock/outcrop	117° 45' 54.936" W	36° 0' 20.520" N	O			O	
Coso068	in-situ rock/outcrop	117° 45' 57.258" W	36° 0' 19.771" N	O			O	
Coso069	in-situ rock/outcrop	117° 45' 57.269" W	36° 0' 19.739" N	O			O	
Coso070	in-situ rock/outcrop	117° 45' 57.175" W	36° 0' 19.793" N	O			O	hem.
Coso071	in-situ rock/outcrop	117° 45' 56.747" W	36° 0' 19.944" N	O			O	
Coso072	travertine /sinter	117° 45' 56.221" W	36° 0' 19.602" N	O		O	O	opl.
Coso075	in-situ rock/outcrop	117° 47' 24.583" W	36° 2' 26.351" N	O		O	O	cdy., hem.
Coso076	alteration coverage	117° 47' 22.063" W	36° 2' 28.014" N	O		O	O	alu., cdy., hem., kln., opl.
Coso077	alteration coverage	117° 47' 22.139" W	36° 2' 28.097" N	O		O	O	alu., hem., kln.
Coso078	alteration coverage	117° 47' 21.761" W	36° 2' 28.115" N	O		O	O	cdy., hem., kln., opl.
Coso079	alteration coverage	117° 47' 30.383" W	36° 2' 21.894" N	O		O	O	alu., cdy., hem., kln., opl.
Coso080	alteration coverage	117° 47' 30.437" W	36° 2' 21.930" N	O		O	O	alu., cdy., kln., opl.
Coso081	in-situ rock/outcrop	117° 47' 30.336" W	36° 2' 22.049" N	O		O	O	hem., kln.
Coso087	in-situ rock/outcrop	117° 52' 56.784" W	35° 59' 35.592" N	O			O	**hem.**
Coso088	in-situ rock/outcrop	117° 52' 56.795" W	35° 59' 35.657" N	O			O	
Coso089	alteration coverage	117° 46' 45.001" W	36° 1' 39.061" N	O		O	O	
Coso090	in-situ rock/outcrop	117° 46' 45.059" W	36° 1' 39.144" N	O		O	O	cdy., hem.
Coso091	in-situ rock/outcrop	117° 46' 45.005" W	36° 1' 39.191" N	O		O	O	**cdy.**, hem.
Coso092	in-situ rock/outcrop	117° 46' 44.904" W	36° 1' 39.288" N	O		O	O	cdy., hem., opl.
Coso093	in-situ rock/outcrop	117° 46' 44.785" W	36° 1' 38.658" N	O		O	O	hem., kln.
Coso094	in-situ rock/outcrop	117° 46' 44.652" W	36° 1' 38.615" N	O		O	O	
Coso095	in-situ rock/outcrop	117° 46' 44.461" W	36° 1' 38.395" N	O		O	O	hem.
Coso096	in-situ rock/outcrop	117° 46' 44.155" W	36° 1' 38.089" N	O			O	**cdy.**
Coso097	in-situ rock/outcrop	117° 46' 40.699" W	36° 1' 34.439" N	O			O	

ID	Description	Longitude	Latitude	P.P.†	A.M.†	pXRF	H.S.†	Mineralogy‡
Coso098	in-situ rock/outcrop	117° 46' 8.040" W	36° 1' 40.793" N	O		O	O	hem.
Coso099	in-situ rock/outcrop	117° 46' 7.122" W	36° 1' 42.683" N	O		O	O	hem.
Coso100	in-situ rock/outcrop	117° 46' 7.032" W	36° 1' 42.719" N	O		O	O	
Coso101	in-situ rock/outcrop	117° 46' 6.755" W	36° 1' 42.906" N	O		O	O	cdy., hem.
Coso102	in-situ rock/outcrop	117° 45' 58.651" W	36° 1' 47.291" N	O		O	O	kln.
Coso103	in-situ rock/outcrop	117° 45' 58.583" W	36° 1' 47.215" N	O			O	kln.
Coso104	in-situ rock/outcrop	117° 49' 21.461" W	36° 1' 49.721" N	O		O	O	hem.
Coso105	in-situ rock/outcrop	117° 49' 21.486" W	36° 1' 49.782" N	O		O	O	
Coso106	in-situ rock/outcrop	117° 48' 58.068" W	36° 1' 38.586" N	O			O	
Coso107	in-situ rock/outcrop	117° 48' 54.666" W	36° 1' 33.204" N	O		O	O	cdy., opl.

†:P.P.: physical property review; A.M.: Automated mineralogy analysis; H.S.: hyperspectral analysis
O: the applied and considered techniques for the mineralogical assessment.
‡:The occurrence of MOI. Bold font in mineralogy refers to the spectra that strongly associated with MOI.

APPENDIX C HISTOGRAMS AND CDF OF RELATIONS BETWEEN SGP

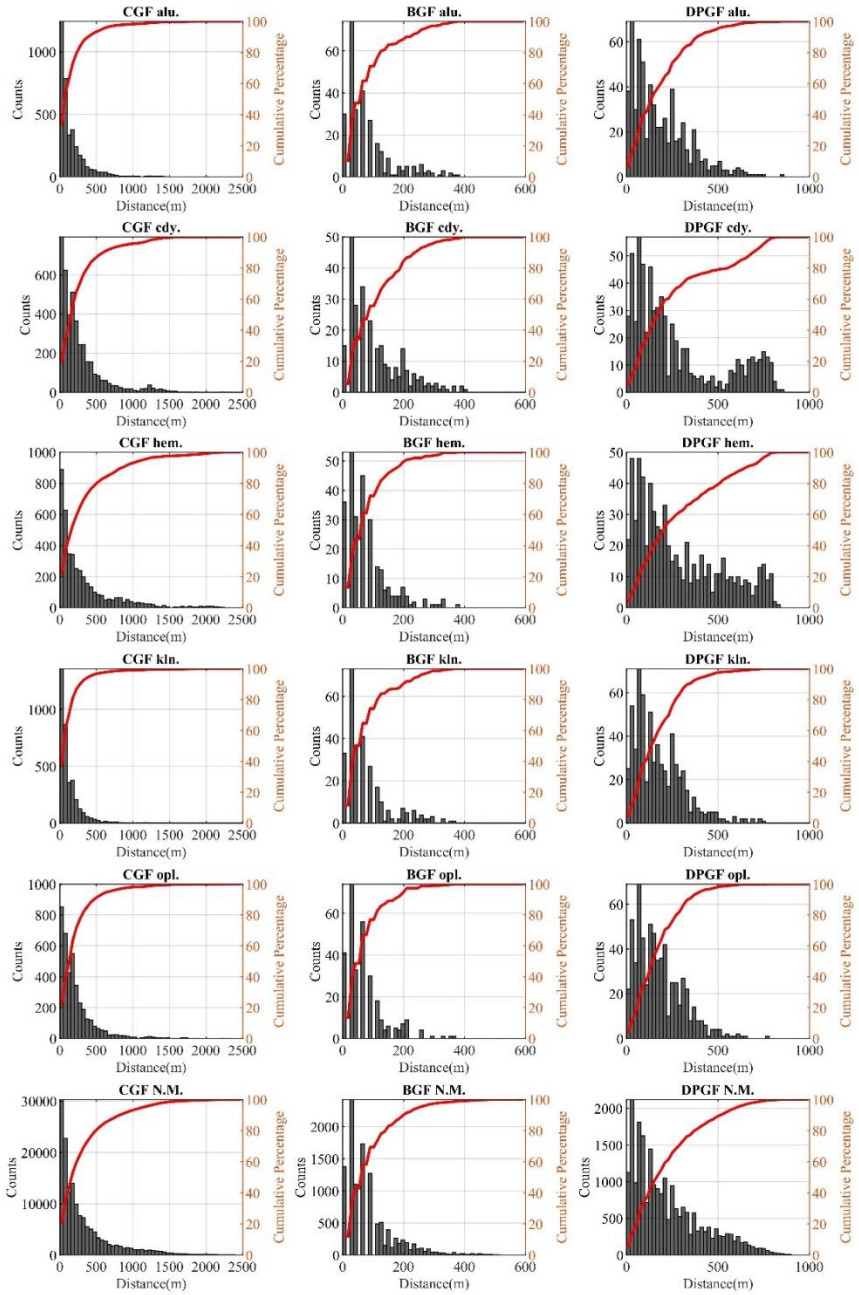

Figure C.1 Histograms and CDF plots of Two-Class Mineral Maps versus Fault Distance Maps.

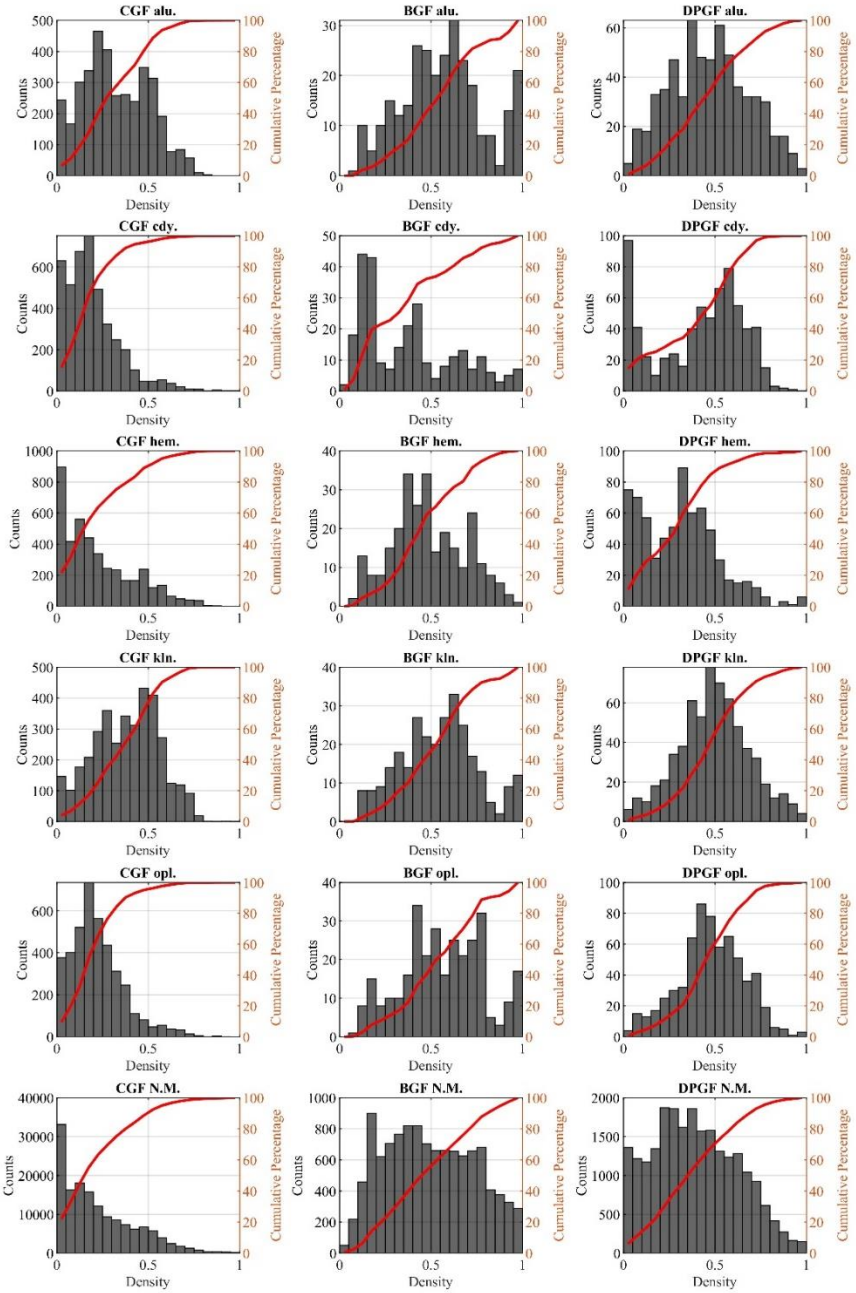

Figure C.2 Histograms and CDF plots of Two-Class Mineral Maps versus Fault Density Maps.

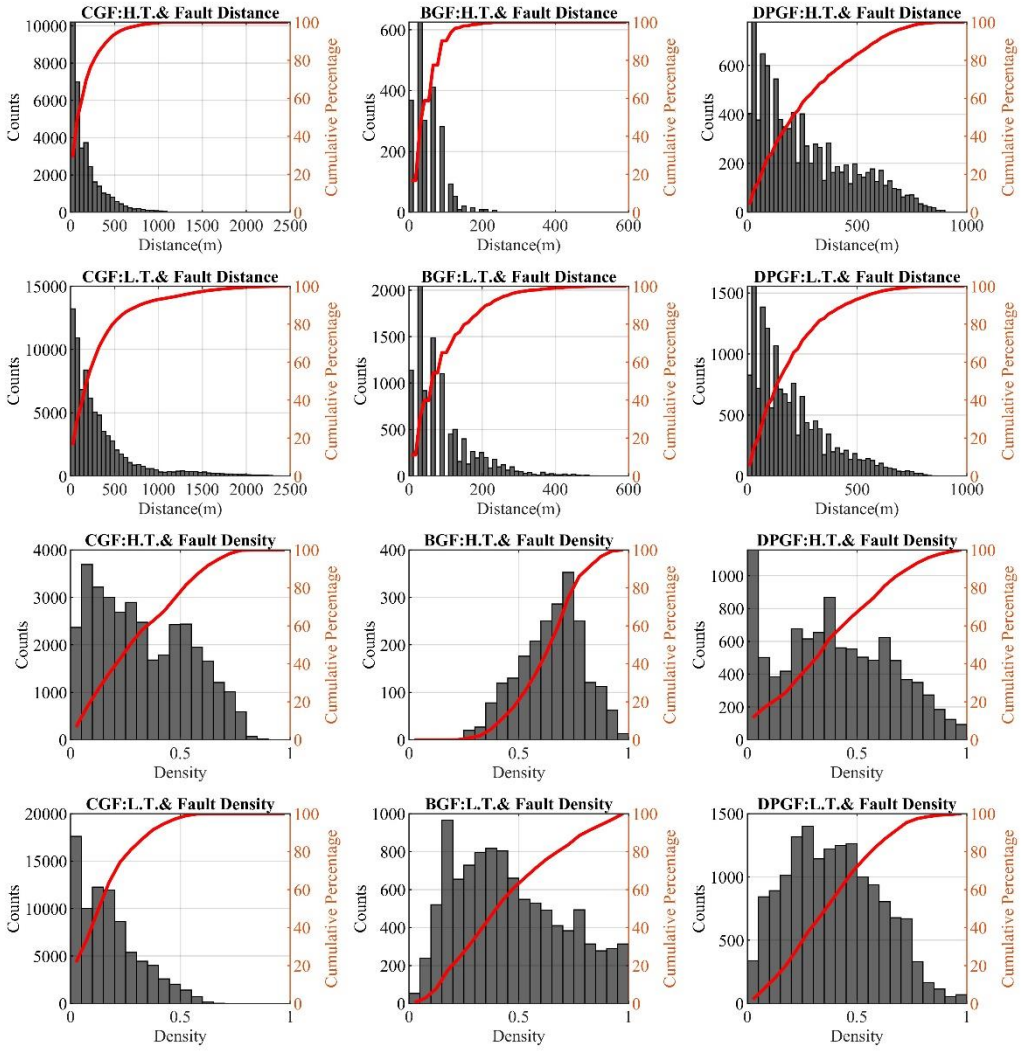

Figure 8C.3 Histograms and CDF plots of Two-class Temperature Maps versus fault datasets. The top two rows correspond to Fault Distance Maps, while the bottom two rows correspond to Fault Density Maps.

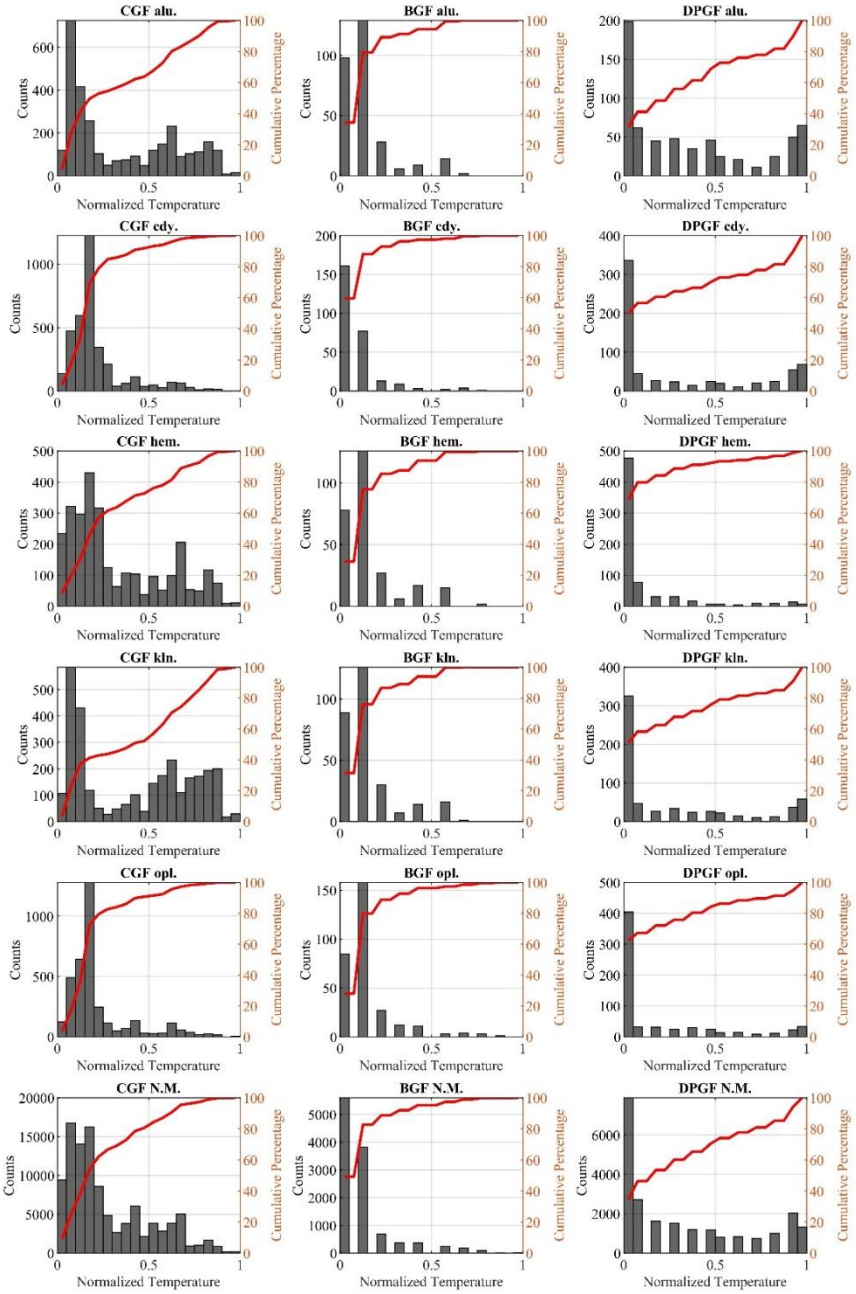

Figure C.4 Histograms and CDF plots of Two-Class Mineral Maps versus Multiclass Temperature Map.

APPENDIX D SUPPLEMENTARY DATA OF LINEAR REGRESSIONS BETWEEN SGP

Table D-1 The p-values of the coefficients and intercepts from the linear regression models of Fault Density Maps fit by Mineral Density Maps.

SGP(x)	CGF		BGF		DPGF	
	intercepts	coefficient	intercepts	coefficient	intercepts	coefficient
alu.	0	0	0	0	0	0
cdy.	0	0	0	0	0	0
hem.	0	0.016	0	0	0	0
kln.	0	0	0	0	0	0
opl.	0	0.002	0	0	0	0

Table D-2 The p-values of the coefficients and intercepts from the linear regression models of Multiclass Temperature Maps fit by Fault Density Map and Mineral Density Maps.

SGP(x)	CGF		BGF		DPGF	
	intercepts	coefficient	intercepts	coefficient	intercepts	coefficient
fault	0	0	0	0	0	0
alu.	0	0	0	0	0	0
cdy.	0	0	0	0	0	0
hem.	0	0	0	0	0	0
kln.	0	0	0	0	0	0
opl.	0	0	0	0	0	0

Table D-3 The AIC values from the regression models of Fault Density Maps fit by Mineral Density Maps.

SGP(x)	CGF		BGF		DPGF	
	AIC	AICc	AIC	AICc	AIC	AICc
alu.	-75864.24	-75864.24	-1350.57	-1350.57	-14077.88	-14077.88
cdy.	-68565.36	-68565.36	-2061.95	-2061.95	-3255.16	-3255.16
hem.	-67546.40	-67546.40	-293.92	-293.91	-7445.66	-7445.66
kln.	-85868.76	-85868.76	-865.22	-865.22	-11594.11	-11594.11
opl.	-67549.81	-67549.81	-6719.54	-6719.54	-5358.50	-5358.50

AIC: raw AIC value; AICc: sample-size corrected AIC value.

Table D-4 The AIC values from the regression models of Multiclass Temperature Maps fit by Fault Density Map and Mineral Density Maps

SGP(x)	CGF		BGF		DPGF	
	AIC	AICc	AIC	AICc	AIC	AICc
fault	-45703.49	-45703.49	-11924.15	-11924.15	18919.78	18919.78
alu.	-27178.15	-27178.14	-10443.43	-10443.43	18931.60	18931.60
cdy.	-19426.82	-19426.82	-10141.86	-10141.86	18763.45	18763.45
hem.	-29570.74	-29570.74	-11540.32	-11540.32	18678.96	18678.96
kln.	-35881.08	-35881.08	-10223.28	-10223.28	17634.41	17634.41
opl.	-18393.71	-18393.71	-11495.43	-11495.43	16678.97	16678.97

AIC: raw AIC value; AICc: sample-size corrected AIC value.

APPENDIX E PERMISSION

Permission to include previously published materials in this dissertation is listed below.

Copyright permission from MDPI, the publisher of Remote Sensing, is not required for the material incorporated into Chapter Two. According to MDPI's open access policy, "No special permission is required to reuse all or part of an article published by MDPI, including figures and tables", "Everyone has free and unlimited access to the full-text of all articles published in MDPI journals", and "Everyone is free to re-use the published material if proper accreditation/citation of the original publication is given" (https://www.mdpi.com/openaccess). Accordingly, the content in Chapter Two included part of materials from the article cited below:

Cavur, M., Yu, Y.T., Demir, E. and Duzgun, S. 2024. Mapping Geothermal Indicator Minerals Using Fusion of Target Detection Algorithms. Remote Sensing, 16, https://doi.org/10.3390/rs16071223.

APPENDIX F ARTICLE ON MINERAL MAPPING WITH VARIOUS METHODOLOGIES

Modified from an article published in Remote Sensing[1].

Mahmut Cavur[2,3], Yu-Ting Yu[3], Ebubekir Demir[3], Sebnem Duzgun[3]

The article entitled “Mapping Geothermal Indicator Minerals Using Fusion of Target Detection Algorithms” was published in “Remote Sensing”. The paper included the methodology of mineral mapping and accuracy assessment, which aimed to explore the influence of various mapping algorithms and fusion combinations. (https://doi.org/10.3390/rs16071223)

F.1 Abstract

Mineral mapping from satellite images provides valuable insights into subsurface mineral alteration for geothermal exploration. In previous studies, eight fundamental algorithms were used for mineral mapping utilizing USGS spectra, a collection of reflectance spectra containing samples of minerals, rocks, and soils created by the USGS. We used an ASD FieldSpec 4 Hi-RES NG portable spectrometer to collect spectra for analyzing ASTER images of the Coso Geothermal Field. Then, we established the ground-truth information and the spectral library by analyzing 97 samples. Samples collected from the field were analyzed using the CSIRO TSG (The Spectral Geologist of the Commonwealth Scientific and Industrial Research Organization). Based on the mineralogy study, multiple high-purity spectra of geothermal alteration minerals were selected from collected data, including alunite, chalcedony, hematite, kaolinite, and opal. Eight mineral spectral target detection algorithms were applied to the preprocessed satellite data with a proposed local spectral library. We measured the highest overall accuracy of 87% for alunite, 95% for opal, 83% for chalcedony, 60% for hematite, and 96% for kaolinite out of these eight algorithms. Three, four, five, and eight algorithms were fused to extract mineral alteration with the obtained target detection results. The results prove that the fusion of algorithms gives better results than using individual ones. In conclusion, this paper discusses the significance of evaluating different mapping algorithms. It proposes a robust fusion approach to extract mineral maps as an indicator for geothermal exploration.

---

[1] Reprinted with open-access permission of Remote Sensing. Cavur, M., Yu, Y.T., Demir, E. and Duzgun, S. 2024. Mapping Geothermal Indicator Minerals Using Fusion of Target Detection Algorithms. Remote Sensing, 16

[2] Corresponding author

[3] Department of Mining Engineering, Colorado School of Mines, Golden, CO 80401, USA

APPENDIX G ARTICLE OF MINERAL MAPPING WITH SPECTRAL VARIABILITY (UNPUBLISHED)

Modified from an article under review by The Journal of Applied Remote Sensing.

Yu-Ting Yu[4,5], Sebnem Duzgun[5], Mahmut Cavur[5]>

The attached article entitled "How Does Variability of Spectra Impact Accuracy of Mineral Mapping in Remote Sensing Using ASTER Imagery?" is under review by the Journal of Applied Remote Sensing.

G.1 Abstract

Mineral mapping is crucial for exploring geothermal energy and mineral resources, yet spectral variability could affect mapping accuracy. This study examines the impact of spectral variability on mapping outcomes, focusing on varied alunite and kaolinite mappings at the Coso Geothermal Field, USA. Specifically, we evaluate how spectra from the local Coso Spectral Library and USGS Spectral Library influence mapping accuracy using ASTER VNIR-SWIR imagery.

Five target detection algorithms—Adaptive Coherence Estimator (ACE), Constrained Energy Minimization (CEM), Matched Filtering (MF), Mixture Tuned Matched Filtering (MTMF), and Spectral Angle Mapper (SAM)—were applied in ENVI software. Accuracy was assessed using mineral density maps compared to ground-truth data from field studies, enabling Receiver Operating Characteristic (ROC) analysis and Area Under the Curve (AUC) metrics.

Results reveal significant variability in AUC values (up to 50%) depending on the algorithms and spectra used. CEM, MF, and MTMF showed superior accuracy and were less sensitive to spectral variability. Local spectra improved mapping accuracy, but USGS spectra performed adequately with CEM, MF, and MTMF algorithms. Notably, using average spectra from the USGS library outperformed selecting a USGS spectrum randomly, highlighting a practical strategy for enhancing mapping reliability.

G.2 Introduction

Geological surveys benefit from remote sensing (RS) that utilizes spectral signals to map alteration minerals and identify zones linked to hydrothermal systems (C. Bishop et al., 2018; Jones et al., 2010; Peyghambari & Zhang, 2021; van der Meer, Hecker, et al., 2014). Mineral maps effectively aid in detecting anomalies of alteration minerals' distribution, which further support explorations of mineral deposits (Adiri et al., 2020; Mars, 2018; Shirmard et al., 2022) and geothermal fields (Calvin et al., 2015; Rodriguez-Gomez et al., 2021; Savitri et al., 2021).

[4] Corresponding author
[5] Department of Mining Engineering, Colorado School of Mines, Golden, CO 80401, USA

Spectral libraries offer valuable references to hyperspectral signals used in mineral mapping. The most widely recognized spectral libraries for Earth's materials like rocks and minerals include the USGS (United States Geological Survey) Spectral Library Version 7 (Kokaly et al., 2017), the USGS Terrestrial Tephra Spectral Library (Leight et al., 2022), NASA ASTER (Advanced Spaceborne Thermal Emission and Reflection Radiometer) Spectral Library (Baldridge et al., 2009), and the National Mineral Reference Collection Digital Spectral Library (Percival et al., 2018). The USGS Spectral Library has been utilized in various mineral mapping studies (Abubakar et al., 2018; Amer et al., 2016; Calvin et al., 2015; Mars, 2018; Sun et al., 2017; van der Meer, van der Werff, et al., 2014). In addition, there are also mineral mapping studies utilizing local spectral libraries established from locally collected spectra (Bedini, 2011; Calvin et al., 2015; Flores et al., 2021; Reath & Ramsey, 2013; Rodriguez-Gomez et al., 2021).

However, it is common for one mineral type's spectra and physical properties to vary across locations. Impurities or trace elements can introduce distinct characteristics in the same kind of mineral, affecting its spectral properties and causing it to display different signals under identical conditions (Fan et al., 2012). For example, the USGS Spectral Library Version 7 often has multiple spectral datasets for a single type of mineral (Kokaly et al., 2017). Despite the spectral variability in spectral libraries, studies usually apply a single spectral variety selected or averaged from the spectral library for their mineral mappings (Abubakar et al., 2018; Amer et al., 2016; Calvin et al., 2015; Cavur et al., 2024; Kratt et al., 2006; Mars, 2018; Moraga, 2022; Sun et al., 2017). The impact of using varied spectral signals on mineral mappings remains uncertain, and the significance of this variation requires further investigation.

It is also unclear how spectral variability will influence mineral maps across different spectral target detection algorithms. The commercial software ENVI has eight algorithms for its Target Detection Wizard toolset (Wolfe & Black, 2018), including Adaptive Coherence Estimator (ACE), Constrained Energy Minimization (CEM), Matched Filtering (MF), Mixture-Tuned Matched Filtering (MTMF), Orthogonal Subspace Projection (OSP), Spectral Angle Mapper (SAM), Target-Constrained Interference-Minimized Filter (TCIMF), and Mixture-Tuned Target-Constrained Interference-Minimized Filter (MTTCIMF). However, studies commonly focus on limited algorithms such as SAM(Abubakar et al., 2018; Park & Choi, 2021), MF (Kratt et al., 2006; Molan et al., 2014), or MTMF(Abubakar et al., 2019; Calvin et al., 2015).

Moreover, most studies could not include sufficient accuracy assessments based on ground-truth information as they did not incorporate field studies (Bedini, 2011; Calvin et al., 2015; Hirai & Tonooka, 2019; Moraga, 2022; Reath & Ramsey, 2013; Roy et al., 2020; Sun et al., 2017). Although some studies performed field surveys to evaluate their mineral maps, they did not cover a statistical accuracy assessment for their vast research areas (Abdelkareem et al., 2018; Abubakar et al., 2019; Ramazani et al., 2022).

In a published case (Abubakar et al., 2018), three mineral spectra chosen from the USGS Spectral Library were utilized, though the selection reason was not discussed. They employed the SAM algorithm for spectral target detection but did not explore other spectra variability and mapping algorithms. They also did not statistically evaluate their map`s accuracy using ground truth data. There is a dearth of supporting information that can justify the choice of spectral variability for various target detection algorithms in mineral mapping.

In mineral mapping, under-prediction could miss valuable targets, while over-prediction can lead to wasted time and budget on unrelated sites. Therefore, there is a critical need for a mineral mapping study with appropriate accuracy assessment metrics based on multiple ground-truth points that can solidly compare mineral maps from varied spectral sources and algorithms. This study aims to explore the impact of using varied spectra on the accuracy of mineral maps. Furthermore, the study evaluates whether the labor-intensive local spectral library creation yields better mineral mapping results for geothermal sites or if the publicly available spectral library yields sufficient accuracy in mineral mapping. For this purpose, we conducted mineral mapping and accuracy assessment focusing on alunite and kaolinite at the Coso Geothermal Field (CGF), USA. Alunite and kaolinite are documented alteration minerals at CGF (Davatzes & Hickman, 2010; Hulen, 1978), the local Coso Spectral Library (Cavur et al., 2023), and the USGS Spectral Library version 7. The selection of alunite and kaolinite was based on their common occurrence in multiple geothermal systems (Savitri et al., 2021) and hydrothermal mineral deposits (Hedenquist & Arribas, 2022), presenting as the indicator minerals of steam-heated alteration (Thompson et al., 1999). To the best of the authors' knowledge, this study is the first in the literature to investigate and quantify the impact of varied spectra on the accuracy of mineral mapping.

G.3 Study Materials

Coso Geothermal Field (CGF)

Coso Geothermal Field (CGF) is located in Inyo County of eastern California, USA, geographically situated in the Coso Range of the Mojave Desert (Figure G.1). The CGF is home to one of the largest geothermal fields in the United States, offering a maximum capacity of around 270 megawatts (MWe) (Monastero, 2002) by four power stations (Navy I & II and BLM East & West in Figure G.1). The tectonic setting facilitated the regional landscape of a series of volcanic activities, resulting in a geology dominated by a diverse range of igneous rocks. These include both plutonic and volcanic rocks from mafic, intermediate, and felsic magma (Duffield & Bacon, 1981; Whitmarsh, 1998). The recent volcanic activity in the Quaternary led to the development of a landscape with rhyolite domes and pyroclastic deposits (Whitmarsh, 1998). Figure G.1 presents the locations of major rhyolite domes (Sugarloaf Mountain and Cactus Peak), and hydrothermal features (Coso Hot Springs, Devil's Kitchen, Nicol Pad, Wheeler Pad, etc.).

Multiple studies have investigated the alteration mineralogy of the CGF since the 1970s (Adams et al., 2000; B. P. Bishop & Bird, 1987; Davatzes & Hickman, 2006; Echols et al., 1986; Galbraith, 1978; Hulen, 1978; Hwang et al., 2014; Kovac et al., 2005; Lutz et al., 1996; Mclin et al., 2006). Studies also highlighted the presence of alunite and kaolinite at CGF due to the hydrothermal alteration (Davatzes & Hickman, 2006; Hulen, 1978). Although some studies applied mineral mappings for geothermal exploration at the CGF (Cavur et al., 2024; Erika, 2022; Moraga, 2022), these studies only considered single spectral varieties for the minerals they mapped. The utilized spectra in those studies are either average from the USGS Spectral Library (Erika, 2022; Moraga & Duzgun, 2022) or selected from the Coso Spectral Library (Cavur et al., 2024), yet the studies do not assess the impact on mineral mappings using varied spectra.

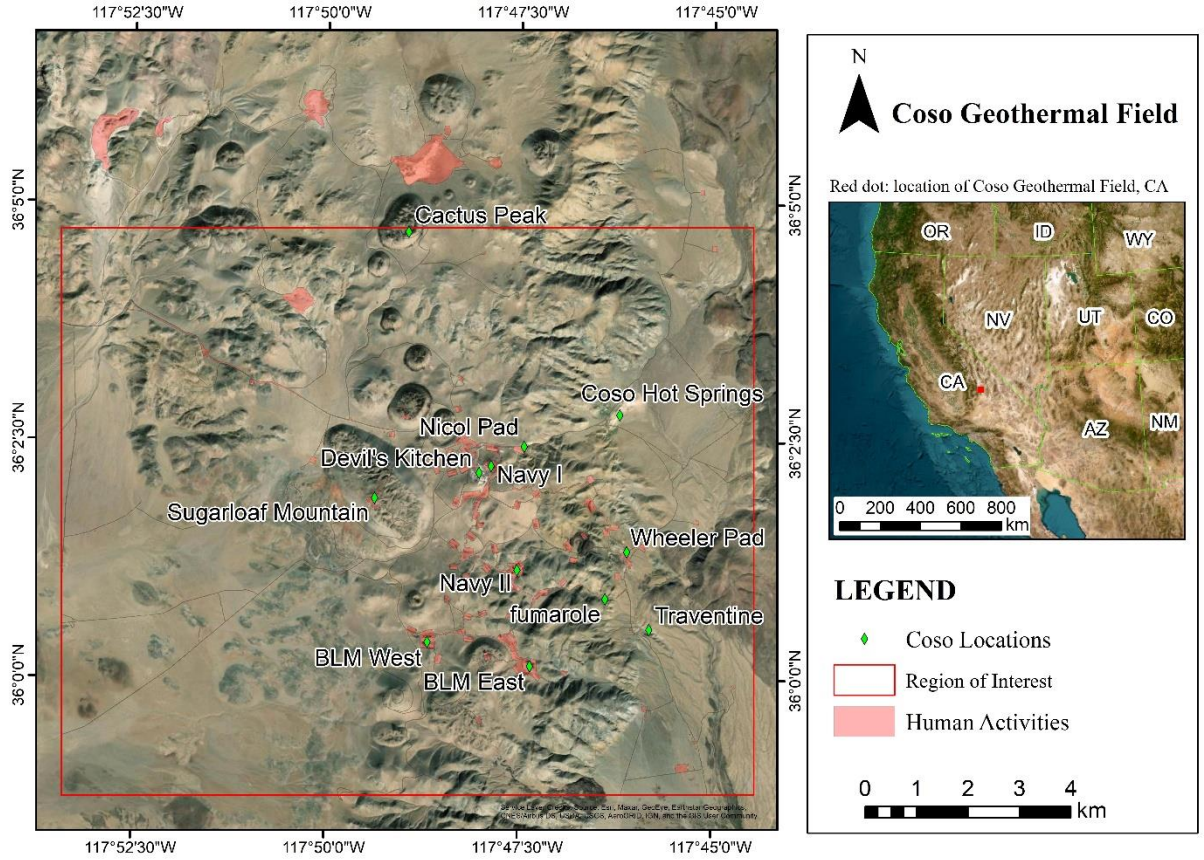

Figure G.1 Map of the Coso Geothermal Field.

Coso Spectral Library

The Coso Spectra Library (Cavur et al., 2023) was a local mineral spectral library available on the website of the Geothermal Data Repository (GDR) (https://gdr.openei.org/submissions/1528). The library was based on analyzing 89 samples collected from the CGF, as shown in Figure G.2. Figure G.3 illustrates the workflow of establishing Coso Spectra Library, starting from sample collection, laboratory measurement, and spectral data processing. The Coso Spectral Library and associated ground-truthing information were established based on mineralogical assessment. The spectra collection of field samples (Figure G.3) was performed in a laboratory by ASD (Analytical Spectral Devices) FieldSpec 4 Hi-RES N.G. with a controlled environment based on the contact probe equipment. The instrument captures the VNIR (visible and near-infrared) and SWIR (short-wave infrared) spectra with 2151 channels from 350 to 2500 nm. White reference spectra were collected before the spectra measurements of each sample. The integration time was set on auto-integration. The collected spectra underwent splice correction using the ViewSpec Pro software to correct the signal gaps between sensors (Gaigalas et al., 2009).

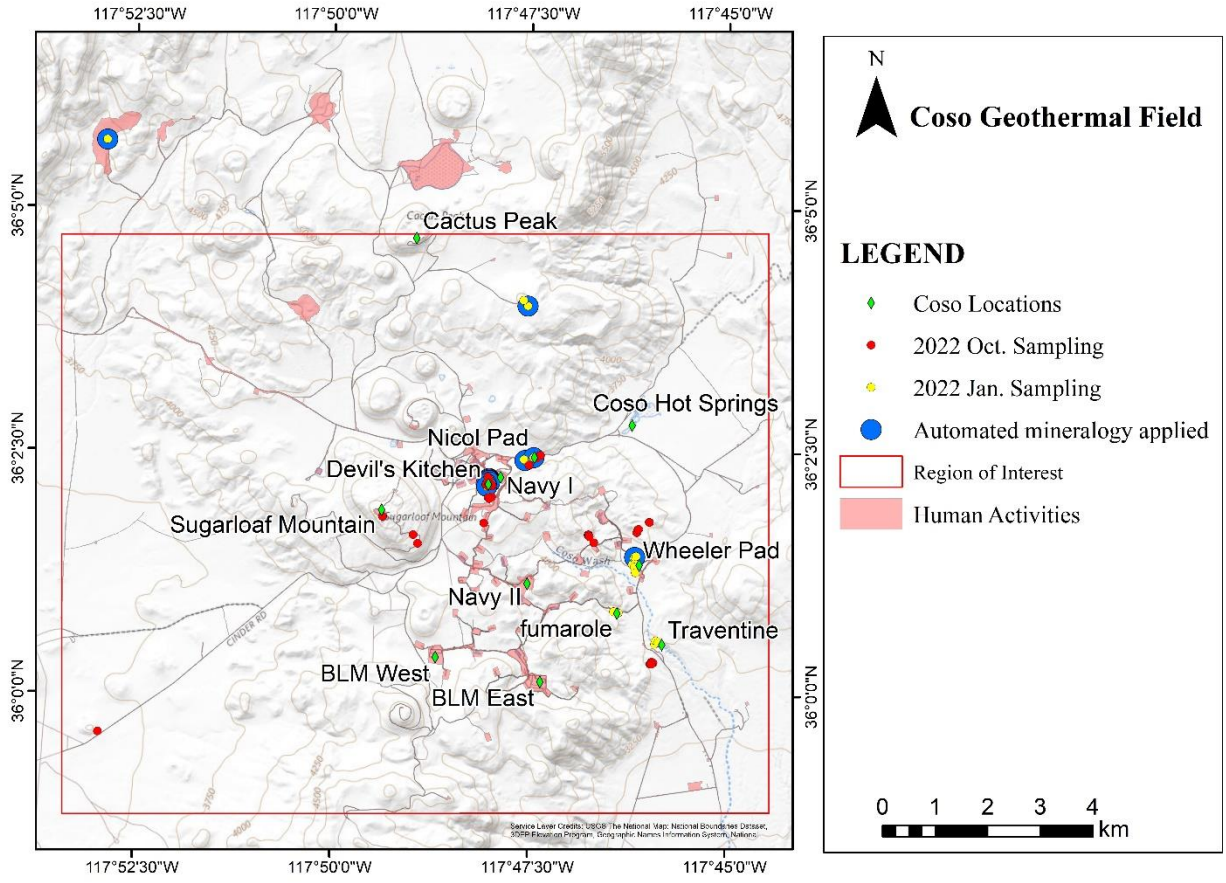

Figure G.2 Sample collection at the CGF.

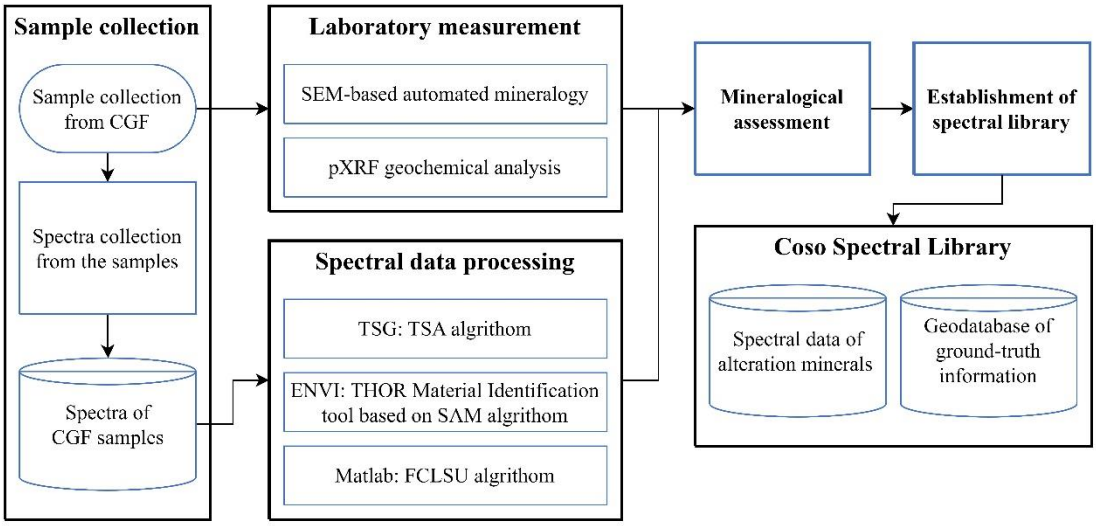

Figure G.3 The flow of establishing Coso Spectral Library and associate ground-truth information.

Due to the prevalence of fine-grained alteration minerals, mineralogy identification is not suitable for solely relying on the samples' physical properties. Therefore, the Coso Spectral Library applied further laboratory measurements and spectral data processing to obtain supporting information for mineralogy, as shown in Figure G.3.

The laboratory measurements (Figure G.3) include SEM (Scanning Electron Microscopy) based automated mineralogy and pXRF (portable X-ray fluorescence spectrometry) geochemical analysis. The library utilizes SEM-based automated mineralogy on selected samples to elucidate the general alteration mineralogy and mineral modal abundance. Along with automated mineralogy, pXRF analysis was employed to infer the samples' geochemistry. The samples from the CGF were analyzed in the Mineral and Materials Characterization (MMC) Facility in the Department of Geology and Geological Engineering at the Colorado School of Mines. 12 of the 89 samples were selected for automated mineralogy to identify the general alteration mineralogy of the CGF (Figure G.2). Due to instrument availability, six samples were analyzed using the TESCAN Integrated Mineral Analyzer (TIMA), whereas six subsequent samples were analyzed using AMICS (Advanced Mineral Identification and Classification) from Bruker. The pXRF analysis measures the chemical abundance in 73 of the 89 samples. The remaining samples were either unsuitable to apply pXRF analysis or duplicate samples. The pXRF measurements were applied non-destructively using a Bruker Tracer 5g handheld XRF spectrometer.

Three different tools were employed in the spectral data processing (Figure G.3) of the collected spectra from CGF. The approaches include the Fully Constrained Linear Spectral Unmixing (FCLSU) algorithm implemented in MATLAB (Borsoi et al., 2021; Heinz & Chang, 2001), the THOR Material Identification tool in ENVI, and The Spectral Geologist (TSG) software developed by the CSIRO (Commonwealth Scientific and Industrial Research Organisation, Australia). The FCLSU attempts

spectral deconvolution for spectral unmixing using a list of potential alteration minerals to unravel the compositional make-up in percent. The THOR Material Identification tool supports comparing the collected spectra and the USGS Spectral Library for matching mineralogy. TSG provides advanced mineralogical identification based on its built-in algorithm with a database of commonly occurring minerals.

The Coso Spectral Library (Figure G.3) synthesizes the mineralogy indications from the CGF samples' physical properties, laboratory measurements, and spectral data processing to establish the spectral library. The dataset includes alteration mineral spectra of alunite (Coso-019, Coso-033, and Coso-034) and kaolinite (Coso-032). Figure G.4 presents the Coso spectra of alunite and kaolinite, including the average alunite spectra (Coso-AVG). Furthermore, the Coso Spectral Library evaluates the presence of alunite and kaolinite in each sample and compiles the information into a geodatabase. This geodatabase, which documents the presence or absence of these minerals along with their coordinates, is essential for assessing the accuracy of mineral mapping and determining whether the distribution of alunite and kaolinite is accurately mapped.

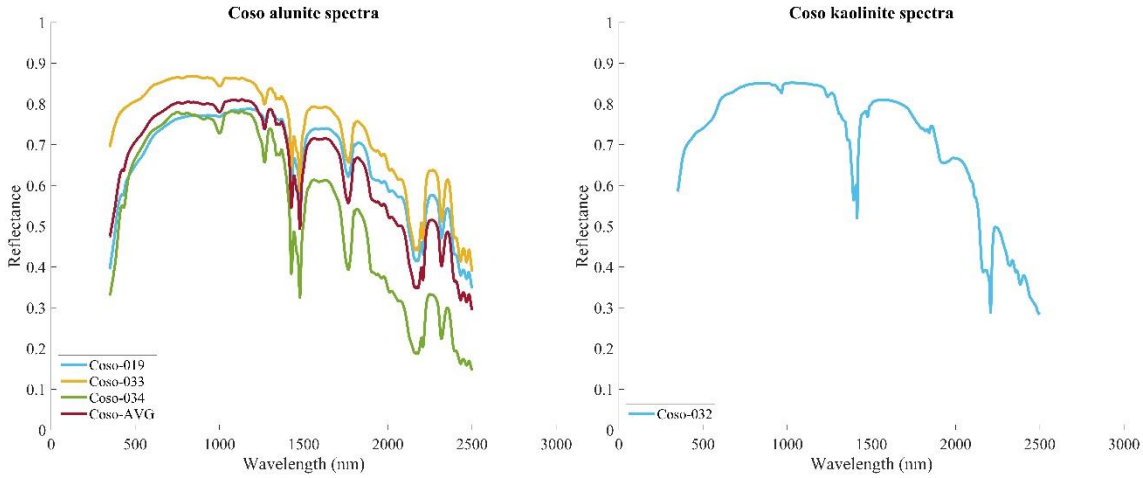

Figure G.4 The alunite and kaolinite spectra of the Coso Spectral Library.

USGS Spectral Library

The USGS Spectral Library version 7 (Kokaly et al., 2017) is a spectral library that includes spectra of minerals, soils, coatings on rocks, vegetation, liquids, organic chemicals, and synthetic materials. The library applied X-ray diffraction (XRD), electron microprobe (EM), X-ray fluorescence (XRF), or petrographic microscopic analyses to ensure the composition of samples. The USGS Spectral Library collected spectra from four spectrometers that could cover different wavelength ranges. Particularly, the library included spectra collected by ASD FieldSpec that covered the range from 350 to 2500 nm and offered a comparable scenario to the Coso Spectral Library.

In this study, we utilized alunite and kaolinite spectra in the USGS Spectral Library, which were collected by the ASD FieldSpec from various locations in the USA. Table G-1 and Table G-2 list the selected spectra and their title, record numbers, and collection locality. None of the samples came from Coso of California. Figure G.5 presents the selected spectra from the USGS library, including the average spectra of the alunite and kaolinite (USGS-AVG). Figure G.4 and Figure G.5 illustrate significant variations in the spectral signatures of the selected minerals from the USGS and Coso Spectral libraries.

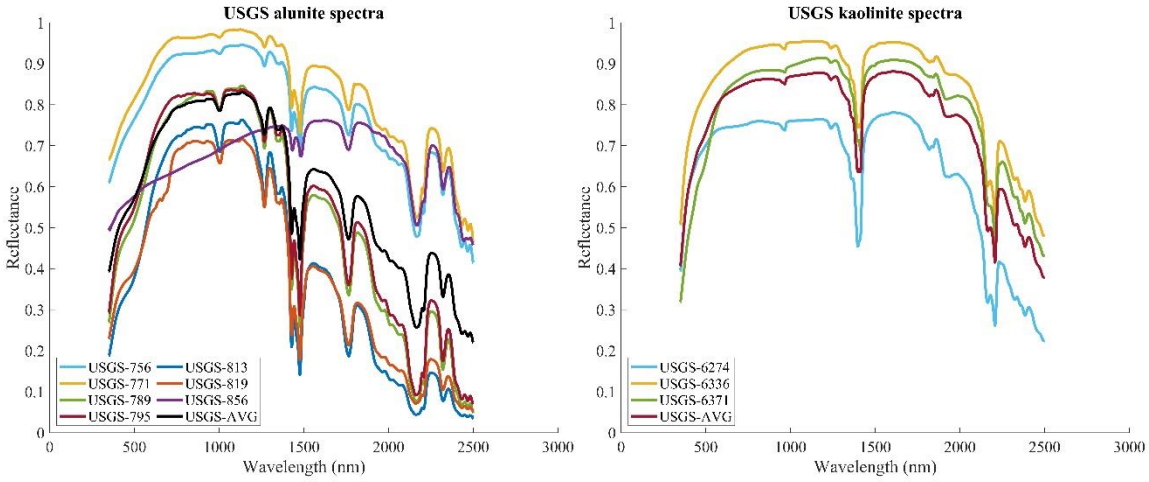

Figure G.5 The alunite and kaolinite spectra of the USGS Spectral Library.

Table G-1 Alunite spectra by ASD FieldSpec in the USGS Spectral Library

Spectrum title	Record number	Collection locality (USA)
Alunite_HS295.1B_ASDFRa_AREF	s07_ASD 765	Utah
Alunite_HS295_ASDFRa_AREF	s07_ASD 771	Utah
Alunite_HS295.3B_ASDFRa_AREF	s07_ASD 789	Utah
Alunite_HS295.3B_ASDNGa_AREF	s07_ASD 795	Utah
Alunite_HS295.4B_ASDFRa_AREF	s07_ASD 813	Utah
Alunite_HS295.6_ASDFRb_AREF	s07_ASD 819	Utah
Alunite_RES-9_Summitv_(400C)_ASDNGb_AREF	s07_ASD 856	Summitville, Colorado

Table G-2 Kaolinite spectra by ASD FieldSpec in the USGS Spectral Library

Spectrum title	Record number	Collection locality (USA)
Kaolinite_CM9_ASDNGb_AREF	s07_ASD 6274	Mesa Alta, New Mexico
Kaolinite_KGa-1_(wxl)_ASDNGb_AREF	s07_ASD 6336	Washington County, Georgia
Kaolinite_KGa-2_(pxl)_ASDNGb_AREF	s07_ASD 6371	Warren County, Georgia

G.4 Methodology

To quantitatively evaluate the impact of different spectra on the accuracy of mineral maps, we follow the methodology outlined in Figure G.6. The proposed methodology starts with mineral mapping (Section 0) using the Coso Spectral Library, the USGS Spectral Library, and the ASTER multispectral image. The mineral maps underwent an accuracy assessment (Section 0), comparing ground-truth information to identify the mapping quality. The result of the accuracy assessment and the correlation coefficient between the spectra were used in an exploratory spectral analysis (Section 0) to determine the relation between the spectra variability and mapping results.

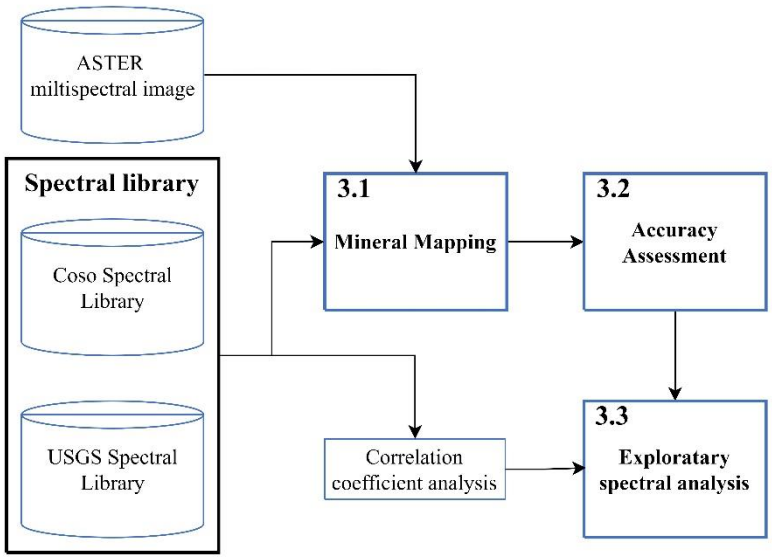

Figure G.6 The research workflow.

Mineral Mapping

Spectra from the Coso Spectral Library and the USGS Spectral Library were used for mineral mapping. For this purpose, available multispectral VNIR-SWIR data from ASTER (AST_L1T) was utilized (NASA LP DAAC, 2015). ASTER sensors acquire spectral signals from the range of VNIR, SWIR, and TIR (thermal infrared) (Baldridge et al., 2009). ASTER's six SWIR bands could facilitate its

ability to study the OH-bearing minerals of alunite and kaolinite (Thomas & Walter, 2002). The satellite image was processed in ENVI for radiometric calibration, atmospheric correction, and normalization. In addition, human activities at CGF (Figure G.1) were masked to avoid misleading interpretations. The Target Detection Wizard in ENVI and an R-based mapping module (Moraga & Duzgun, 2022) were utilized for mineral mapping. The toolsets resample the target spectra (Figure G.3 and Figure G.4) regarding the ASTER dataset bands to compare with the imagery pixels (Figure G.7 and Figure G.8). It could be observed that the spectral patterns are not identical after the resampling. Among the target detection algorithms in ENVI, we focused on the algorithms that do not require the assignment of non-target spectra. The applied target detection algorithms were Adaptive Coherence Estimator (ACE), Constrained Energy Minimization (CEM), Matched Filtering (MF), Mixture Tuned Matched Filtering (MTMF), and Spectral Angle Mapper (SAM).

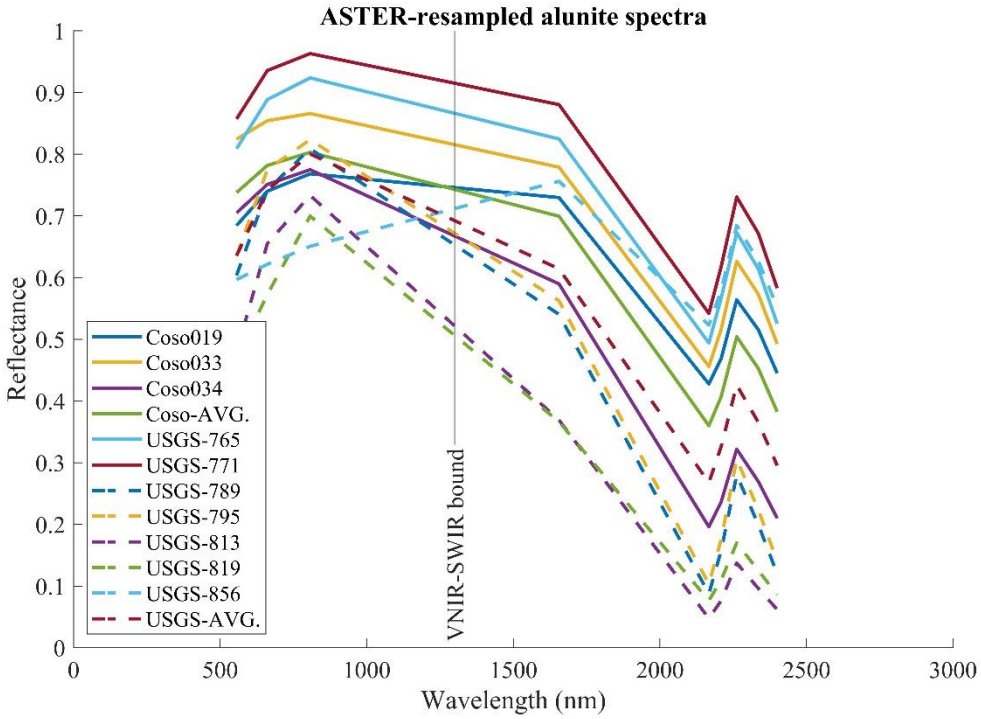

Figure G.7 The resampled alunite spectra in ASTER bands.

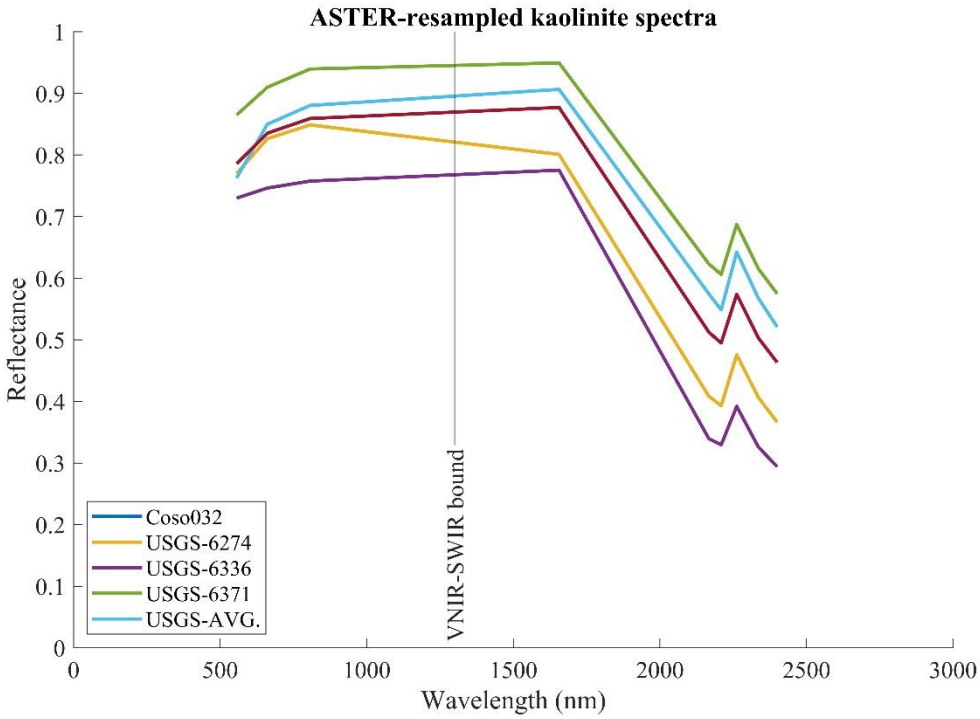

Figure G.8 The resampled kaolinite spectra in ASTER bands.

Accuracy Assessment

All mineral maps underwent an accuracy assessment using Python-based modules (Cavur et al., 2024) to compare the mineral presence at sampling locations and the mineral maps. The modules first convert mineral maps to mineral density maps and then compare the density maps with ground-truth CGF samples to create confusion matrices. Receiver Operating Characteristic (ROC) curves and corresponding Area Under the Curve (AUC) values (Hanley & McNeil, 1982) were generated by collecting true and false positive rates from confusion matrices at gradually changing density map thresholds. AUC value is an indicator to compare the performance of prediction models. It ranges from zero to one, where one represents the most effective prediction model, and zero indicates the least effective. An AUC value of 0.5 refers to a scenario of random prediction. In this study, higher AUC values reflect more accurate mineral maps. The procedure allows us to evaluate the difference between the mappings using various spectra from the CGF and USGS by comparing the AUC values and the corresponding averages and ranges. In addition, it also examines the differences between the maps using various mapping algorithms.

Exploratory Spectral Analysis

Beyond the accuracy assessment, we explore if the spectra with higher similarity also offer a similar level of mineral map quality. For this purpose, we define the control group as the Coso spectra that produce mineral maps with the highest AUC and then compute correlation coefficients between these control group spectra and other studied spectra. We assess if those spectra with higher correlation coefficients also provide higher AUC levels that are close to the control groups. Correlation coefficients were computed in three wavelength ranges: the whole spectra (350–2500 nm), VNIR (350–1300 nm), and SWIR (1300–2500 nm). In addition, we identified if the similarity in particular spectral sections associated with respective AUC values demonstrates stronger correlations. We specifically focused on identifying spectral sections that would contribute to the similarity of mapping results.

G.5 Result and Discussion

Mineral Maps

The selected Coso and USGS spectra (Figure G.7 and Figure G.8) were used to create mineral maps from the ASTER dataset. The mineral maps were converted to point density maps for the next step of accuracy assessment. The mineral density maps of the alunite and kaolinite based on different mapping algorithms are organized in Figure G.9 and Figure G.10, respectively. Alunite and kaolinite generally have similar mapped patterns with clusters northeast and west of CGF. However, the detailed patterns on maps varied between spectra. For example, the alunite maps using the spectra USGS-819, USGS-856, and USGS-AVG based on the SAM algorithm are visually different (lower-right of Figure G.9). In addition, different mapping algorithms could yield different results. The CEM, MF, and MTMF algorithms presented similar mapping results with few areas of high mineral density northeast of CGF (Coso Hot Springs and Devil's Kitchen). The mineral maps of these three algorithms also showed slight variations due to varied spectra.

In contrast, the ACE and SAM algorithms produced mineral maps with more high-mineral-density areas. The mapped patterns of these two algorithms showed distinct variations due to the application of varied spectra. The mapping results suggest that algorithms ACE and SAM are more sensitive to spectral variability.

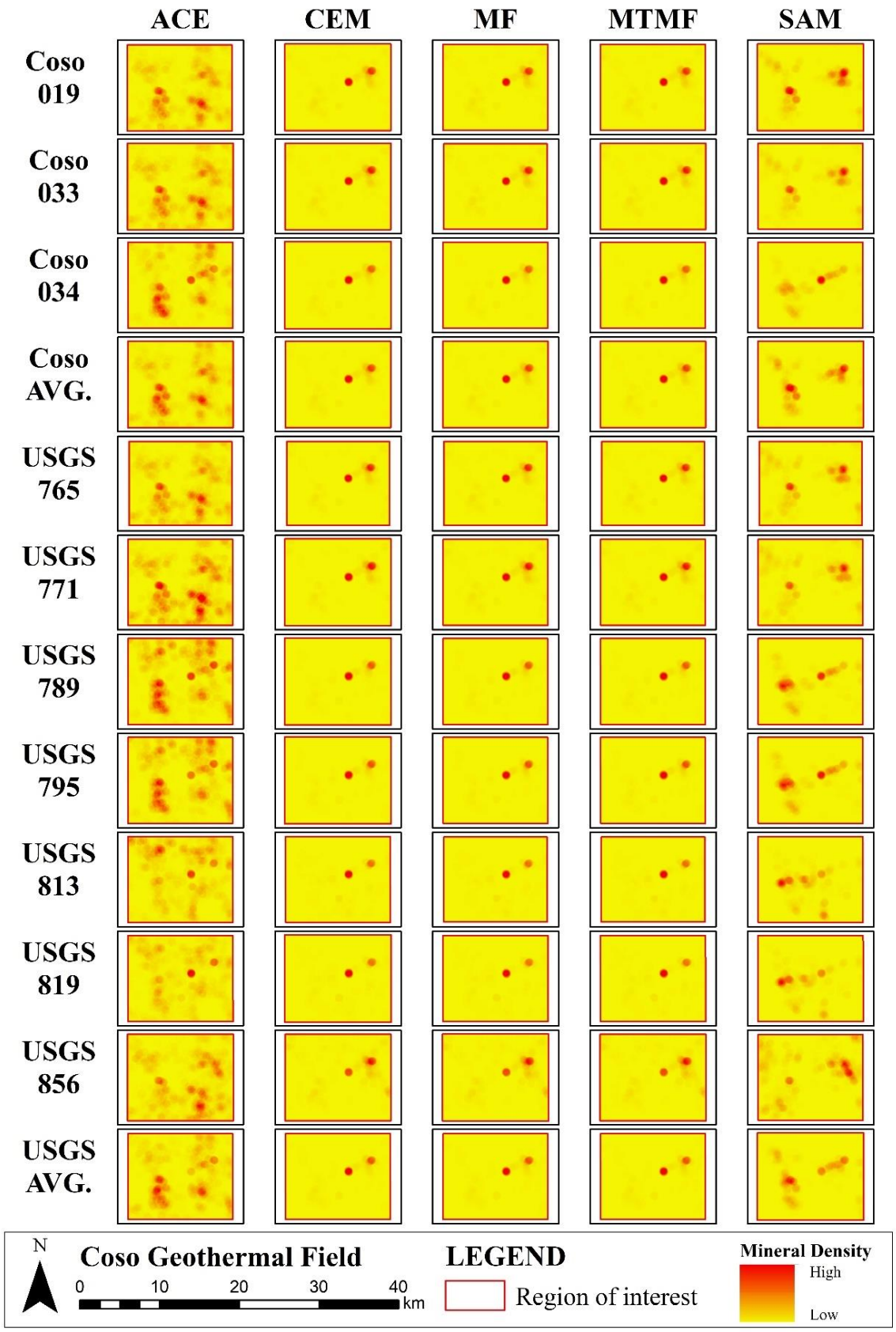

Figure G.9 The alunite mineral density maps. Each raw is one spectrum from the Coso Spectral Library and the USGS spectral library. Each column refers to one mapping algorithm.

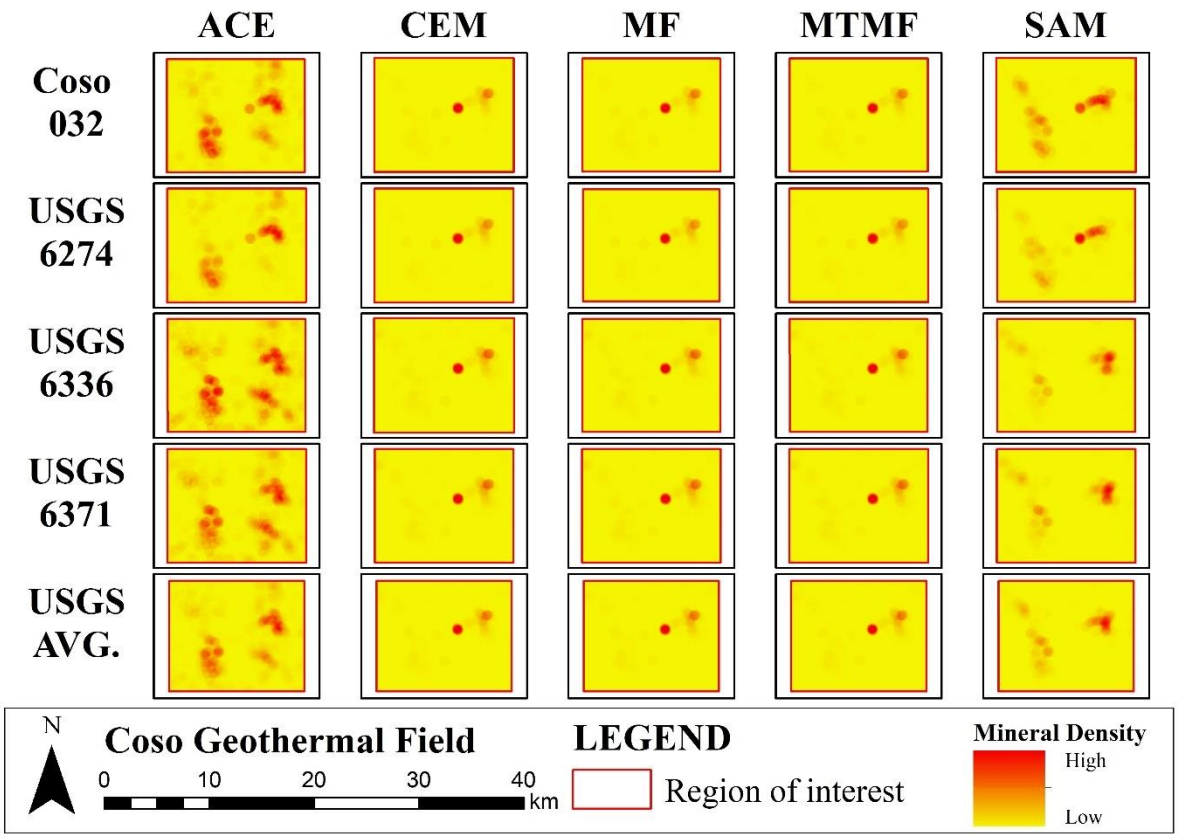

Figure G.10 The kaolinite mineral density maps. Each raw is one spectrum from the Coso Spectral Library and the USGS spectral library. Each column refers to one mapping algorithm.

Accuracy Assessment

The accuracy assessment was based on evaluating the ROC curves and the AUC values. The ROC curves of varied alunite and kaolinite spectra for each mapping algorithm are organized in Figure G.11 and Figure G.12. It can be observed that the ROC curves of the algorithm ACE and SAM presented a higher level of variations than CEM, MF, and MTMF. The corresponding AUC values and associated statistics by each spectrum are summarized in Table G-3. Table G-4 summarizes the statistics of AUC by each mapping algorithm. The higher average AUCs refer to more accurate maps, and the lower AUC ranges refer to more precise maps.

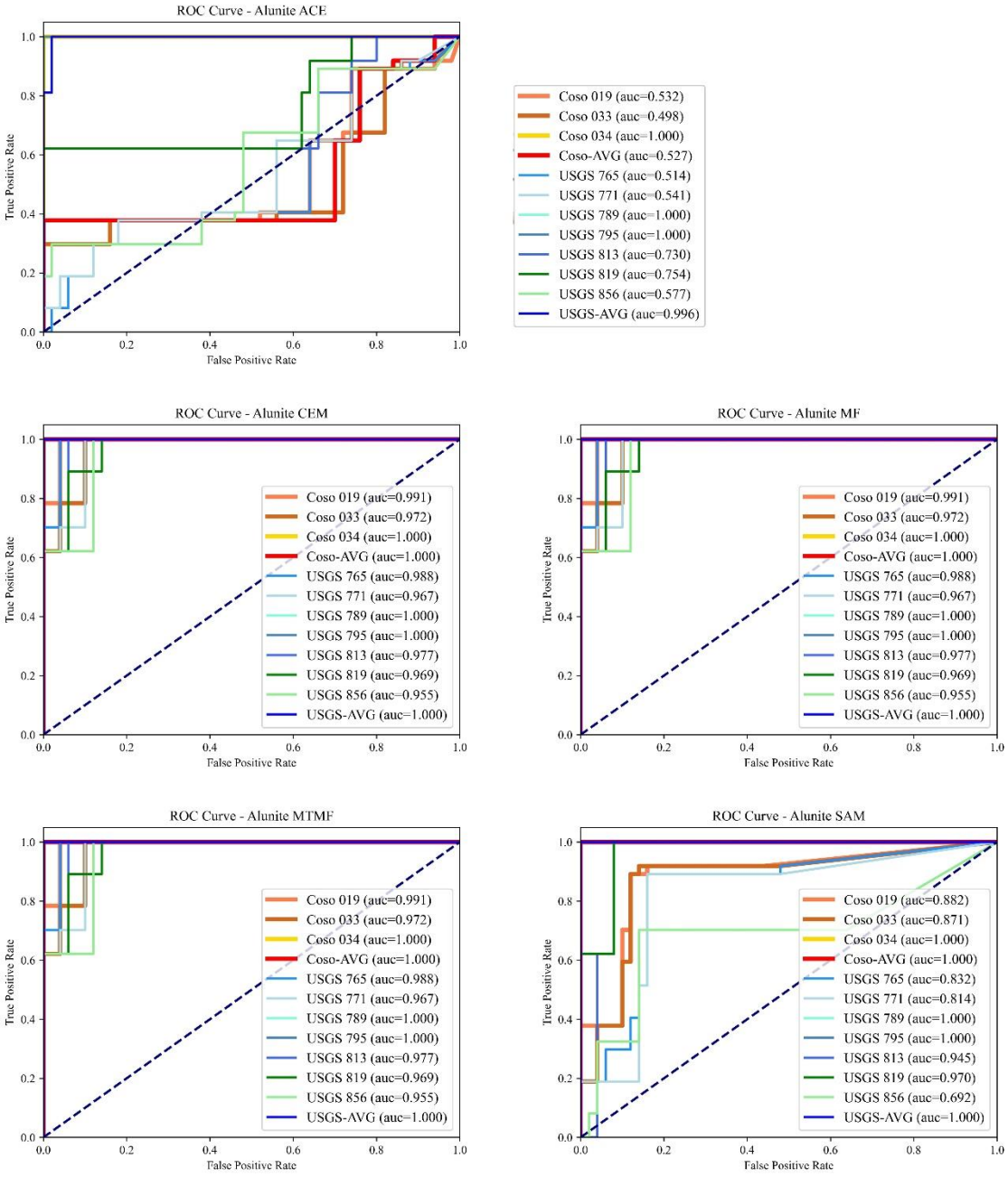

Figure G.11 The ROC curves and AUC values from accuracy assessments of alunite mappings.

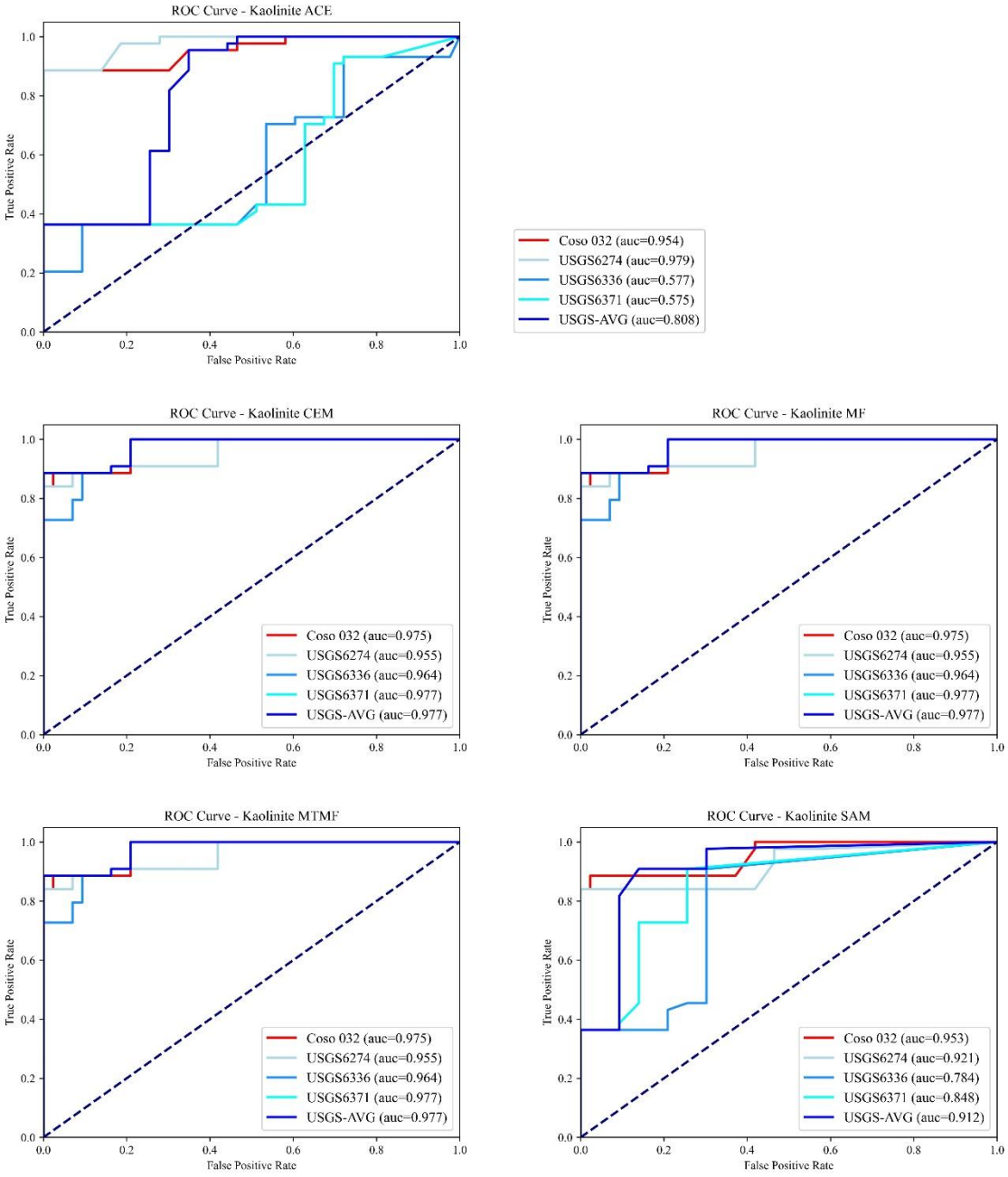

Figure G.12 The ROC curves and AUC values from accuracy assessments of kaolinite mappings.

According to Table G-3, the alunite maps showed that multiple spectra Coso-034, USGS-789, USGS-795, and USGS-AVG have the highest accuracy. The performance has an average AUC of up to one and an AUC range low to zero. The lowest average AUC was 0.827 by USGS-856. For the kaolinite maps, the spectrum Coso-032 yielded the most accurate map. The average AUC was 0.966, and the AUC range was 0.022. The USGS-AVG and USGS-6274 also provided accurate mineral maps with average AUCs higher than 0.93, and AUC ranges lower than 0.17. The lowest average AUC was 0.851 by USGS-6336.

In general, the local spectra provided higher accuracy for mineral maps. Notably, the Coso-034 of alunite and Coso-32 of kaolinite used for the mineral maps bring about the highest average AUCs and the lowest AUC ranges, indicating better map quality. Although the local alunite spectra Coso-019 and Coso-033 yielded lower average AUC than Coso-034, the Coso Spectral Library documented that Coso-034 went through more detailed analyses than Coso-019 and Coso-033 (Cavur et al., 2023), which would be the reason for the better mapping quality.

Table G-3 The AUC values and associated statistics by spectrum. The highest average AUCs and the lowest AUC ranges were highlighted underlined.

Mineral	Spectra	ACE	CEM	MF	MTMF	SAM	Average AUC	AUC Range
alunite	**Coso-019**	0.532	0.991	0.991	0.991	0.882	0.877	0.459
	Coso-033	0.498	0.972	0.972	0.972	0.871	0.857	0.474
	Coso-034	1.0	1.0	1.0	1.0	1.0	1.0	0.0
	Coso-AVG	0.527	1.0	1.0	1.0	1.0	0.905	0.473
	USGS-765	0.514	0.988	0.988	0.988	0.832	0.862	0.474
	USGS-771	0.541	0.967	0.967	0.967	0.814	0.851	0.426
	USGS-789	1.0	1.0	1.0	1.0	1.0	1.0	0.0
	USGS-795	1.0	1.0	1.0	1.0	1.0	1.0	0.0
	USGS-813	0.730	0.977	0.977	0.977	0.945	0.921	0.247
	USGS-819	0.754	0.969	0.969	0.969	0.970	0.926	0.216
	USGS-856	0.577	0.955	0.955	0.955	0.692	0.827	0.378
	USGS-AVG	0.996	1.0	1.0	1.0	1.0	0.999	0.004
kaolinite	**Coso 032**	0.954	0.975	0.975	0.975	0.953	0.966	0.022
	USGS-6274	0.979	0.955	0.955	0.955	0.921	0.953	0.058
	USGS-6336	0.577	0.964	0.964	0.964	0.784	0.851	0.387
	USGS-6371	0.575	0.977	0.977	0.977	0.848	0.871	0.402
	USGS-AVG	0.808	0.977	0.977	0.977	0.912	0.930	0.169

The results also show that multiple USGS spectra contribute to the maps with average AUC levels higher than 0.9, but some USGS spectra result in the lowest average AUCs. We found that using the average spectra from the USGS library yields relatively better maps. Both USGS-AVG spectra offered the second-highest average AUC and second-lowest AUC range among the USGS spectra. By randomly selecting a USGS spectrum for mineral mapping, the average AUC of the alunite map could change from 0.827 (USGS-856) to 1.0 (USGS-789, USGS-795), and the average AUC of the kaolinite map could change from 0.851 (USGS-6336) to 0.953 (USGS-6274). Using USGS average spectra for mineral mapping can avoid inaccurate mineral maps based on a randomly chosen spectrum from the USGS Spectral Library.

Based on Table G-3, it was further observed that the AUC levels varied following the mapping algorithms. The AUCs of CEM, MF, and MTMF are generally the highest, whereas those of ACE and SAM remain lower in comparison. One exception occurs in the case of USGS-819 and USGS-6274, where ACE and SAM were slightly higher by 0.024 and 0.001. The other exception occurs in the case of Coso-034, Coso-AVG(alunite), USGS-789, USGS-795, and USGS-AVG (alunite), where ACE and/or SAM reached the same AUC of CEM, MF, and MTMF at one. Other than the aforementioned two exceptions, the AUCs of ACE and SAM are notably lower. The difference between the AUCs of CEM/MF/MTMF and ACE corresponds to 14 AUC ranges out of 17 studied cases of spectra.

The average AUC and AUC range by each mapping algorithm are summarized in Table G-4 for further investigation. CEM, MF, and MTMF algorithms provided the highest average AUCs, and the lowest AUC ranges for alunite and kaolinite, suggesting that they are the most accurate and precise algorithms. The algorithm ACE has the lowest average AUC and the highest AUC range for both alunite and kaolinite. The average AUC and the AUC range of SAM was in between CEM/MF/MTMF and ACE for alunite and kaolinite.

Table G-4 The statistics of AUC by each mapping algorithm

Mineral	Spectra	ACE	CEM	MF	MTMF	SAM
alunite	**Average AUC**	0.722	0.985	0.985	0.985	0.917
	AUC Range	0.502	0.045	0.045	0.045	0.308
kaolinite	**Average AUC**	0.779	0.970	0.970	0.970	0.884
	AUC Range	0.404	0.022	0.022	0.022	0.169

In this study, varied spectra significantly impact the ACE algorithm by changing the AUC level from more than 40 percent (kaolinite) to 50 percent (alunite). Varied spectra also impact the SAM algorithm by changing the AUC level from around 17 percent (kaolinite) to 31 percent (alunite). Meanwhile, the impact of varied spectra on the algorithms of CEM, MF, and MTMF remains less than five percent. It was found

that varied input spectra greatly change the AUC level of ACE and SAM., whereas CEM, MF, and MTMF present better consistency. The finding suggests that CEM, MF, and MTMF algorithms are less sensitive to spectral variability while providing accurate and precise mineral maps. On the other hand, the algorithms ACE and SAM are more sensitive to spectral variability.

In this study, the best-performing mapping algorithms that offered the highest average AUC and lowest AUC range were CEM, MF, and MTMF, followed by SAM. The ACE algorithm yielded the lowest average AUC and highest AUC range. The findings align with earlier studies compiled in Table G-5 (Cavur et al., 2024; Jawak et al., 2022b; Shang et al., 2020). These earlier studies also found that CEM, MF, and MF have close performance that is better than SAM. The performance of the ACE algorithm in other previous studies was varied, but it was also identified to be the worst in two earlier studies.

The ranking of algorithms' performance reflects the characteristics of the algorithms: CEM, MF, and MTMF have close results because their logic of calculation was similar (Boardman & Kruse, 2011; Chang et al., 2000). ACE enhances the contrast between signals to increase target identification from background (Jin et al., 2009), potentially introducing more mapping variations and false predictions. Previous studies indicate that SAM struggles when target spectra are unevenly distributed and exhibit high dispersions among the analyzed pixels. (Manolakis & Shaw, 2002). Therefore, the nature of mineral spectral variability and irregular distribution may be the reason for lowering accuracy.

Table G-5 The studies comparing algorithm performance.

Previous studies	Comparison of performance
(Cavur et al., 2024)	CEM = MF = MTMF > SAM > ACE
(Jawak et al., 2022b)	ACE > MF > CEM > MTMF > SAM
(Shang et al., 2020)	CEM = MF > MTMF > SAM > ACE

Based on the accuracy assessment, it was identified that local spectra Coso-034 and Coso-032 resulted in the mineral maps with the highest AUC of alunite and kaolinite, respectively. Therefore, Coso-034 and Coso-032 were selected as the control groups to explore the difference between the mineral maps by varied spectra. By subtracting the normalized mineral density map, inspecting the regions where each spectrum presented higher and lower estimations than the control group was possible. The comparison maps are shown in Figure G.13 and Figure G.14. Once again, it was observed that varied spectra carried out different intensity and distribution patterns on mineral maps. The difference between each mapping algorithm also supports the findings from ROC curves and AUC values. The algorithms ACE and SAM have more areas of variations on maps, showing that these algorithms have lower precision on mapping results regarding spectral variability.

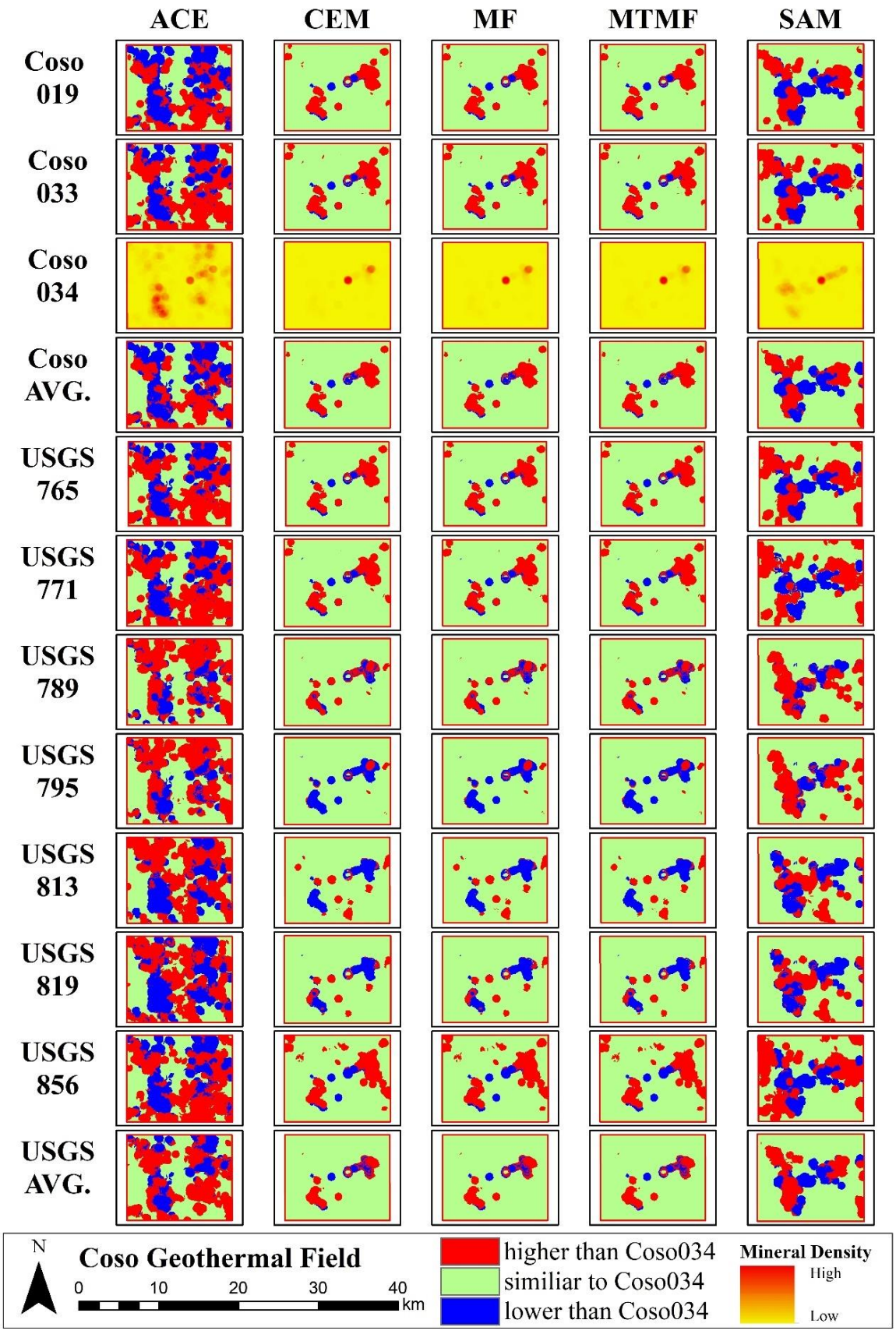

Figure G.13 Comparison of alunite maps based on a control group of Coso-034.

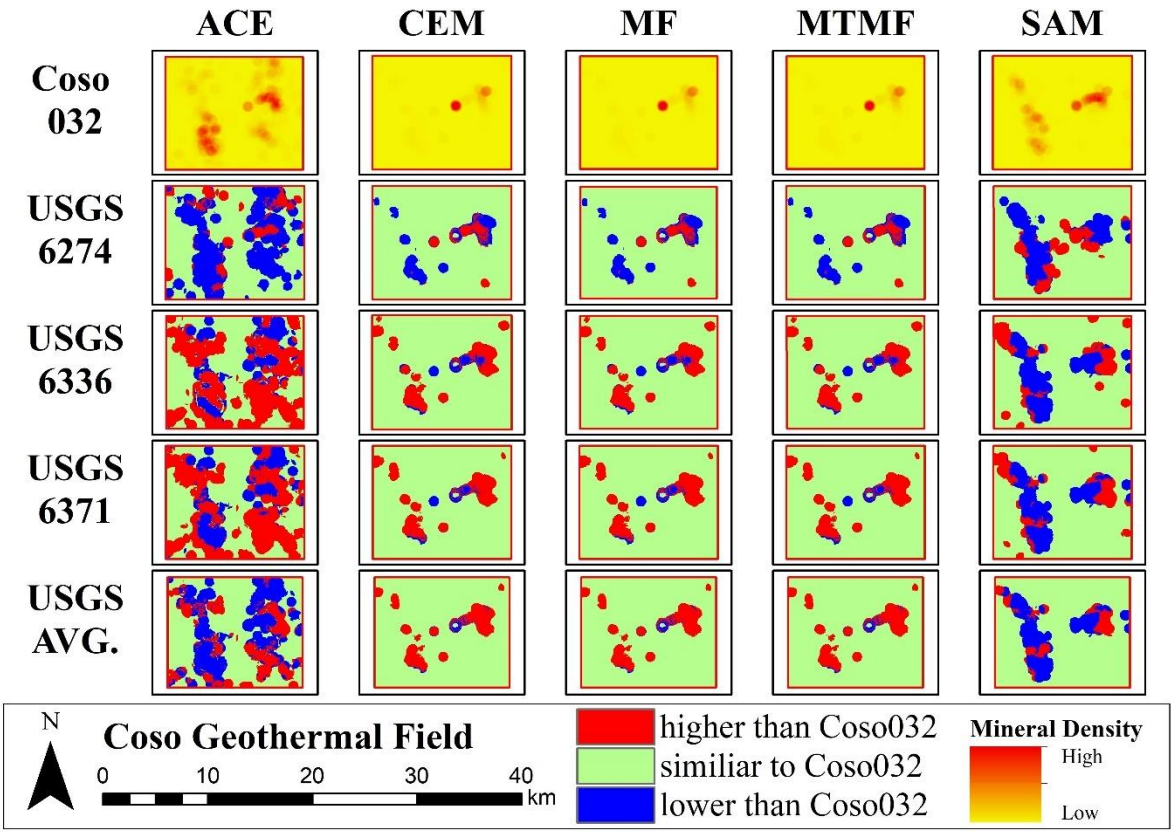

Figure G.14 Comparison of kaolinite maps based on a control group of Coso-032.

Exploratory Spectral Analysis

This step evaluates whether the AUC levels reflect the similarity between the studied spectra. The correlation coefficients were calculated between the control group spectra (Coso-034 and Coso-032) and the other studied spectra. The correlation coefficients between the whole spectra, VNIR, and SWIR are present in Table G-6 and Table G-7, along with the average AUCs from Table G-3. We set evaluation thresholds at 0.99 for a strong correlation coefficient and 0.95 for a high average AUC.

In the case of alunite mapping, the high average AUCs other than Coso-034 are USGS-789, USGS-795, and USGS-AVG. Coso-034 presents strong whole-spectra correlations with Coso-AVG, USGS-789, and USGS-795. In addition, it presents strong SWIR correlations with Coso-AVG, USGS-789, USGS-795, and USGS-AVG. Meanwhile, Coso-034 only presents a strong VNIR correlation with Coso-AVG. The strong correlations of whole-spectra and SWIR better correspond with the high average AUCs than VNIR correlations, especially the SWIR correlations. There was an exception in that the strong correlations between Coso-034 and Coso-AVG did not reflect on the high average AUC. However, the Coso-AVG has the highest AUCs at 1.0 by CEM, MF, MTMF, and SAM algorithms (Table G-3). It was the ACE algorithm that lowered the average AUC with a notably lower AUC (0.527), and we have identified that the ACE algorithm is more sensitive to spectral variability while offering lower AUC

levels. Therefore, the connection between the high AUC level (0.95) and the strong correlations between the spectra is still valid.

Table G-6 Correlation coefficients of alunite Coso-034 with other alunite spectra. The underlined coefficients reach the 99 percent threshold. The underlined average AUCs represent the mineral maps with the highest accuracy other than the control group.

The correlation coefficient of:	whole spectra	VNIR	SWIR	Average AUC
	350-2500nm	350-nm1300	1300-2500nm	
Coso-019	0.932	0.957	0.975	0.877
Coso-033	0.970	0.972	0.969	0.857
Coso-034	1*	1*	1*	1*
Coso-AVG	0.991	0.993	0.990	0.905
USGS-765	0.959	0.926	0.976	0.862
USGS-771	0.954	0.931	0.972	0.851
USGS-789	0.985	0.924	0.993	1
USGS-795	0.989	0.940	0.994	1
USGS-813	0.964	0.905	0.964	0.921
USGS-819	0.966	0.884	0.971	0.926
USGS-856	0.400	0.724	0.864	0.827
USGS-AVG (alunite)	0.978	0.915	0.993	0.999

*: control group

Table G-7 Correlation coefficients of kaolinite Coso-032 with other kaolinite spectra. The underlined coefficients reach the 99 percent threshold. The underlined average AUCs represent the mineral maps with the highest accuracy other than the control group.

The correlation coefficient of:	Whole spectra	VNIR	SWIR	Average AUC
	350-2500nm	350-nm1300	1300-2500nm	
Coso-032	1*	1*	1*	0.966*
USGS-6274	0.985	0.924	0.995	0.953
USGS-6336	0.945	0.974	0.993	0.851
USGS-6371	0.838	0.973	0.993	0.871
USGS-AVG (kaolinite)	0.947	0.972	0.996	0.930

*: control group

In the case of kaolinite mapping, the highest AUC was Coso-032, followed by USGS-6274 and USGS-AVG. Coso-032 presents strong whole-spectra correlations with USGS-6274. In addition, it presents strong SWIR correlations with every USGS spectra. In contrast, Coso-032 did not present strong VNIR correlations with the USGS spectra. The stronger correlations of whole-spectra and SWIR better correspond with the high average AUCs than VNIR correlations, especially the SWIR correlations. Although all the SWIR coefficients are higher than 0.99, the SWIR coefficients of USGS-6274 and USGS-AVG are slightly higher than USGS-6336 and USGS-6371, the average AUC of USGS-6274 and USGS-AVG are also higher than USGS-6336 and USGS-6371. The findings suggest that the connection between high average AUC and strong SWIR correlations was still valid. The results indicate the importance of utilizing the SWIR spectra in mapping OH-bearing alteration minerals like alunite and kaolinite.

G.6 Conclusion

This study explores the influence of spectral variability with multiple mapping algorithms in mineral mapping. We obtained alunite and kaolinite mineral maps for the CGF using spectra from the Coso Spectral Library and USGS Spectral Library. The result of accuracy assessments with ground-truth information reveals that different spectral variabilities and mapping algorithms can significantly influence mineral maps and their accuracies.

Based on the ROC curves and AUCs from the accuracy assessment, it was observed that local CGF spectra offered the highest AUCs for the alunite map (Coso-034) and kaolinite map (Coso-032). The local spectra proved their ability to create accurate mineral maps. Using the USGS spectra sometimes offers AUCs as high as 1.0. However, it also resulted in some of the lowest average AUCs in this study. We observed that using the average USGS spectra yields higher average AUCs and lower ranges among all the mineral maps by USGS spectra. Therefore, for cases without local spectra, we suggest using the average spectrum from the USGS Spectral Library instead of a randomly selected one to improve mineral mapping accuracy.

It was observed that different mapping algorithms offer varied levels of average AUC and AUC range in this study. With the different spectra used in mapping, the mineral maps by the ACE algorithm provided the lowest average AUC and the highest AUC range. On the other hand, CEM, MF, and MTMF algorithms offered the highest average AUC and lowest AUC ranges. These algorithms are less sensitive to spectral variability while providing accurate mineral maps. The SAM algorithm offered mineral maps with performance between ACE and CEM/MF/MTMF.

For the ACE algorithm, varied alunite spectra impact mineral mapping by dropping the AUC from 1.0 to 0.5. Varied kaolinite spectra also impact mineral mapping by dropping the AUC from 0.98 to 0.58. It shows that random selection of target spectrum in mineral mapping with the ACE algorithm produces

AUC ranges of more than 50 percent for alunite maps and more than 40 percent for kaolinite. In contrast, CEM, MF, and MTMF algorithms not only provided accurate mineral maps but also kept the AUC ranges within five percent despite the spectral variability. Therefore, we suggest that utilizing the CEM, MF, and MTMF algorithms can minimize the impact of spectral variability and improve the accuracy of mineral maps.

Overall, for studies that cannot establish a local spectral library for mineral mapping, this study recommends applying the average mineral spectra from the USGS Spectral Library with algorithms CEM, MF, and MTMF to secure good mapping qualities. This study also confirms that the SWIR band contributes most to mapping alunite and kaolinite.

APPENDIX H ARTICLE OF DATA-DRIVEN STUDY ON SGP (UNPUBLISHED)

Modified from an article under review by Geoenergy.

Yu-Ting Yu[6,7], H. Sebnem Duzgun[7], Mahmut Cavur[7], Ebubekir Demir[7], Andrew E. Sabin[8]

The attached article entitled "A Data-Driven Approach to Understanding the Relations Between Parameters Used for Geothermal Exploration" is under review by Geoenergy.

H.1 Abstract

Understanding the relations between indicator minerals, faults, and temperatures is crucial for effective geothermal exploration. This study employs a novel data-driven analysis to investigate these relations across three distinct geothermal fields in the USA: Coso, Brady, and Desert Peak. Utilizing fault maps, land surface temperatures (LST), and indicator mineral maps (alunite, chalcedony, hematite, kaolinite, opal), non-spatial analyses (Kolmogorov-Smirnov tests, ANOVA, and linear regression) were combined with spatial analysis (colocation analysis) to uncover associated patterns.

At Coso and Brady, alunite and kaolinite are closely linked to faults and elevated LSTs, while chalcedony shows negative correlations. Hematite aligns positively with LST but negatively with faults, and opal correlates positively with faults but not with LST. These trends align with geothermal alteration models involving acidic sulfate fluids and alkali-chloride discharges. Desert Peak's blind geothermal system contrasts with the negative relations between its indicator minerals, faults, and LSTs.

This research provides insights on integrating diverse datasets to enhance exploration strategies and reduce uncertainty: Fault surveys are essential for identifying heat and fluid pathways, while LST surveys are critical for detecting blind systems. Additionally, the study underscores the need for data-driven approaches to explore subtle geological characteristics in geothermal exploration.

H.2 Introduction

Geothermal energy can provide a sustainable baseload energy supply and enhance regional energy independence (Troccoli, 2009). However, geothermal exploration requires lengthy, costly geological surveys to understand resource potential, including fluid pathways, fluid characteristics, and temperature ranges (Gehringer & Loksha, 2012; Harvey et al., 2014; Moeck, 2014). Geological uncertainties add complexities to any exploration program, thereby increasing the risks and costs in geothermal systems' early exploration and development (Cole et al., 2016; Wall et al., 2017; Witter et al., 2019).

[6] Corresponding author
[7] Department of Mining Engineering, Colorado School of Mines, Golden, CO 80401, USA
[8] Navy Geothermal Program Office, 429 E. Bowen Road, China Lake, CA 93555, USA

Geothermal systems are found in multiple geological settings, including both magmatic and amagmatic settings (Jolie et al., 2021; Sigurdsson et al., 2015). Geothermal field exploration in all systems typically includes geologic mapping, geochemical and geophysical studies, and drilling with logging (Ármannsson & Fridriksson, 2009; Boden, 2016; D'amore & Panichi, 1985; Domra Kana et al., 2015; Gasperikova & Cumming, 2020; Harvey et al., 2014; Minissale, 2018; Ochieng, 2014; Rodriguez-Gomez et al., 2021; Stober & Bucher, 2021; van der Meer, Hecker, et al., 2014; Witter et al., 2019; Wright et al., 1985). Mapping has various objectives, including determining the structural setting of a prospective area and identifying any surficial features associated with active or paleo-hydrothermal systems like fumaroles, hot springs, and hydrothermal alteration assemblages (Boden, 2016; Harvey et al., 2014). Assessing the distribution of geothermal features across multiple fields provides insights into the overall setting of a potential geothermal system, aiding in identifying critical indicators and efficiently targeting geothermal resources.

Mapping the types and distribution of indicator minerals is also valuable in geothermal exploration (Browne, 1978; Savitri et al., 2021; Villeneuve et al., 2019). Various alteration minerals may reflect regional temperatures (Browne, 1978; Henley & Ellis, 1983; Reyes, 1990), pH levels (Reyes, 1990), permeability (Lagat, 2009; Reyes, 1990), and the paleo-fluid chemistries (Reyes, 1990; Vidal et al., 2018). Remote sensing (RS) in geothermal exploration utilizes spectral signals of vast areas to detect the distribution of alteration minerals (C. Bishop et al., 2018; Calvin & Pace, 2016; Kratt et al., 2010; Rodriguez-Gomez et al., 2021; Savitri et al., 2021; Simpson & Rae, 2018). Spectral mineral mapping has been widely applied by using RS data from different platforms, such as ASTER (Calvin et al., 2015; Cavur et al., 2024; van der Meer, Hecker, et al., 2014), Landsat 8 (Nait Amara et al., 2019; Salamba et al., 2019), or WorldView-3 (Kruse & Perry, 2013; Mars, 2018). These studies demonstrate the powerful ability and potential of mineral mapping in geothermal exploration, as large areas can be quickly prioritized for more detailed field analyses based on interpretations of these RS data.

Faults serve as conduits for hydrothermal fluids in geothermal systems (Curewitz & Karson, 1997; Lemgruber-Traby et al., 2023; McNamara et al., 2019; Siler, 2023; Trainor-Guitton et al., 2023). Exploration efforts can be more effectively directed by identifying the structural setting of a prospective area and distinguishing between active and inactive faults. There is also a close relation between fault systems and mineral alteration in many geothermal systems (Liotta et al., 2020, 2021; Micklethwaite et al., 2010; Taussi et al., 2023). Geothermal exploration can be refined when fault maps are integrated with mineral alteration maps (Carranza et al., 2008; Jolie et al., 2015; Mahzari et al., 2021). Fault mapping traditionally relies on ground-based geologic mapping, but recently, emerging RS techniques, including LiDAR, have improved the efficiency of fault mapping (Ahmadi & Pekkan, 2021; Bemis et al., 2014; Cawood et al., 2017).

Land surface temperatures (LST) are directly linked to geothermal gradients. A region with higher LST generally suggests a potential for a geothermal system, as it may be a proxy for deeper, elevated temperatures (Boden, 2016; Domra Kana et al., 2015; Harvey et al., 2014; Sekioka & Yuhara, 1974; van der Meer, Hecker, et al., 2014). LST can be acquired through ground-based surveys employing temperature probes (Blake et al., 2020; Coolbaugh, Sladek, et al., 2007; Zehner et al., 2012; Zimmerman et al., 2023). Using satellite images like ASTER or Landsat 8 with RS analyses is another way to acquire LST. (Coolbaugh, Kratt, et al., 2007; Gemitzi et al., 2021; Silvestri et al., 2020), which can be used alone or integrated with ground-based temperature mapping.

Several geothermal studies incorporate maps of (1) indicator minerals and faults (Achieng et al., 2017; Vaughan et al., 2005), (2) faults and LST (Chan et al., 2018; Gemitzi et al., 2021), (3) indicator minerals and LST (Reath & Ramsey, 2013; Rodriguez-Gomez et al., 2021), but the studies mainly focused on visual comparisons between the distribution of limited attributes. While some researchers have explored all three parameters of indicator minerals, faults, and LSTs in geothermal research (Abubakar et al., 2019; Calvin et al., 2015), an in-depth, data-driven analysis of their relations is lacking, especially regarding how these connections apply across geothermal fields in different geological settings. There is still much to discover about the relations between mineral maps, fault maps, and LSTs. Furthermore, there is a shortage of data-driven research supporting these relations in geothermal exploration, as well as the applicability of these relations across different geothermal systems. With the growing application of machine learning (ML) and artificial intelligence (AI) in geothermal exploration (Muther et al., 2022; Okoroafor et al., 2022), some studies have included the three parameters above (Assouline et al., 2019; Moraga et al., 2022; Mudunuru et al., 2022). However, to fully leverage AI and ML performance, systematic data-driven research is needed to assess relations between parameters for modeling.

To address these challenges, we introduce a data-driven approach integrating multiple statistical learning methods to uncover relations among three exploration parameters (hereafter referred to as Selected Geothermal Parameters, SGP): indicator minerals, faults, and LSTs. For this purpose, we collected and curated datasets of SGP from three operating geothermal systems: the Coso geothermal field (CGF) in California, USA, as well as the Brady geothermal fields (BGF) and Desert Peak geothermal fields (DPGF) in Nevada, USA. We employed spatial and non-spatial analysis to statistically elucidate significant relations among SGP across several geothermal areas to enhance understanding of geothermal exploration.

H.3 The Study Areas

The Coso geothermal field (CGF, Figure H.1a) is approximately 260 km northeast of Los Angeles and about 50 km northwest of Ridgecrest in south-eastern California, USA. It is situated at the Coso Range of the Mojave Desert east of the Sierra Nevada.

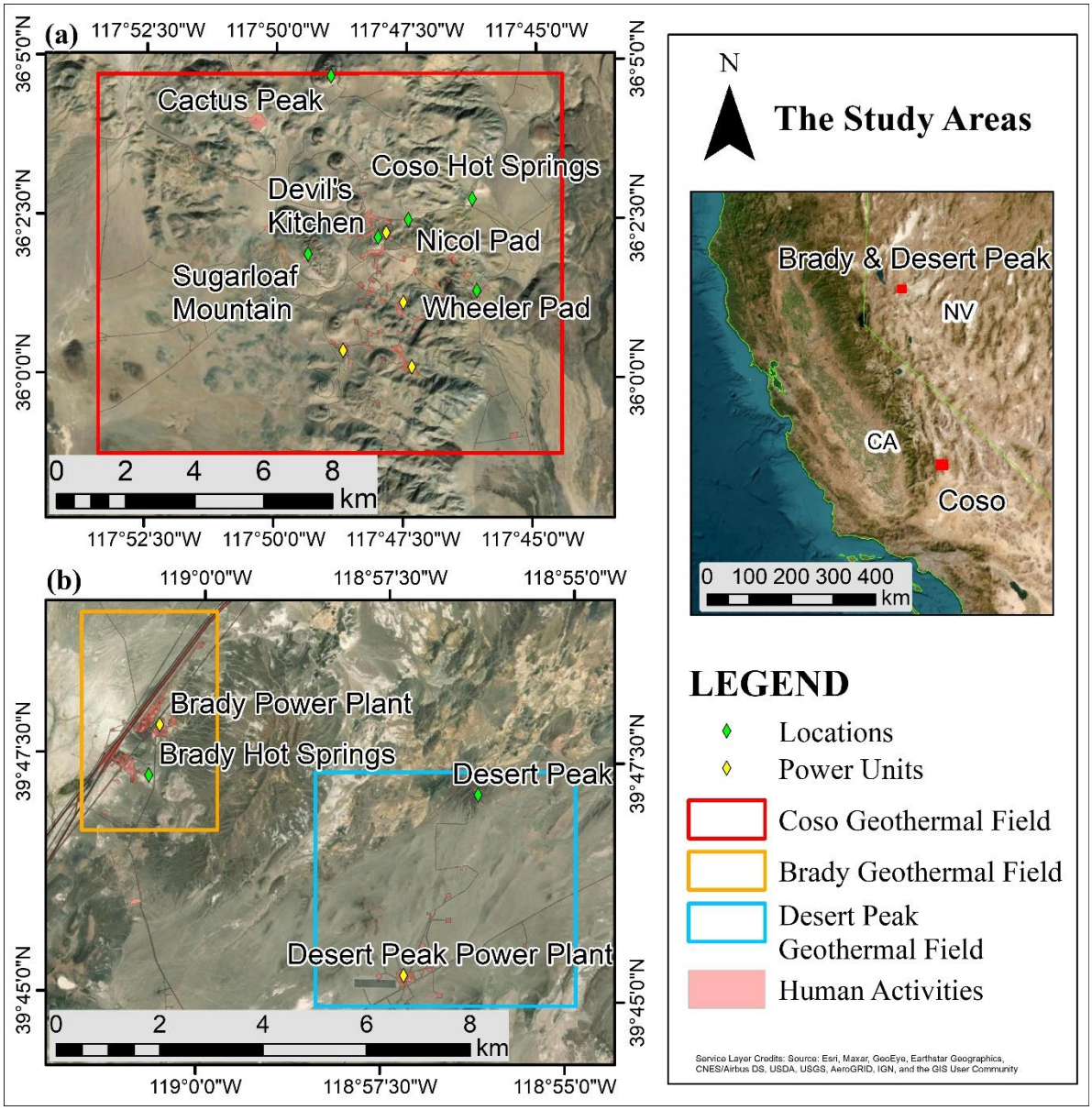

Figure H.1 The study areas. The human activities are the regions masked in mineral mapping to exclude them from the mineral mapping exercise. The study areas, inside the red, orange, and blue boxes, are approximately 148 km^2, 11 km^2, and 23 km^2, respectively.

The CGF is spatially and temporally associated with the Coso Volcanic Field (CVF), with CGF located at the center of the CVF. The CVF is a Pleistocene-Holocene age, a bimodal field comprised mostly of rhyolite domes and flows, pyroclastic successions, and minor amounts of basalt flows and cinder cones (Duffield & Bacon, 1981; Whitmarsh, 1998). Figure H.1a shows the select landmarks from the CGF, including hydrothermal alteration (Devil's Kitchen, Coso Hot Springs, Nicol Pad, and Wheeler Pad), rhyolite domes (Sugarloaf Mountain and Cactus Peak), and the power blocks.

The CGF is home to one of the largest geothermal fields in the U.S., with a capacity of 270 MWe (Monastero, 2002) derived from four power blocks (Figure H.1 a). It is a volcanic geothermal field in an

extensional tectonic setting (Jolie et al., 2021; Monastero et al., 2005; Sigurdsson et al., 2015). The resource is hosted by altered Jurassic and Cretaceous granitic and metamorphic rocks. The surface volcanic features and the heat are the product of the shallow rhyolite magma chamber that underlies the CVF (Duffield & Bacon, 1981; Manley & Bacon, 2000; Whitmarsh, 1998).

The Brady geothermal field (BGF) and the Desert Peak geothermal field (DPGF) are approximately 70 km northeast of Reno within the Great Basin west central Nevada (Figure H.1 b). The power generation capacities are 26.1 MWe at BGF and 32.5 MWe at DPGF (Faulds et al., 2006). Figure H.1 b presents the locations of the geothermal power plants and the area's major landmarks (Brady Hot Springs and Desert Peak).

The CGF, BGF, and DPGF are all within the Basin and Range physiographic province. Unlike the CGF, however, no active volcanism is associated with the BGF or the DPGF (Jolie et al., 2021; Kratt et al., 2006; Sigurdsson et al., 2015). The BGF and DPGF are primarily comprised of Tertiary volcanic and sedimentary rocks that overlie Mesozoic age metamorphic and plutonic basement rocks (Benoit et al., 1982; Faulds et al., 2003). They are within a northeast-trending zone locally referred to as the Humboldt structural zone (Faulds et al., 2003; Rowan & Wetlaufer, 1981)Both geothermal fields are characterized by the Humboldt structural zone's northeast striking, normal, and left-lateral faults and localized high-heat flows. These faults serve as the main conduits for the up-flow of geothermal fluids (Faulds et al., 2012, 2017; Kratt et al., 2006). Although BGF and DPGF are in similar geological settings, their surface features differ. Brady contains geothermal manifestations, including fumaroles and silica sinter (Faulds et al., 2012, 2017). By contrast, Desert Peak is a blind geothermal system with no apparent geothermal feature on the surface (Benoit et al., 1982; Calvin et al., 2015; Craig et al., 2021).

Table H-1 lists selected features from the three study areas, obtained from the Open Energy Information (Brodt-Giles, 2014). Table H-1 lists the geologic features in the three areas, including the types of geological settings, reservoir conditions, and surficial geothermal manifestations. The variabilities across the study areas facilitate this study in assessing the transferability of relations between SGP.

Table H-1 Geothermal features of the CGF, BGF, and DPGF.

	CGF	BGF	DPGF
Geological settings	magmatic	amagmatic	amagmatic
Geothermal surface manifestations	present	present	absent
Average temperature of geofluid*	275°C	187 °C	213 °C
Depth to reservoir top*	500 m	300 m	762 m
Depth to reservoir bottom*	3500 m	1676 m	1280 m
Average depth to reservoir.*	2000 m	988 m	1021 m
Study area dimensions	148 km^2	11 km^2	23 km^2

*: data from the Open Energy Information (Brodt-Giles, 2014).

H.4 Methodology

We followed a two-stage methodology. The first stage is data collection and preparation of the SGP. The second is non-spatial and spatial analyses to explore the relation between the SGP.

Data Collection and Preparation

SGP datasets of the CGF, BGF, and DPGF are acquired and preprocessed according to the needs of statistical analysis. We organized all the raster datasets with 30-metre by 30-metre pixel resolution, using the resolution of the mineral maps. The raster datasets were transformed into points for statistical analyses. A total of seven datasets were derived from the SGP: Two-Class Mineral Maps, Mineral Density Maps, Fault Trace, Fault Distance Maps, Fault Density Maps, Multiclass Temperature Maps, and Two-class Temperature Maps. The following sections provide the details of the data collection and preparation.

Indicator Mineral Map.

The mineral mapping was based on multispectral VNIR-SWIR (visible and near-infrared to short-wave infrared) images from ASTER (Advanced Spaceborne Thermal Emission and Reflection Radiometer) satellite (NASA LP DAAC, 2015). ASTER data were analyzed by using mineral spectra from the Coso Spectral Library (Cavur et al., 2023) for the CGF and from the USGS Spectral Library (Kokaly et al., 2017) for the BGF and DPGF. The indicator minerals—alunite, chalcedony, hematite, kaolinite, and opal—were chosen because they occur across all three study areas (Erika, 2022). Mineral

maps were created using ENVI software and an R-based mapping module (Moraga & Duzgun, 2022). Regions of human activities (Figure H.1) were masked to minimize interference from human-made objects.

We used five target detection algorithms in ENVI, as they don't require assigning non-target spectra (Jin et al., 2009; Wolfe & Black, 2018) for the mapping of each indicator mineral. These algorithms are ACE (Adaptive Coherence Estimator), CEM (Constrained Energy Minimization), MF (Matched Filtering), MTMF (Mixture Tuned Matched Filtering), and SAM (Spectral Angle Mapper). This process initially produced 25 mineral maps (5 minerals × 5 algorithms). To enhance mapping accuracy, the outputs for each mineral were fused into a single map, resulting in five final indicator mineral maps. It has been demonstrated that combining results from multiple algorithms can improve the reliability of mineral mapping (Cavur et al., 2024).

The workflow of indicator mineral map data preparation is presented in Figure H.2. Two datasets based on the indicator mineral maps were prepared for data analysis. The first dataset is the Two-Class Mineral Maps. The pixels where indicator minerals were mapped were converted point datasets in GIS. In addition, we summarized pixels lacking indicator minerals and created point datasets to represent background conditions where no indicator mineral was present. Second, the mineral maps were converted to Mineral Density Maps through the Kernel Density tool in ArcGIS. After conducting a series of tests on various distance bands, a 1000-metre distance band was optimal. This distance band effectively preserves most details in the mineral densities for each study area. Mineral Density Maps were normalized by rescaling to a range of 0 to 1.

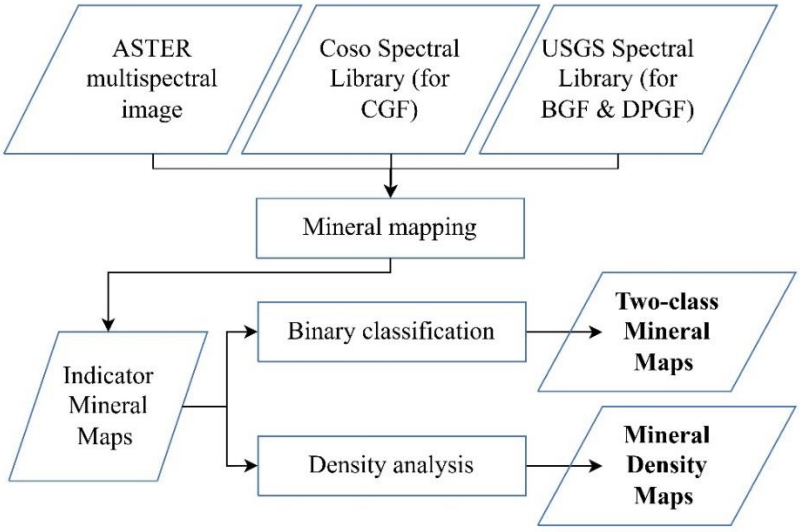

Figure H.2 Workflow of indicator mineral map data preparation. Two datasets, in bold, were prepared based on initial indicator mineral maps: Two-Class Mineral Maps (right) and Mineral Density Maps (bottom-right).

Fault Map.

We compiled the fault maps of polylines in GIS from previous literature for the CGF (Blankenship, 2016; Duffield & Bacon, 1981; Hulen, 1978; Jennings & Bryant, 2010; Whitmarsh, 1998) and BGF-DPGF (Faulds et al., 2012, 2017). The workflow of fault map data preparation is presented in Figure H.3. Three datasets were derived from the fault traces. First, the polylines of fault were converted to Fault Trace with an interval of 30 meters, due to set resolution. Second, Fault Distance Maps are raster data that indicate the distance to the closest fault from each pixel. Third, Fault Density Maps were generated using the Kernel Density tool in ArcGIS, with a 1000-metre distance band applied to ensure detailed representation across all study areas. The Fault Density Maps were normalized by rescaling to a range of 0 to 1.

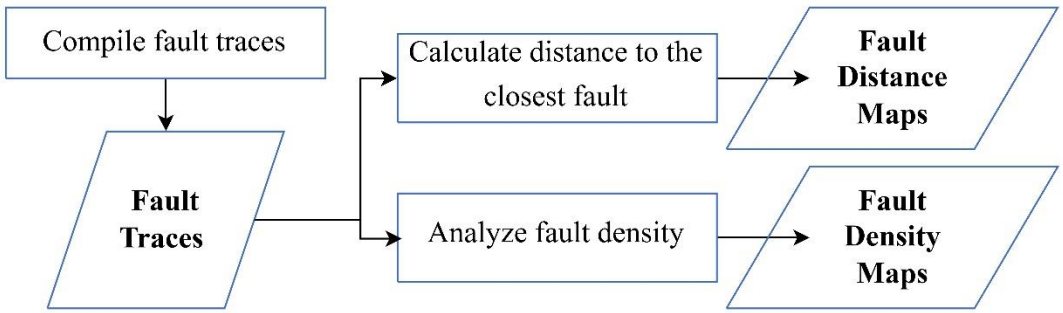

Figure H.3 Workflow of fault map data preparation. Three datasets, in bold, were prepared based on faults: Fault Traces (left), Fault Distance Maps (upper-right), and Fault Density Maps (bottom-right).

Land Surface Temperature (LST).

Figure H.4 presents the workflow for preparing LST data. The LST used for the CGF was based on a 2-metre temperature probe survey (Blake et al., 2020; Zimmerman et al., 2023). Measured and corrected temperatures were interpolated to obtain raster data using the Kriging tool in ArcGIS. LST datasets for the BGF and DPGF were obtained from Landsat 8 data from the Geothermal Data Repository (GDR, https://gdr.openei.org/submissions/1305). The LST raster data of Landsat 8 was pre-processed to study the BGF and the DPGF (Moraga, 2022; Moraga et al., 2021b, 2021a). Two datasets were prepared using the LSTs. First, Multiclass Temperature Maps were normalized by rescaling LST from 0 to 1. Second, Two-class Temperature Maps were generated in need of categorized data in the analysis. Multiclass Temperature Maps were reclassified into high- and low-temperatures using Jenk's Natural Break optimization in ArcGIS, which minimizes differences within each class while maximizing differences between each class.

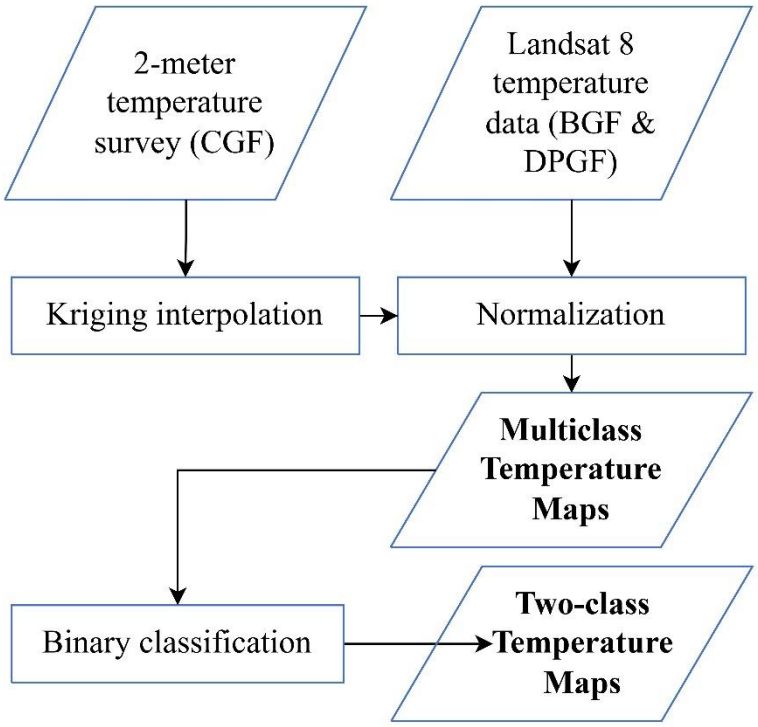

Figure H.4 Workflow of LST data preparation. Two datasets, in bold, were prepared based on LSTs: Multiclass Temperature Maps (right) and Two-class Temperature Maps (bottom-right).

Data Analyses

The data analyses explore possible relations between SGP. Table H-2 illustrates adopted data analysis methods and corresponding input datasets. We tested the hypothesis of relations between SGP by using non-spatial and spatial analyses. The non-spatial analyses include histograms with CDF (cumulative distribution function) plots, two-sample Kolmogorov-Smirnov test (K-S test), one-way analysis of variance (ANOVA), and linear regression. The spatial analysis includes colocation analysis. The input datasets are varied for each analytical method and hypothesis, as listed in the table. The application of various approaches concurrently assesses the patterns identified in each technique. The non-spatial analyses provided inference on possible connections between the SGP, while the spatial analysis explored the spatial relations of SGP.

Non-spatial analysis.

Selected input datasets listed in Table H-2 were joined in GIS. Histograms with CDF plots are constructed to explore potential patterns between the SGP. The histograms with CDF plots help compare each indicator mineral's data distribution against faults and LSTs. They also help compare the distribution of high- and low-temperature data against faults. We used the K-S test, ANOVA, and linear regression to make inferences from histograms with CDF plots. The evaluation was conducted using Matlab functions of kstest2, anova1, and fitlm.

K-S test is a nonparametric test that compares two datasets by analyzing the maximum absolute difference between their CDFs and judges whether they have comparable distributions. (Marsaglia et al., 2003; Massey Jr, 1951; Miller, 1956). We examined whether each indicator mineral presented distinct distributions relative to faults and LSTs, compared to the background condition where no indicator minerals were mapped. Additionally, we examined whether high- and low- temperatures present distinct distributions relative to faults.

ANOVA indicates whether various datasets have a common mean or distribution (Dunn & Clark, 1986; Wackerly et al., 2008). While the K-S test identifies differences in distributions, ANOVA complements this by providing a quantitative framework to evaluate variations between datasets. Following the K-S test, we compare the distributions of each indicator mineral regarding their relations to faults and LSTs. We also compare the distributions of high- and low-temperatures regarding their relations to faults.

Linear regression could provide models that indicate the relationship between a dependent variable and one or more independent variables (Dumouchel & O'Brien, 1989; Holland & Welsch, 1977; Street et al., 1988). We used simple linear regression, $y=a+bx$, where a is the intercept and b is the slope, indicating the degree of correlation between y (dependent variable) and x (independent variable). Correlation (b) is the key parameter to interpret the relation between indicators. The regression models explore the positive or negative correlation between the SGP. We applied the regression by setting the Fault Density Maps and Multiclass Temperature Maps as the dependent variables while setting the other datasets as independent variables (Table H-2).

Spatial analysis.

It evaluates the spatial relations of SGP using colocation analysis (Leslie & Kronenfeld, 2011; F. Wang et al., 2017), which examines two groups of SGP points to determine if one group colocates with the other neighboring group. Since colocation analysis requires an assigned distance band, multiple distance bands were tested and reviewed based on the plots of the LCLQ (local colocation quotient) and p-value to decide the best distance band. The selected distance band of 750 meters minimized the p-values on plots' tails (maximums & minimums) while optimizing the LCLQ level. The analysis outputs provide four LCLQ types between the SGP: Significant Isolated, Not Significant Isolated, Significant, Colocated, Not Significant Colocated, and Undefined. The distribution of LCLQ types helps identify where the SGP are colocated or isolated. In addition, the colocation patterns were compared with the known reservoir extension (Demir et al., 2024) to explore the connections between SGP colocations and their proximity to reservoirs. The colocation analysis was applied to compare (1) fault traces and neighboring indicator minerals, (2) fault traces and neighboring high temperatures, and (3) the high temperatures and neighboring indicator minerals.

Table H-2 Adopted data analysis methods and corresponding input datasets.

Relation between:	**Hypothesis**	**Analyses used for hypothesis testing**			
		Non-spatial analysis		**Spatial analysis**	
		Method	**Input data**	**Method**	**Input data**
Indicator mineral & fault	**H0:** Patterns of indicator minerals are not related to faults **H1:** Patterns of indicator minerals are related to faults	• Histograms & CDF plots • K-S test • ANOVA • Linear regression	• Two-class Mineral Maps † • Mineral Density Maps‡ • Fault Distance Maps† • Fault Density Maps†‡	Colocation analysis	• Two-class Mineral Maps • Fault Traces
Indicator mineral & LST	**H0:** Patterns of indicator minerals are not related to LST **H1:** Patterns of indicator minerals are related to LST		• Two-class Mineral Maps† • Mineral Density Maps‡ • Multiclass Temperature Maps†‡		• Two-class Mineral Maps • Two-class Temperature Maps
Fault & LST	**H0:** Patterns of fault are not related to LST **H1:** Patterns of faults are related to LST		• Multiclass Temperature Maps‡ • Two-class Temperature Maps† • Fault Distance Maps† • Fault Density Maps†‡		• Two-class Temperature Maps • Fault Traces

H0:null hypothesis; **H1:** alternative hypothesis;

†: used in histograms, CDF plots, K-S tests, and ANOVA; ‡: used in linear regressions.

H.5 Results

With both non-spatial and spatial analysis. The results reveal that different indicator minerals present varied distributions against faults and LST. High- and low- temperatures also present different distributions against faults. In addition, the behaviors of SGP are different at CGF and BGF from DPGF. We used the following abbreviations for tables and figures in subsequent sections: alu. (alunite), cdy. (chalcedony), hem. (hematite), kln. (kaolinite), opl. (opal), N.M. (no indicator mineral), H.T. (high-temperature zones), and L.T. (low-temperature zones).

Non-Spatial Analysis

In the non-spatial analysis, the histograms with CDF plots reveal multiple potential trends where each indicator minerals and temperature levels exhibit distinct patterns regarding fault proximity. The K-S test, ANOVA, and linear regression prove that each indicator mineral has different tendencies toward faults and LSTs. High-temperature areas also present different fault tendencies on fault proximity than low temperatures. The analyses also identified that LST at DPGF displays weaker connections with both indicator minerals and faults than the other study areas. The following sections summarize the key findings from the non-spatial analyses.

Histograms with CDF plot.

Histograms with CDF plots show the distribution of datasets. Due to the large number of datasets, this section presents a few examples to support discussions. They reveal several potential patterns between the SGP. Figure H.5 presents an example of histograms and CDF plots that show the patterns between Two-Class Mineral Maps and Fault Distance Maps at CGF. The CDF plots shift toward the top-left corner for distributions closer to faults, whereas they move away from the top-left corner for distributions further to faults. In the case of CGF, alunite, chalcedony, kaolinite, and opal are closer to faults than the background (N.M.). Alunite and kaolinite show stronger tendencies toward faults. Overall, for all study areas, the indicator minerals were observed to be closer to faults than the backgrounds in each study area. Comparable patterns were also discovered between Two-Class Mineral Maps and Fault Density Maps, where indicator minerals tend to occur at higher fault densities than backgrounds. The relations between indicator minerals and faults varied noticeably among individual minerals.

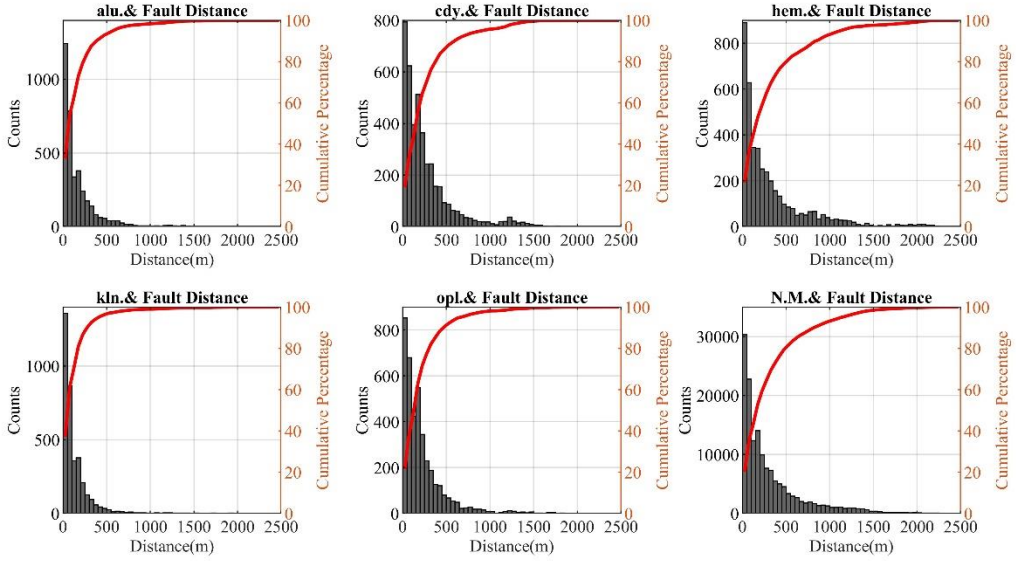

Figure H.5 Histograms (gray boxes) and CDF plots (red lines) of the patterns between Two-Class Mineral Maps and Fault Distance Maps at CGF. Multiple minerals show distributions closer to faults than the locations without indicator minerals (bottom-right), with CDF plots shifting closer to the top-right corners. The patterns between minerals are also different.

Figure H.6 presents an example of histograms and CDF plots that show the patterns between Two-class Temperature Maps and Fault Distance Maps in each study area. Similar to Figure H.5, the CDF plots shift toward the top-left corner for distributions closer to faults. High- and low- temperatures have different patterns against faults in each study area. In geothermal systems with surface manifestations (CGF and BGF), high temperatures are closer to faults. In the blind system (DPGF), the opposite pattern is observed. Similarly, high temperatures correspond to areas of higher fault density in CGF and BGF but occur in lower fault-density regions in DPGF.

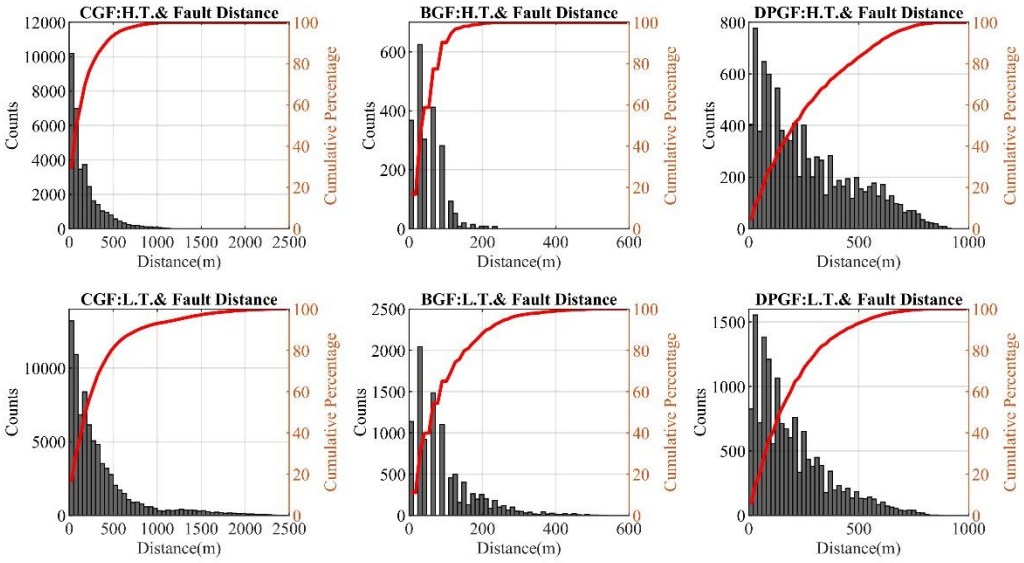

Figure H.6 Histograms (gray boxes) and CDF plots (red lines) of the patterns between Two-Class Temperature Maps and Fault Distance Maps at each study area. High temperatures (top) of CGF (left) and BGF (middle) show distributions closer to faults than DPGF (right).

Figure H.7 presents an example of histograms and CDF plots that show the patterns between Two-Class Mineral Maps and Multiclass Temperature Maps at CGF. The CDF plots shift further from the top-left corner if distributions are close to higher temperatures. In the case of CGF, alunite and kaolinite occur at higher temperature areas, while chalcedony and opal are associated with lower temperature areas compared to the background (N.M.). Overall, for all study areas, the patterns between Two-Class Mineral Maps and Multiclass Temperature Maps are inconsistent. Still, it was observed that tendencies varied between indicator minerals.

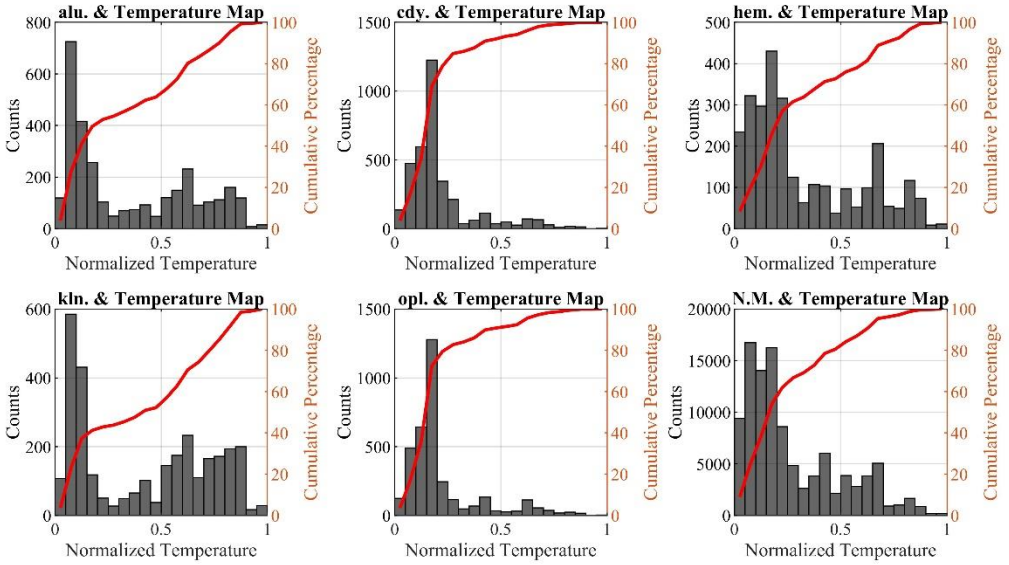

Figure H.7 Histograms (gray boxes) and CDF plots (red lines) of the patterns between Two-Class Mineral Maps and Multiclass Temperature Maps at CGF. Alunite and kaolinite are closer to higher temperatures, while chalcedony and opal are closer to lower temperatures.

K-S test.

The K-S test evaluates whether two datasets originate from the same distribution with a null hypothesis that the datasets originate from the same distribution. Table H-3 summarizes the findings of the K-S test, indicating whether the null hypothesis was rejected or not in each test.

Table H-3 The K-S test result. The null hypothesis was rejected in most cases, showing that the distributions of datasets are primarily different.

SGP	Fault Distance Map			Fault Density Map			Multiclass Temperature Map		
	CGF	BGF	DPGF	CGF	BGF	DPGF	CGF	BGF	DPGF
alu. vs. N.M.	1	0	1	1	1	1	1	1	0
cdy. vs. N.M.	1	1	1	1	1	1	1	1	1
hem. vs. N.M.	1	0	1	0	1	1	1	1	1
kln. vs. N.M.	1	0	1	1	1	1	1	1	1
opl. vs. N.M.	1	1	1	1	1	1	1	1	1
H.T. vs. L.T.	1	1	1	1	1	1	NA		

0: failed to reject the null hypothesis, and 1: reject the null hypothesis

The results show that the null hypothesis of the K-S test was predominantly rejected, which means that the datasets exhibit distinct distributions. The distribution of indicator minerals differed from the background (N.M.) regarding the Fault Distance Map, Fault Density Map, and Multiclass Temperature Map. Simultaneously, high and low temperatures exhibited distinct distributions against the faults.

Since the K-S test cannot identify the intensity of difference between datasets, further ANOVA and linear regression were applied to explore the relations and indicate the differences in distribution between the SGP.

ANOVA.

ANOVA compares the data distribution and discovers the level of difference. The Two-Class Mineral Map and Temperature Map datasets were studied with the control groups (blue in Figure H.8) of N.M. (no indicator mineral) and H.T. (high-temperature). The ANOVA results are given in Figure H.8, indicating the Significant (red) and Insignificant (gray) Differences to the control group.

All Significant Differences identified by ANOVA corresponded to rejections in the K-S test, highlighting a strong agreement between the two methods. While the K-S test detected some additional differences that ANOVA did not, all failed rejections in the K-S test were consistently classified as insignificant by ANOVA.

In the analyses for indicator minerals and faults, each indicator mineral's tendencies varied. Compared with the background (N.M.) at each study area, alunite, kaolinite, and opal presented tendencies toward smaller fault distances and higher fault density, or at least close to the background. In contrast, chalcedony and hematite are similar in having background patterns or lower fault proximity. No apparent patterns between the mineral maps and fault maps were observed in ANOVA to differentiate the study areas.

In the analyses for LST and faults, the outcome reflects the characteristics of the blind geothermal field at DPGF. The high temperatures at CGF and BGF presented tendencies toward smaller fault distances and higher fault density. In contrast, the high temperatures at DPGF were further from faults, and the tendency with fault density was not as evident as in CGF and BGF. The finding indicates that the behavior between faults and LST differed in a blind geothermal system like DPGF.

In the analyses for indicator minerals and LSTs, the indicator minerals did not present evident and consistent patterns across all study areas. At CGF and BGF, alunite, hematite, and kaolinite tend to be at higher temperatures, while chalcedony and opal tend to be at lower temperatures or close to the background. In contrast, the case of DPGF showed that hematite, kaolinite, and opal tend to be at lower temperatures. This difference between CGF, BGF, and DPGF indicates that the behavior between indicator minerals and LSTs also differed in a blind geothermal system.

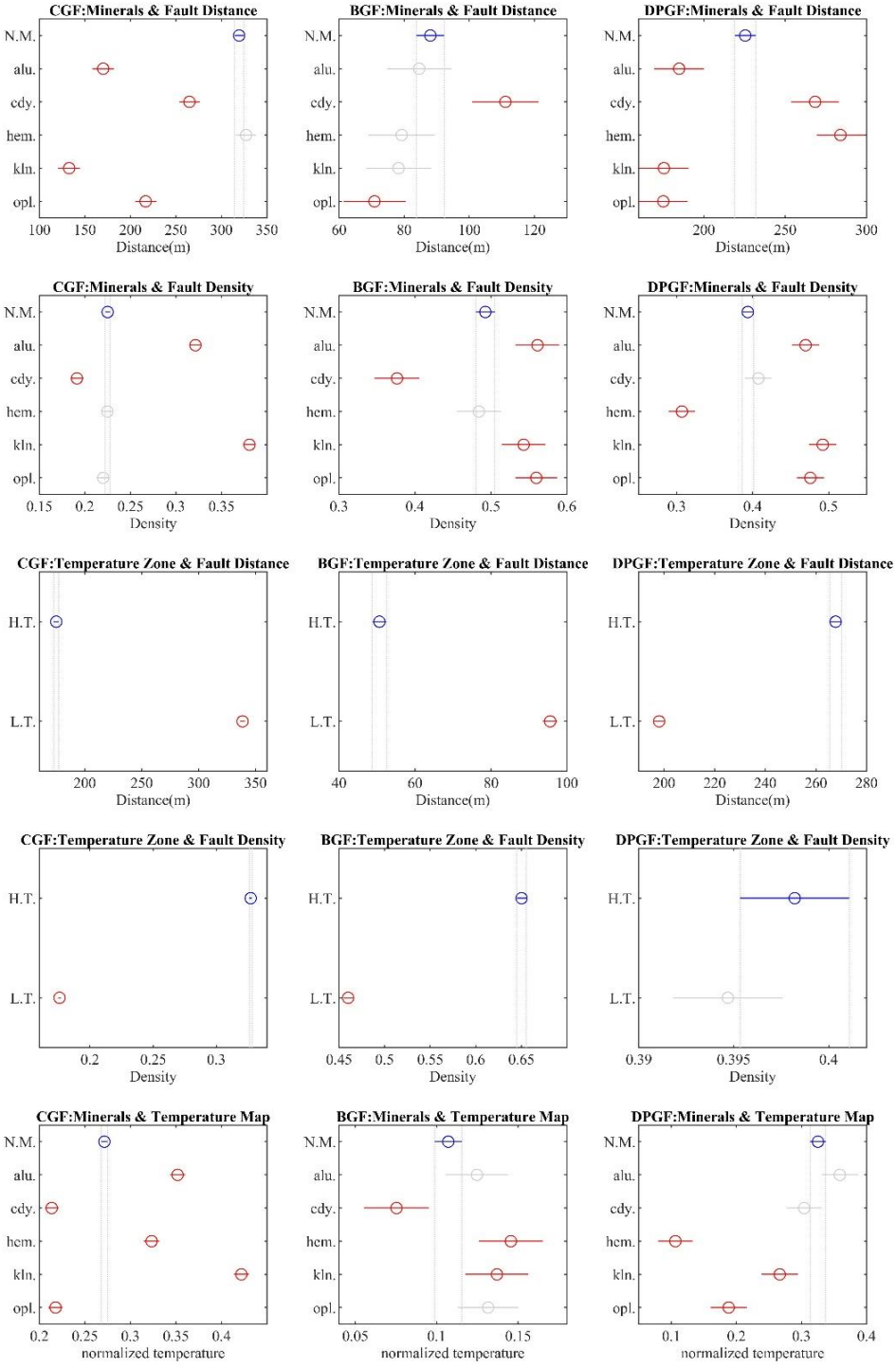

Figure H.8 The multiple comparisons of ANOVA. The plots show the mean estimates (circles) and 95% confidence intervals (bars) for each group of SGP. Red symbols highlight groups with Significant Differences from the control group (blue). Gray symbols indicate groups with Insignificant Differences where confidence intervals overlap with the control group.

Linear regression.

The linear regression cross-evaluates the ANOVA results from a different approach. The regression provides correlation coefficients that indicate whether the SGP are positively or negatively correlated in each study area. Table H-4 presents the intercepts and coefficients for Fault Density Maps as the dependent variable (y) and Mineral Density Maps as the independent variable (x).

Table H-5 shows the results for Multiclass Temperature Maps as the dependent variable (y), with Fault Density Maps and Mineral Density Maps as the independent variable (x). The p-values of the intercepts and coefficients are mostly 0, except for a few non-zero cases with a maximum p-value of 0.016. The p-values denote the significance of the regression models.

Table H-4 Regression parameters for Fault Density Maps against Mineral Density Maps

SGP (x)	**Fault Density (y)**					
	CGF		**BGF**		**DPGF**	
	intercept	**coefficient**	**intercept**	**coefficient**	**intercept**	**coefficient**
alu.	0.206	0.415†	0.397	0.318†	0.190	0.590†
cdy.	0.236	-0.130†	0.609	-0.497†	0.412	-0.107 ‡
hem.	0.229	-0.010 ‡	0.456	0.142‡	0.462	-0.561 †
kln.	0.200	0.474†	0.422	0.277†	0.262	0.504 †
opl.	0.227	0.014 ‡	0.263	0.582†	0.339	0.362†

†: Significant Differences in ANOVA; ‡: Insignificant Differences in ANOVA.

Table H-5 Regression parameters for Multiclass Temperature Maps against Fault Density and Mineral Density Maps

SGP (x)	**Multiclass Temperature (y)**					
	CGF		**BGF**		**DPGF**	
	intercept	**coefficient**	**intercept**	**coefficient**	**intercept**	**coefficient**
fault	0.144	0.584†	-0.016	0.253 †	0.346	-0.073‡
alu.	0.240	0.548†	0.071	0.124‡	0.340	-0.065‡
cdy.	0.291	-0.221†	0.129	-0.087 †	0.345	-0.181‡
hem.	0.213	0.666†	0.049	0.226 †	0.345	-0.235 †
kln.	0.232	0.573†	0.084	0.094 †	0.406	-0.331†
opl.	0.284	-0.185†	0.028	0.203‡	0.406	-0.561†

†: Significant Differences in ANOVA; ‡: Insignificant Differences in ANOVA.

The correlation coefficients from the regression models were compared with the ANOVA outcomes. None of the coefficients conflicts with the tendencies of Significant Differences in ANOVA (see Table H-4 and Table H-5). The regression models consolidate these substantial differences and offer additional insights into the insignificant ones in ANOVA, eventually enhancing overall analysis.

It was found in each study area that alunite, kaolinite, and opal positively correlate with Fault Density Maps, while chalcedony and hematite show lower or negative correlations (Table H-4). The patterns against Multiclass Temperature Maps varied according to the study area. At CGF and BGF, alunite, hematite, and kaolinite show positive correlations with Multiclass Temperature Maps. Whereas all indicator minerals at DPGF negatively correlate with Multiclass Temperature Maps (Table H-5). Fault Density Maps and Multiclass Temperature Maps correlate positively at CGF and BGF but negatively at DPGF, following ANOVA results between Two-class Temperature Maps and Fault Density Maps. The linear regression further indicates that the behavior between SGP at DPGF differed, with elevated LST weakly correlated with the indicator minerals and faults.

Spatial Analysis

The colocation analysis examines the distributions of colocated SGP and helps reveal their relations against reservoirs. The results corroborated the non-spatial analysis, showing that mineral maps of different indicator minerals exhibit diverse tendencies against faults or LSTs. Some indicator minerals exhibit comparable distributions in similar regions. The following sections illustrate the findings from the spatial analysis. Figure H.9 shows an example of colocation maps between faults and indicator minerals at CGF.

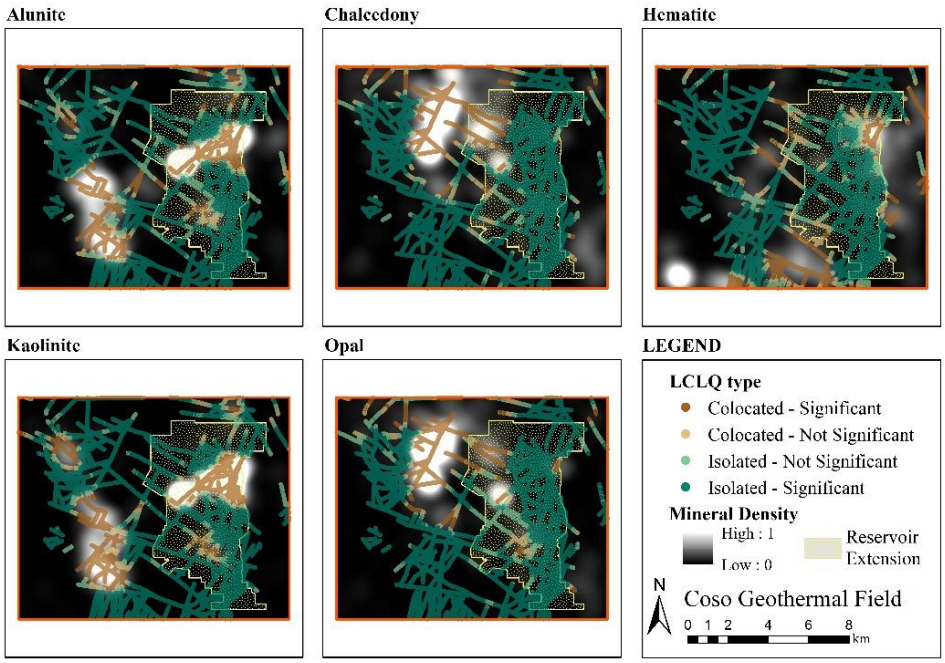

Figure H.9 Colocation maps of faults and neighboring indicator minerals at CGF.

Faults and indicator minerals.

At CGF, alunite and kaolinite show similar colocations in two major clusters, with the eastern one within the reservoir. Chalcedony and opal have similar colocations in the north. Hematite has colocations surrounding the reservoir, but some hematite in the southwest was not colocated with faults. Chalcedony, hematite, and opal are generally colocated with faults on the reservoir's edge.

At BGF, alunite, kaolinite, and opal present similar colocation patterns within the reservoir's western part. Chalcedony has limited colocations within the known reservoir. Hematite has colocations at the northern and eastern edges of the reservoir. At DPGF, alunite and kaolinite have similar patterns with major colocations northeast of the reservoir. Chalcedony, hematite, and opal present distinctive patterns that generally fall outside the reservoir. Chalcedony and hematite also exist further from faults.

Alunite and kaolinite consistently exhibit similar colocations across all study areas, whereas opal demonstrates variable patterns, aligning with chalcedony, alunite, or kaolinite, depending on the site. Hematite shows distinct patterns compared to other indicator minerals in each study area. Notably, alunite and kaolinite are the most prevalent indicator minerals colocate with faults within reservoirs. Opal also colocates with faults in the reservoir of CGF and BGF but not in the DPGF. Chalcedony and hematite have the lowest levels of fault colocation, typically found at the peripheries of the reservoirs. In DPGF, only a few instances of mapped chalcedony, hematite, and opal are colocated with faults within the reservoir.

Faults and LSTs.

Faults present strong colocations with high temperatures around the reservoir of CGF. At BGF, faults colocate with high temperatures in the northeast and southwest of the study area. The northern clusters fall within the known reservoir. Some faults are colocated with high temperatures at DPGF, but those faults actually follow the thin regions of lower temperatures, suggesting weaker connections between fault and LST at DPGF.

LSTs and indicator minerals.

At CGF, alunite and kaolinite have similar colocations with significant clusters in the reservoir. Chalcedony, hematite, and opal have fewer colocations within the reservoir and mainly occur on the reservoir's edge. At BGF, alunite, kaolinite, and opal have similar colocations with significant clusters in the reservoir. Chalcedony has limited observed colocations in the reservoir. Hematite has colocations mainly on the edge of the known reservoir. At DPGF, alunite and kaolinite have similar patterns with major colocations northeast of the reservoir. Chalcedony and hematite have major colocations that fall on the western edge of the reservoir, at an area without faults. Opal has limited observed colocations in the reservoir.

Based on the colocation between high temperatures and indicator minerals, it was found again that alunite and kaolinite have similar patterns, while chalcedony, hematite, and opal did not consistently follow other indicator minerals. Furthermore, alunite and kaolinite are the most common indicator minerals colocating with high temperatures within reservoirs. In contrast, chalcedony and hematite have lower levels of colocations within the reservoirs and are often located at the edge of the reservoirs. Although chalcedony and hematite have major colocations at the western edge of the DPGF reservoir, that is also a region without faults. Opal colocation patterns vary across reservoirs. At CGF, it follows chalcedony distribution but shows more colocations within the reservoir. At BGF, opal colocates with alunite and kaolinite, extending south beyond the reservoir boundary. In contrast, at DPGF, opal has limited colocations within the reservoir area.

H.6 Discussion

The patterns of indicator minerals from the non-spatial analyses are summarized in Table H-6. Patterns of indicator minerals against the Fault Distance Map were based on ANOVA, while those against the Fault Density Map and Multiclass Temperature Map were determined using both linear regressions and ANOVA. Indicator minerals were categorized into two groups based on their relation with faults. Alunite, kaolinite, and opal showed positive associations, while chalcedony and hematite showed negative associations. The connections between indicator minerals and LST reveal the differences between the study areas. The study found that alunite, hematite, and kaolinite are positively related to elevated LSTs at CGF and BGF. However, these minerals are negatively associated with elevated LSTs at DPGF. In addition, chalcedony and opal have weaker relations to elevated LSTs at CGF and BGF. Overall, the correlation tendencies of indicator minerals with faults and LSTs varied by mineral. However, in the blind geothermal system, indicator minerals were not associated with elevated LSTs. Additionally, non-spatial analyses revealed a strong association between faults and elevated LSTs at CGF and BGF, whereas DPGF exhibits an opposite relation.

Table H-6 Relations between SGP from non-spatial analyses.

Sites	SGP	alu.	cdy.	hem.	kln.	opl.
CGF	Fault Distance Map	+	+	**x**	+	+
	Fault Density Map	+	-	-	+	+
	Multiclass Temperature Map	+	-	+	+	-
BGF	Fault Distance Map	**x**	-	**x**	**x**	+
	Fault Density Map	+	-	+	+	+
	Multiclass Temperature Map	+	-	+	+	+
DPGF	Fault Distance Map	+	-	-	+	+
	Fault Density Map	+	-	-	+	+
	Multiclass Temperature Map	-	-	-	-	-

+: positively related; -: negatively related; x: limited pattern

The spatial analyses of colocation further support the idea that indicator minerals exhibit various behaviors regarding faults and LSTs. Alunite and kaolinite consistently display similar spatial patterns, colocating with faults and high temperatures within reservoirs, while chalcedony and hematite show fewer colocations and mostly near reservoir edges. Opal's distribution varies by study area, showing moderate to high colocation with faults and high temperatures at CGF and BGF but not at DPGF. In addition, the

colocations between faults and high temperatures also suggest a weaker connection between faults and LSTs in blind geothermal fields such as DPGF.

In summary, the study discovered multiple patterns on each indicator mineral: Alunite and kaolinite were strongly associated with faults across all study areas and positively correlated with elevated LSTs at CGF and BGF. Chalcedony showed limited associations with both faults and elevated LSTs. Hematite displayed weak associations with faults but positive correlations with elevated LSTs at CGF and BGF. Opal was associated with faults, but its correlation with elevated LSTs was weaker than alunite and kaolinite.

Alunite and kaolinite mineralized regions in hydrothermal systems have long been identified as an alteration assemblage formed when acidic, sulfur-rich fluids from magmatic sources interact with surrounding rocks (Arribas Jr, 1995; Sillitoe, 1993; White & Hedenquist, 1995). In active geothermal systems, this can be manifest as steam-heated, hydrothermally altered ground (advanced argillic alteration), which generally utilizes faults as major channels to rise (Hedenquist & Arribas, 2022; Jolie et al., 2021). This study demonstrates a strong association of alunite and kaolinite with fault systems and LSTs at CGF and BGF, driven by the rapid ascent of hydrothermal fluids along high-angle faults (Faulds et al., 2017; Monastero et al., 2005; Siler et al., 2021; Whitmarsh, 1998).

Opal in geothermal fields is often associated with silica sinters formed by the discharging of alkali-chloride near-neutral hot water (Hedenquist & Arribas, 2022; Jolie et al., 2021; Rodgers et al., 2004). The discharge of fluids is strongly influenced by groundwater levels and geology, leading to surface manifestations with footprints varied from those significant halos of advanced argillic alteration. The alteration model is supported by the strong connection between opal and fault maps and the relatively weaker connection between opal and LSTs. This also explains why opal sometimes follows alunite and kaolinite at the alteration halo, but sometimes on the edges of geothermal reservoirs. The chalcedony and hematite in this study showed limited links with faults, suggesting that the genesis of these minerals on the surface may not be associated with fluid supplies from faults. Instead, other parameters such as weathering or rock-forming may contribute more to these mineral occurrences on surfaces.

The SGP tendencies at DPGF differed from those of CGF and BGF. All indicator minerals exhibited negative correlations with LST at DPGF. Additionally, faults at DPGF were negatively associated with elevated LSTs, contrasting the positive relations observed at CGF and BGF. These findings highlight the significance of ground-based temperature surveys in blind geothermal systems, where LST anomalies are not linked to faults or indicator minerals.

H.7 Conclusion

This study investigated the relations between the SGP (indicator mineral maps, fault maps, and LSTs) from three geothermal fields (CGF, BGF, and DPGF) using a novel data-driven approach. This study demonstrates that mapping alunite, kaolinite, or opal through spectral RS can support targeting fault zones in geothermal fields. The result also highlights the importance of LST surveys in exploring blind geothermal areas.

We identified multiple relations that would advance data collection and analysis efforts for geothermal exploration. At CGF and BGF, alunite and kaolinite are correlated with faults and elevated LSTs. This indicates that these minerals serve as reliable indicators of active hydrothermal systems, in which faults function as pathways for ascending hydrothermal fluids. The presence of alunite and kaolinite is linked to acidic, sulfur-rich hydrothermal fluids, and their spatial distribution may indicate the location of reservoirs like CGF and BGF. Opal is positively correlated with faults but is negatively correlated with elevated LSTs. The formation of opal is associated with silica sinter from discharged near-neutral hot waters, accounting for its variable association with LSTs. Chalcedony and hematite show relatively limited or no significant associations with faults and elevated LSTs, suggesting their formation may be influenced more by surface or near-surface processes rather than deep hydrothermal fluid.

Unlike CGF and BGF, all indicator minerals at DPGF exhibit negative correlations with elevated LST. This indicates that the LST anomalies at DPGF are inconsistent with the occurrence of the indicator minerals. The faults at DPGF exhibit a negative correlation with elevated LSTs. The findings contrast with the positive correlations observed at CGF and BGF, suggesting that the behaviors between SGP may fundamentally differ in blind geothermal fields like DPGF. However, the examination still provides insights into the SGP distribution in blind geothermal sites.